MOLECULAR GAS IN NEARBY MERGING GALAXIES

CLOUD-SCALE MOLECULAR GAS PROPERTIES IN NEARBY MERGING GALAXIES

By Nathan Brunetti, M.Sc. B.Sc.

A Thesis Submitted to the School of Graduate Studies in Partial Fulfilment of the Requirements for the Degree Doctor of Philosophy

TITLE: Cloud-scale molecular gas properties in nearby merging galaxies

AUTHOR: Nathan Brunetti, M.Sc. (McMaster University) B.Sc. (University of Massachusetts Amherst)

SUPERVISOR: Dr. Christine D. Wilson

NUMBER OF PAGES: xxiii, 287

Abstract

In this thesis we present cloud-scale ALMA observations of two local mergers, NGC 3256 and NGC 4038/9 (the "Antennae"), in CO J=2–1. Through a pixel-based analysis of NGC 3256 we measure molecular-gas properties and compare to nearby spiral galaxies from the PHANGS-ALMA survey. NGC 3256 exhibits high mass surface densities, velocity dispersions, peak brightness temperatures, virial parameters, and internal turbulent pressures. High surface densities are expected to accompany its high star-formation rate, and high brightness temperatures may indicate warmer gas, heated by the vigorous star formation. Large virial parameters and internal pressures imply the molecular gas is not bound by self-gravity, but we explore how material external to clouds could alter this. We argue the molecular gas in NGC 3256 is smoother than in nearby spiral galaxies down to 55 pc.

We also perform a cloud analysis of our NGC 3256 observations, identifying 185 clouds, and find similar results to the pixel analysis. We calculate additional cloud properties including eccentricity, CO luminosity, CO-estimated mass, virial mass, size-linewidth coefficient, and free-fall time. Properties in NGC 3256 are extreme compared to clouds from PHANGS-ALMA, including slightly larger clouds and shorter free-fall times. Cloud eccentricities in NGC 3256 are similar to those in PHANGS-ALMA galaxies, possibly indicating similar average cloud dynamical states. The shape of the cloud mass function in NGC 3256 is similar to many PHANGS-ALMA galaxies.

Finally, we analyse our NGC 4038/9 observations using the same pixel methods as used in NGC 3256. NGC 4038/9 also harbours extreme molecular-gas properties and potentially smoother emission compared to spiral galaxies, but not as extreme as NGC 3256. We find the most-massive spiral galaxies have central molecular-gas properties similar to the mergers. Virial parameters in NGC 4038/9 are similar to many spiral galaxies, making it quite different from NGC 3256, potentially due to their different

merger stages. Comparison of the overlap region of NGC 4038/9 in CO (2–1) to CO (3–2) shows general agreement.

Acknowledgements

First, thanks so much to Dr. Christine Wilson for working with me over these years and giving me some incredible opportunities along the way. From first meeting at NRAO lunch talks, to laughing about the Oxford University Press editor removing Oxford commas from my paper, to discussing open questions left from my thesis. I have been lucky to have you as a knowledgeable and patient guide on this path.

Thanks also to my supervisory committee, Dr. Alison Sills and Dr. Bill Harris, who inspired me with exciting scientific discussions in committee meetings, classes, and their offices when I had "just a quick question." You made sure I took time to step back to understand the motivations and guiding questions for an analysis when I wanted to jump right into the details.

Thanks to Dr. Doug Welch for use of the "astro" computer, which made the data processing necessary for this thesis significantly less complicated and arduous.

Thanks to all the people in the P&A department at McMaster who made it a second home and became a second family. I felt so much support and drive to do good for others from you all. A special thanks to my fellow grad students, new and long-since departed, who have made me feel welcome right from my first day. There were some great times camping, going for coffee, getting lost on the way to/from journal club, bugging strangers to view the Moon through telescopes, Halloween parties, arguing about lab-manual edits, helping me move, talking about Twitch streamers, and much more.

I am so fortunate to have had an incredible amount of support from my parents and family along my way through grad school. Always showing interest in my progress, also helping me move (who knows how many times at this point?), making comforting places for me to escape to, and the countless other big and small things you have done for me. Thank you.

Finally, I know I could not have accomplished this without Jess, so thank you for making the journey with me. You always reminded me that I had to nurture the other sides of my life to also succeed in my work. Whether it was House M.D. marathons, dumpling cooking adventures, pots of tea on the weekend, long walks, or even longer drives to and from Massachusetts. My life is so much richer with you in it. Let's see what else we can accomplish together.

Contents

List of Figures

List of Tables

List of Abbreviations

IRAS	*Infrared Astronomical Satellite*
AAS	American Astronomical Society
ACA	Morita Atacama Compact Array
AD	Anderson-Darling
AGN	active galactic nucleus
ALMA	Atacama Large Millimeter/Submillimeter Array
CARTA	Cube Analysis and Rendering Tool for Astronomy
CASA	Common Astronomy Software Applications
CFE	cluster-formation efficiency
CI	confidence interval
CMB	cosmic microwave background
CN	the cyanide radical
CO	carbon monoxide
CS	carbon monosulfide
Dec.	declination
DVC	Data Version Control
FIRE-2	Feedback In Realistic Environments-2
FoV	field of view
FWHM	full width at half maximum
GMC	giant molecular cloud
GOR	green occupancy ratio
HCN	hydrogen cyanide
HWHM	half width at half maximum
IDL	Interactive Data Language

IMF	initial mass function
IR	infrared
ISM	interstellar medium
KDE	kernel density estimator
KS	Kolmogorov-Smirnov
LIRG	luminous infrared galaxy
LVG	large velocity gradient
MAE	mean absolute error
MS	measurement set
MUSE	Multi-Unit Spectroscopic Explorer
NAASC	North American ALMA Science Center
NED	NASA/IPAC Extragalactic Database
NTCO	New Technologies for Canadian Observatories
PA	position angle
PAH	polycyclic aromatic hydrocarbons
PCA	principal component analysis
PDF	probability density function
PHANGS-ALMA	Physics at High Angular resolution in Nearby GalaxieS with ALMA
PPV	position-position-velocity
R.A.	right ascension
RMS	root-mean-square
S/N	signal-to-noise
SDSS	Sloan Digital Sky Survey
SED	spectral energy distribution
SFE	star-formation efficiency
SFR	star-formation rate
SN	supernova
SPW	spectral window
sSFR	specific star-formation rate

TP	total power
U/LIRG	ultra/luminous infrared galaxy
UV	ultra violet
VLT	Very Large Telescope
vph	vehicles per hour
WMAP	Wilkinson Microwave Anisotropy Probe

Co-authorship

Chapters 2, 3, and 4 of this thesis contain original scientific research written by myself, Nathan Brunetti. Chapter 2 has been published as a peer-reviewed journal article in the Monthly Notices of the Royal Astronomical Society (MNRAS). The citation for this work is: Brunetti N., Wilson C. D., Sliwa K., Schinnerer E., Aalto S., Peck A. B., MNRAS, Volume 500, Issue 4, pp. 4730–4748. This work was co-authored with my supervisor, Dr. Christine D. Wilson. The third author, Dr. Kazimierz Sliwa, led the observing proposal for acquiring the data analysed in this work and provided helpful comments and suggestions on the article draft. The remaining authors, Dr. Eva Schinnerer, Dr. Susanne Aalto, and Dr. Alison B. Peck, aided in preparing the observing proposal and provided helpful comments and suggestions on the article draft. Chapter 3 has been submitted to MNRAS for peer review and publication. The author list for this work is: Brunetti N., Wilson C. D. This work was co-authored with my supervisor, Dr. Christine D. Wilson. Chapter 4 is in preparation and will be submitted to a peer-reviewed journal. The author list for this work is: Brunetti N., Wilson C. D. This work was co-authored with my supervisor, Dr. Christine D. Wilson.

I hereby grant an irrevocable, non-exclusive license to McMaster University and Library and Archives Canada to reproduce the material as part of this thesis.

1 | Introduction

1.1 Star formation and galaxy evolution

The formation of stars within galaxies is more than an individual part of the whole that can be understood in isolation. Instead, star formation is a necessary component in describing how galaxies have evolved through the age of the universe due to how the process of star formation shapes galaxies. In turn, star formation is influenced by the galaxy in which it takes place. Physical mechanisms that span spatial scales from several kiloparsecs, like galactic shear and radial flows of gas, all the way through to micrometers, like the formation of molecular hydrogen on the surfaces of interstellar dust grains, influence star formation and are in turn influenced by it. It is because of the interplay between stellar feedback and galactic processes, occurring at vastly different physical scales, that the progress of star formation is so rich in complexity.

Through this Chapter I will summarize why star formation is an important part of our understanding of galaxy evolution. I will present the current picture of the mechanisms that impact star formation and the ways it affects the galaxy in which it takes place. More specifically, I will describe the pieces that make up the Kennicutt-Schmidt star-formation law that relates the fuel for star formation to the rate at which stars form, I will highlight some of the implications of such a relation, and I will use the Kennicutt-Schmidt law to illuminate how starburst and/or merging galaxies are peculiar as motivation for the detailed study of mergers presented throughout this thesis. Emphasis will be given to observational measures of these galactic properties, as the original work presented here is largely of an observational nature, but theoretical descriptions are included as well.

Stars cause galaxy evolution through feedback on their surrounding environment. Feedback can be from the direct radiation emitted by stars, winds launched from their atmospheres, supernovae (SNe) from massive stars, and even through the collective stellar mass contributing to the galactic gravitational potential. Stellar radiation heats the interstellar medium (ISM) by directly heating dust grains (e.g Draine 2003) as well as through the photoelectric effect ejecting electrons from dust that collisionally heat the gas (e.g. Tielens & Hollenbach 1985; McKee 1989; Hollenbach & Tielens 1999; Draine 2003). The ionization fraction of a galaxy can be dramatically altered by the radiation from stars as they form HII regions, especially in the presence of clustered star formation (e.g. Matzner 2002; Krumholz et al. 2006; Hopkins et al. 2012). Material driven by stellar winds and SNe kinematically reshapes and shock-heats the ISM (McKee

& Ostriker 1977; Matzner 2002; Hopkins et al. 2011, 2012). The metallicity of the ISM is also enhanced by winds and SNe as metals produced within stars are launched into their surroundings (e.g. Scalzo et al. 2014; Seitenzahl et al. 2013; Seitenzahl & Townsley 2017; Karakas & Lugaro 2016; Krumholz & Ting 2018). Clustered SNe can even have the combined power to blow superbubbles out of a galaxy (e.g. Mac Low & McCray 1988; Nath & Shchekinov 2013; Sharma et al. 2014; Keller et al. 2014, 2015), helping to drive galactic outflows and fountains (e.g. Mathews & Baker 1971; Larson 1974; Keller et al. 2015, 2020).

The scale heights of the gas discs in spiral galaxies are partially determined by stellar influences. The weight of the disc (of which stars make a non-negligible portion) works to confine material towards the midplane while all the ways stars inject energy into their surroundings contribute pressure support against that gravitational confinement (e.g. McKee & Ostriker 1977; Narayan & Jog 2002; Ostriker & Shetty 2011; Elmegreen 2011; Benincasa et al. 2016; Krumholz et al. 2018). This pressure balance also sets the environment in which molecular clouds are embedded and appears to result in most clouds in spiral galaxies being bound by self gravity (Sun et al. 2020a; see Sections 1.2 and 1.4 for discussion of the importance of molecular gas in the star-formation process).

It is also true that star formation is in turn influenced by large-scale galactic processes, such that star formation is also a product of galaxy evolution. The other massive components of a galaxy (dark matter, gas, and dust) contribute to the total galactic potential that weighs on the clouds that form stars, helping to keep many of them bound and potentially able to collapse. The total mass of a galaxy also changes how much impact stellar feedback has on the galaxy. Material can be more easily ejected from dwarf galaxies by SNe compared to massive galaxies (e.g. Larson 1974; White & Frenk 1991; Somerville & Primack 1999; Benson et al. 2003) where it often rains back down on to the disc (e.g. Muratov et al. 2015; Keller et al. 2016). Shear caused by the differential rotation of disc galaxies can stretch or tear apart clouds, modify the cloud fragmentation scale by changing the gravitational stability of the disc, alter the cloud collision rate and relative velocities of collisions, and cause the tidal disruption of clouds through close cloud encounters (e.g. Goldreich & Lynden-Bell 1965; Elmegreen & Elmegreen 1983; Elmegreen 1987; Binney & Tremaine 1987; Dobbs 2008; Dobbs et al. 2011; Dobbs & Pringle 2013; Tasker & Tan 2009; Jeffreson & Kruijssen 2018). Shear also acts as a large-scale driver of turbulence that can contribute stabilizing pressure to the disc (e.g.

McNally et al. 2009; Benincasa et al. 2016).

Kiloparsec-long galactic bars alter the orbital motions of stars and gas, which can result in net flows of gas to the outskirts or into the centres of galaxies (e.g. Athanassoula 1992; Sellwood & Wilkinson 1993; Piner et al. 1995; Regan & Teuben 2004; Sormani et al. 2015). These gas flows to the centres of barred galaxies result in central gas enhancements (e.g. Sakamoto et al. 1999; Jogee et al. 2005; Sheth et al. 2005; Regan et al. 2006; Kuno et al. 2007) and enhanced circumnuclear star formation (e.g. de Jong et al. 1984; Ho et al. 1997; Ellison et al. 2011; Lin et al. 2017; Utomo et al. 2017; Chown et al. 2019). Utomo et al. (2017) found enhanced central star-formation rates (SFRs) were greater than central gas enhancements leading to shorter central gas depletion times in barred galaxies compared to unbarred and isolated galaxies. Interestingly, while star formation along bars in massive galaxies appears to be roughly as efficient (i.e. similar molecular-gas depletion times) as in the discs of nearby spiral galaxies (Díaz-García et al. 2021), star formation along bars is most often observed in low-mass galaxies (Fraser-McKelvie et al. 2020). The efficiency of star formation along bars in low-mass galaxies has not been fully explored, so the question remains open of whether the greater frequency of star formation appearing within bars of lower-mass galaxies is caused by enhanced molecular-gas masses or efficiencies within the bars.

When galaxies merge, star formation within the progenitor galaxies is dramatically altered, and the resulting merger remnant can be left in a very different star-formation mode than the progenitors began in. Bursty periods of intense (Larson & Tinsley 1978; Ellison et al. 2008, 2013; Hani et al. 2020) and more efficient (Daddi et al. 2010; Yamashita et al. 2017; Herrero-Illana et al. 2019; Wilson et al. 2019; Kennicutt & de los Reyes 2021) star formation are triggered throughout the merging process. A merger can then end as a quenched elliptical galaxy or possibly a more disc-like remnant with an enhanced SFR that slowly declines over about $500\,\mathrm{Myr}$ (Moreno et al. 2019; Hani et al. 2020; Quai et al. 2021). Even close encounters of galaxies appear to be enough to perturb the ISM resulting in enhanced SFRs (e.g. Barton et al. 2000; Ellison et al. 2008; Scudder et al. 2012; Moreno et al. 2019; Patton et al. 2013, 2020). Further details of galaxy interactions and mergers and their numerous impacts on the ISM and star formation are presented in Section 1.6.

Since our understanding of galaxy evolution must include how galaxies have changed over the age of the universe, and the SFR on average has changed dramatically in that

time, exploring the causes and consequences of those SFR changes will help describe the cosmic evolution of galaxies. It has been well established that the total SFR per unit volume rose after the Big Bang to a peak around redshift 1 to 2 and then began a slow decline of about an order of magnitude to the present day (e.g. Madau & Dickinson 2014). We know such a change in the SFR should result in large differences in the amount of stellar feedback which would not only affect future star formation but also the morphology, metallicity, and gas properties of galaxies. Also, kinematic forms of feedback, from winds and SNe, had more impact on galaxies in the early universe on average since galaxies were less massive. The rate of galaxy mergers was also higher in the past (e.g. Romano et al. 2021), meaning a higher fraction of galaxies were more often in the midst of merger-driven transformations and the resulting modes of extreme star formation.

1.2   Molecular gas

Star formation occurs in the cold and dense molecular gas of the ISM. Thus, the molecular-gas properties act as part of the initial conditions for the processes that accumulate gas in galaxies and cause it to collapse, forming stars. The molecular ISM is arranged in an almost fractal hierarchy of structures (due to its estimated three-dimensional fractal dimension being between 2.3 and 2.6 where a value of 2 is expected for classical surfaces and $\gtrsim 3$ for fractal surfaces, e.g. Falgarone et al. 1991; Lee 2004; Sánchez et al. 2007) spanning a wide range of spatial scales, temperatures, and densities. At the larger-scale end of that hierarchy are giant molecular clouds (GMCs), which are the birthplaces of most stars, often observed to be marginally gravitationally bound (e.g. Larson 1981; Solomon et al. 1987; Heyer et al. 2001; Hughes et al. 2013; Rosolowsky et al. 2021) and closely associated with young star-forming regions (e.g. Blitz et al. 1982; Heyer et al. 1996; Fukui et al. 1999; Wong et al. 2008; Schruba et al. 2010; Schinnerer et al. 2019; Chevance et al. 2020). GMCs have been observed in the Milky Way (e.g. Larson 1981; Solomon et al. 1987; Heyer et al. 2001, 2009; Ginsburg et al. 2016; Miville-Deschênes et al. 2017), the Magellanic Clouds (Cohen et al. 1988; Mizuno et al. 2001a,b, 2006; Fukui et al. 2008; Wong et al. 2011; Gordon et al. 2014), and other nearby galaxies (e.g. Vogel et al. 1987; Wilson & Scoville 1990; Wilson & Reid 1991; Wilson & Rudolph 1993; Wilson 1994; Engargiola et al. 2003; Leroy et al.

2006; Hughes et al. 2013; Rosolowsky et al. 2003; Rosolowsky 2007; Rosolowsky et al. 2021). Their masses (roughly 10^2 to 10^7 $M_\odot$) and sizes ($\gtrsim 20$ pc) show they are capable of forming many individual stars, potentially across different populations that are separated spatially and temporally. Observations of young star clusters embedded within or disrupting GMCs lend evidence for this picture (see Lada & Lada 2003 and references therein).

Average temperatures around 10 to 20 K (Goldsmith 1987) are maintained through cooling by molecular-line radiation and shielding from external radiation due to their high densities, balanced by cosmic-ray heating and photoelectric heating on cloud surfaces from irradiated dust grains (de Jong et al. 1980; Goldsmith 1987; Hollenbach & Tielens 1999). Densities averaged over entire GMCs are typically $\gtrsim 100$ hydrogen nuclei per cubic centimetre (Larson 1981; Goldsmith 1987; ≈ 3 $M_\odot$ pc^{-3} when including a factor of 1.36 for elements heavier than hydrogen or ≈ 200 $M_\odot$ pc^{-2} for a spherical cloud with a radius of 50 pc), but on smaller scales the densities can be much higher, leading to regions that collapse to form stars. While GMCs are typically the smallest molecular-gas structures studied in extra-galactic work, due to limited resolution and the distances to external galaxies, the regions of overdensities within clouds such as filaments, clumps, and cores are important for the details of how individual clusters and stars form (using the nomenclature of e.g. Williams et al. 2000).

Early work analysing GMCs in the Milky Way by Larson (1981) led to several empirical relations between properties of the clouds, referred to as Larson's relations or laws. The first relation is between two observable quantities of a molecular cloud, its size (R) and line width (σ_v). Larson (1981) found the power-law relation $\sigma_v \propto R^{0.38}$, and given its similarity to the relation for Kolmogorov (1941) subsonic turbulent flows of $\sigma_v \propto R^{1/3}$, suggested it was evidence for the linewidths originating from supersonic turbulent motions. While the exponent has since been estimated to be closer to 0.5 (e.g. Milky-Way studies Solomon et al. 1987; Falgarone et al. 2009; Rice et al. 2016; Miville-Deschênes et al. 2017; and extragalactic studies Bolatto et al. 2008; Faesi et al. 2018), simulations of supersonic turbulence indicate the size-linewidth relation is consistent with supersonic turbulent motions (Kritsuk et al. 2013). Next, by estimating the total mass of each cloud, M, Larson (1981) found it was also correlated with the line width as $\sigma_v \propto M^{0.20}$, as expected for clouds that are roughly gravitationally bound or in approximate virial equilibrium. Subsequent studies of molecular clouds in a greater

variety of environments and with more sensitive data have found a wider range of dynamical states in observed clouds, with the need for additional external pressure on clouds to keep them bound (Heyer et al. 2009; Field et al. 2011; Hughes et al. 2013; Sun et al. 2020a). Rearranging Larson's first two relations results in the average volume density of H_2, $\langle n \rangle$, going as $\langle n \rangle \propto R^{-1.10}$. This relation implies the product $\langle n \rangle R$ is approximately constant, with units of mass per area, so that the column densities of the observed clouds are approximately constant. Later studies have found similar results in the Milky Way (e.g. Solomon et al. 1987; Roman-Duval et al. 2010), though systematic shifts in the average surface density between galaxies have been observed (e.g. Hughes et al. 2013; Sun et al. 2018; Rosolowsky et al. 2021).

The spectrum of GMC masses, or the cloud mass function, can provide insights into cloud formation mechanisms and the formation of star clusters from clouds. The cloud mass function is expected to be a power law that possibly truncates at high mass, now often fit by a Schechter (1976) function

$$\psi(M) = \mathrm{d}N/\mathrm{d}M \propto M^{\beta} \exp\left(-M/M_{\star}\right) \qquad (1.1)$$

where β is the power-law index at low masses and $M_{\star}$ is the characteristic mass roughly where the mass function steepens or turns over at high masses (e.g. Mok et al. 2020; Rosolowsky et al. 2021). The upper-mass cutoff can be either physical, encoding information about processes that limit the growth of the most massive clouds, or statistical, where the mass of the most-massive cloud scales with the total number of clouds simply due to sampling of the cloud mass function. A lower-mass cutoff is less well defined as it represents the transition from structures identified as clouds to the denser sub-structures within clouds (e.g. clumps). The power-law index is theoretically expected to be around −2 (Elmegreen & Falgarone 1996; Fleck 1996; Wada et al. 2000; Guszejnov et al. 2018), and observational estimates of the index in the Milky Way and nearby galaxies have ranged from −0.9 to −3.4 (Rosolowsky 2005; Blitz et al. 2007; Gratier et al. 2012; Rice et al. 2016; Mok et al. 2020; Rosolowsky et al. 2021). The slopes of the cloud and cluster mass functions are roughly consistent from observations (Zhang & Fall 1999; Fall & Chandar 2012; Chandar et al. 2017; Krumholz et al. 2019; Mok et al. 2020), implying the star-formation efficiency (SFE) does not depend on mass. Fall et al. (2010) was able to reproduce the consistency in mass function slopes analytically when the surface

density of clouds was independent of their mass, i.e. with roughly constant surface density clouds as often measured within galaxies. A further prediction was that the SFE depends on the cloud/clump surface density, and for a typical GMC surface density their estimated SFE roughly matches those observed in protoclusters.

The most abundant component of the molecular ISM is H_2, with traces of other elements at the level of $\lesssim 10^{-4}$ atoms per hydrogen (Bolatto et al. 2013) coming together to make a host of other molecules. Some of these molecules also combine as solids to form dust grains that are made mostly of silicate and carbonaceous material. Dust grains range in size from about 0.4 to 1000 nm and make up about one per cent of the mass in Galactic GMCs (Draine 2003); however substantial variations in the dust mass fraction region-to-region and galaxy-to-galaxy have been measured (e.g Welty et al. 2012; Rémy-Ruyer et al. 2014; Roman-Duval et al. 2014, 2017; Williams et al. 2022).

This H_2-dominated composition poses a difficulty in observing the molecular ISM. The low mass of the H_2 molecule means rotational and vibrational transitions require high gas temperatures of $T \gtrsim 100$ K to excite. Upper energy levels above the ground state are $E/k_B \approx 510$ K for the lowest para rotational transition (proton spins aligned parallel), $E/k_B \approx 1015$ K for the lowest ortho rotational transition (proton spins aligned antiparallel), and $E/k_B \approx 6471$ K for the lowest vibrational transition (Dabrowski 1984). Rotational emission from H_2 is estimated to trace 1 to 30 per cent of the gas in galaxies (Roussel et al. 2007) since this combination of density and temperature is almost never achieved in the molecular gas, partly because those conditions easily dissociate molecular hydrogen. However, the trace amounts of heavier elements that make up other molecules do offer emission routes that are abundant at the conditions of the molecular ISM.

Perhaps the most straightforward, conceptually, is the thermal emission from the dust that is mixed in with the molecular gas. Dust grains at a temperature of 10 K will radiate an approximately blackbody spectrum that peaks at wavelengths around 100 μm (e.g. Erickson et al. 1981; Schwartz 1982; Gordon & Jewell 1987; Gordon 1988; Andre et al. 1993) and is optically thin at wavelenghts $\gtrsim 200$ μm (e.g. Hildebrand 1983; Gordon & Jewell 1987; Gordon 1988). Observations in the far infrared (IR) around the peak of the spectrum and at longer wavelengths in the millimetre can constrain the total dust spectrum, and thus the mean temperature and wavelength-dependent emissivity of the dust along the line of sight. The volume of optically thin emitting dust can be estimated from the observed flux density combined with the dust temperature and emissivity via

the radiative transfer equation, and with an estimate of the size of the dust grains this can be converted to a dust mass (Hildebrand 1983). For example, even with a flux density measurement at just a single wavelength and assumed dust temperature and emissivity, the mass can be estimated as

$$M_{\mathrm{d}} = \frac{S_\lambda d^2}{\kappa_\lambda B(\lambda, T_{\mathrm{d}})} \qquad (1.2)$$

where M_{d} is mass of dust along the line of sight, S_λ is the flux of the emitting region at wavelength λ, d is the distance to the emitting source, κ_λ is the dust opacity per unit column density at wavelength λ, and $B(\lambda, T_{\mathrm{d}})$ is the Planck function evaluated at the temperature of the dust T_{d} also at wavelength λ (e.g. Hildebrand et al. 1977; Johnstone et al. 2000). In Equation 1.2, κ_λ contains information both about the emissivity of the dust and size distribution of dust grains. With an estimate of the dust mass, the H_2 mass can be estimated with knowledge of the abundance of dust relative to H_2 (known as the gas-to-dust ratio; e.g. Hildebrand 1983). A serious limitation to estimating molecular-gas masses from dust emission is that it is intrinsically a continuum measurement that does not provide any line-of-sight kinematic information. Also, significant integration times or even possibly observations from multiple telescopes may be necessary to observe enough of the dust spectrum for a fit that can accurately constrain the dust properties (e.g. Gordon 1988; Andre et al. 1993; Gordon et al. 2014). Using Equation 1.2 carries additional uncertainties from estimating the dust properties elsewhere and applying them to the source of interest, as well as not being able to determine if other emission sources (e.g. free-free) are also present that can lead to overestimating the dust flux density.

Another common option for observing the molecular gas in galaxies is to target another molecule in the gas phase besides H_2. Carbon monoxide (CO) has rotational transitions that are readily excited in the temperatures and densities of typical GMCs, resulting in the strongest emission spectral lines that trace the bulk of the molecular gas. Its high abundance actually makes it at first appear to be ill-suited as a tracer of the total mass through observations since it is typically optically thick. However, if the GMCs are in virial equilibrium then their sizes are proportional to their masses (under the assumption that they are spherical), and so their surface areas are also proportional to their masses (Bolatto et al. 2013). Even though the clouds are optically thick, the observed flux will be proportional to the emitting surface area and so the integrated spectral-line intensity can be related to the mass. This method is limited to environments where

clouds are not significantly obscuring each other along our line of sight, which does not appear to be an issue at the densities in nearby spiral galaxies viewed nearly face-on, but may become relevant at high molecular-gas densities and for edge-on viewing angles.

A proportionality "constant" between the integrated CO intensity and the molecular-gas mass, known as the CO-to-H_2 conversion factor, absorbs all of the assumptions of virial equilibrium, cloud geometry, cloud density structure, cloud temperature structure, cloud optical-depth variations, the degree of CO excitation, cloud size distribution, and abundance of CO relative to H_2 (Bolatto et al. 2013). Over a carefully chosen sample of clouds the conversion factor may have a fairly well-defined average, but there are plenty of reasons to expect that it will vary between regions within a galaxy and between galaxies. The conversion factor is typically used in two forms. One relates the integrated line intensity, $W(CO)$, to the H_2 column density, $N(H_2)$, as

$$N(H_2) = X_{CO}W(CO). \tag{1.3}$$

The other relates the CO luminosity, L_{CO}, to the total molecular-gas mass, M_{mol}, as

$$M_{mol} = \alpha_{CO}L_{CO}. \tag{1.4}$$

Units are chosen so that in the inner disc of the Milky Way ($1\,\mathrm{kpc} \lesssim R \lesssim 9\,\mathrm{kpc}$) and averaged over scales of tens of parsecs or larger, values of $X_{CO} = 2 \times 10^{20}\,\mathrm{cm}^{-2}(\mathrm{K\,km\,s}^{-1})^{-1}$ or $\alpha_{CO} = 4.3\,\mathrm{M_\odot}(\mathrm{K\,km\,s}^{-1}\,\mathrm{pc}^2)^{-1}$ are typical (within a factor of about 1.3, Bolatto et al. 2013). Bolatto et al. (2013) suggests an uncertainty of about two around the Milky-Way conversion factor for other normal star-forming galaxies.

Significant variations in the conversion factor on smaller scales are expected given all the details of cloud properties it contains, and those variations are observed within clouds in the Milky Way (e.g. Pineda et al. 2010; Liszt & Pety 2012). However, resolved studies of nearby galaxies (e.g. Weiß et al. 2001; Israel 2009a,b; Sandstrom et al. 2013; Teng et al. 2021) have found systematic variations across galaxies on large scales as well, primarily as low central conversion factors or radial gradients with lower factors towards the centres. A radial change in the average conversion factor has also been measured in the Milky Way (Sodroski et al. 1995; Dahmen et al. 1998; Strong et al. 2004). Both radial gradients in metallicity resulting in lower CO abundance relative to

H_2 and larger gas velocity dispersions in the centres of galaxies (allowing more spectral-line emission to escape the optically thick clouds for the same amount of mass) can drive the conversion factor down in the centres of galaxies (e.g. Wilson 1995; Leroy et al. 2011; Genzel et al. 2012; Bolatto et al. 2013). Ultra/luminous infrared galaxies (U/LIRGs) and starbursting galaxies often have conversion factors estimated to be much lower than the Milky Way, with the typical value around $\alpha_{CO} = 0.8\,M_\odot(K\,km\,s^{-1}\,pc^2)^{-1}$ (e.g. Downes & Solomon 1998). Large velocity dispersions and warm gas in U/LIRGs and starbursts are suspected to be the main drivers of their low conversion factors (Narayanan et al. 2011; Papadopoulos et al. 2012). The conversion factor is not as well constrained in these extreme systems, with an observed spread of about a factor of three (Bolatto et al. 2013).

All of the conversion-factor values discussed so far are typical for converting specifically CO (1–0) flux to molecular-gas mass. Each rotational transition requires a separate conversion factor since the degree each energy state is populated is different at a given temperature and density. In practice, these differences between transitions are measured as the relative strengths of one transition to the other, e.g. CO (2–1) to CO (1–0) and often written as R_{21}. Then the CO-to-H_2 conversion factor for CO (1–0) is scaled by the appropriate ratio of transition strengths to estimate the conversion factor for the desired transition. Since the temperatures and densities of the molecular gas in the ISM vary from place to place within a galaxy, as well as between galaxies, the relative strengths of the CO transitions also vary (Saintonge et al. 2017; Leroy et al. 2013, 2021a). Considerable effort has been made in constraining the CO conversion factor and transition ratios in a variety of systems, and considering the wealth of kinematic information spectral-line observations provide, it is often worth targeting CO spectral lines. Bulk motions can be estimated for modeling the dynamical structure of the gas (Dutrey et al. 1994; Benedict et al. 1996; Downes & Solomon 1998; e.g.), thermal and turbulent energies within clouds can be estimated from spectral-line widths (e.g. Larson 1981), and clouds along the line of sight that are at different relative velocities can be separated to remove some of the limitation associated with viewing-angle obscuration.

It is also possible to observe similar rotational transitions of the rarer isotopologues of $^{12}C^{16}O$ (e.g. ^{13}CO, $C^{18}O$, etc.) to estimate the mass of molecular gas. These transitions are usually optically thin in GMCs but may also become optically thick at high densities (e.g. an optical depth of one can be reached at a visual extinction of

about five for ^{13}CO at Milky-Way isotopic abundances; Bolatto et al. 2013). Being optically thin means the flux is proportional to the amount of material along the line of sight (see e.g. Pineda et al. 2010 for common expressions for estimating the column density of ^{13}CO). The abundance of the particular species relative to ^{12}C^{16}O, and thus to H$_2$, is needed to convert the flux to a mass estimate (analogous to the gas-to-dust ratio). Isotopic abundances are well measured in the Milky Way (e.g. Wilson & Rood 1994), but may vary significantly in other galaxies (Kennicutt & Evans 2012). Being a spectral-line observation means it carries all of the kinematic information and benefits described for ^{12}C^{16}O. The main limitation to this method is that the emission is fainter so it is harder to detect beyond the densest parts of the nearest GMCs. In practice, this limitation means the isotopologues of CO are not as useful for measuring the total molecular gas, but where it is detected it can provide independent constraints on the mass.

Finally, if the size and spectral-line width of a GMC can be measured, then its mass can be estimated using the virial theorem (e.g. Solomon et al. 1987). Physical requirements that must be met for this method to be accurate are that the emission must trace the majority of the mass in the cloud, the cloud must be in virial equilibrium, and the density and temperature structure of the cloud must be known (e.g. Bertoldi & McKee 1992; Bolatto et al. 2013). Simplifying assumptions are often used, such as clouds being spherical, isothermal, and isodensity structures where CO traces all of the molecular gas. In addition, the cloud must be resolved spatially and spectrally, which limits this method to the nearest regions and galaxies (e.g. Scoville et al. 1987). Finally, a method for consistently identifying the size of non-transient, coherent clouds must be employed, which often means automating the identification of irregularly-shaped sources in noisy and resolution-limited observations (e.g. GaussClumps Stutzki & Guesten 1990; ClumpFind Williams et al. 1994; (py)cprops Rosolowsky & Leroy 2006, Rosolowsky et al. 2021; scimes Colombo et al. 2015; etc.).

1.3 Measuring the star-formation rate observationally

To explore the connection between the molecular gas that is the fuel for star formation and the rate at which stars are formed, there must be ways to empirically measure the SFR in galaxies throughout the universe. The SFR is typically constructed with units of mass

per time, as in the amount of mass in stars that have formed during some time. Many methods for observationally measuring the SFR exist, though they broadly fall into two categories. The first is to count the number of young stars in a region to estimate how much mass has recently appeared in stars, and to combine this number count with the average age of the stars to estimate the SFR. Young stellar objects are typically targeted for this method, and with rough lifetimes of about 2 Myr (Evans et al. 2009; Heiderman et al. 2010; Gutermuth et al. 2011) these SFR estimates are usually assumed to be an average over that time-scale. Since this technique is limited to the nearest star-forming regions within the Milky Way and Magellanic Clouds (e.g. being complete only for young stellar objects with masses greater than about $8 \, M_\odot$; Ochsendorf et al. 2016) it will not constitute very many of the SFR estimates discussed in this thesis, so we do not elaborate further (but see e.g. Kennicutt & Evans 2012 and references therein for additional detail). The other category is to measure the amount of radiation associated with some stage of stellar evolution, convert that to the amount of mass in stars that must be present to produce that radiation, and then estimate the total mass in stars from the observed massive fraction by using an assumed stellar initial mass function (IMF). The duration of the evolutionary stage associated with the form of radiation observed then provides the time-scale to form the rate.

Radiation-based estimates of the SFR often target processes related to massive stars since their high luminosities produce most of the signal we detect. Also, their short lifetimes reduce the time lag (and thus additional processes that can alter the observed signal) between the actual formation of the stars in a region and the radiation production. Emission processes that are related to longer time-scales are also desirable, in part because they can be combined with shorter-time-scale techniques to piece together estimates of the SFR over time, also known as star-formation histories.

Ultra violet (UV)-continuum as well as UV and optical spectral-line emission (e.g. Hα) are commonly used to estimate SFR because of the simple connection to the presence of massive stars. Since massive stars directly radiate substantial UV continuum, and again only over their short lifetimes, observations of this emission are proportional to the number of massive stars that formed within roughly 10 to 200 Myr (Hao et al. 2011; Murphy et al. 2011). Not all of the UV light emitted by massive stars escapes the region where they are located, however, with some photons ionizing nearby gas which can then emit spectral lines as the atoms recombine with electrons. While an extra physical step

is involved in producing e.g. Hα emission, it is still closely linked to the number of massive stars in a region and probes star formation about 3 to 10 Myr old (Hao et al. 2011; Murphy et al. 2011). The main observational limitation of using UV emission for estimating the SFR is that it is strongly attenuated by dust, which is abundant in the dense clouds where stars form. The patchy spatial distribution of dust means average UV emission over large regions is dominated by the least-obscured stars (Calzetti et al. 1994). As a result, many corrections for extinction have been proposed, based on colour/spectral slope measurements combined with assumed intrinsic stellar colours (e.g. Calzetti et al. 1994; Gordon et al. 2001; Kong et al. 2004; Salim et al. 2007; Hao et al. 2011).

At much longer wavelengths, radio continuum and radio spectral line emission can avoid most of the difficulty with dust extinction. One mechanism to produce radio-continuum emission is through free-free emission from ionized gas as electrons are accelerated by positive ions, which dominates the globally integrated emission from galaxies in the range of about 1.5 to 10 mm (30 to 200 GHz; Condon 1992). Also, emission of long-wavelength spectral lines as electrons cascade down through outer orbitals when recombining with hydrogen and other elements (called radio recombination lines) is common. So like in the UV, the observed radio emission is proportional to the number of massive stars in a region and can be related to an estimate of the SFR (e.g. Mezger & Henderson 1967; Klein & Graeve 1986; Klein et al. 1988; Turner & Ho 1994; Kobulnicky & Johnson 1999), but without missing or underestimating the amount of deeply embedded stars present. Radio continuum probes the SFR over about 100 Myr (Murphy et al. 2011).

Spatial resolution can be an impediment at these long wavelengths, but the ability to use ground-based interferometers (e.g. the Very Large Array, Atacama Large Millimeter/Submillimeter Array (ALMA), etc.) makes resolution much less of a problem. Contamination from other astrophysical processses in the radio is another difficulty to varying degrees depending on the observed wavelength. Synchrotron at long wavelengths and thermal-dust emission at short radio wavelengths begin to dominate the observed radio emission (Condon 1992), requiring multi-band measurements to estimate their contributions so they can be removed for the most accurate SFR estimates (e.g. Israel & van der Hulst 1983; Niklas et al. 1997; Murphy et al. 2011). While the long wavelengths broadly mean this emission is not usually attenuated by dust, grains can grow large enough in dense regions (and/or with the accumulation of ice mantles)

that extinction appears at (sub)millimetre wavelengths (Draine 2003; Shirley et al. 2011). This technique also suffers from generally low signal-to-noise (S/N) due to radio continuum making up less than 10^{-4} of the bolometric luminosity in galaxies without active nuclei (Condon 1992).

Synchrotron emission actually also has a role in estimating SFR beyond being a contaminant to free-free measurements. A tight empirical relation between synchrotron emission around 1.4 GHz and far-IR emission has been observed for some time across several orders of magnitude in luminosity (known as the radio-IR correlation; e.g. de Jong et al. 1985; Condon 1992; Helou et al. 1985; Yun et al. 2001; Bell 2003). There is a natural connection between the massive stars that heat the dust-producing IR emission and those which explode as SNe accelerating cosmic rays along magnetic field lines to produce synchrotron emission. What is not as well understood is why the correlation is so tight across stellar mass (e.g. Yun et al. 2001; Wu et al. 2008) and mergers/non-mergers (e.g. Condon et al. 1993, 2002; Murphy 2013) given the myriad processes that affect the cosmic-ray properties as they propagate through a galaxy (e.g. Murphy 2009).

Another way to estimate SFR relies on the heating of interstellar dust by stars. As stellar UV radiation makes its way through the nearby ISM, it is readily absorbed by dust which causes the dust to heat up. The dust can be warmed to around 10 to 50 K and will emit roughly blackbody radiation that peaks around 100 μm (3 THz) and extends into the IR and longer radio wavelengths (Draine 2003). The thermal dust spectral energy distribution (SED) is complicated by numerous spectral features around 5 to 20 μm originating from polycyclic aromatic hydrocarbons (PAH) (e.g. Draine 2003), but SFRs have also been observed to correlate with PAH luminosities (e.g. Roussel et al. 2001; Förster Schreiber et al. 2004; Wu et al. 2005a; Calzetti et al. 2007). A measurement of the total IR luminosity can be related to the amount of requisite UV radiation, the number of massive stars, and thus the SFR (e.g. Kennicutt 1998; Pérez-González et al. 2006; Kennicutt et al. 2009; Kennicutt & Evans 2012). Calibrations for estimating the total IR luminosity from single and/or multiple photometric bands have been common using e.g. the *Infrared Astronomical Satellite* (*IRAS*) (Sanders & Mirabel 1996; Sanders et al. 2003), *Spitzer* (Dale & Helou 2002; Boquien et al. 2010), and *Herschel* telescopes (Boquien et al. 2011; Elbaz et al. 2011; Galametz et al. 2013). Time-scales of the SFR that are related to IR emission are about 10 to 100 Myr (total IR: Hao et al. 2011, Murphy et al. 2011; 24 μm: Rieke et al. 2009; 70 μm: Calzetti et al. 2010). Dust extinction is

usually not a problem as the emission is optically thin in all but the densest molecular cores.

Several limitations to this technique do exist, such as historically low spatial resolution compared to other parts of the spectrum due to the need for space-based observatories. Also, observations at multiple wavelengths are needed to accurately constrain the dust SED since the shape and peak depend on both the dust temperature and its optical properties. The assumption of a single population of dust particles at a single temperature is often too simplistic to describe the observed SED: models containing at least two components of "warm" and "cool" dust (e.g. Galliano et al. 2005; Galametz et al. 2009), a distribution of sizes, and/or optical properties (e.g. Meny et al. 2007; Paradis et al. 2010) are preferred by the data. IR contamination emitted directly from older/lower-mass stars (e.g. Lonsdale Persson & Helou 1987; Walterbos & Greenawalt 1996) as well as contamination from other sources of heating like active galactic nuclei (AGN) (e.g. Wu et al. 2010, 2011) and shocks (Draine 2003) must be accounted for in estimating the dust SED.

Since SNe and SN remnants, massive stars, and massive X-ray binaries all emit X-rays and are associated with recent star formation, X-rays can be used to trace the SFR as well. X-ray emission from galaxies is also correlated with some other SFR tracers (e.g. IR and synchrotron Bauer et al. 2002; Ranalli et al. 2003; Symeonidis et al. 2011) which means calibrations for estimating SFR from X-ray observations have been produced by bootstrapping from the IR or radio calibrations (e.g. Ranalli et al. 2003; Persic et al. 2004; Colbert et al. 2004; Lehmer et al. 2010). SFR estimates from X-rays with energies from 2 to 10 keV probe time-scales up to about 100 Myr (Ranalli et al. 2003). Estimates are complicated by decisions about which X-ray emission sources to include in the calibration (e.g. the Persic et al. 2004 recipe includes only X-ray binary luminosity). Also, X-rays emitted from AGN accretion discs act as a contaminant that must be excluded.

Finally, combinations of these various techniques are common and have the potential for the most complete estimates of the total SFR in galaxies. Combinations of unobscured and obscured SFR tracers (e.g. far UV and IR) are typical, to leverage the strengths of the different observations. Multi-wavelength estimates of the SFR can also be fed back into exploring uncertainties in the monochromatic tracers (e.g. Calzetti et al. 2010). Kennicutt & Evans (2012) provide a summary of different combined SFR estimators,

with emphasis on UV plus IR or radio from Hao et al. (2011) and Kennicutt et al. (2009).

1.4 The Kennicutt-Schmidt relation

The relation between the total gas content and the global SFR in galaxies has long been assumed to be a power law, starting from the first proposals for the volume density form of the relation by Schmidt (1959). Schmidt (1963) recast the relation as surface densities in the form

$$\Sigma_{\text{SFR}} = A\Sigma_{\text{gas}}^n, \tag{1.5}$$

which helps to counteract the artificial correlation that could appear since the conversions from observed quantities to gas mass and SFR both depend on the distance to the galaxy. Early studies worked with "global" measurements of the SFR and gas surface densities, where these quantities were measured across an entire galaxy and then normalized by an estimate of the tracer's emitting area (e.g. $\Sigma_{\text{SFR}} = \text{SFR}/\pi R_{\text{gal}}^2$). As telescope resolution and sensitivity improved, the "resolved" form became possible to measure on scales of about a kiloparsec down to several hundred parsecs. In this case, the surface brightness of SFR and gas-mass tracers within each pixel are converted to the SFR or gas surface density at multiple positions across the galaxy.

The observational global relation by Kennicutt (1998) showed spiral galaxies, IR-luminous starbursts, and circumnuclear starbursts all followed a tight power law with index of 1.40 ± 0.15. This henceforth-known Kennicutt-Schmidt relation spanned over five orders of magnitude in global average total-gas surface density and used a sample of 61 normal star-forming discs and 36 IR-selected starburst galaxies. An updated analysis of the global Kennicutt-Schmidt relation across a larger sample of spiral and starburst galaxies by Kennicutt & de los Reyes (2021) found a similar though slightly steeper slope of 1.50 ± 0.05 with total gas surface density. Figure 1.1 shows the global molecular Kennicutt-Schmidt relation (discussed further below) from Kennicutt & de los Reyes (2021). Kennicutt & de los Reyes (2021) also found that all types of galaxies exhibited nearly as tight a relation when the gas surface density was normalized by a dynamical time-scale (the orbital time in this case), a form of star-formation law that had been initially proposed by Silk (1997) and Elmegreen (1997). In addition to providing powerful evidence for the role gas density plays in determining the rate at
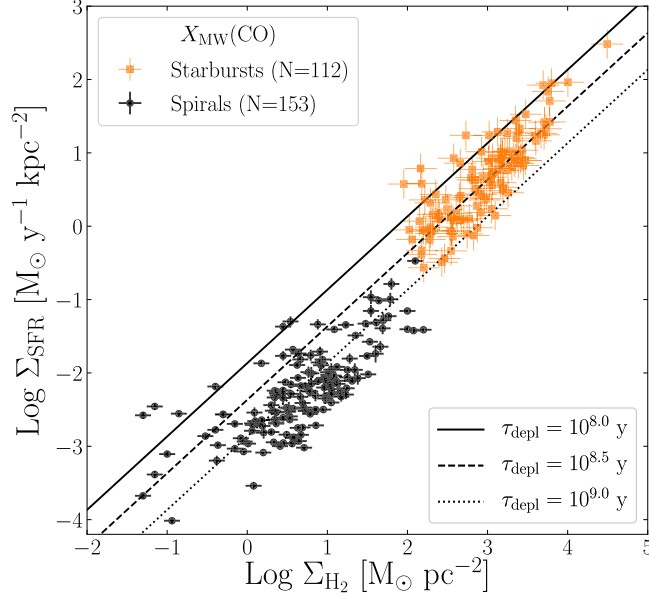
FIGURE 1.1: Global Kennicutt-Schmidt relation between the SFR and molecular gas mass surface density from Kennicutt & de los Reyes (2021). Starbursts are shown in orange and non-starburst galaxies in black, with the number of each given in the legend. Solid, dashed, and dotted lines indicate constant molecular-gas depletion times, $t_{dep} = \Sigma_{gas}/\Sigma_{SFR}$. The median t_{dep} for the starburst sample is 240 Myr compared to 3200 Myr for the non-starburst sample. A typical Milky Way CO-to-H_2 conversion factor, $X_{MW}(CO)$, was used for all galaxies. Note that many of the starburst galaxies are likely better described by a lower conversion factor which would shift the points to lower molecular gas surface densities by as much as 0.7 dex. ©American Astronomical Society (AAS). Reproduced with permission.

which stars form, the Kennicutt-Schmidt relation has been useful as a prescription for the star-formation process in numerical simulations that cannot resolve the details of how gas collapses to form stars (e.g. Vogelsberger et al. 2014; Schaye et al. 2015).

The slope of the observed Kennicutt-Schmidt relation can be predicted theoretically by assuming that the SFR averaged over galaxies acts largely on time-scales of self-gravitation. Given an amount of gas that could potentially form stars, the SFR would be set by how quickly the gas can collapse under its own gravity

$$\rho_{SFR} \propto \frac{\rho_{gas}}{t_{ff}} \tag{1.6}$$

where ρ_{SFR} is the SFR volume density, ρ_{gas} is the volume density of the gas, and t_{ff} is the

free-fall time of the gas (Elmegreen 2015). The free-fall time can be eliminated by using the relation between the gas volume density and the free-fall time of self-gravitating gas, $t_{ff} \propto \rho_{gas}^{-1/2}$. If the scale height of the galactic disc is constant (which may be a reasonable approximation in the inner parts of galaxies, e.g. Heyer & Dame 2015), then $\rho_{gas} = \Sigma_{gas}/2H$. Assuming that the star-forming scale height is the same as the gas, since star formation is occurring within the gas, then the SFR surface density should be proportional to the gas surface density as

$$\Sigma_{SFR} \propto \Sigma_{gas}^{3/2}. \tag{1.7}$$

Recent studies of both the global (e.g. de los Reyes & Kennicutt 2019) and resolved (e.g. Kennicutt et al. 2007; Bigiel et al. 2008, 2014; Leroy et al. 2008) relations have found that the SFR surface density is weakly dependent on the atomic gas surface density but exhibits a tight dependence on the molecular gas surface density with a slope near one. Figure 1.2 shows how using these different gas phases causes the Kennicutt-Schmidt relation to differ, as measured by de los Reyes & Kennicutt (2019). There are also deeper complexities to the Kennicutt-Schmidt relation that have been confirmed recently using global measurements. Extending the sample of gas measurements to low surface densities with a sample of 19 low surface brightness spiral galaxies, Wyder et al. (2009) revealed a steepening of the relation. This steepening was seen in both the total gas surface density relation as well as when the gas surface density was normalized by the orbital time-scale. Accompanying the change in the slope was additional scatter. Filho et al. (2016) and Roychowdhury et al. (2017) also observed this steepening of the Kennicutt-Schmidt slope at low gas surface densities, this time in low-metallicity dwarf galaxies.

One explanation for the change of slope and/or weakening correlation at low surface densities involves a universal transition surface density of the ISM from a mix of atomic and molecular at high surface densities to predominantly atomic at low surface densities (e.g. Leroy et al. 2008, 2013; Bigiel et al. 2014). When the ISM is mostly atomic there would be little correlation between the total gas surface density and SFR, but the total-gas relation would approach the linear relation seen in only molecular gas when the ISM is roughly an even mixture of atomic and molecular gas.

Some theoretical explanations for the change of slope at low gas surface densities
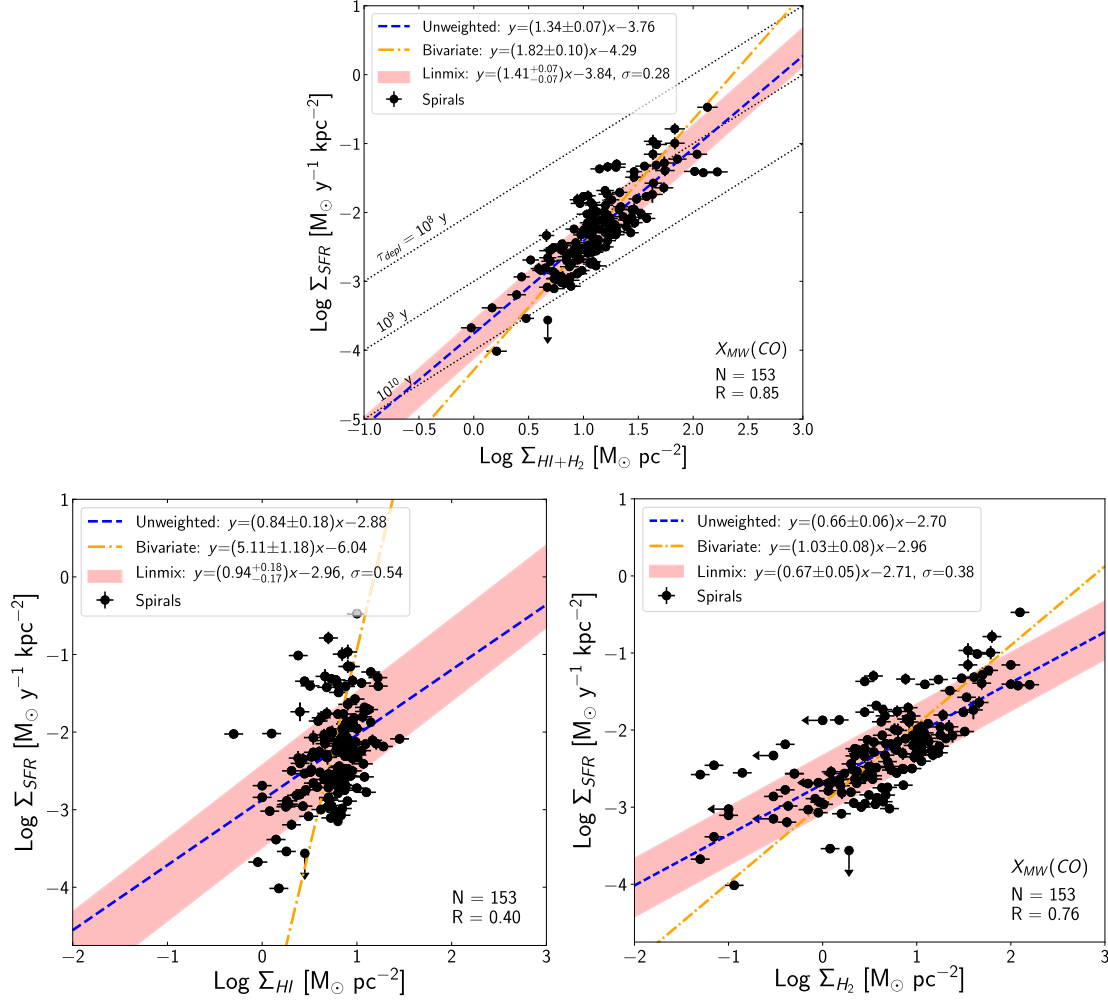
FIGURE 1.2: Global Kennicutt-Schmidt relations between SFR surface density and total-gas mass surface density (top), atomic-gas surface density (bottom-left), and molecular-gas surface density (bottom-right) for non-starburst galaxies from de los Reyes & Kennicutt (2019). Black points in the molecular-gas relation are the same as in Figure 1.1. Dotted lines in the total-gas panel indicate constant t_{dep}. A typical Milky Way CO-to-H_2 conversion factor, $X_{MW}(CO)$, was used for all galaxies. The Pearson product-moment correlation coefficients, R, are shown in each panel. The red band, blue-dashed line, and yellow dot-dashed line show several power-law fits with their best-fitting parameters given in the legends. Note the small intrinsic scatter (σ), reasonably high R, and roughly consistent fit results between techniques in the total- and molecular-gas relations compared to the large scatter, low R, and very different fit results in the atomic-gas relation. ©AAS. Reproduced with permission.

avoid invoking thresholds in the volumetric form of Equation 1.5 by instead incorporating dynamical and/or structural changes at different gas densities. For example, a change from roughly constant disc scale heights in spiral galaxies to scale heights that vary inversely with the gas surface density in dwarf galaxies could result in a change in the expected slope from $n \approx 1.5$ to $n \approx 2$ (e.g. Ferguson et al. 1998; Elmegreen & Hunter 2015).

Another explanation combines the relation between the molecular-gas fraction and the hydrostatic pressure (Blitz & Rosolowsky 2006) with theoretical models of star formation in supersonically turbulent molecular clouds. Here, the change in slope occurs as a result of the molecular-gas fraction dropping as the gas surface density decreases (Krumholz & McKee 2005).

Still another approach recasts the relation as an "extended Schmidt law" by relating the surface density of SFR to $\Sigma_{gas}\Sigma_\star^{0.5}$ (Dopita 1985; Shi et al. 2011; Roychowdhury et al. 2017; de los Reyes & Kennicutt 2019). This approach has been successful in bringing galaxies with low gas surface densities in line with higher surface density spiral galaxies. Feedback from young massive stars effectively injects pressure into the ISM that must be balanced by the weight of the disc (Orr et al. 2018). One contribution to the pressure balance is a stellar-potential term proportional to $\Sigma_{gas}\Sigma_\star^{0.5}$ and the other is a gas self-gravity term proportional to $\Sigma_{gas}^{1.5}$ (e.g. Blitz & Rosolowsky 2004; Kim et al. 2011; Kim & Ostriker 2015). In systems with low gas surface densities, the stellar-potential term dominates resulting in the extended Schmidt law following a single power law from low to high gas surface densities.

At the other extreme of high gas mass and SFR surface densities, there have long been indications of a separate or bimodal global Kennicutt-Schmidt relation relative to star-forming spiral galaxies (e.g. Daddi et al. 2010; Genzel et al. 2010). A common criticism of the results from Daddi et al. (2010) and Genzel et al. (2010) concerns their use of two separate CO-to-H_2 conversion factors, one for spiral galaxies and another for starburst galaxies. Since a systematic shift in the conversion factor often results in the Kennicutt-Schmidt relations differing by a similar amount, there has been uncertainty about the reality of the change in the Kennicutt-Schmidt relation at high surface densities. For example, using a surface density dependent prescription for the conversion factor did reduce the difference between the resolved relation for spiral and global relation for starburst galaxies, while also producing a steeper slope (Narayanan

et al. 2012). Kennicutt & de los Reyes (2021) measured the global average gas and SFR surface densities across 114 starburst circumnuclear discs and strongly barred galaxies, for comparison with the global measurements of 165 spiral galaxies analysed by de los Reyes & Kennicutt (2019). While the starburst and spiral galaxies followed a single tight Kennicutt-Schmidt relation when fit together, Kennicutt & de los Reyes (2021) also found significant evidence for a change of slope and an offset in the total-gas Kennicutt-Schmidt relation when the two samples were fit separately. They measured a shallower slope of 0.98 ± 0.07 and an offset to higher SFR surface densities at a given gas surface density in the starburst sample. Importantly, Kennicutt & de los Reyes (2021) found that significant differences in the slope and/or intercept of the power law could not be eliminated regardless of the conversion-factor prescription used. They also found that the difference also appeared when relating the SFR surface density and dust mass surface density. Since the dust masses are measured independently from the gas mass, this result implies that the break in the Kennicutt-Schmidt relation cannot be a result of the conversion factor.

Kennicutt & de los Reyes (2021) claim a change in the dominant form of gas in the ISM, from being roughly equal between atomic and molecular in spiral galaxies to dominated by molecular gas in starburst galaxies, would suffice to explain the change in slope observed at high gas surface densities. This explanation has been proposed by Bigiel et al. (2008) and Leroy et al. (2008) in spatially-resolved studies of the Kennicutt-Schmidt relation and continues the progression described above as the ISM transitions from mostly atomic, to a mixture, to mostly molecular. In favor of this, Kennicutt & de los Reyes (2021) do not measure a change in slope within the molecular-gas Kennicutt-Schmidt relation implying the dilution of the relation from increasing atomic-gas fraction is omitted. However, competing explanations in this high surface density regime also exist, again avoiding thresholds in the Kennicutt-Schmidt relation by considering how the constant effective volume density for emission from molecular-gas tracers compares to the average interstellar volume density (Elmegreen 2018). Physical explanations for the offset in the Kennicutt-Schmidt relations between spiral and starburst galaxies are summarized in Section 1.5.

A persistent difference between resolved and global forms of the observed Kennicutt-Schmidt relation that should be kept in mind is the degree of scatter. When observed on decreasing spatial scales, the scatter in the Kennicutt-Schmidt relation eventually

increases, largely due to stochasticity in the star-formation process dominating the region-to-region variations (scatter at small scales ranging from 0.1 to 0.4 dex; e.g. Kennicutt et al. 2007; Leroy et al. 2008; Bigiel et al. 2008; Verley et al. 2010; Rahman et al. 2012; Viaene et al. 2014). Factors such as how much of the stellar initial mass function is sampled in each resolution element, contamination from non-SFR related Hα and dust emission, and spatially varying stellar age distributions (e.g. young star clusters) all contribute uncertainty as well as scatter in resolved measurements of the Kennicutt-Schmidt relation. Above about 300 pc the relation is typically observed to tighten back up (Onodera et al. 2010; Schruba et al. 2010).

While observations spanning entire galaxies down to several hundred parsecs are beginning to show the same results for the Kennicutt-Schmidt relation, there is still much to be explored. Constraining which mechanisms cause the changes in slope seen now at both low and high gas surface densities, or more likely, constraining the importance of the different mechanisms must be pursued. Also it is important to determine if and why the "classic" Kennicutt-Schmidt relation can be improved across all classes of galaxies by the inclusion of additional properties like the orbital times, free-fall times (Krumholz et al. 2012), and/or the stellar mass surface density. There are also avenues to explore in spatially-resolved measurements within extreme galaxies, such as U/LIRGs, where interactions and mergers may be inducing yet another change in the molecular-gas Kennicutt-Schmidt relation at the highest gas surface densities in the centres of these systems (Sánchez-García et al. 2021).

1.5 Times and efficiencies

An interesting quantity can be estimated from the Kennicutt-Schmidt relation for each point in the space by dividing the x-axis values by the y-axis values, which gives the instantaneous gas depletion time

$$t_{\mathrm{dep}} = \frac{\Sigma_{\mathrm{gas}}}{\Sigma_{\mathrm{SFR}}}. \tag{1.8}$$

Lines of constant t_{dep} added to plots of the Kennicutt-Schmidt relation have a slope of one (in logarithmic space) with short t_{dep} in the upper-left region and long t_{dep} in the lower-right region (e.g. see Figures 1.1 and 1.2). As mentioned previously, the

slope of the relation between the logarithms of SFR and the molecular gas surface density is often around one which results in many galaxies scattering around the same molecular-gas t_{dep}. Bigiel et al. (2011) showed that 30 nearby galaxies exhibit a roughly constant molecular-gas t_{dep} of about 2 Gyr measured on 1 kpc scales, and they found only a very weak dependence of t_{dep} on the molecular-gas surface density. However, their sample was primarily disc galaxies that only spanned molecular-gas surface densities from about 5 to $100 \, M_{\odot} \, pc^{-2}$. Since t_{dep} will depend on the slope and offset of the Kennicutt-Schmidt relation, and there are significant changes in both when observing at the highest and lowest gas surface densities, there should also be differences in t_{dep} across the full range of observed gas surface densities. Of importance to this thesis is the change in the offset of the Kennicutt-Schmidt relation observed globally in starburst galaxies compared to nonstarbursting galaxies (e.g. Kennicutt & de los Reyes 2021). This offset results in starbursting galaxies also exhibiting a roughly constant t_{dep}, but five to eight times shorter than t_{dep} in nonstarbursting galaxies. Kennicutt & de los Reyes (2021) also point out that since the offset is seen with both total gas and molecular gas surface densities, there must be other physical mechanisms causing the offset, in addition to the transition in the dominant gas phase of the ISM that they argue can explain the change in the Kennicutt-Schmidt slope. Suggested mechanisms include intrinsic differences in the efficiency of star formation, differences in the small-scale structure of the molecular ISM (of particular interest in this thesis), and a top-heavy IMF.

Resolved observations at even higher molecular gas surface densities have shown a steepening slope in the Kennicutt-Schmidt relation (e.g. Gao & Solomon 2004; Shi et al. 2018; Wilson et al. 2019; Sánchez-García et al. 2021) which would result in further variations in t_{dep} as a function of gas surface density. Wilson et al. (2019) found molecular-gas t_{dep} from about 600 to 20 Myr over a range of surface densities from about 300 to $10\,000 \, M_{\odot} \, pc^{-2}$. Also, Utomo et al. (2017) found that the molecular-gas t_{dep} was shorter in the centres of nonstarbursting galaxies where the gas surface densities are higher. Colombo et al. (2018) estimate roughly constant ratios of molecular-gas t_{dep} to orbital time within each Hubble type, which when combined with shorter orbital times in the centres of galaxies implies also shorter t_{dep}. Whether it is simply a single offset to lower values of t_{dep}, or t_{dep} decreasing with increasing gas surface density, whatever process is driving star formation to consume its fuel more rapidly at higher surface densities is yet to be identified.

While comparing t_{dep} between regions and galaxies is useful for understanding how star formation is unfolding in different systems, it is useful to also have a time-scale for comparison that depends on properties just within an observed region. As explained when motivating Equation 1.6, forming stars from gas will take at least as long as the free-fall time, t_{ff}, making it a good minimum gas depletion time limit. Since t_{ff} depends on the volume density of the gas, various assumptions have been employed to convert observed gas surface densities to volume densities. Often the inaccessible third spatial dimension in disc galaxies is assumed from observations of gas scale heights (e.g. Yim et al. 2014; Heyer & Dame 2015; Utomo et al. 2018; Bacchini et al. 2019b; Yim et al. 2020). It can also be estimated dynamically through combinations of the mass surface density and gas velocity dispersion by assuming the gas disc is in hydrostatic equilibrium between gravity and internal gas pressures (e.g. Banerjee et al. 2011; Elmegreen 2011; Elmegreen & Hunter 2015; Benincasa et al. 2016; Utomo et al. 2018; Wilson et al. 2019; Bacchini et al. 2019a, 2020).

Average estimates for volume densities of GMCs in the Milky Way and nearby spiral galaxies are around 50 to $1000\,\mathrm{cm}^{-3}$ (e.g. Bolatto et al. 2008; Roman-Duval et al. 2010), resulting in $t_{\mathrm{ff}} \approx 1$ to $10\,\mathrm{Myr}$ compared with $t_{\mathrm{dep}} \approx 2000\,\mathrm{Myr}$. Even at the highest gas surface densities in the most actively star-forming galaxies t_{dep} is about an order of magnitude longer than t_{ff} (Wilson et al. 2019). It is well documented that, relative to the time it would take all of the molecular gas in a galaxy to free fall under its own gravity, instantaneous estimates for how quickly star formation is using up the molecular gas are actually not quick at all (see reviews by McKee & Ostriker 2007; Krumholz 2014). As summarized in Section 1.1, there are many feedback mechanisms through which stars exert influence on their host galaxy, and these mechanisms are thought to be instrumental in producing the long t_{dep} observed. In Section 1.1 we also discussed ways in which the larger galactic environment is involved in the star-formation process, with several processes acting to limit or reduce the SFR.

A common way to compare t_{dep} and t_{ff} is to calculate the star-formation efficiency relative to the free-fall time

$$\epsilon_{\mathrm{ff}} = \frac{t_{\mathrm{ff}}}{t_{\mathrm{dep}}}. \tag{1.9}$$

The fact that star formation can occur, at most, at the rate of the free-fall time ensures that ϵ_{ff} is always less than one, like a proper efficiency. In fact, measurements of ϵ_{ff}

on roughly kiloparsec scales are generally less than a few per cent in the Milky Way and the discs of nearby spiral galaxies, and up to about about 10 to 20 per cent for individual molecular clouds (see review in Krumholz et al. 2019). While both t_{ff} and t_{dep} are offset to lower values in starbursts relative to disc galaxies, the difference in t_{dep} is greater on average leading to about an order of magnitude higher ϵ_{ff} in starbursts. However, the efficiencies are still only at the level of five to seven per cent on 500 pc scales in starbursts (Wilson et al. 2019; however with a wide range of estimates down to 0.1 percent from e.g. García-Burillo et al. 2012). A significant advantage to making observational estimates of ϵ_{ff} is that many theoretical models base their predictions of the (in)efficiency of star formation on it (Krumholz & McKee 2005; McKee & Ostriker 2007; Murray 2011; Krumholz et al. 2012; Federrath & Klessen 2012; Padoan et al. 2012; Raskutti et al. 2016; Lee et al. 2016; Evans et al. 2014). Despite ϵ_{ff} being unitless, it is usually called the star-formation efficiency *per* free-fall time in the literature, which conveys that when multiplied by the molecular-gas mass, ϵ_{ff} gives an estimate of the mass of new stars formed within a free-fall time (i.e. $M_{\star} = \epsilon_{ff} M_{mol} = t_{ff} \mathrm{SFR}$).

There are galaxy-to-galaxy and region-to-region varitions of ϵ_{ff}, such as anticorrelations with the total stellar mass of the galaxy (Utomo et al. 2018), virial parameter of the gas (Schruba et al. 2019), and GMC mass (e.g. Ochsendorf et al. 2017). Ochsendorf et al. (2017) tested the anticorrelation with GMC mass against predictions from turbulence-regulated analytical star-formation models finding that the models instead predicted a correlation. This discrepancy likely highlights the difficulty in observationally identifying the mass of molecular gas that will be directly involved in star formation since that mass does not scale with total cloud mass.

Another quantity that is unfortunately also often called the SFE (sometimes denoted by ϵ) in the literature is the inverse of t_{dep}

$$\epsilon = \frac{\Sigma_{SFR}}{\Sigma_{gas}} \tag{1.10}$$

which has units of inverse years (making it more of a depletion frequency than a true efficiency). Like t_{dep} it is easy to measure and plot in the Kennicutt-Schmidt relation space, with lines of constant ϵ also having a slope of one in log-log space but with high ϵ in the upper-left region and low ϵ in the lower-right region. Since this quantity is effectively how many instantaneous depletion times would occur per year with the current

SFR and gas content, the values in nearby disc galaxies are often around $10^{-9}\,\mathrm{yr}^{-1}$ in total molecular gas and ranging from 10^{-7} to $10^{-6}\,\mathrm{yr}^{-1}$ in dense molecular gas (e.g. Usero et al. 2015). Like t_{dep}, ϵ combines the (recent) rate of star formation with the current reservoir of gas so different clouds or galactic regions can be compared. Work has been done using ϵ or t_{dep} to distinguish between e.g. star-formation models that claim the SFR is controlled by the available mass of gas above a density threshold (which would result in ϵ being roughly constant everywhere, e.g. Gao & Solomon 2004; Wu et al. 2005b; Lada et al. 2010, 2012; Evans et al. 2014), or models that are based on the idea that all properties of a cloud affect its ϵ (e.g. Krumholz & McKee 2005; Krumholz & Thompson 2007; Federrath & Klessen 2012; Usero et al. 2015; Bigiel et al. 2016).

1.6 Galaxy interactions and mergers

Much of the large-scale structure in the universe has grown through hierarchical merging of smaller objects to build up larger galaxies, groups, and clusters (e.g. White & Frenk 1991). Given the dramatic effects galaxy mergers have on star formation processes, it is crucial to understand how galaxy mergers change galaxies and the gas and stars within them. Li et al. (2007) has shown that after acquiring roughly one per cent of its present-day mass, each dark matter halo has undergone 3 ± 2 major mergers (progenitor mass ratios $\gtrsim 1/3$). In other words, essentially all massive galaxies have had their star formation histories impacted by mergers. Gravitational interactions between galaxies that do not necessarily end in merging also result in measurable differences in star formation activity and gas properties. For example, Patton et al. (2013) found the signature of enhanced star formation in galaxy pairs out to projected separations of $150\,\mathrm{kpc}$ in a sample of $\sim 2.11 \times 10^5$ galaxies observed in the Sloan Digital Sky Survey (SDSS), and Patton et al. (2020) found significant specific SFR enhancements out to $280\,\mathrm{kpc}$ three-dimensional separations in numerical cosmological simulations.

Whether a galaxy interaction remains an event at a distance or eventually leads to the galaxies merging is determined by the orbital properties of the progenitors. If the galaxies will merge, their orbital properties also play a role in how the merger unfolds and the properties of the remnant that is left behind (e.g. Barnes 1992; Dubinski et al. 1996; Naab & Burkert 2003; Boylan-Kolchin et al. 2005). The derivation by Binney & Tremaine (1987) of the interactions of two identical, spherical, non-rotating galaxies

showed that all possible encounters are determined by the orbital energy per unit mass and the orbital angular momentum per unit mass. If tidal effects are considered, then any bound orbit will actually end with a merger as orbital energy is transferred into the internal energies of the galaxies (Mo et al. 2010). Tidal interactions can even cause some unbound orbits to lead to mergers, if the orbital angular momentum is low enough (Mo et al. 2010).

However, the orbital energy and angular momentum must be low enough for the merger to happen within a Hubble time to be of interest in studying mergers that are observed throughout the universe today. Practically speaking, mergers must have taken much less time than the current age of the universe since the properties of the environment and progenitors would have evolved significantly over so much time. Using the age of the universe as a simple limit translates to mergers mostly ocurring within groups of galaxies, not clusters, since the velocity dispersion of the collection of galaxies must be less than or near the internal velocities of the orbiting galaxies (Mo et al. 2010). A more subtle detail encoded in the orbital angular momentum that impacts how a merger unfolds is how the orbital spin is aligned with the spin of the progenitor galaxies. Toomre & Toomre (1972) showed that alignment of all the spins (called a prograde merger) results in much larger tidal tails produced during each close passage (with many subsequent follow-up studies, e.g. Gerhard 1981; Hernquist 1992; Dubinski et al. 1996, 1999; Mo et al. 1998; Springel & White 1999).

The progenitor mass ratio also contributes to how a galaxy merger evolves and the resulting remnant (e.g. Dubinski et al. 1996; Springel & White 1999; Naab & Burkert 2003; Boylan-Kolchin et al. 2005). The exact ratio that divides major and minor mergers is arbitrary, but the delineation often discussed is around 1/3 or 1/4 (e.g. Mo et al. 2010). Since the close orbits of galaxies cause the overall gravitational potential to rapidly change (on the time-scale of orbits internal to the progenitors), the orbital energies of the constituents of the progenitors also rapidly change, a process referred to as violent relaxation (e.g. van Albada 1982). Major mergers can dramatically change the morphologies of the progenitors, such that the remnant can be of an entirely different type (e.g. disc/spiral progenitors leaving an elliptical-like remnant; White 1978, 1979; Gerhard 1981; Barnes 1988; Hernquist 1992; Kormendy et al. 2009). Minor mergers (also referred to as accretion events) have less morphologically destructive outcomes, with the remnant resembling the more-massive progenitor but often with the addition

of "shells", "ripples", and/or "plumes" (e.g. Arp 1966; Malin & Carter 1980; Dupraz & Combes 1986; Hernquist & Quinn 1988; Seitzer & Schweizer 1990).

Another important property of mergers is the gas mass fractions of the progenitor galaxies (e.g. Hernquist 1992, 1993; Barnes & Hernquist 1996; Dubinski et al. 1996; Boylan-Kolchin et al. 2005; Cox et al. 2006; Hani et al. 2020), which also typically corresponds to the morphological types of the progenitors as well (e.g. late types often being more gas rich than early types). While dark matter and stars are collisionless (Davis et al. 1985), only influenced by gravity during mergers, the gas is also subject to pressure forces and shocks (e.g. Barnes & Hernquist 1996). Radiative cooling of the gas also plays a role in the gas dynamics (e.g. Dalgarno & McCray 1972; Goldsmith & Langer 1978). Finally, the presence of gas means there is the potential for star formation and all of the associated feedback processes that do not exist with gas-poor progenitors. Galaxy mergers have long been seen as the main route for forming circumnuclear starbursts that can power U/LIRGs (e.g. Sanders & Mirabel 1996). Gas-rich mergers can involve prominent tidal tails and bridges produced from merging disc galaxies, shock-heating of the gas, tidal torques funnelling gas to the centres of galaxies forming central gas concentrations (e.g. Hernquist 1989; Barnes & Hernquist 1991; Blumenthal & Barnes 2018), nuclear starbursts driven by the high central gas mass surface densities (Sanders & Mirabel 1996; Ellison et al. 2008, 2013; Patton et al. 2013; Thorp et al. 2019), and enhanced turbulence in the gas from tidal shocks and high levels of star formation (e.g. Ostriker & Shetty 2011; Krumholz et al. 2018).

For the purposes of this thesis, we step through the broad stages of gas-rich galaxy mergers, focusing on the changes to gas properties and the SFR. Details described here are specifically from the results of Moreno et al. (2019), who simulated a suite of 24 pairs of idealized (non-cosmological) merging galaxies using the Feedback In Realistic Environments-2 (FIRE-2) model (Hopkins et al. 2018). Their approach was to explore a range of merger orbits with pairs of galaxies with mass ratios of 2.5:1 to investigate the impact on the multi-phase ISM and SFR in the period between first and second pericentre passage (they call this the "galaxy-pair period" lasting between 1 and 5 Gyr depending on the orbital parameters). The sums of the different gas phase masses and SFRs in the interacting galaxies are compared to the same sums in identical but isolated galaxies. Figure 1.3 shows the SFR vs. time in their fiducial simulation run as absolute rates in the merging and isolated galaxies (top) and as ratios of the merger SFR to the

isolated SFR (bottom). Figure 1.4 shows the same for the different temperature/density phases of the gas. Vertical dashed lines are, from left to right, the time of first pericentre passage, the time of second pericentre passage, and the time of coalescense. Results from the rest of the simulation suite follow the same general trends and are included in the following description.

Gas enhancements leading up to the first pericentre passage (Figure 1.4) include hot gas produced in shocks in the outskirts of the progenitors and cold-dense gas enhanced by the influx of cool gas. Accompanying the enhancement of cold-dense gas is a brief spike (over ≈ 25 Myr) in the SFR, reaching an enhancement of about a factor of five. The SFR enhancement then settles down to roughly a factor of two above the isolated case that is sustained for about 1.5 Gyr, before slowly dropping over another Gyr. During and just after the first pericentre passage, the warm gas is suppressed relative to the isolated galaxies to a median ratio of about 0.9 as it transfers into cool gas. Like in the isolated galaxies, the warm gas in the mergers slowly depletes, but more rapidly and especially around pericentre passages. The cool gas is slightly suppressed after first pericentre passage as it is converted into an enhancement in cold-dense gas. Cool gas does slowly replenish to the isolated-galaxies levels while slowly depleting in total mass in both the isolated and merging scenarios. Cold-dense gas also slowly depletes in the isolated and interacting galaxies, but maintains a median enhancement of 1.2 over several Gyr between first and second pericentre passages. An ultra-dense regime shows a median enhancement of 3.4 that lasts for about 1 Gyr after first passage, with brief enhancements up to factors of about 10 in some galaxy pairs at some times (see figure 16 from Moreno et al. 2019 for the enhancement of this phase over time).

During the second pericentre passage, the SFR quickly jumps to an enhancement of about a factor of ten that is sustained for about 250 Myr, lasting until after coalescense of the two progenitor galaxies. Following coalescense, the SFR gradually drops to almost the same level as the isolated galaxies over about 1.75 Gyr. The hot gas mass again ramps up starting about 250 Myr before second passage, where it stays enhanced by a factor of about 100 until coalescense. The warm, cool, and cold-dense gas masses all drop after second passage with cool and cold-dense gas doing so rapidly. All phases are suppressed relative to the isolated galaxies by factors of a few, except for the hot-gas phase. Conversion of both warm and cool gas to cold-dense causes the cold-dense gas mass to rebound to isolated-galaxy levels just before coalescense. All gas regimes drop
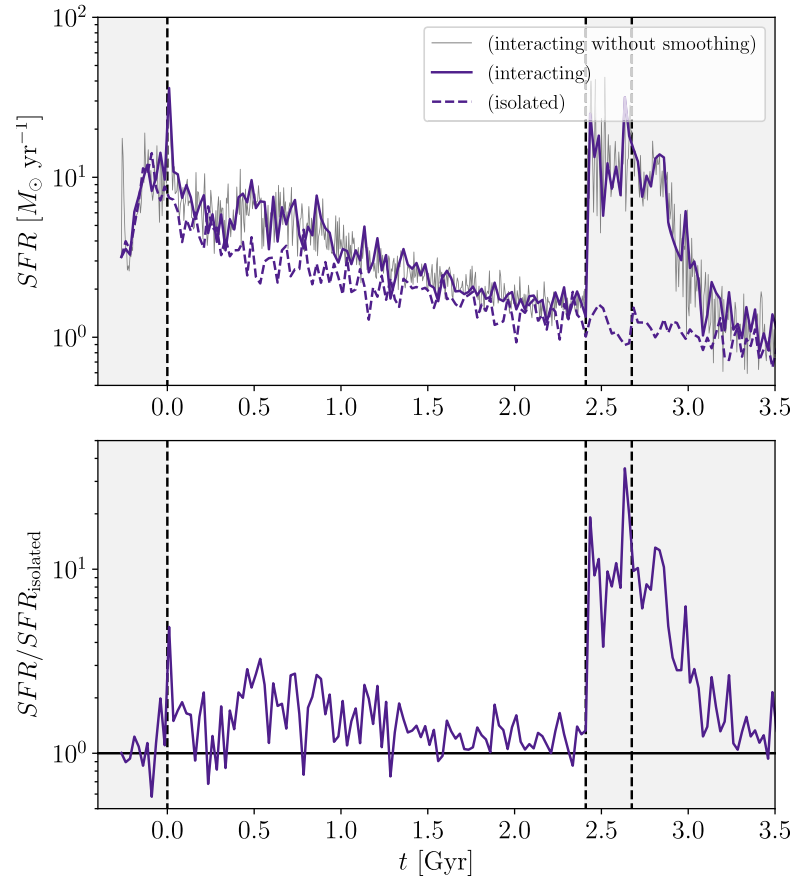
FIGURE 1.3: SFR vs. time for a single merging pair of galaxies from the fiducial run of the FIRE-2 simulation suite from Moreno et al. (2019). *Top:* SFR vs. time in the merging galaxies in 5 Myr snapshots are in gray and smoothed to 25 Myr snapshots in solid purple. The sum of the SFR in the two galaxies when isolated is in dashed purple. *Bottom:* SFR in the merging galaxies normalized by the SFR in the isolated galaxies vs. time. Vertical dashed lines show times of, from left to right, the first pericentre passage, the second pericentre passage, and coalescense. The region in white marks the "galaxy-pair period." Reproduced from figure 6 of "Interacting galaxies on FIRE-2: the connection between enhanced star formation and interstellar gas content" (Moreno et al. 2019).
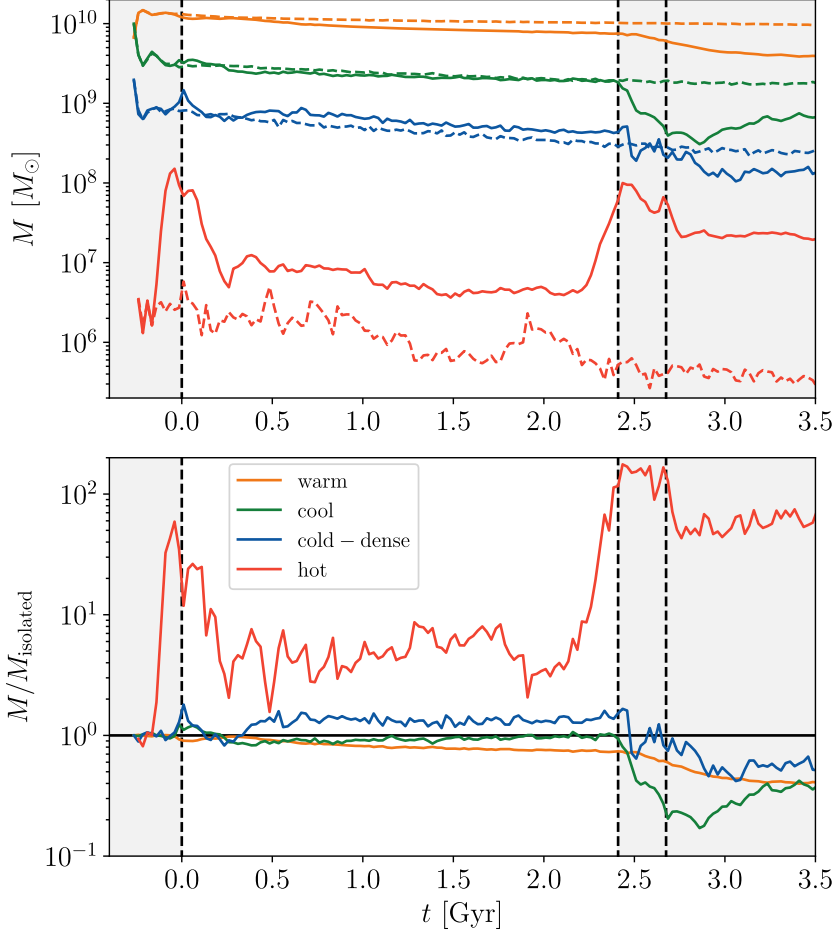
FIGURE 1.4: The same as Figure 1.3 but showing the masses in each gas phase vs. time. Gas-phase definitions are: hot, $T > 10^6$ K; warm, $T < 10^6$ K, $n < 0.1$ cm^{-3} and 8000 K $< T < 10^6$ K, $n > 0.1$ cm^{-3}; cool, $T < 8000$ K, 0.1 cm^{-3} $< n < 10$ cm^{-3} and 300 K $< T < 8000$ K, $n < 0.1$ cm^{-3}; and cold-dense, $T < 300$ K, $n > 10$ cm^{-3}. Reproduced from figure 7 of "Interacting galaxies on FIRE-2: the connection between enhanced star formation and interstellar gas content" (Moreno et al. 2019).

in mass after coalescense, with warm and cold-dense slowly depleting and becoming further suppressed. Cool gas goes from being the most-suppressed regime at coalescense to making a gradual rebound after coalescense as warm gas is converted into cool. The published data end about 1.75 Gyr after coalescense with hot gas enhanced by a factor of about 50 and the other phases suppressed to about 0.4 the isolated-galaxy levels. It appears there may still be an enhancement about a Gyr after coalescense in ultra-dense gas, but low levels of this densest phase in the isolated galaxies after roughly the first 1 Gyr make it difficult to measure the merger enhancement/suppression.

Moreno et al. (2021) carried out radial analyses of these simulations to explore where the SFR and gas enhancements/suppressions occur, as well as separating the results between the primary and secondary galaxies (again focusing on the galaxy-pair period). Increases in the cool gas, cold-dense gas, and stellar masses were primarily in the central regions of both galaxies, but strong suppression of the central SFE in the primary soon after first pericentre passage keeps its central star formation enhancement weak. The majority of secondaries experience enhanced central SFE. Global SFR enhancements are typically driven by central SFR enhancements due to the combination of enhanced cold-dense gas mass and enhanced SFE. On the other hand, global suppression of SFR in the primary is usually caused by suppressed central SFE despite enhanced cold-dense gas masses. Moreno et al. (2021) broadly describe these results as the majority of central SFR enhancements being fuel driven and central SFR suppression being efficiency driven. Starting with the second pericentre passages and lasting until more than a Gyr after coalescense, central cool/cold-dense gas and SFE are significantly enhanced, in both primary and secondary, producing strong SFR enhancement during this time.

For galaxy evolution after merger events, and in a much larger sample of simulated galaxies (though at lower resolution), Hani et al. (2020) analysed more than 27 000 post-merger galaxies in the IllustrisTNG cosmological simulation suite (Marinacci et al. 2018). Looking at galaxies just after they underwent a merger (within ≈ 160 Myr), both star-forming (67 per cent) and passive (33 per cent) galaxies were found. Star-forming post mergers exhibited a mean specific SFR enhancement of 2.073 ± 0.020 relative to control galaxies that gradually decreased over about 500 Myr back to non-merger levels. Control galaxies were chosen to have not had a merger with mass ratio ≥ 0.1 within 2 Gyr and were matched to the post-merger galaxies on redshift, stellar mass, number of galaxies within 2 Mpc, and the distance to the nearest neighbour galaxy.

1.7 The PHANGS-ALMA survey

The Physics at High Angular resolution in Nearby GalaxieS with ALMA (PHANGS-ALMA) survey[1] is designed to tackle many of the open questions about the properties of molecular gas in nearby spiral galaxies, and the interactions of the gas with other components of galaxies (Leroy et al. 2021c). The main sample of the survey mapped 75 massive ($M_\star \gtrsim 6 \times 10^9 \, \mathrm{M_\odot}$) and star-forming ($\mathrm{SFR}/M_\star > 10^{-11} \, \mathrm{yr}^{-1}$) galaxies within 17 Mpc in ^{12}CO (2–1) at approximately 1″ resolution. Each galaxy was mapped such that about 80 to 90 per cent of the total CO emission was captured. At this angular resolution, galaxies are observed at about 45 to 150 pc physical scales, or with roughly one GMC per resolution element. Data were obtained using ALMA's 12 m main array and both components of the Morita Atacama Compact Array (ACA) that includes the 7 m array and total power (TP) telescopes to capture emission on all scales from 1″ and larger. Total CO fluxes were recovered along with structure on scales larger than GMCs (for details of data processing and imaging, see Leroy et al. 2021b).

Many studies using PHANGS-ALMA data have already been published, some on subsets of the galaxies and others on the entire sample; I only highlight several of the more relevant here. Following an initial analysis of 15 galaxies by Sun et al. (2018), Sun et al. (2020b) analysed the CO mass surface densities and velocity dispersions on a pixel-by-pixel basis over the entire set of galaxies, making the most complete and homogeneous census of molecular-gas properties in nearby spiral galaxies to date. Rosolowsky et al. (2021) carried out a complementary cloud-based analysis on a subset of galaxies, also providing a very rich and homogeneous set of cloud measurements in nearby spiral galaxies. Utomo et al. (2018) used an early set of PHANGS-ALMA observations to estimate ϵ_{ff} on GMC scales and averaged over ≈ 1 kpc regions in 12 galaxies. Estimates of the pressure balance between turbulent energy within clouds and the external weight of the clumpy ISM were analysed by Sun et al. (2020a), who find that most molecular gas exists in environments that provide sufficient pressure to be marginally bound. Leroy et al. (2021a) reported measurements of flux ratios for CO (2–1)/CO (1–0), CO (3–2)/CO (2–1), and CO (3–2)/CO (1–0) across 43, 34, and 20 galaxies, respectively. These ratios are crucial for converting CO (3–2) and CO (2–1) fluxes to total molecular gas masses as well as determining properties of the molecular

---

[1] http://phangs.org/

gas such as temperature, density, and opacity. Detailed studies of individual galaxies have also been carried out, given the highly resolved nature of the PHANGS-ALMA maps, such as environmental variations in the SFE in NGC 628 (Kreckel et al. 2018), mapping electron temperatures in NGC 1672 (Ho et al. 2019), and measurements of the most massive molecular cloud in NGC 628 (Herrera et al. 2020).

Multiwavelength studies have been a natural extension of PHANGS-ALMA. Gallagher et al. (2018) measured the dense-gas fraction in five galaxies with CO and hydrogen cyanide (HCN) observations (EMPIRE Bigiel et al. 2016; Cormier et al. 2018; Jiménez-Donaire et al. 2019) to find that sub-kiloparsec dense gas fractions correlate with molecular gas mass surface density. Building upon PHANGS-ALMA are surveys with the *Hubble Space Telescope*[2] (Lee et al. 2022) and the Multi-Unit Spectroscopic Explorer (MUSE) on the Very Large Telescope (VLT) (Emsellem et al. 2021) observing 38 and 19 galaxies, respectively. Topics such as metallicity variations and mixing scales of the ISM (Kreckel et al. 2019, 2020; Williams et al. 2022), the time-scales of cloud and star formation at multiple physical scales (Kreckel et al. 2018; Schinnerer et al. 2019; Chevance et al. 2020), star cluster identification and association with molecular clouds (Wei et al. 2020; Turner et al. 2021; Kim et al. 2021), and much more can then be investigated in nearby spiral galaxies. Of particular importance to this thesis is that PHANGS-ALMA offers a spectacular characterization of nearby spiral galaxies that makes for a powerful control in comparison to extreme systems such as U/LIRGs and mergers.

1.8 This thesis

The broad goal of this thesis is to observe molecular-gas in nearby merging galaxies at GMC scales to explore why these systems appear to form a separate relation from spiral and low surface density galaxies in the Kennicutt-Schmidt relation. We target the molecular gas because it is the direct fuel for current star formation and thus its properties are the intial conditions for star formation. Studies of the Kennicutt-Schmidt relation on the scales of entire galaxies have shown starbursts are different but cannot show why, so observations of structures within galaxies are needed as constraints to any theories aiming to explain the difference. Observations at scales roughly the size of

---

[2]https://archive.stsci.edu/hlsp/phangs-hst

GMCs, as expected from observations of nearby spiral galaxies, offer the best chance to find evidence for why ϵ_{ff} is often different in mergers compared to spiral galaxies. GMCs are roughly the largest molecular structures within the ISM we expect to (sometimes) be gravitationally bound and so will be the easiest structures to observe in distant systems that are directly related to the onset of future star formation. Currently, we do not have much observational evidence for what GMCs in mergers and starbursts typically look like, so we must start with what we know of GMCs in spiral galaxies. Aiming to measure the molecular-gas properties at such small scales means we must target the closest mergers and U/LIRGs.

In Chapter 2 we present the highest spatial resolution observations in CO (2–1) to date (55 pc) of the merger and nearest luminous infrared galaxy (LIRG), NGC 3256. We derive molecular-gas properties on a pixel-by-pixel basis, and by comparing to an early sub-sample of the PHANGS-ALMA survey we show NGC 3256 has high mass surface densities, velocity dispersions, peak brightness temperatures, virial parameters, and internal turbulent pressures. High peak brightness temperatures imply warmer gas in NGC 3256 than in nearby spirals observed by PHANGS-ALMA, and large virial parameters point to largely gravitationally unbound molecular gas unless significant external pressure and/or mass is present to confine the clouds. We calculate very small changes in the surface density, velocity dispersion, and peak brightness temperature median values with spatial resolution (from 55 to 120 pc) compared to most of the PHANGS-ALMA galaxies, which may indicate a smoother molecular ISM in NGC 3256.

In Chapter 3 we expand on the pixel-based analysis of our observations of NGC 3256 with a complementary cloud-finding method. We identify 185 spatially and spectrally resolved clouds at 90 pc resolution for a direct comparison to the cloud-finding analysis of a sub-sample of PHANGS-ALMA galaxies by Rosolowsky et al. (2021). NGC 3256 again appears extreme compared to the PHANGS-ALMA galaxies in nearly all cloud properties derived. We show that clouds in NGC 3256 have larger velocity dispersions, luminosities, CO-estimated masses, mass suface densities, virial masses, virial parameters, size-linewidth coefficients, and internal turbulent pressures than most clouds in PHANGS-ALMA galaxies. Cloud radii also appear slightly larger in NGC 3256, despite our expectations that the cloud-finding technique would simply identify clouds near the spatial-resolution limit. Combining the nearly indistinguishable distribution of cloud eccentricities in NGC 3256 compared to PHANGS-ALMA galaxies with its narrower

distribution of virial parameters, we suggest that the average dynamical state of molecular clouds in NGC 3256 is not very different from nearby spirals, but that it exhibits a narrower range of cloud dynamical states. We also find general agreement between our pixel and cloud-based analyses of NGC 3256, but with evidence for the complementary nature of the methods.

In Chapter 4 we apply the same pixel-based analysis as in Chapter 2 to observations of the nearest major merger NGC 4038/9 ("the Antennae") in CO (2–1) and also at 55 pc resolution. We compare our results to those of PHANGS-ALMA, now their entire sample of 70 nearby spiral galaxies (Sun et al. 2020b), and to our results from NGC 3256. While we find the Antennae merger also has some of the highest mass surface densities, velocity dispersions, peak brightness temperatures, and turbulent pressures, it exhibits a very wide range of virial parameters that are often consistent with those measured in the PHANGS-ALMA galaxies. We also show that peak brightness temperatures and virial parameters are higher in NGC 3256 than NGC 4038/9, as well as velocity dispersions measured near the nuclei. Merger stage may be driving the more extreme molecular-gas properties observed in the later-stage merger, NGC 3256, compared to the earlier-stage merger, NGC 4038/9.

Finally, in Chapter 5 we conclude with a discussion of the primary results of this thesis. Broader implications derived from the combination of our results will be discussed, along with potential next steps motivated by our findings.

Several appendices are included at the end of this thesis for further detail. Appendix A describes our imaging procedure for the observations of NGC 3256 presented and analysed in Chapters 2 and 3. Appendix B shows the relations used in the completeness tests of Chapter 3 between the physical properties of the synthetic clouds and their three-dimensional Gaussian parameters as injected into the data cube. Appendix C summarizes my data-science internship that took place from June to December, 2019 at the vehicle traffic company Miovision in Kitchener, Ontario.

Bibliography

van Albada T. S., 1982, MNRAS, 201, 939

Andre P., Ward-Thompson D., Barsony M., 1993, ApJ, 406, 122

Arp H., 1966, ApJS, 14, 1

Athanassoula E., 1992, MNRAS, 259, 345

Bacchini C., Fraternali F., Iorio G., Pezzulli G., 2019a, A&A, 622, A64

Bacchini C., Fraternali F., Pezzulli G., Marasco A., Iorio G., Nipoti C., 2019b, A&A, 632, A127

Bacchini C., Fraternali F., Pezzulli G., Marasco A., 2020, A&A, 644, A125

Banerjee A., Jog C. J., Brinks E., Bagetakos I., 2011, MNRAS, 415, 687

Barnes J. E., 1988, ApJ, 331, 699

Barnes J. E., 1992, ApJ, 393, 484

Barnes J. E., Hernquist L. E., 1991, ApJ, 370, L65

Barnes J. E., Hernquist L., 1996, ApJ, 471, 115

Barton E. J., Geller M. J., Kenyon S. J., 2000, ApJ, 530, 660

Bauer F. E., Alexander D. M., Brandt W. N., Hornschemeier A. E., Vignali C., Garmire G. P., Schneider D. P., 2002, AJ, 124, 2351

Bell E. F., 2003, ApJ, 586, 794

Benedict G. F., Smith B. J., Kenney J. D. P., 1996, AJ, 112, 1318

Benincasa S. M., Wadsley J., Couchman H. M. P., Keller B. W., 2016, MNRAS, 462, 3053

Benson A. J., Bower R. G., Frenk C. S., Lacey C. G., Baugh C. M., Cole S., 2003, ApJ, 599, 38

Bertoldi F., McKee C. F., 1992, ApJ, 395, 140

Bigiel F., Leroy A., Walter F., Brinks E., de Blok W. J. G., Madore B., Thornley M. D., 2008, AJ, 136, 2846

Bigiel F., et al., 2011, ApJ, 730, L13

Bigiel F., Cormier D., Schmidt T., 2014, Astronomische Nachrichten, 335, 470

Bigiel F., et al., 2016, ApJ, 822, L26

Binney J., Tremaine S., 1987, Galactic dynamics. Princeton Univ. Press, Princeton, NJ

Blitz L., Rosolowsky E., 2004, ApJ, 612, L29

Blitz L., Rosolowsky E., 2006, ApJ, 650, 933

Blitz L., Fich M., Stark A. A., 1982, ApJS, 49, 183

Blitz L., Fukui Y., Kawamura A., Leroy A., Mizuno N., Rosolowsky E., 2007, in Reipurth B., Jewitt D., Keil K., eds, Protostars and Planets V. Univ. Arizona Press, Tuscon, AZ, p. 81

Blumenthal K. A., Barnes J. E., 2018, MNRAS, 479, 3952

Bolatto A. D., Leroy A. K., Rosolowsky E., Walter F., Blitz L., 2008, ApJ, 686, 948

Bolatto A. D., Wolfire M., Leroy A. K., 2013, ARA&A, 51, 207

Boquien M., et al., 2010, ApJ, 713, 626

Boquien M., et al., 2011, AJ, 142, 111

Boylan-Kolchin M., Ma C.-P., Quataert E., 2005, MNRAS, 362, 184

Calzetti D., Kinney A. L., Storchi-Bergmann T., 1994, ApJ, 429, 582

Calzetti D., et al., 2007, ApJ, 666, 870

Calzetti D., et al., 2010, ApJ, 714, 1256

Chandar R., Fall S. M., Whitmore B. C., Mulia A. J., 2017, ApJ, 849, 128

Chevance M., et al., 2020, MNRAS, 493, 2872

Chown R., et al., 2019, MNRAS, 484, 5192

Cohen R. S., Dame T. M., Garay G., Montani J., Rubio M., Thaddeus P., 1988, ApJ, 331, L95

Colbert E. J. M., Heckman T. M., Ptak A. F., Strickland D. K., Weaver K. A., 2004, ApJ, 602, 231

Colombo D., Rosolowsky E., Ginsburg A., Duarte-Cabral A., Hughes A., 2015, MN-RAS, 454, 2067

Colombo D., et al., 2018, MNRAS, 475, 1791

Condon J. J., 1992, ARA&A, 30, 575

Condon J. J., Helou G., Sanders D. B., Soifer B. T., 1993, AJ, 105, 1730

Condon J. J., Cotton W. D., Broderick J. J., 2002, AJ, 124, 675

Cormier D., et al., 2018, MNRAS, 475, 3909

Cox T. J., Dutta S. N., Di Matteo T., Hernquist L., Hopkins P. F., Robertson B., Springel V., 2006, ApJ, 650, 791

Dabrowski I., 1984, Canadian Journal of Physics, 62, 1639

Daddi E., et al., 2010, ApJ, 714, L118

Dahmen G., Huttemeister S., Wilson T. L., Mauersberger R., 1998, A&A, 331, 959

Dale D. A., Helou G., 2002, ApJ, 576, 159

Dalgarno A., McCray R. A., 1972, ARA&A, 10, 375

Davis M., Efstathiou G., Frenk C. S., White S. D. M., 1985, ApJ, 292, 371

Díaz-García S., et al., 2021, A&A, 654, A135

Dobbs C. L., 2008, MNRAS, 391, 844

Dobbs C. L., Pringle J. E., 2013, MNRAS, 432, 653

Dobbs C. L., Burkert A., Pringle J. E., 2011, MNRAS, 413, 2935

Dopita M. A., 1985, ApJ, 295, L5

Downes D., Solomon P. M., 1998, ApJ, 507, 615

Draine B. T., 2003, ARA&A, 41, 241

Dubinski J., Mihos J. C., Hernquist L., 1996, ApJ, 462, 576

Dubinski J., Mihos J. C., Hernquist L., 1999, ApJ, 526, 607

Dupraz C., Combes F., 1986, A&A, 166, 53

Dutrey A., Guilloteau S., Simon M., 1994, A&A, 286, 149

Elbaz D., et al., 2011, A&A, 533, A119

Ellison S. L., Patton D. R., Simard L., McConnachie A. W., 2008, AJ, 135, 1877

Ellison S. L., Nair P., Patton D. R., Scudder J. M., Mendel J. T., Simard L., 2011, MNRAS, 416, 2182

Ellison S. L., Mendel J. T., Patton D. R., Scudder J. M., 2013, MNRAS, 435, 3627

Elmegreen B. G., 1987, ApJ, 312, 626

Elmegreen B. G., 1997, in Franco J., Terlevich R., Serrano A., eds, Rev. Mex. Astron. Astrofís. Conf. Ser. Vol. 6, 1st Guillermo Haro Conference on Astrophysics: Starburst Activity in Galaxies. p. 165

Elmegreen B. G., 2011, ApJ, 737, 10

Elmegreen B. G., 2015, ApJ, 814, L30

Elmegreen B. G., 2018, ApJ, 854, 16

Elmegreen B. G., Elmegreen D. M., 1983, MNRAS, 203, 31

Elmegreen B. G., Falgarone E., 1996, ApJ, 471, 816

Elmegreen B. G., Hunter D. A., 2015, ApJ, 805, 145

Emsellem E., et al., 2021, preprint (arXiv:2110.03708),

Engargiola G., Plambeck R. L., Rosolowsky E., Blitz L., 2003, ApJS, 149, 343

Erickson E. F., Knacke R. F., Tokunaga A. T., Haas M. R., 1981, ApJ, 245, 148

Evans Neal J. I., et al., 2009, ApJS, 181, 321

Evans Neal J. I., Heiderman A., Vutisalchavakul N., 2014, ApJ, 782, 114

Faesi C. M., Lada C. J., Forbrich J., 2018, ApJ, 857, 19

Falgarone E., Phillips T. G., Walker C. K., 1991, ApJ, 378, 186

Falgarone E., Pety J., Hily-Blant P., 2009, A&A, 507, 355

Fall S. M., Chandar R., 2012, ApJ, 752, 96

Fall S. M., Krumholz M. R., Matzner C. D., 2010, ApJ, 710, L142

Federrath C., Klessen R. S., 2012, ApJ, 761, 156

Ferguson A. M. N., Wyse R. F. G., Gallagher J. S., Hunter D. A., 1998, ApJ, 506, L19

Field G. B., Blackman E. G., Keto E. R., 2011, MNRAS, 416, 710

Filho M. E., Sánchez Almeida J., Amorín R., Muñoz-Tuñón C., Elmegreen B. G., Elmegreen D. M., 2016, ApJ, 820, 109

Fleck Robert C. J., 1996, ApJ, 458, 739

Förster Schreiber N. M., Roussel H., Sauvage M., Charmandaris V., 2004, A&A, 419, 501

Fraser-McKelvie A., et al., 2020, MNRAS, 495, 4158

Fukui Y., et al., 1999, PASJ, 51, 745

Fukui Y., et al., 2008, ApJS, 178, 56

Galametz M., et al., 2009, A&A, 508, 645

Galametz M., et al., 2013, MNRAS, 431, 1956

Gallagher M. J., et al., 2018, ApJ, 868, L38

Galliano F., Madden S. C., Jones A. P., Wilson C. D., Bernard J. P., 2005, A&A, 434, 867

Gao Y., Solomon P. M., 2004, ApJ, 606, 271

García-Burillo S., Usero A., Alonso-Herrero A., Graciá-Carpio J., Pereira-Santaella M., Colina L., Planesas P., Arribas S., 2012, A&A, 539, A8

Genzel R., et al., 2010, MNRAS, 407, 2091

Genzel R., et al., 2012, ApJ, 746, 69

Gerhard O. E., 1981, MNRAS, 197, 179

Ginsburg A., et al., 2016, A&A, 586, A50

Goldreich P., Lynden-Bell D., 1965, MNRAS, 130, 125

Goldsmith P. F., 1987, in Hollenbach D. J., Thronson Harley A. J., eds, Astrophysics and Space Science Library Vol. 134, Interstellar Processes. Springer, Dordrecht, p. 51

Goldsmith P. F., Langer W. D., 1978, ApJ, 222, 881

Gordon M. A., 1988, ApJ, 331, 509

Gordon M. A., Jewell P. R., 1987, ApJ, 323, 766

Gordon K. D., Misselt K. A., Witt A. N., Clayton G. C., 2001, ApJ, 551, 269

Gordon K. D., et al., 2014, ApJ, 797, 85

Gratier P., et al., 2012, A&A, 542, A108

Guszejnov D., Hopkins P. F., Grudić M. Y., 2018, MNRAS, 477, 5139

Gutermuth R. A., Pipher J. L., Megeath S. T., Myers P. C., Allen L. E., Allen T. S., 2011, ApJ, 739, 84

Hani M. H., Gosain H., Ellison S. L., Patton D. R., Torrey P., 2020, MNRAS, 493, 3716

Hao C.-N., Kennicutt R. C., Johnson B. D., Calzetti D., Dale D. A., Moustakas J., 2011, ApJ, 741, 124

Heiderman A., Evans Neal J. I., Allen L. E., Huard T., Heyer M., 2010, ApJ, 723, 1019

Helou G., Soifer B. T., Rowan-Robinson M., 1985, ApJ, 298, L7

Hernquist L., 1989, Nature, 340, 687

Hernquist L., 1992, ApJ, 400, 460

Hernquist L., 1993, ApJS, 86, 389

Hernquist L., Quinn P. J., 1988, ApJ, 331, 682

Herrera C. N., et al., 2020, A&A, 634, A121

Herrero-Illana R., et al., 2019, A&A, 628, A71

Heyer M., Dame T. M., 2015, ARA&A, 53, 583

Heyer M. H., Carpenter J. M., Ladd E. F., 1996, ApJ, 463, 630

Heyer M. H., Carpenter J. M., Snell R. L., 2001, ApJ, 551, 852

Heyer M., Krawczyk C., Duval J., Jackson J. M., 2009, ApJ, 699, 1092

Hildebrand R. H., 1983, QJRAS, 24, 267

Hildebrand R. H., Whitcomb S. E., Winston R., Stiening R. F., Harper D. A., Moseley S. H., 1977, ApJ, 216, 698

Ho L. C., Filippenko A. V., Sargent W. L. W., 1997, ApJ, 487, 591

Ho I. T., et al., 2019, ApJ, 885, L31

Hollenbach D. J., Tielens A. G. G. M., 1999, Reviews of Modern Physics, 71, 173

Hopkins P. F., Quataert E., Murray N., 2011, MNRAS, 417, 950

Hopkins P. F., Quataert E., Murray N., 2012, MNRAS, 421, 3488

Hopkins P. F., et al., 2018, MNRAS, 480, 800

Hughes A., et al., 2013, ApJ, 779, 46

Israel F. P., 2009a, A&A, 493, 525

Israel F. P., 2009b, A&A, 506, 689

Israel F. P., van der Hulst J. M., 1983, AJ, 88, 1736

Jeffreson S. M. R., Kruijssen J. M. D., 2018, MNRAS, 476, 3688

Jiménez-Donaire M. J., et al., 2019, ApJ, 880, 127

Jogee S., Scoville N., Kenney J. D. P., 2005, ApJ, 630, 837

Johnstone D., Wilson C. D., Moriarty-Schieven G., Joncas G., Smith G., Gregersen E., Fich M., 2000, ApJ, 545, 327

de Jong T., Boland W., Dalgarno A., 1980, A&A, 91, 68

de Jong T., Clegg P. E., Soifer B. T., Rowan-Robinson M., Habing H. J., Houck J. R., Aumann H. H., Raimond E., 1984, ApJ, 278, L67

de Jong T., Klein U., Wielebinski R., Wunderlich E., 1985, A&A, 147, L6

Karakas A. I., Lugaro M., 2016, ApJ, 825, 26

Keller B. W., Wadsley J., Benincasa S. M., Couchman H. M. P., 2014, MNRAS, 442, 3013

Keller B. W., Wadsley J., Couchman H. M. P., 2015, MNRAS, 453, 3499

Keller B. W., Wadsley J., Couchman H. M. P., 2016, MNRAS, 463, 1431

Keller B. W., Kruijssen J. M. D., Wadsley J. W., 2020, MNRAS, 493, 2149

Kennicutt Robert C. J., 1998, ApJ, 498, 541

Kennicutt R. C., Evans N. J., 2012, ARA&A, 50, 531

Kennicutt R. C., de los Reyes M. A. C., 2021, ApJ, 908, 61

Kennicutt Robert C. J., et al., 2007, ApJ, 671, 333

Kennicutt Robert C. J., et al., 2009, ApJ, 703, 1672

Kim C.-G., Ostriker E. C., 2015, ApJ, 815, 67

Kim C.-G., Kim W.-T., Ostriker E. C., 2011, ApJ, 743, 25

Kim J., et al., 2021, MNRAS, 504, 487

Klein U., Graeve R., 1986, A&A, 161, 155

Klein U., Wielebinski R., Morsi H. W., 1988, A&A, 190, 41

Kobulnicky H. A., Johnson K. E., 1999, ApJ, 527, 154

Kolmogorov A., 1941, Akademiia Nauk SSSR Doklady, 30, 301

Kong X., Charlot S., Brinchmann J., Fall S. M., 2004, MNRAS, 349, 769

Kormendy J., Fisher D. B., Cornell M. E., Bender R., 2009, ApJS, 182, 216

Kreckel K., et al., 2018, ApJ, 863, L21

Kreckel K., et al., 2019, ApJ, 887, 80

Kreckel K., et al., 2020, MNRAS, 499, 193

Kritsuk A. G., Lee C. T., Norman M. L., 2013, MNRAS, 436, 3247

Krumholz M. R., 2014, Phys. Rep., 539, 49

Krumholz M. R., McKee C. F., 2005, ApJ, 630, 250

Krumholz M. R., Thompson T. A., 2007, ApJ, 669, 289

Krumholz M. R., Ting Y.-S., 2018, MNRAS, 475, 2236

Krumholz M. R., Matzner C. D., McKee C. F., 2006, ApJ, 653, 361

Krumholz M. R., Dekel A., McKee C. F., 2012, ApJ, 745, 69

Krumholz M. R., Burkhart B., Forbes J. C., Crocker R. M., 2018, MNRAS, 477, 2716

Krumholz M. R., McKee C. F., Bland-Hawthorn J., 2019, ARA&A, 57, 227

Kuno N., et al., 2007, PASJ, 59, 117

Lada C. J., Lada E. A., 2003, ARA&A, 41, 57

Lada C. J., Lombardi M., Alves J. F., 2010, ApJ, 724, 687

Lada C. J., Forbrich J., Lombardi M., Alves J. F., 2012, ApJ, 745, 190

Larson R. B., 1974, MNRAS, 169, 229

Larson R. B., 1981, MNRAS, 194, 809

Larson R. B., Tinsley B. M., 1978, ApJ, 219, 46

Lee Y., 2004, Journal of Korean Astronomical Society, 37, 137

Lee E. J., Miville-Deschênes M.-A., Murray N. W., 2016, ApJ, 833, 229

Lee J. C., et al., 2022, ApJS, 258, 10

Lehmer B. D., Alexander D. M., Bauer F. E., Brandt W. N., Goulding A. D., Jenkins L. P., Ptak A., Roberts T. P., 2010, ApJ, 724, 559

Leroy A., Bolatto A., Walter F., Blitz L., 2006, ApJ, 643, 825

Leroy A. K., Walter F., Brinks E., Bigiel F., de Blok W. J. G., Madore B., Thornley M. D., 2008, AJ, 136, 2782

Leroy A. K., et al., 2011, ApJ, 737, 12

Leroy A. K., et al., 2013, AJ, 146, 19

Leroy A. K., et al., 2021a, preprint (arXiv:2109.11583),

Leroy A. K., et al., 2021b, ApJS, 255, 19

Leroy A. K., et al., 2021c, ApJS, 257, 43

Li Y., Mo H. J., van den Bosch F. C., Lin W. P., 2007, MNRAS, 379, 689

Lin L., Li C., He Y., Xiao T., Wang E., 2017, ApJ, 838, 105

Liszt H. S., Pety J., 2012, A&A, 541, A58

Lonsdale Persson C. J., Helou G., 1987, ApJ, 314, 513

Mac Low M.-M., McCray R., 1988, ApJ, 324, 776

Madau P., Dickinson M., 2014, ARA&A, 52, 415

Malin D. F., Carter D., 1980, Nature, 285, 643

Marinacci F., et al., 2018, MNRAS, 480, 5113

Mathews W. G., Baker J. C., 1971, ApJ, 170, 241

Matzner C. D., 2002, ApJ, 566, 302

McKee C. F., 1989, ApJ, 345, 782

McKee C. F., Ostriker J. P., 1977, ApJ, 218, 148

McKee C. F., Ostriker E. C., 2007, ARA&A, 45, 565

McNally C. P., Wadsley J., Couchman H. M. P., 2009, ApJ, 697, L162

Meny C., Gromov V., Boudet N., Bernard J. P., Paradis D., Nayral C., 2007, A&A, 468, 171

Mezger P. G., Henderson A. P., 1967, ApJ, 147, 471

Miville-Deschênes M.-A., Murray N., Lee E. J., 2017, ApJ, 834, 57

Mizuno N., et al., 2001a, PASJ, 53, 971

Mizuno N., Rubio M., Mizuno A., Yamaguchi R., Onishi T., Fukui Y., 2001b, PASJ, 53, L45

Mizuno N., Muller E., Maeda H., Kawamura A., Minamidani T., Onishi T., Mizuno A., Fukui Y., 2006, ApJ, 643, L107

Mo H. J., Mao S., White S. D. M., 1998, MNRAS, 295, 319

Mo H., van den Bosch F., White S., 2010, Galaxy formation and evolution. Cambridge Univ. Press, Cambridge, UK

Mok A., Chandar R., Fall S. M., 2020, ApJ, 893, 135

Moreno J., et al., 2019, MNRAS, 485, 1320

Moreno J., et al., 2021, MNRAS, 503, 3113

Muratov A. L., Kereš D., Faucher-Giguère C.-A., Hopkins P. F., Quataert E., Murray N.,

2015, MNRAS, 454, 2691

Murphy E. J., 2009, ApJ, 706, 482

Murphy E. J., 2013, ApJ, 777, 58

Murphy E. J., et al., 2011, ApJ, 737, 67

Murray N., 2011, ApJ, 729, 133

Naab T., Burkert A., 2003, ApJ, 597, 893

Narayan C. A., Jog C. J., 2002, A&A, 394, 89

Narayanan D., Krumholz M., Ostriker E. C., Hernquist L., 2011, MNRAS, 418, 664

Narayanan D., Krumholz M. R., Ostriker E. C., Hernquist L., 2012, MNRAS, 421, 3127

Nath B. B., Shchekinov Y., 2013, ApJ, 777, L12

Niklas S., Klein U., Wielebinski R., 1997, A&A, 322, 19

Ochsendorf B. B., Meixner M., Chastenet J., Tielens A. G. G. M., Roman-Duval J., 2016, ApJ, 832, 43

Ochsendorf B. B., Meixner M., Roman-Duval J., Rahman M., Evans Neal J. I., 2017, ApJ, 841, 109

Onodera S., et al., 2010, ApJ, 722, L127

Orr M. E., et al., 2018, MNRAS, 478, 3653

Ostriker E. C., Shetty R., 2011, ApJ, 731, 41

Padoan P., Haugbølle T., Nordlund Å., 2012, ApJ, 759, L27

Papadopoulos P. P., van der Werf P., Xilouris E., Isaak K. G., Gao Y., 2012, ApJ, 751, 10

Paradis D., et al., 2010, A&A, 520, L8

Patton D. R., Torrey P., Ellison S. L., Mendel J. T., Scudder J. M., 2013, MNRAS, 433, L59

Patton D. R., et al., 2020, MNRAS, 494, 4969

Pérez-González P. G., et al., 2006, ApJ, 648, 987

Persic M., Rephaeli Y., Braito V., Cappi M., Della Ceca R., Franceschini A., Gruber D. E., 2004, A&A, 419, 849

Pineda J. L., Velusamy T., Langer W. D., Goldsmith P. F., Li D., Yorke H. W., 2010, A&A, 521, L19

Piner B. G., Stone J. M., Teuben P. J., 1995, ApJ, 449, 508

Quai S., Hani M. H., Ellison S. L., Patton D. R., Woo J., 2021, MNRAS, 504, 1888

Rahman N., et al., 2012, ApJ, 745, 183

Ranalli P., Comastri A., Setti G., 2003, A&A, 399, 39

Raskutti S., Ostriker E. C., Skinner M. A., 2016, ApJ, 829, 130

Regan M. W., Teuben P. J., 2004, ApJ, 600, 595

Regan M. W., et al., 2006, ApJ, 652, 1112

Rémy-Ruyer A., et al., 2014, A&A, 563, A31

de los Reyes M. A. C., Kennicutt R. C., 2019, ApJ, 872, 16

Rice T. S., Goodman A. A., Bergin E. A., Beaumont C., Dame T. M., 2016, ApJ, 822, 52

Rieke G. H., Alonso-Herrero A., Weiner B. J., Pérez-González P. G., Blaylock M., Donley J. L., Marcillac D., 2009, ApJ, 692, 556

Roman-Duval J., Jackson J. M., Heyer M., Rathborne J., Simon R., 2010, ApJ, 723, 492

Roman-Duval J., et al., 2014, ApJ, 797, 86

Roman-Duval J., Bot C., Chastenet J., Gordon K., 2017, ApJ, 841, 72

Romano M., et al., 2021, A&A, 653, A111

Rosolowsky E., 2005, PASP, 117, 1403

Rosolowsky E., 2007, ApJ, 654, 240

Rosolowsky E., Leroy A., 2006, PASP, 118, 590

Rosolowsky E., Engargiola G., Plambeck R., Blitz L., 2003, ApJ, 599, 258

Rosolowsky E., et al., 2021, MNRAS, 502, 1218

Roussel H., Sauvage M., Vigroux L., Bosma A., 2001, A&A, 372, 427

Roussel H., et al., 2007, ApJ, 669, 959

Roychowdhury S., Chengalur J. N., Shi Y., 2017, A&A, 608, A24

Saintonge A., et al., 2017, ApJS, 233, 22

Sakamoto K., Okumura S. K., Ishizuki S., Scoville N. Z., 1999, ApJ, 525, 691

Salim S., et al., 2007, ApJS, 173, 267

Sánchez-García M., et al., 2021, preprint (arXiv:2111.03876),

Sánchez N., Alfaro E. J., Pérez E., 2007, ApJ, 656, 222

Sanders D. B., Mirabel I. F., 1996, ARA&A, 34, 749

Sanders D. B., Mazzarella J. M., Kim D. C., Surace J. A., Soifer B. T., 2003, AJ, 126, 1607

Sandstrom K. M., et al., 2013, ApJ, 777, 5

Scalzo R. A., Ruiter A. J., Sim S. A., 2014, MNRAS, 445, 2535

Schaye J., et al., 2015, MNRAS, 446, 521

Schechter P., 1976, ApJ, 203, 297

Schinnerer E., et al., 2019, ApJ, 887, 49

Schmidt M., 1959, ApJ, 129, 243

Schmidt M., 1963, ApJ, 137, 758

Schruba A., Leroy A. K., Walter F., Sandstrom K., Rosolowsky E., 2010, ApJ, 722, 1699

Schruba A., Kruijssen J. M. D., Leroy A. K., 2019, ApJ, 883, 2

Schwartz P. R., 1982, ApJ, 252, 589

Scoville N. Z., Yun M. S., Clemens D. P., Sanders D. B., Waller W. H., 1987, ApJS, 63, 821

Scudder J. M., Ellison S. L., Torrey P., Patton D. R., Mendel J. T., 2012, MNRAS, 426, 549

Seitenzahl I. R., Townsley D. M., 2017, Nucleosynthesis in Thermonuclear Supernovae. Springer, Cham, pp 1151–1184

Seitenzahl I. R., Cescutti G., Röpke F. K., Ruiter A. J., Pakmor R., 2013, A&A, 559, L5

Seitzer P., Schweizer F., 1990, in Wielen R., ed., Dynamics and Interactions of Galaxies. Springer, Berlin, Heidelberg, p. 270

Sellwood J. A., Wilkinson A., 1993, Reports on Progress in Physics, 56, 173

Sharma P., Roy A., Nath B. B., Shchekinov Y., 2014, MNRAS, 443, 3463

Sheth K., Vogel S. N., Regan M. W., Thornley M. D., Teuben P. J., 2005, ApJ, 632, 217

Shi Y., Helou G., Yan L., Armus L., Wu Y., Papovich C., Stierwalt S., 2011, ApJ, 733, 87

Shi Y., et al., 2018, ApJ, 853, 149

Shirley Y. L., Huard T. L., Pontoppidan K. M., Wilner D. J., Stutz A. M., Bieging J. H., Evans Neal J. I., 2011, ApJ, 728, 143

Silk J., 1997, ApJ, 481, 703

Sodroski T. J., et al., 1995, ApJ, 452, 262

Solomon P. M., Rivolo A. R., Barrett J., Yahil A., 1987, ApJ, 319, 730

Somerville R. S., Primack J. R., 1999, MNRAS, 310, 1087

Sormani M. C., Binney J., Magorrian J., 2015, MNRAS, 454, 1818

Springel V., White S. D. M., 1999, MNRAS, 307, 162

Strong A. W., Moskalenko I. V., Reimer O., Digel S., Diehl R., 2004, A&A, 422, L47

Stutzki J., Guesten R., 1990, ApJ, 356, 513

Sun J., et al., 2018, ApJ, 860, 172

Sun J., et al., 2020a, ApJ, 892, 148

Sun J., et al., 2020b, ApJ, 901, L8

Symeonidis M., et al., 2011, MNRAS, 417, 2239

Tasker E. J., Tan J. C., 2009, ApJ, 700, 358

Teng Y.-H., et al., 2021, preprint (arXiv:2111.05844),

Thorp M. D., Ellison S. L., Simard L., Sánchez S. F., Antonio B., 2019, MNRAS, 482, L55

Tielens A. G. G. M., Hollenbach D., 1985, ApJ, 291, 722

Toomre A., Toomre J., 1972, ApJ, 178, 623

Turner J. L., Ho P. T. P., 1994, ApJ, 421, 122

Turner J. A., et al., 2021, MNRAS, 502, 1366

Usero A., et al., 2015, AJ, 150, 115

Utomo D., et al., 2017, ApJ, 849, 26

Utomo D., et al., 2018, ApJ, 861, L18

Verley S., Corbelli E., Giovanardi C., Hunt L. K., 2010, A&A, 510, A64

Viaene S., et al., 2014, A&A, 567, A71

Vogel S. N., Boulanger F., Ball R., 1987, ApJ, 321, L145

Vogelsberger M., et al., 2014, MNRAS, 444, 1518

Wada K., Spaans M., Kim S., 2000, ApJ, 540, 797

Walterbos R. A. M., Greenawalt B., 1996, ApJ, 460, 696

Wei W., et al., 2020, MNRAS, 493, 3178

Weiß A., Neininger N., Hüttemeister S., Klein U., 2001, A&A, 365, 571

Welty D. E., Xue R., Wong T., 2012, ApJ, 745, 173

White S. D. M., 1978, MNRAS, 184, 185

White S. D. M., 1979, MNRAS, 189, 831

White S. D. M., Frenk C. S., 1991, ApJ, 379, 52

Williams J. P., de Geus E. J., Blitz L., 1994, ApJ, 428, 693

Williams J. P., Blitz L., McKee C. F., 2000, in Mannings V., Boss A. P., Russell S. S., eds, Protostars and Planets IV. Univ. Arizona Press, Tuscon, AZ, p. 97

Williams T. G., et al., 2022, MNRAS, 509, 1303

Wilson C. D., 1994, ApJ, 434, L11

Wilson C. D., 1995, ApJ, 448, L97

Wilson C. D., Reid I. N., 1991, ApJ, 366, L11

Wilson T. L., Rood R., 1994, ARA&A, 32, 191

Wilson C. D., Rudolph A. L., 1993, ApJ, 406, 477

Wilson C. D., Scoville N., 1990, ApJ, 363, 435

Wilson C. D., Elmegreen B. G., Bemis A., Brunetti N., 2019, ApJ, 882, 5

Wong T., et al., 2008, MNRAS, 386, 1069

Wong T., et al., 2011, ApJS, 197, 16

Wu H., Cao C., Hao C.-N., Liu F.-S., Wang J.-L., Xia X.-Y., Deng Z.-G., Young C. K.-S., 2005a, ApJ, 632, L79

Wu J., Evans Neal J. I., Gao Y., Solomon P. M., Shirley Y. L., Vanden Bout P. A., 2005b, ApJ, 635, L173

Wu Y., Charmandaris V., Houck J. R., Bernard-Salas J., Lebouteiller V., Brandl B. R., Farrah D., 2008, ApJ, 676, 970

Wu Y., et al., 2010, ApJ, 723, 895

Wu Y., et al., 2011, ApJ, 734, 40

Wyder T. K., et al., 2009, ApJ, 696, 1834

Yamashita T., et al., 2017, ApJ, 844, 96

Yim K., Wong T., Xue R., Rand R. J., Rosolowsky E., van der Hulst J. M., Benjamin R., Murphy E. J., 2014, AJ, 148, 127

Yim K., Wong T., Rand R. J., Schinnerer E., 2020, MNRAS, 494, 4558

Yun M. S., Reddy N. A., Condon J. J., 2001, ApJ, 554, 803

Zhang Q., Fall S. M., 1999, ApJ, 527, L81

2 | Highly turbulent gas on GMC-scales in NGC 3256, the nearest luminous infrared galaxy

This chapter represents an unchanged version of the paper *Highly turbulent gas on GMC-scales in NGC 3256, the nearest luminous infrared galaxy*, published in the refereed journal, *Monthly Notices of the Royal Astronomical Society*. The full reference is given below.

Brunetti N.[1], Wilson C. D.[1], Sliwa K.[2], Schinnerer E.[2], Aalto S.[3], Peck A. B.[4], MNRAS, Volume 500, Issue 4, pp. 4730–4748

[1]*Department of Physics and Astronomy, McMaster University, Hamilton, ON L8S 4M1, Canada*

[2]*Max-Planck-Institut für Astronomie, Königstuhl 17, D-69117, Heidelberg, Germany*

[3]*Department of Space, Earth and Environment, Chalmers University of Technology, Onsala Space Observatory, 43992 Onsala, Sweden*

[4]*Gemini Observatory, Northern Operation Center, 67-0 N. A'Ohoku Place, Hilo, HI, USA*

Abstract

We present the highest resolution CO (2–1) observations obtained to date ($0\farcs25$) of NGC 3256 and use them to determine the detailed properties of the molecular interstellar medium in the central 6 kpc of this merger. Distributions of physical quantities are reported from pixel-by-pixel measurements at 55 and 120 pc scales and compared to disc galaxies observed by PHANGS-ALMA. Mass surface densities range from 8 to 5500 $M_\odot \, pc^{-2}$ and velocity dispersions from 10 to 200 $km \, s^{-1}$. Peak brightness temperatures as large as 37 K are measured, indicating the gas in NGC 3256 may be hotter than all regions in nearby disc galaxies measured by PHANGS-ALMA. Brightness temperatures even surpass those in the overlap region of NGC 4038/9 at the same scales. The majority of the gas appears unbound with median virial parameters of 7 to 19, although external pressure may bind some of the gas. High internal turbulent pressures of 10^5 to $10^{10} \, K \, cm^{-3}$ are found. Given the lack of significant trends in surface density, brightness temperature, and velocity dispersion with physical scale we argue the molecular gas is made up of a smooth medium down to 55 pc scales, unlike the more structured medium found in the PHANGS-ALMA disc galaxies.

Key words: ISM: clouds – ISM: kinematics and dynamics – ISM: jets and outflows – galaxies: ISM – galaxies: interactions – galaxies: jets.

2.1 Introduction

Molecular gas is the immediate fuel for star formation and thus an important ingredient in galaxy evolution. In the Milky Way and nearby galaxies, giant molecular clouds (GMCs) are the dominant structures within the molecular interstellar medium (ISM) (Dame et al. 1987; Solomon et al. 1987; Wilson & Scoville 1990; Fukui et al. 1999; Mizuno et al. 2001; Engargiola et al. 2003; Leroy et al. 2006; Rosolowsky 2007) and are the sites of current and future star formation (Blitz & Thaddeus 1980; Genzel & Stutzki 1989; Mizuno et al. 1995). However, different galactic environments exhibit molecular gas properties that vary widely while also maintaining ongoing star formation (e.g. Rosolowsky & Blitz 2005; Heyer et al. 2009; Wong et al. 2011; Leroy et al. 2015). A complete description of the evolution of molecular gas properties and their connections to star formation must include explanations spanning the full range of observed regimes.

Wide distributions of molecular gas mass surface densities and velocity dispersions have been observed in many regions within the Milky Way and nearby galaxies (e.g. Heyer et al. 2001, 2009; Wong et al. 2011; Bolatto et al. 2008; Colombo et al. 2014; Rosolowsky & Blitz 2005; Leroy et al. 2015; Utomo et al. 2015; Sun et al. 2018). The largest and most uniform extragalactic sample was analysed by Sun et al. (2018) including 11 galaxies in the Physics at High Angular resolution in Nearby GalaxieS with ALMA (PHANGS-ALMA) survey (Leroy et al. 2020, in preparation), along with 4 galaxies from the literature. They found these properties vary systematically such that a narrow range of virial parameters (~1 to 3) is present. As an estimate of the balance between the kinetic energy, K, and gravitational energy, U_{g}, within a molecular cloud, the virial parameter, $\alpha_{\mathrm{vir}} \equiv 2K/U_{\mathrm{g}}$, can indicate the likelihood of collapse and the ability to form stars (McKee & Zweibel 1992; Federrath & Klessen 2012; Krumholz et al. 2012; Padoan et al. 2017). These galaxies were also found to exhibit internal turbulent pressures ranging across 4 to 5 orders of magnitude. The internal pressure, $P_{\mathrm{turb}} \propto \sigma^2/R$, can be estimated from observational properties of clouds and comparing the pressure to the surface density of the cloud can provide another estimate its dynamical state (Keto & Myers 1986; Heyer et al. 2009; Field et al. 2011; Leroy et al. 2015). These results imply the majority of molecular gas is kept close to dynamical equilibrium or collapse while the internal energy varies dramatically. Combining those molecular gas observations with measurements of the atomic and stellar surface densities, Sun et al.

(2020a) estimated the external pressure exerted on GMCs. They found that maintaining dynamical equilibrium over such a large range of internal pressures requires taking into account the full external pressure exerted on GMCs from the atomic, stellar, and clumpy molecular components of the galaxy.

While the PHANGS-ALMA analyses cover a range of galactic environments, they lack a direct comparison with observations of more extreme systems that bracket their sample. Do the scalings found by Sun et al. (2018) hold as gas masses, gas densities, and star formation rates continue to climb? For example, star formation efficiencies per free-fall time within ultra/luminous infrared galaxies (U/LIRGs) have been estimated to be higher than in disc galaxies. Calculated on scales of ~500 pc in five U/LIRGs, Wilson et al. (2019) find efficiencies per free-fall time ~5 to 10 times higher than those found by Utomo et al. (2018) for disc galaxies between 60 to 120 pc. To effect a change in the rate at which molecular gas is converted to stars, there is likely a change in the structure and dynamics of the molecular gas from which the stars form. In this work, we concentrate on the starburst regime for studying these questions.

Many U/LIRGs are gas-rich major mergers where the structure of the ISM is strongly influenced by galaxy-scale dynamics (Sanders & Mirabel 1996; Farrah et al. 2001; Veilleux et al. 2002). Tidal torques on the gas lead to bulk gas inflow towards the centres of mergers (e.g. Noguchi 1988; Mihos & Hernquist 1996; Iono et al. 2004). These gas motions can enhance star formation by adding additional external pressure on to GMCs, or they could suppress star formation through the release of gravitational potential energy injecting turbulent energy into the molecular gas (Krumholz et al. 2018). Enhanced star formation is observed in merger systems which means that the ISM is also subjected to large amounts of clustered stellar, supernova, and cosmic-ray-heating feedback which can dramatically shape the ISM and subsequent star formation (Dale & Bonnell 2008; Klassen et al. 2012; Howard et al. 2017; Keller et al. 2020; Booth et al. 2013; Girichidis et al. 2016). The stellar activity can also pump turbulent energy into the molecular gas. The exact balance of these competing processes is not well constrained, nor is their coupling to GMC scales in these highly active systems.

Very high angular resolution observations are required to resolve GMC sizes of 50 to 100 pc in these distant systems. As the nearest LIRG, NGC 3256 is a prime target to explore these effects on molecular gas in a merger for comparison with nearby disc galaxies. At a distance of 44 Mpc (CMB-corrected redshift from NED adopting *WMAP*

five-year cosmology of $H_0 = 70.5\,\mathrm{km\,s^{-1}\,Mpc^{-1}}$, $\Omega = 1$, and $\Omega_\mathrm{m} = 0.27$), the Atacama Large Millimeter/Submillimeter Array (ALMA) can readily resolve molecular gas on the scale of GMCs. Its infrared (IR) luminosity is $L_{8-1000\,\mu\mathrm{m}} \sim 4 \times 10^{11}\,\mathrm{L_\odot}$ (Sanders et al. 2003) and total star formation rate is $\sim 50\,\mathrm{M_\odot\,yr^{-1}}$ (Sakamoto et al. 2014). It is a late-stage merger (Stierwalt et al. 2013) with two distinguishable nuclei separated by ~1.1 kpc (Sakamoto et al. 2014; adjusted to our assumed distance of 44 Mpc) that share a common envelope. The relatively face-on northern nucleus is producing a molecular outflow aimed roughly along the line of sight (see diagrams in Sakamoto et al. 2014; Harada et al. 2018), which is powered by the starburst (Sakamoto et al. 2014). The southern nucleus is nearly edge-on with an extremely collimated jet being launched in the north-south direction. Calculations by Sakamoto et al. (2014) found that the energy budget for the southern jet likely has a contribution from a highly obscured active galactic nucleus (AGN). This is consistent with IR and X-ray observations by Ohyama et al. (2015) indicating an AGN in the southern nucleus. Modeling of resolved multi-line and multi-transition molecular observations by Michiyama et al. (2018) also suggest the southern outflow may contain two phases produced by the interaction of the jet with the ISM.

In this paper we present the highest resolution carbon monoxide (CO) observations obtained to date of NGC 3256 and use them to study the detailed properties of the molecular ISM. Section 2.2 summarizes our observations and imaging procedure. Section 2.3 describes the steps used in analysing NGC 3256 to reproduce the methods used by Sun et al. (2018). In Section 2.4, we compare physical quantities such as surface density, velocity dispersion, peak brightness temperature, virial parameter, and turbulent pressure to those from the preliminary PHANGS-ALMA sample reported by Sun et al. (2018). We discuss the implications for the structure of the ISM in NGC 3256 in Section 2.5. Section 2.6 summarizes the conclusions and future work.

2.2 Data

2.2.1 Observations

Spectral line and continuum observations were carried out with the 12 m main array, the 7 m Morita Atacama Compact Array (ACA), and the total power (TP) antennas

recovering all spatial scales down to ~0″.25. Two separate configurations of the 12 m array were used. Table 2.1 briefly summarizes the observations.

The J=2–1 rotational transition of CO and J=5–4 transition of carbon monosulfide (CS) were each targeted with two overlapping spectral windows (SPWs). This was done to ensure the spectral line wings from the nuclear outflow and jet would be captured. Enough line-free channels were available to produce a continuum map as well.

2.2.2 Calibration

Calibration was carried out at the observatory and we produced our own cubes. Common Astronomy Software Applications (CASA) was used for both calibration and imaging (McMullin et al. 2007). Software versions used are summarized in Table 2.1.

We inspected the calibration quality by plotting amplitudes and phases versus frequency, time, and *uv* distance for all calibrator sources. We found that flagging the two antennas with the greatest separations from the array centre improved the synthesized beam pattern and root-mean-square (RMS) noise. Significant continuum emission is detected in all interferometric SPWs at the positions of the two nuclei so we performed continuum subtraction, fitting with a zeroth-order polynomial in the frequency ranges 226.599 to 227.427 GHz, 229.134 to 229.497 GHz, and 229.759 to 230.208 GHz.

Due to the complexity of combining observations from so many different dates, configurations, and arrays we found that performing all gridding and SPW combination with the *mstransform* task, before producing cubes, gave the best results. Our criteria for quality in this step were small RMS noise variations from channel to channel and minimal discontinuities in the resultant spectra when transitioning from one SPW to the other.

Dirty CO cubes were produced from the calibrated and continuum-subtracted *uv* data using the *tclean* task in CASA version 5.4.0-68. Channels were gridded to 3.906 MHz width (about 5.131 km s^{-1}), starting at 2004 km s^{-1} and ending at 3599 km s^{-1}.

The TP data were calibrated and imaged with the ALMA single dish pipeline. The baseline subtraction step was modified to handle the fact that the CO line emission extended to one end of each SPW. Despite the modified baseline fitting, there still existed a difference of up to ~9 per cent between the line intensities between the two CO SPWs. We tested the total flux measurement by manually stitching together the two TP SPWs and making an integrated intensity map from this cube. We found at least ~83 per

TABLE 2.1: Summary of observations and calibration methods.

Array	Observation Date	Repeats	Minimum Baseline[a] (m)	Maximum Baseline[a] (m)	Calibration Type	CASA Version
12 m	1 September, 2016	1	12	1713	Pipeline	4.7.0 r38335; PL 38366 Cycle4-R2-B
12 m	7 September, 2016	1	14	2861	Pipeline	4.7.0 r38335; PL 38366 Cycle4-R2-B
12 m	10 March, 2016	1	13	429	Manual	4.6.0 r36590
7 m	2 November, 2015	1	9	44	Manual	4.5.1 r35996
7 m	5 November, 2015	2	8	43	Manual	4.5.1 r35996
7 m	6 November, 2015	2	7	44	Manual	4.5.1 r35996
7 m	7 November, 2015	2	8	43	Manual	4.5.1 r35996
7 m	15 December, 2015	2	7	43	Manual	4.5.1 r35996
TP	5 December, 2015	4	. . .	. . .	Pipeline	4.5.2 r36115; PL 36252 Cycle3-R4-B
TP	6 December, 2015	2	. . .	. . .	Pipeline	4.5.2 r36115; PL 36252 Cycle3-R4-B
TP	15 December, 2015	6	. . .	. . .	Pipeline	4.5.2 r36115; PL 36252 Cycle3-R4-B
TP	5 March, 2016	1	. . .	. . .	Pipeline	4.5.2 r36115; PL 36252 Cycle3-R4-B

Notes. All interferometric observations were multiple-pointing mosaics covering an area with a radius approximately 30″, centred on R.A.: $10^h27^m51^s$ Dec.: −43°54′15″. SPWs were centred at 227.526, 229.284, 241.790, and 243.547 GHz. Each had a bandwidth of 1.875 GHz and native spectral resolution of 1.953 MHz.

[a] Projected for source position on the sky.

cent of the flux was recovered in the interferometric observations using the combined 12 and 7 m data. Given the uncertainties in the baseline subtraction process, we chose not to incorporate the TP observations into imaging the interferometric data to avoid introducing artefacts.

2.2.3 Imaging CO

To help guide the clean algorithm in modeling emission on both scales larger than the synthesized beam and point sources, we ran multi-scale and point-source cleaning in two separate passes. The first pass was a shallow multi-scale clean using very extended hand-drawn clean masks and excluding point-source models. The second pass continued cleaning but this time using only point-source models. New masks were produced in the second pass because only compact emission remained and new masks were made to closely follow those features. Masking was accomplished primarily with the automultithresh algorithm, but we also manually edited the masks at each major cycle.

2.3 Analysis

Following Sun et al. (2018), we convolved the dirty and cleaned CO cubes to have circular synthesized beams with full widths at half maximum (FWHMs) of 55 pc, 80 pc, and 120 pc. Pixels in the convolved cubes were resampled to a coarser grid of square pixels that were FWHM/2 on a side, thus Nyquist sampling the beams.

To derive physical properties of the molecular gas traced by the CO observations we calculated moment 0 (integrated intensity) and 2 (intensity-weighted velocity dispersion) maps. Signal masks for moment map calculations were produced following the procedure[1] used by Sun et al. (2018) (hereafter referred to as the Sun thresholding), and we refer the reader to their description of the algorithm outlined in their Section 3.2. These signal masks were then used in producing moment maps with the standard functions in the spectral-cube library (Ginsburg et al. 2019). The Sun thresholding appeared superior to standard n-σ thresholding due to its conservative treatment of the outer regions of our

---

[1]The PYTHON script for producing the signal masks were obtained from https://github.com/astrojysun/Sun_Astro_Tools/blob/master/sun_astro_tools/spectralcube.py.

field of view, its ability to extract low signal-to-noise (S/N) emission without introducing significant numbers of noisy pixels, and being the only method that made the northern outflow clearly visible in the moment 2 map.

To convert the integrated intensity maps to mass surface density units we adopt the U/LIRG CO-to-H_2 conversion factor (Downes & Solomon 1998), including a factor of 1.36 to account for helium. Following the procedure of He et al. (2020) to determine the appropriate conversion factor we use the stellar mass of NGC 3256 from Howell et al. (2010) of $1.14 \times 10^{11}\,M_\odot$ and estimate the expected specific star-formation rate (sSFR) using the xGASS star-forming main sequence fit $\log \mathrm{sSFR_{MS}} = -0.344(\log M_\star - 9) - 9.822$ from Catinella et al. (2018). Using the $M_\star$ and star formation rate we calculate the ratio of the actual sSFR to the main sequence expected sSFR to be 15. This ratio puts NGC 3256 well away from the star-forming main sequence locus indicating a probability near 100 per cent of NGC 3256 being in a starburst phase (Sargent et al. 2014). The conversion factor recipe from Violino et al. (2018) is $\alpha_{CO} = (1 - f_{SB}) \times \alpha_{CO,MS} + f_{SB} \times \alpha_{CO,SB}$, where f_{SB} is the probability of a galaxy being in a starburst phase. $\alpha_{CO,MS}$ and $\alpha_{CO,SB}$ are the main sequence and starburst conversion factors expected in the 2-Star Formation Mode framework of Sargent et al. (2014). Using this recipe we estimate that the conversion factor would be dominated by the starburst value so we adopt it for simplicity.

We adopt the mean ratio CO J=2–1 / 1–0 = 0.79 from the xCOLD GASS sample (Saintonge et al. 2017) which is consistent with the ratio of 0.80 ± 0.22 measured in NGC 3256 by Aalto et al. (1995) in a single-dish beam roughly the size of our field of view (FoV). This ratio results in a conversion factor from the integrated 2–1 line to molecular gas mass of $\alpha_{CO} = 1.38\,M_\odot\,\mathrm{pc}^{-2}(\mathrm{K\,km\,s^{-1}})^{-1}$. The 2–1 / 1–0 ratio may be larger in U/LIRGs (Papadopoulos et al. 2012; Saito et al. 2017; He et al. 2020) than the normal spirals studied by xCOLD GASS, which would result in the surface densities presented here overestimating the true surface densities. It is also likely there is considerable variation in the line ratio within NGC 3256 (Harada et al. in preparation).

As in Sun et al. (2018), we corrected the velocity dispersion estimates measured in the moment 2 maps for the finite channel widths using Equations 15 to 17 from Leroy et al. (2016). To measure the correlation between channels we calculated the Pearson correlation coefficient between each channel ("x-value") and the next channel ("y-value"). The correction is always less than $1\,\mathrm{km\,s^{-1}}$ but we chose to apply it to all of

our measured velocity dispersions to replicate the procedure of Sun et al. (2018).

Figure 2.1 shows mass surface density and velocity dispersion maps of NGC 3256, convolved to synthesisized beam sizes of 55 and 120 pc. Gray contours at $10^3\,\mathrm{M_\odot\,pc^{-2}}$ are shown in the top row. The bottom row includes gray ellipses marking the inclination-projected central 1 kpc radii, centred on the positions of the nuclei, and gray polygons marking pixels heavily contaminated by the southern jet, identified in the velocity dispersion maps.

The FoV shown is centred at R.A. $10^\mathrm{h}27^\mathrm{m}51^\mathrm{s}$ declination (Dec.) $-43°54'16''$, and it covers 0.73 arcmin in R.A. and 0.54 arcmin in Dec.. Pixels west of an R.A. of approximately $10^\mathrm{h}27^\mathrm{m}50.3^\mathrm{s}$ are excluded from our analysis. In this region there are elevated velocity dispersions measured coming from two-component spectral profiles. While multicomponent lines near the centre of the system appear to be produced by multiple gas components along the line of sight, we believe some of the two-component profiles in the west are the result of imperfectly cleaned sidelobes of the interferometric synthetic beam. It also appears material from the outskirts of the progenitors are overlapping along the line of sight (Sakamoto et al. 2014), producing spectral profiles that are too complex for the moment-based analysis here. For this reason, we exclude pixels from that part of the maps from the measurements we present.

2.4 Results

In this section, we present mass-weighted Gaussian kernel density estimator (KDE) distributions of the mass surface densities, velocity dispersions, peak brightness temperatures, virial parameters, and internal turbulent pressures in NGC 3256. The distributions measured in the PHANGS-ALMA early sample from Sun et al. (2018) are also shown for comparison. Virial parameters and turbulent pressures are calculated in the same way as by Sun et al. (2018) and assuming the diameter of the cloud is equal to the beam FWHM.

Distributions include measurements from all pixels containing significant emission and smoothed to 55 and 120 pc. We also calculated distributions for 80 pc but do not show them because they always land midway between the distributions from 55 and 120 pc. A bandwidth of 0.1 dex was used for all distributions except the internal turbulent pressure where a bandwidth of 0.2 dex was used instead. This matches the KDE calculations of
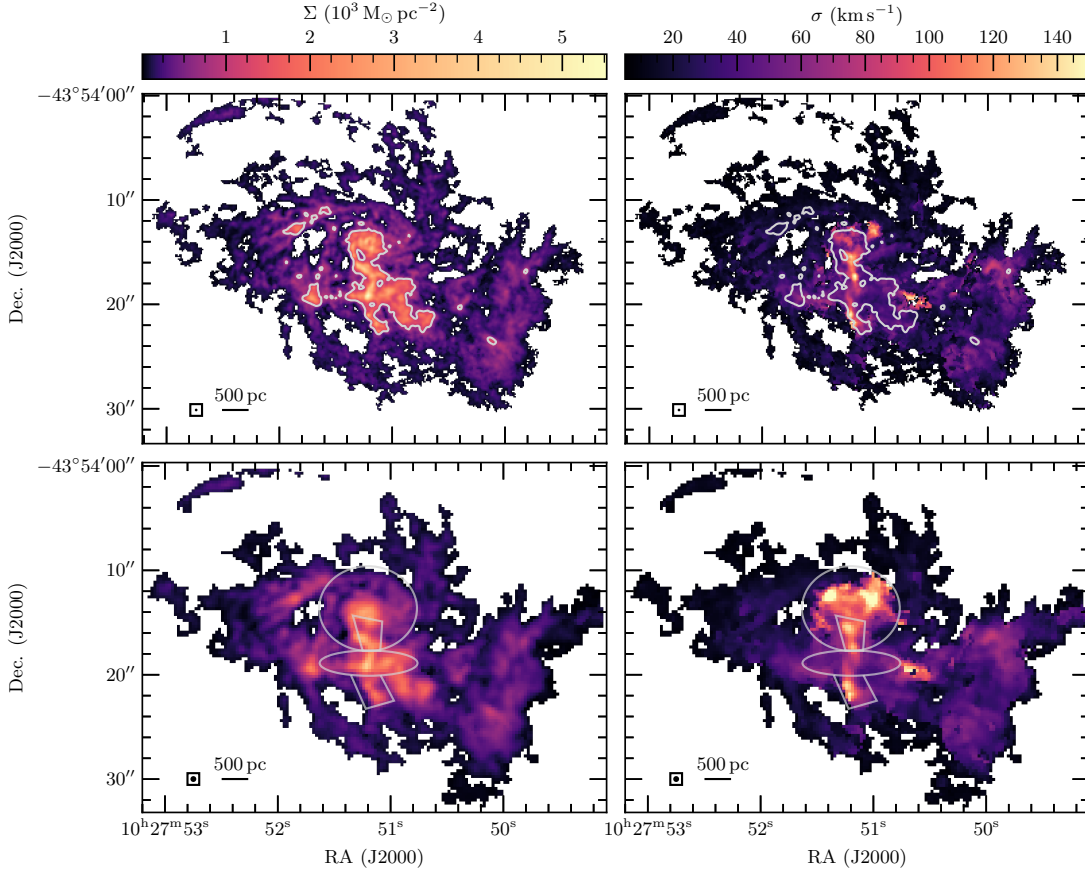
FIGURE 2.1: Maps of molecular gas mass surface density (left) and velocity dispersion (right), with a synthesized beam FWHM of 55 pc (top) and 120 pc (bottom). Contours in the top row are at a surface density of 1000 $M_\odot$ pc^{-2}. The same contours are in the left and right frames. Gray ellipses in the bottom row mark the central 1 kpc, projected to account for the inclination angles of the nuclei. Gray polygons indicate pixels affected by the southern jet, identified in the dispersion maps, that are not included in the distributions of measured quantities shown in subsequent figures. Pixels west of an right ascension (R.A.) of approximately $10^h27^m50.3^s$ are also excluded from our distribution analyses due to complex spectral features and potential interferometric-sidelobe contamination. The beam sizes are represented by the black circles in the bottom-left corners of each frame. The U/LIRG conversion factor of 1.38 $M_\odot$ pc^{-2}(K km s^{-1})$^{-1}$ was used to convert the integrated intensity maps from K km s^{-1} to $M_\odot$ pc^{-2}. Multiplying the surface densities by ~4.5 would convert to the Galactic conversion factor of 6.25 $M_\odot$ pc^{-2}(K km s^{-1})$^{-1}$. Both of these conversion factors include a factor of 1.36 to account for helium.

Sun et al. (2018) where the bandwidth for their pressures was misreported as 0.1 dex (J. Sun, private communication).

In the following plots, distributions of pixels from the entire mapped FoV are shown as solid lines, pixels within a radius of 1 kpc from the nuclei as dotted lines, and pixels outside the central 1 kpc radius as dashed lines (referred to here as the non-nuclear pixels and equivalent to the disc pixels in Sun et al. 2018). The nuclear peaks in our continuum map were used as the positions of the nuclei.

We then projected the boundaries of the central kiloparsec circles to account for the inclination angles of 30° for the northern nucleus (Sakamoto et al. 2014) and 75° for the southern nucleus. Although Sakamoto et al. (2014) estimate an inclination angle of 80° for the southern nucleus, we adopt 75° because it better captures the apparent thickness of the southern disc in these data. However, the difference is small as an inclination of 75° results in about 8 pixels across the minor axis in the 120 pc maps while 80° would result in 5 pixels. The gray ellipses in the bottom row of Figure 2.1 show these central region boundaries. We do not correct the measurements for these inclinations because the disturbed morphology makes it unclear where the boundaries of the inclination regions should be or how to transition between them. There is also the complication of how to deal with overlapping material from the two nuclei. Not including inclination corrections will cause our surface density measurements to overestimate the true values perpendicular to any discs present.

Gray polygons indicate pixels associated with the southern jet and those pixels are excluded from all distributions and total masses used to normalize the KDEs. Table 2.2 presents the 16th, 50th, and 84th percentiles for the different regions of NGC 3256, at each resolution. Comparisons of these percentiles for NGC 3256 and the PHANGS-ALMA sample at 120 pc resolution are presented in Figures 2.2 to 2.6.

2.4.1 Mass surface density

At all resolutions, NGC 3256 exhibits surface density distributions with a maximum centred near 2000 $M_\odot$ pc^{-2} and a shoulder centred near 600 $M_\odot$ pc^{-2} (see Figure 2.2). We measure that at least 85 per cent of the area out to 2 kpc from the midpoint between the two nuclei has $\Sigma \gtrsim 100\,M_\odot$ pc^{-2}, independent of resolution.

The mass in the higher surface density peak of the distribution is dominated by pixels in the nuclear regions, but there is a significant contribution from pixels outside

TABLE 2.2: Mass-weighted percentiles of all measured and derived quantities from NGC 3256, by region and resolution.

Region	Beam Size (pc)	Σ $(M_\odot\,pc^{-2})$			σ $(km\,s^{-1})$			T_{peak} (K)			α_{vir}			P_{turb} $(10^6\,K\,cm^{-3})$		
		16	50	84	16	50	84	16	50	84	16	50	84	16	50	84
Non-nuclear	55	150	390	1300	12	25	43	2.7	5.1	11	5.5	11	26	2.3	26	170
	80	150	380	1200	13	27	45	2.4	4.6	10	4.3	8.8	20	1.8	20	120
	120	140	370	1200	14	28	47	2.2	4.2	9.5	3.4	6.8	15	1.3	15	92
Nuclei Combined	55	520	1400	2500	27	46	71	5.8	12	19	6.1	13	28	36	270	930
	80	520	1400	2500	34	55	89	5.4	11	17	5.6	13	29	48	250	970
	120	500	1500	2400	45	66	100	5.1	9.9	16	5.2	12	34	75	210	720
Northern Nucleus	55	410	870	2400	20	42	72	5.1	11	20	6.2	13	29	18	160	820
	80	410	870	2300	25	62	95	4.8	9.7	19	6.7	18	40	18	280	1000
	120	390	850	2200	44	85	110	4.4	8.6	15	7.4	19	63	30	260	800
Southern Nucleus	55	970	1700	2800	36	49	70	6.5	13	18	5.9	12	24	160	330	1200
	80	980	1700	2600	39	51	73	6.3	12	17	4.7	9.7	19	130	250	940
	120	1100	1700	2500	45	54	76	6.4	12	16	4.1	7.6	13	98	190	620

the central kiloparsec as well. Contours in the top row of Figure 2.1 show the pixels with $\Sigma > 1000\,M_\odot\,pc^{-2}$. The majority of these pixels lie in the nuclear and southern jet regions, though not all nuclear pixels are at these high surface densities.

The lower surface density shoulder of the pixel distribution is a roughly equal mix of nuclear and non-nuclear pixels, but switches to being dominated by the non-nuclear pixels around $600\,M_\odot\,pc^{-2}$. The central high density region is better described in the northern nucleus of NGC 3256 by a radius of 250 pc than the 1 kpc used for the PHANGS-ALMA galaxies. Considering the extra-nuclear high surface density lines of sight and low surface density pixels within the central kiloparsec, a careful decomposition of the gas emission using spatial and spectral dimensions will be crucial to fully understand the complex morphology of this merger. The pixel distributions throughout this section provide bulk measurements of the gas properties, but evaluation of those properties ultimately needs to be done on a sightline-by-sightline basis.

Comparing the mass surface densities measured in NGC 3256 to PHANGS-ALMA in the bottom row of Figure 2.2, NGC 3256 occupies the high end of the distributions observed in the PHANGS-ALMA sample. The nuclei of most PHANGS-ALMA galaxies are consistent with the nuclei and upper range of the non-nuclear distribution in NGC 3256. Most disc distributions from PHANGS-ALMA overlap with the lower half of the non-nuclear distribution in NGC 3256.

2.4.2 Velocity dispersion

Velocity dispersions in NGC 3256 from all pixels and resolutions show a broad distribution in Figure 2.3, ranging from 10 to $200\,km\,s^{-1}$ and with a single peak near $50\,km\,s^{-1}$. The distribution does broaden towards higher dispersions going from 55 to 120 pc resolution. The non-nuclear distribution peaks near $30\,km\,s^{-1}$ (independent of resolution), and the nuclear distribution peak increases from near $50\,km\,s^{-1}$ at 55 pc to $70\,km\,s^{-1}$ at 120 pc. Separating the nuclei in Table 2.2 shows that while both nuclei shift to higher dispersions at lower resolution, the northern nucleus has a much stronger trend with resolution. The trend in the northern nucleus contains significant contamination from the outflow, driven by the northern nucleus, that becomes worse as the resolution is made coarser. This is due to improved surface brightness sensitivity at lower resolution
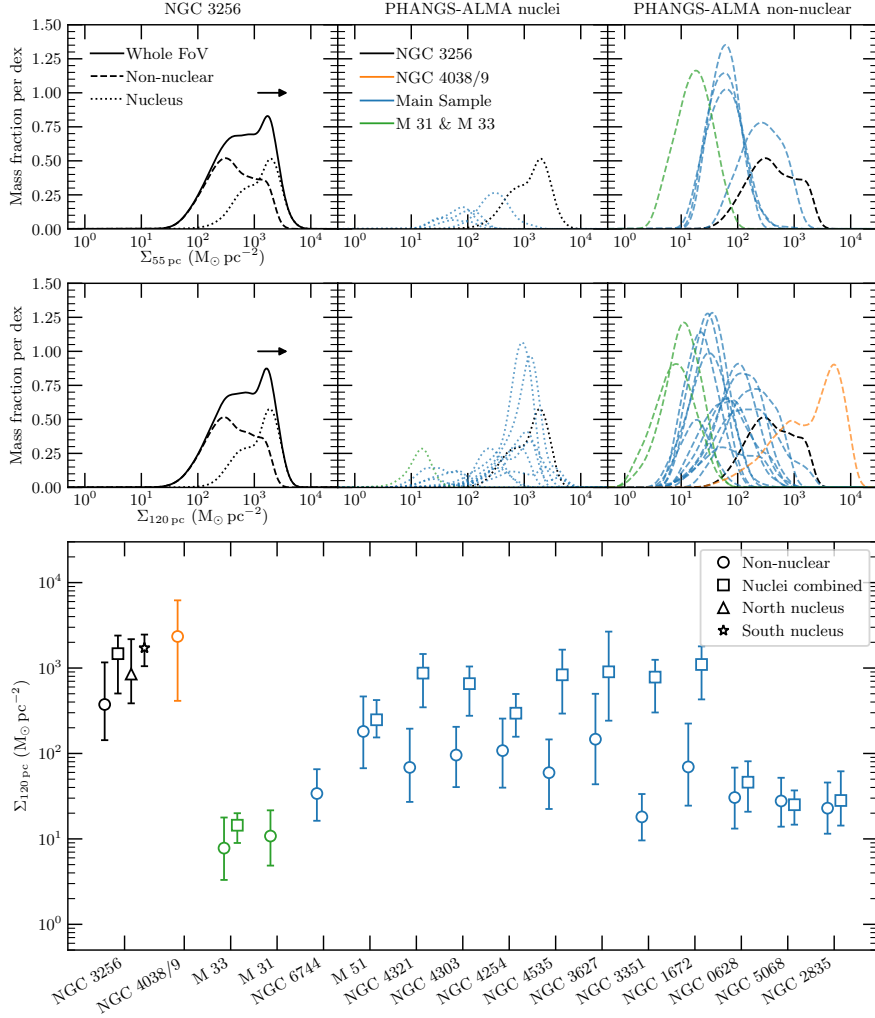
FIGURE 2.2: Molecular gas mass surface densities measured in NGC 3256 and the Sun et al. (2018) PHANGS-ALMA sample. Measurements for NGC 3256 are made in maps with beam FWHM of 55 and 120 pc and pixels half those lengths on a side. PHANGS-ALMA distributions come from maps with beam FWHM of 45 and 120 pc and pixels half those lengths on a side. ***Top and middle rows:*** Solid lines are pixel distributions from the entire FoV, dashed lines are non-nuclear region pixels, and dotted lines are nuclear region pixels. Arrows show how values would shift if we adopt the Milky Way CO conversion factor of $6.25 \, M_\odot \, pc^{-2} (K \, km \, s^{-1})^{-1}$ (used for all PHANGS-ALMA galaxies) instead of the LIRG conversion factor of $1.38 \, M_\odot \, pc^{-2} (K \, km \, s^{-1})^{-1}$. PHANGS-ALMA galaxies are separated into nuclear and disc regions in the centre and right panels, respectively, with the corresponding curves from NGC 3256 reproduced from the left panels. ***Bottom row:*** Mass-weighted medians shown as symbols and ranges encompassing the inner 68 per cent of the distributions shown as error bars for NGC 3256 and the Sun et al. (2018) sample. All percentiles are calculated from the 120 pc maps.

increasing the detection of very wide spectral wings from the outflow. The high dispersion blobs in the 120 pc resolution map that are mostly absent in the 55 pc map are sightlines that are most affected by the outflow contribution.

Figure 2.3 shows that the velocity dispersions for NGC 3256 are significantly higher than most of the PHANGS-ALMA sample. Almost no dispersions in the PHANGS-ALMA sample are as high as in the nuclei of NGC 3256, except for NGC 3627 discussed in Section 2.4.7. The nuclei of some PHANGS-ALMA galaxies overlap with the lower half of the NGC 3256 non-nuclear distribution.

2.4.3 Peak brightness temperature

The peak brightness temperature distributions from all pixels in NGC 3256 are centred near 7 K, range from 1 to 40 K, are slightly skewed to higher temperatures, and do not change significantly with resolution (see Figure 2.4). The non-nuclear distribution peaks at ~3 K and the combined nuclei distribution peaks at ~15 K, but the inner 68 per cent of both distributions overlap significantly (3 to 11 K for the non-nuclear and 6 to 19 K for the nuclei).

While the nuclear and non-nuclear distributions in NGC 3256 overlap considerably, there is still a difference of about two in the median brightness temperatures between them. Assuming the sizes of molecular structures are not significantly different between those regions, this difference would indicate gas kinetic temperatures that are at most two times higher in the nuclei.

Similar to the velocity dispersions, the brightness temperatures in NGC 3256 reach higher values than all of the galaxies in the PHANGS-ALMA sample. Figure 2.4 shows that most of the PHANGS-ALMA centres and the disc of M51 are consistent with only the non-nuclear distribution from NGC 3256.

2.4.4 Virial parameter

Figure 2.5 shows the virial parameter distributions for all pixels in NGC 3256 peak around 10 but with long tails to near 1 and above 100. Changing the resolution slightly broadens the distributions when going from 55 to 120 pc. This occurs because at 55 pc the nuclear and non-nuclear distributions are very similar (except for more mass present in the non-nuclear pixels). At lower resolution, the non-nuclear pixels shift towards
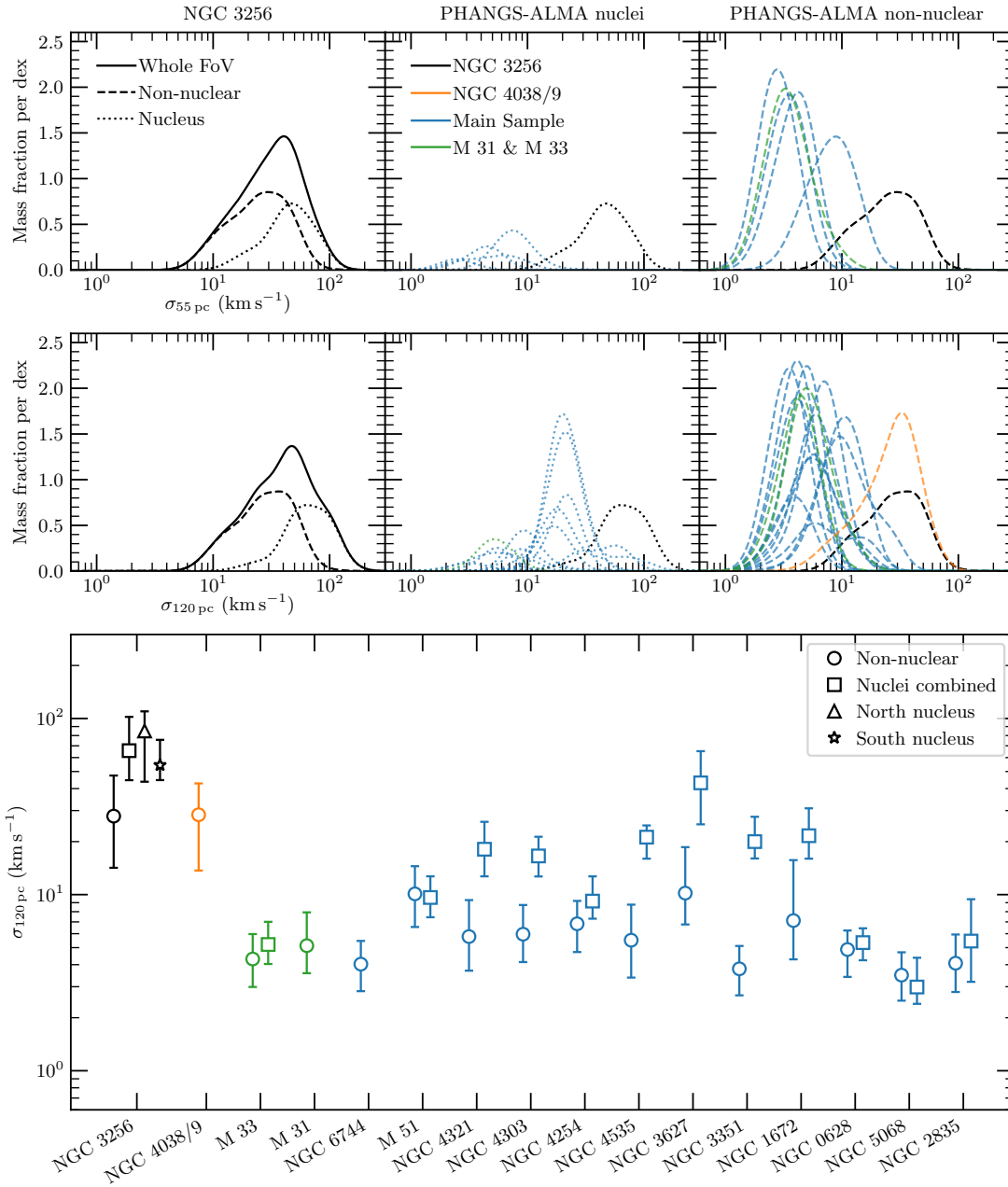
FIGURE 2.3: Same as Figure 2.2 except for distributions of velocity dispersion measurements.
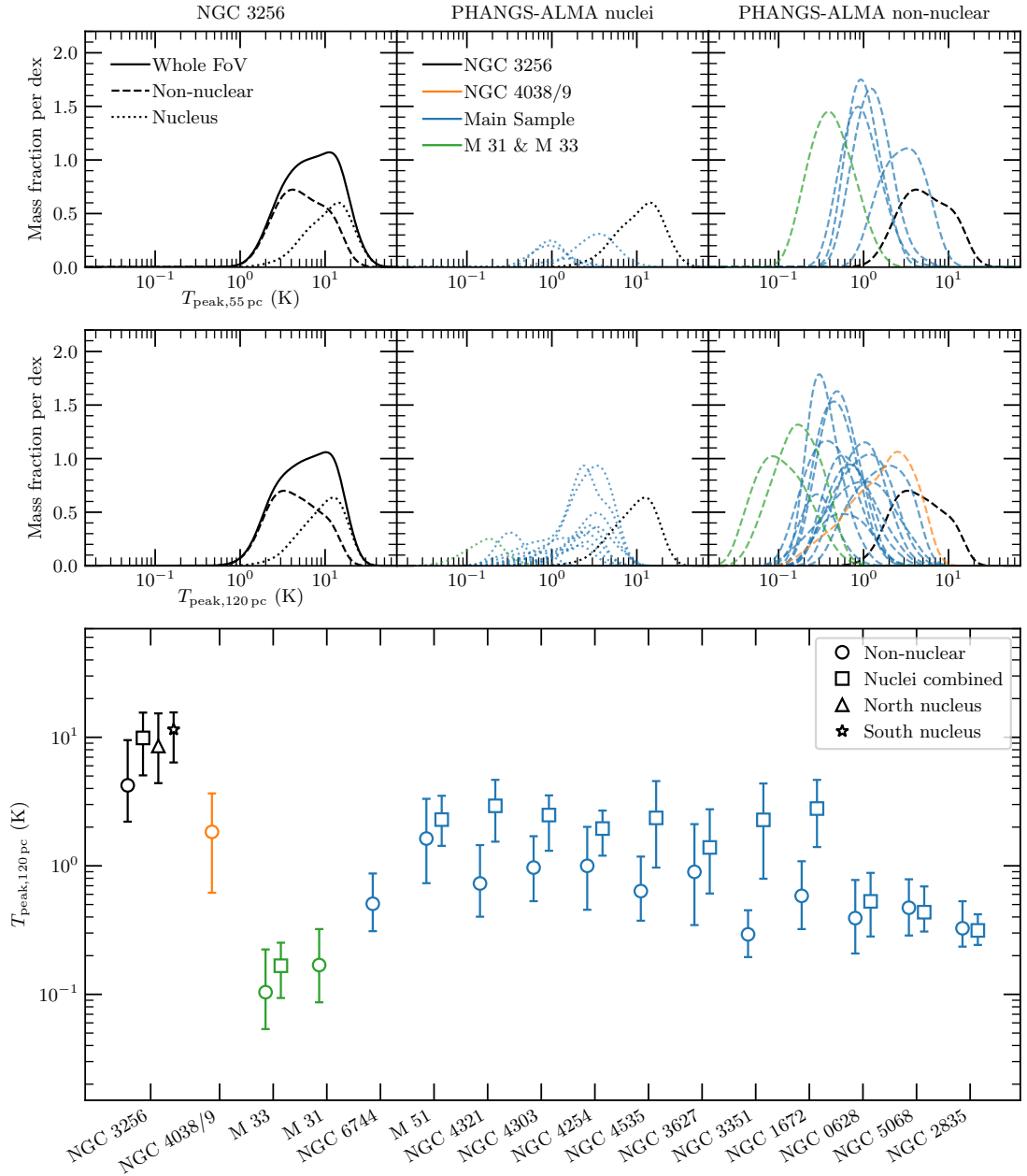
FIGURE 2.4: Same as Figure 2.2 except for distributions of peak brightness temperature measurements.

lower virial parameters, peaking around 6 at 120 pc, while the peak of the nuclear pixel distribution does not move. Table 2.2 shows these changes are even more complex since the northern nucleus exhibits higher virial parameters at lower resolution but the southern nucleus shows the opposite trend. Non-nuclear virial parameters become slightly lower at lower resolution, but most of the mass has overlapping distributions between resolutions. In the simple framework of balancing internal kinetic energy with self-gravity, the gas at these scales is not bound by gravity alone. It is worth highlighting here that changing from the U/LIRG to the Galactic conversion factor would result in the distributions being centred around two and would change the gas from being clearly unbound to marginally bound. Further analysis will have to wait for a better constrained CO conversion factor, possibly through a cloud decomposition of these data.

NGC 3256 appears quite different from most of the PHANGS-ALMA sample in virial parameter, as shown in Figure 2.5. Most of the PHANGS-ALMA distributions hover around α_{vir} of about one or two. Roughly half of the galaxies in the PHANGS-ALMA sample sit well below the distributions measured in NGC 3256. Interestingly, M31 and M33 are the most consistent with the distributions from NGC 3256 which may be due to properties unique to the ISM regime in those galaxies as well as observational effects (see Sections 5.2.4 and 5.2.5 from Sun et al. 2018). A combination of reduced beam-filling factors at low surface densities, missing self-gravity from an underestimated CO conversion factor (also at low surface densities), and more dominant external pressures from larger fractions of atomic gas may be driving the higher virial parameters seen in M31 and M33.

2.4.5 Internal turbulent pressure

Internal turbulent pressure measured in all pixels exhibits the most complex distribution, with up to four peaks spanning a range from 10^5 to 10^{10} K cm^{-3} (see Figure 2.6). It appears most of the mass at the highest pressures originates from the nuclear regions, and that the nuclear regions have almost a single narrowly peaked distribution around 5×10^8 K cm^{-3}. The additional nuclear component near 10^7 K cm^{-3} comes from pixels with surface densities below $1000\,\mathrm{M_\odot\,pc^{-2}}$ (i.e. pixels not within the contours in Figure 2.1) but that still lie within 1 kpc of the centre of the northern nucleus. While close to the northern nucleus in projection, these pixels have pressures consistent with the distribution from the non-nuclear pixels, indicating the gas properties are only at
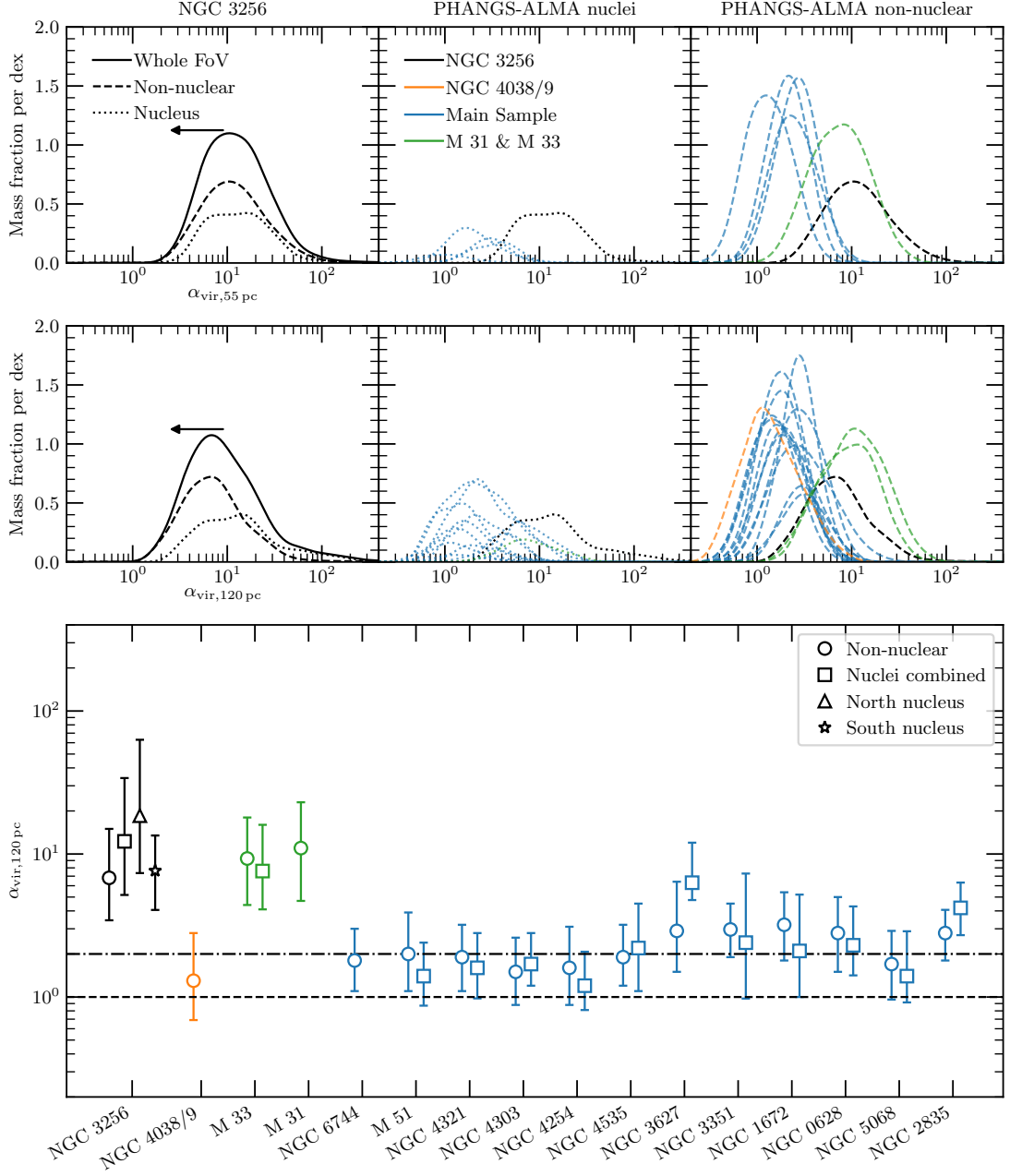
FIGURE 2.5: Same as Figure 2.2 except for distributions of virial parameter measurements. The horizontal dashed line shows $\alpha_{\mathrm{vir}} = 1$ (virial equilibrium) and the dash-dotted line shows $\alpha_{\mathrm{vir}} = 2$ (approximately bound or collapsing). The U/LIRG conversion factor of $1.38\,M_{\odot}\,\mathrm{pc}^{-2}(\mathrm{K\,km\,s}^{-1})^{-1}$ was used to calculate the surface densities for NGC 3256. Dividing the virial parameters of NGC 3256 by ~4.5 would convert to the Galactic conversion factor of $6.25\,M_{\odot}\,\mathrm{pc}^{-2}(\mathrm{K\,km\,s}^{-1})^{-1}$ (used for all PHANGS-ALMA galaxies).

their most extreme very close to the centres of the nuclei. The southern nuclear region does not include such low pressures.

The comparison to the PHANGS-ALMA sample in Figure 2.6 is quite similar to that for the velocity dispersion. The main difference is that the nuclear pressure distributions from NGC 3256 are not as extreme as the dispersions. This results in some of the PHANGS-ALMA main sample nuclei being consistent with the nuclei of NGC 3256. There is still a large fraction of discs and even whole galaxies from PHANGS-ALMA that have pressures two to three orders of magnitude lower than NGC 3256. The effect of the conversion factor choice is relatively small for the measured pressures given the width of the distributions. If the assumptions used to derive the turbulent pressure hold in NGC 3256 it contains some of the highest pressures in this sample of galaxies.

2.4.6   Two-dimensional view

Two-dimensional Gaussian KDEs of non-nuclear velocity dispersion versus surface density are shown in the top panel of Figure 2.7. A bandwidth of 0.1 dex was used, and contours enclose 20, 50, and 80 per cent of the mass.

NGC 3256 is offset from the trend in the PHANGS-ALMA main sample and overlap region of NGC 4038/9. Most of this offset would be removed by switching NGC 3256 to the Galactic CO conversion factor. Figure 2.7 makes it obvious that when using the U/LIRG conversion factor there is significant overlap in non-nuclear surface densities in NGC 3256 and the PHANGS-ALMA main sample. If the surface densities for NGC 3256 are correct then the main driver pushing it off the PHANGS-ALMA trend is its high velocity dispersions.

The bottom panel of Figure 2.7 shows the same two-dimensional KDE but for NGC 3256 alone, at 55 pc resolution. Separate distributions for the non-nuclear, northern, and southern nucleus pixels are shown. The gap between peaks in the non-nuclear distribution is wider at higher resolution, driven mainly by a change in the surface densities. A similar bimodality is present in the northern nucleus, but the peaks are slightly shifted to higher surface densities than the non-nuclear peaks. The southern nucleus exhibits a unimodal distribution with its peak quite similar to the higher non-nuclear peak.

The bimodal distribution in the non-nuclear pixels appears to originate from measurements of truly non-nuclear pixels and some pixels that contain a contribution from
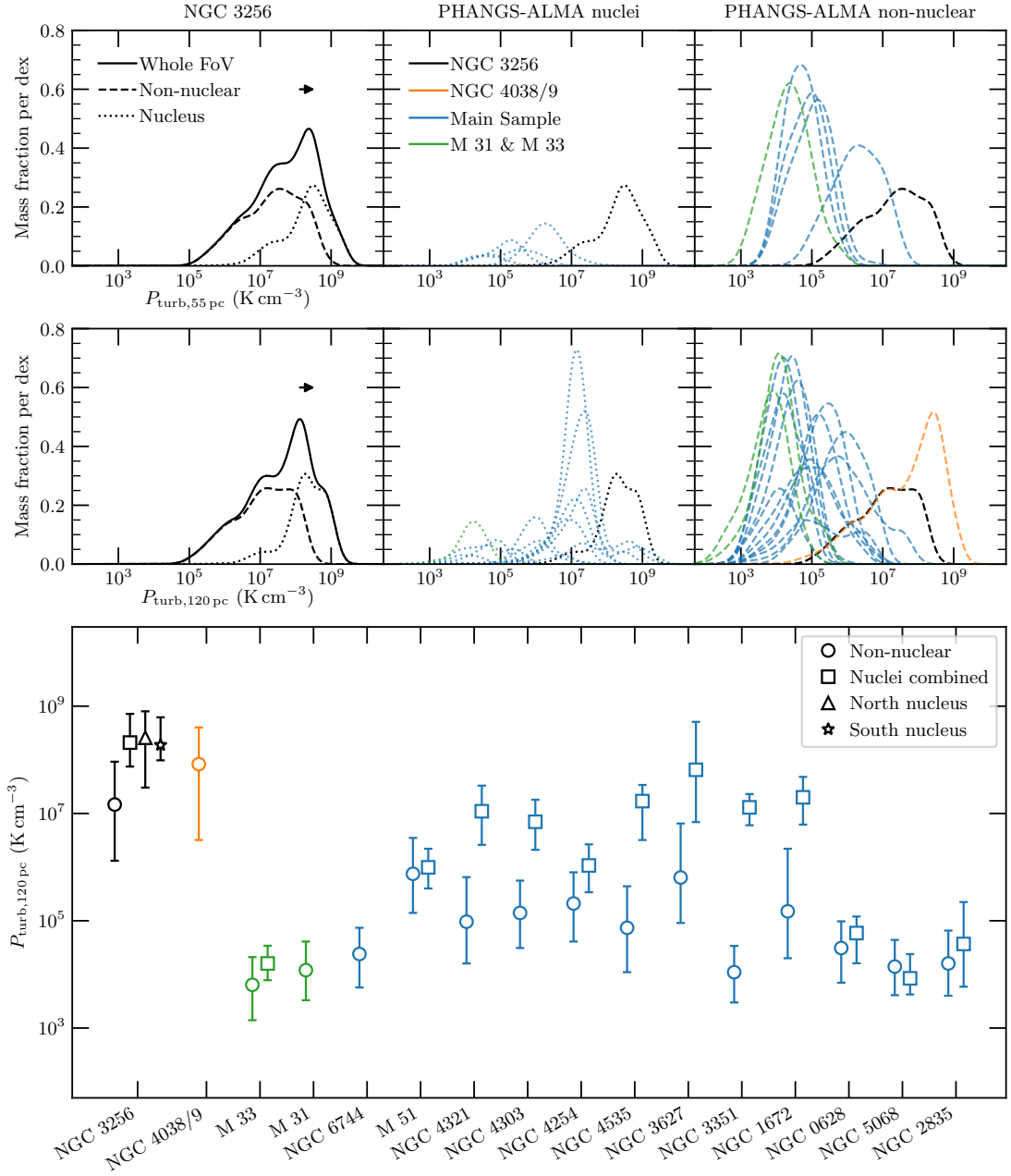
FIGURE 2.6: Same as Figure 2.2 except for distributions of internal turbulent pressure measurements. The U/LIRG conversion factor of $1.38 \, M_\odot \, pc^{-2} (K \, km \, s^{-1})^{-1}$ was used to calculate the surface densities used here for NGC 3256. Multiplying the pressures by ~4.5 would convert to the Galactic conversion factor of $6.25 \, M_\odot \, pc^{-2} (K \, km \, s^{-1})^{-1}$ (used for all PHANGS-ALMA galaxies).
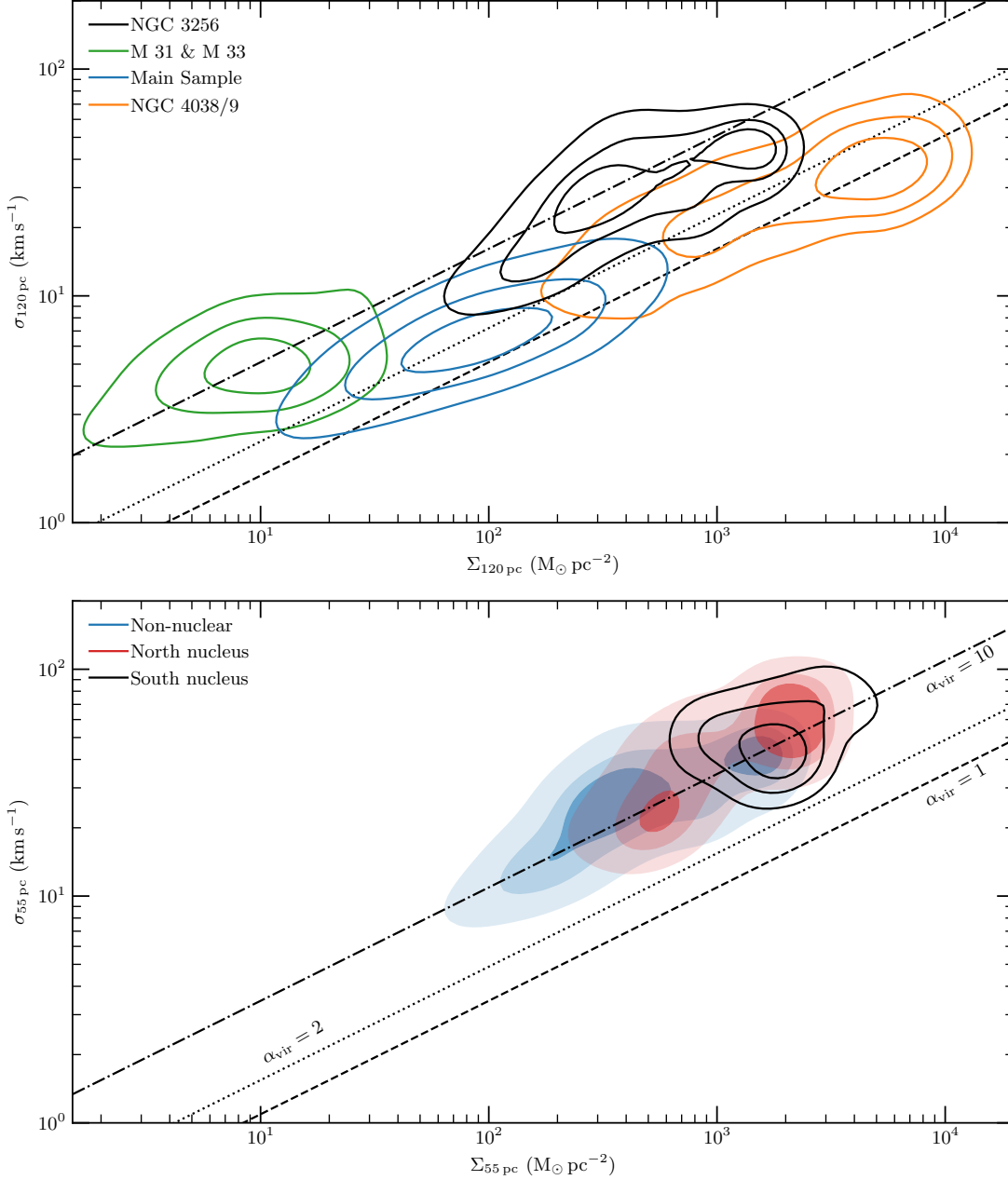
FIGURE 2.7: Velocity dispersion vs. mass surface density with contours enclosing 20, 50, and 80 per cent of the total mass. Lines of constant virial parameter are shown to emphasize the difference in dynamical state between the PHANGS-ALMA main sample and NGC 3256. All PHANGS-ALMA galaxies use the Galactic CO conversion factor of $6.25\,M_\odot\,pc^{-2}(K\,km\,s^{-1})^{-1}$ while NGC 3256 uses the U/LIRG of $1.38\,M_\odot\,pc^{-2}(K\,km\,s^{-1})^{-1}$. ***Top:*** Distributions from non-nuclear regions only, measured in 120 pc resolution maps. ***Bottom:*** All regions observed in NGC 3256 at 55 pc resolution.

the nuclear jet and/or outflow activity. Since the higher peak in the non-nuclear distribution is slightly closer to the peak in the southern nucleus distribution, it may be that the southern nucleus is the main contaminant to the non-nuclear pixels. This is reasonable since the jet from the southern nucleus may not be perfectly excluded from the non-nuclear pixels. It is also more likely the central 1 kpc boundary is not as accurate as for the northern nucleus due to the nearly edge-on orientation of the southern nucleus.

Bimodality in the northern nucleus distribution again points to the central gas structure being made up of a central region of high surface density with radius ~250 pc surrounded by more non-nuclear-like gas from 250 pc outward.

2.4.7 Two detailed comparison studies

Here we provide a more detailed comparison of two galaxies with NGC 3256, as they each present interesting cases. NGC 4038/9 is an important system for comparison because it is the only other merger analysed at the same resolution and in the same manner. It is the nearest merger at 22 Mpc (Schweizer et al. 2008) and contains $\sim 2 \times 10^{10}\,M_\odot$ in molecular gas (Gao et al. 2001). Star formation rates vary throughout the system, with the overlap region analysed by Sun et al. (2018) (data originally presented by Whitmore et al. 2014) undergoing vigorous star formation ($>4\,M_\odot\,\mathrm{yr}^{-1}$, Brandl et al. 2009; Klaas et al. 2010; Bemis & Wilson 2019). Simulations place it at an intermediate merger stage, ~40 Myr after its second pass (Karl et al. 2010). There does not appear to be any conclusive evidence of currently active nuclear outflows in the system.

We also examine NGC 3627 because it has extreme properties similar to NGC 3256 that often set it apart from the rest of the main PHANGS-ALMA sample. It is also a useful galaxy for comparison because it appears to follow the trends of extreme surface densities and dispersions relative to unbarred spiral galaxies shown by Sun et al. (2020b) in the full PHANGS-ALMA of 70 galaxies. It is at a distance of ~11 Mpc (Lee & Jang 2013), is part of the Leo Triplet, shows evidence for LINER/Seyfert 2 nuclear activity (Peng et al. 1998), has a stellar mass of $\sim 10^{11}\,M_\odot$ (Karachentsev & Kudrya 2014), and molecular gas mass of $\sim 10^{10}\,M_\odot$ (Law et al. 2018). Optical images show a bar and two asymmetric spiral arms (Ptak et al. 2006) likely originating from interactions with NGC 3628 (Rots 1978; Soida et al. 2001). These morphological features also stand out in CO observations (Law et al. 2018; Sun et al. 2018). There is no evidence for currently active nuclear outflows in this system either.

NGC 4038/9

The surface density distribution of NGC 4038/9 is the only one to significantly exceed all measurements of surface densities from NGC 3256, as shown in Figure 2.2. About 50 per cent of the gas mass in the overlap region lies at surface densities above NGC 3256. Both the non-nuclear pixels and the nuclei of NGC 3256 are consistent with the lower half of the distribution from NGC 4038/9. About half the mass in the non-nuclear pixels of NGC 3256 lies at surface densities below the NGC 4038/9 distribution. It is important to note that the Galactic conversion factor was used to calculate the mass surface densities for NGC 4038/9, as was done by Sun et al. (2018). In Section 2.5.5, we discuss the applicability of the Galactic conversion factor to the overlap region of NGC 4038/9, and how the comparison to NGC 3256 changes if the U/LIRG conversion factor was used instead.

Figure 2.3 shows that medians and widths of the velocity dispersion distributions in NGC 4038/9 and the non-nuclear pixels of NGC 3256 are very similar. The distributions also show similar shapes, with a sharper drop at high dispersions and a longer tail at low dispersions. However, the majority of mass in the nuclear pixels of NGC 3256 has velocity dispersions higher than the NGC 4038/9 distribution.

For peak brightness temperatures in Figure 2.4, most of the gas measured in NGC 3256 is at higher values than NGC 4038/9. The lower half of the non-nuclear distribution in NGC 3256 overlaps with the upper half of the NGC 4038/9 distribution. Almost all of the mass in the nuclei of NGC 3256 has peak brightness temperatures above NGC 4038/9. This difference could be the result of higher molecular gas kinetic temperatures in NGC 3256 compared to the overlap region. It is reasonable to expect the gas to be warmer in NGC 3256 when its star formation rate surface densities range from 1.3 to 3.5 $M_\odot$ yr^{-1} kpc^{-2} on 512 pc scales in the non-nuclear regions (Wilson et al. 2019) compared to 0.21 to 0.84 $M_\odot$ yr^{-1} kpc^{-2} in the overlap region on kiloparsec scales (Bemis & Wilson 2019). Additionally, a ^{12}CO/^{13}CO J=1–0 ratio towards NGC 3256 of 35 (Aalto et al. 1991a) and of 13 towards the overlap region of NGC 4038/9 (Aalto et al. 1991b) may be indicative of higher gas temperatures in NGC 3256. However, while the difference in this line ratio likely indicates a difference in the gas properties of these two systems, additional transitions must be observed and modelled to determine if differing gas temperatures are truly present. For example, Zhu et al. (2003) included 2–1 and 3–2 ratios for some positions in the overlap region and still arrived at large velocity gradient

solutions with temperatures of ~30 K or 120 K. The ratio can also be complicated by the different merger stages where late-stage mergers likely have more ^{12}CO produced via massive star formation processes (e.g. Sliwa et al. 2017; Brown & Wilson 2019).

The combination of higher surface densities but similar velocity dispersions results in virial parameters in NGC 4038/9 being significantly below all regions in NGC 3256 (see Figure 2.5). NGC 4038/9 shows a very similar distribution to most of the galaxies in the PHANGS-ALMA main sample. This can be seen in Figure 2.7 where NGC 4038/9 extends the trend seen in the discs of the main sample. The internal turbulent pressures calculated for NGC 4038/9 are consistent with all but the lowest portion of the NGC 3256 distributions, as shown in Figure 2.6. Such similar internal pressures between the two mergers may be the result of similar driving mechanisms of turbulence, but their differing virial parameters appear to indicate dynamically important differences in the state of their gas density enhancements. Caveats related to the calculation of virial parameter and turbulent pressure, which also apply to NGC 4038/9, are discussed in Section 2.5.

NGC 3627

Figure 2.2 shows that the disc of NGC 3627 has some of the highest surface densities among the PHANGS-ALMA main sample, only matched by M51 and the centre of NGC 4254. The upper half of the disc distribution overlaps with the non-nuclear and northern nucleus distribution of NGC 3256. The centre of NGC 3627 has the highest measured surface densities in the main sample, and even slightly exceeding the highest values from NGC 3256. Only the overlap region of NGC 4038/9 has higher surface densities. This is consistent with the comparison by Sun et al. (2020b) of the centres of 43 barred spiral galaxies having a ~20 times higher mass-weigthed median surface density than pixels outside the central regions of 13 unbarred spiral galaxies. The centre of NGC 3627 also exhibits the broadest distribution of all of the centres from the main sample shown in Figure 2.2 as well as the nuclei of NGC 3256. Only the distribution from the overlap region of NGC 4038/9 is wider.

Velocity dispersions in the disc of NGC 3627 lie above the majority of the measurements in the main sample in Figure 2.3, but they only overlap with the lower ~25 percent of the non-nuclear distribution from NGC 3256. However, the central distribution in NGC 3627 is consistent with both the upper half of the non-nuclear distribution and the

lower half of the nuclei in NGC 3256. This is again consistent with the full PHANGS-ALMA sample where Sun et al. (2020b) measure a ~5 times higher mass-weighted velocity dispersion in their barred compared to unbarred galaxies, and again the width of the central distribution in NGC 3627 is one of the broadest compared to all centres from PHANGS-ALMA shown in Figure 2.3.

Despite relatively wide distributions of peak brightness temperatures in NGC 3627 (see Figure 2.4), both the disc and centre are consistent with most of the main sample. Brightness temperature distributions from NGC 3627 overlap with roughly the lower half of temperatures measured in the non-nuclear pixels of NGC 3256. The surface densities and velocity dispersions are similar to the mergers analysed here, and may be due to recent interactions with NGC 3628. However, the peak brightness temperatures of NGC 3627 are more in line with its relatively modest star formation rate of ~5 $M_\odot$ yr^{-1} (Calzetti et al. 2015), or surface densities on about 300 pc scales reaching up to ~0.3 $M_\odot$ yr^{-1} kpc^{-2} (Watanabe et al. 2011). Cormier et al. (2018) report ^{12}CO/^{13}CO J=1–0 ratios around 10 across NGC 3627, making it more similar to the overlap region in NGC 4038/9 than NGC 3256. This could be another case of kinetic temperatures being higher in NGC 3256, which is particularly interesting given how similar the other gas properties are between it and NGC 3627.

The centre of NGC 3627 stands out as having the highest virial parameters in the PHANGS-ALMA main sample in Figure 2.5. It overlaps with the upper half of the non-nuclear distribution in NGC 3256, and is also consistent with both nuclei. The disc also exhibits quite high virial parameters for the main sample, overlapping with the non-nuclear and southern nucleus distributions from NGC 3256. This consistency is driven by the similar surface densities and velocity dispersions measured in NGC 3627 and NGC 3256. Figure 2.6 shows similar results for the internal turbulent pressures. Sun et al. (2018) show the dispersions versus surface densities for just NGC 3627, split into disc and central regions, exhibiting a trend offset from the main sample like NGC 3256.

2.5 Discussion

2.5.1 ISM structure

Sun et al. (2018) measure increasing median velocity dispersions with increasing beam

FWHM (between 0.07 and 0.18 dex in the discs and 0.03 and 0.1 dex in the centres). This is indicative of the structured nature of the turbulent ISM because turbulent motions are expected to decrease at smaller scales (as in the size-linewidth relation; Larson 1981). A correlation between velocity dispersion and beam size is also measured in NGC 3256, but is very weak in all regions except the northern nucleus. The median dispersions in the non-nuclear region pixels increase by 0.05 dex, in the northern nucleus by 0.31 dex (see Section 2.4.2 for a discussion of how increased sensitivity to the nuclear outflow at lower resolution is likely the source of this trend), and in the southern nucleus by 0.04 dex. So despite more than a factor of two change in physical beam size, there does not appear to be evidence for the turbulent size-linewidth relation at these scales.

Another signature of the structured ISM in the PHANGS-ALMA sample is in the decreasing median surface densities with increasing beam size (between 0.17 and 0.39 dex in the discs and 0.08 and 0.45 dex in the centres). This is caused by decreasing beam dilution as the resolution approaches the size of the clouds making up the ISM. In contrast, median surface densities in NGC 3256 only decrease by 0.02 dex, 0.01 dex, and not at all in the non-nuclear, northern, and southern nucleus, respectively. If the molecular gas is smooth across the physical scales analysed here, and star-forming overdensities primarily exist on scales smaller than 55 pc, then we would expect no trend in surface brightness with resolution.

We can also use our measurements of the peak brightness temperatures to probe the structure of the gas in NGC 3256. Given the optically thick nature of low-J transitions of CO, the brightness temperature approximately traces the kinetic temperature of the molecular gas. Taking the beam filling factor into account means the brightness temperature actually represents a lower limit for the kinetic temperature. If the emitting clouds are smaller than our 55 pc beam then the change in filling factor between 120 and 55 pc would be expected to result in a change of 0.68 dex, the ratio of beam areas. This scenario does not fit because we see only a 0.08 dex increase in the median brightness temperature in the 55 pc measurements compared to 120 pc.

If we assume the clouds are spherical we can instead solve for the diameter that would give the measured change in brightness temperature between 55 and 120 pc. Doing so we find the structures need to be ~110 pc across. Since we should be able to resolve this size in our 55 pc map, this size is not consistent with the constant surface densities and dispersions measured as a function of beam size. This scenario would also not

explain why the brightness temperature increases marginally between 80 and 55 pc and by roughly the same factor as between 120 and 80 pc.

The median temperature change can be explained if both the filling factor and the kinetic temperature of the gas are allowed to change between resolutions. However, if we assume the emitting sources are smaller than 55 pc and adopt the geometric change in the filling factor expected between our largest and smallest beam, then the kinetic temperatures would have to decrease by a factor of four as the beam FWHM decreases, which seems excessive.

One option not ruled out is that the bulk of the molecular gas is in a smooth medium that largely fills the volume but does not break up into higher density clouds, even at 55 pc scales. In this scenario, the similarity of brightness temperature distributions across resolutions arises for the same reason we see no trend in surface density with resolution. So the lack of any strong trends with resolution in velocity dispersion, surface density, and brightness temperature indicates the molecular ISM in all regions observed in this merger has smoother structure than disc galaxies, at the same physical sizes.

2.5.2 Gas dynamics

Figure 2.5 shows a significant difference in median virial parameters measured in NGC 3256 and the PHANGS-ALMA sample. Lines of constant virial parameter in Figure 2.7 show how those differing virial parameters result in an offset between the two samples, potentially originating from a real difference in the dynamical states of the molecular gas.

The majority of gas across the PHANGS-ALMA galaxies is nearly self-gravitating or slightly over-pressurized across almost 2 dex in surface density and 1 dex in velocity dispersion. The gas in NGC 3256 instead has enough excess velocity dispersion over about ~1 dex in both surface density and dispersion that the gas appears to be nowhere near self-gravitating. However, both of these interpretations of the virial parameters do not include the contribution of external pressure confinement in estimating the boundedness of the gas in clouds.

Sun et al. (2020a) conclude that the contribution of external weight from atomic, stellar, and molecular mass in a clumpy ISM can balance the over-pressurization seen in the PHANGS-ALMA sample and bring much of the gas into being bound in GMCs. Assuming the high virial parameters estimated in NGC 3256 are solely from the omission

of external pressure, we can estimate the external mass surface densities required for pressure equilibrium within each beam. We find there would have to be between 65 and 4200 $M_\odot$ pc^{-2} in external mass confining the molecular clouds in the non-nuclear pixels of NGC 3256, and up to 10^4 $M_\odot$ pc^{-2} for some pixels in the nuclei. We summarize our method in Appendix 2.A.

Stellar mass surface densities of nearby spirals can cover much of this mass range from ~60 to 2000 $M_\odot$ pc^{-2} (Leroy et al. 2008; Jiménez-Donaire et al. 2019). Engargiola et al. (2003) measured ~10^9 $M_\odot$ of atomic gas in the central 5 kpc of NGC 3256, giving an average atomic gas surface density of about 51 $M_\odot$ pc^{-2}. Including an estimate here for the contribution from large-scale and diffuse molecular gas external to the densest regions on GMC scales is not straightforward with an analysis like that of Sun et al. (2020a). However, from these estimates it seems plausible that a portion of the densest molecular gas we observe in NGC 3256 is being pressure confined by external matter. However, the highest dispersion gas likely does not have enough external pressure to be in pressure equilibrium with the surrounding material.

Estimates of pressures surrounding GMCs in systems like NGC 3256 have been made previously. HI cloud collisions have been estimated to produce localized pressures of ~10^8 K cm^{-3} but result in average ambient pressures of only ~5.5×10^5 K cm^{-3} (Jog & Solomon 1992). Wilson et al. (2003) estimate external pressures for supergiant molecular complexes in NGC 4038/9 due to the hot ISM to be on average 6×10^5 K cm^{-3}. They further argue that the low X-ray filling factor results in their pressure estimate being consistent with the localized pressure of Jog & Solomon (1992). Compared to NGC 3256, the localized pressures from Jog & Solomon (1992) exceed the non-nuclear pressures by an order of magnitude and are consistent with the pressures measured within the central 1 kpc of the nuclei. However, the ambient pressures in these models are too low by two to three orders of magnitude. Jog & Solomon (1992) explain that GMCs may be subject to the localized pressure if they are uniformly surrounded by and in direct contact with several HI clouds. Given the difference of up to an order of magnitude between the HI and molecular gas surface densities in NGC 3256, it is unlikely the atomic component is the dominant source of pressure confinement.

Johnson et al. (2015) estimated the external pressure on the Firecracker molecular cloud in NGC 4038/9 from the overlying molecular material to be ~10^7 K cm^{-3}. Comparing this to the requisite external pressure of ~10^9 K cm^{-3} needed to explain the

velocity dispersion of the gas showed additional sources of pressure (like cloud-cloud collisions) were needed. Given the similar internal pressures but lower surface densities in NGC 3256 compared to NGC 4038/9, it is even less likely that external molecular gas could gravitationally bind the gas in NGC 3256. Tsuge et al. (2020a,b) estimated external pressures of ~10^8 to 10^9 K cm^{-3} due to molecular cloud collisions for the five giant molecular complexes in NGC 4038/9. Similar external pressures could account for some of the highest internal pressures in NGC 3256, but would beg the question of whether there is enough molecular gas in the central 6 kpc of NGC 3256 undergoing cloud-cloud collisions to produce the pressures estimated here.

Returning to the offset of NGC 3256 relative to the PHANGS-ALMA sample in Figure 2.7, NGC 3256 makes it clear that the velocity dispersion-surface density parameter space does not capture the full picture of the dynamics of molecular gas. The tight correlation seen across the PHANGS-ALMA main sample may be an artefact of selecting dynamically similar galaxies that are massive, disc-dominated, and star forming.

Related to this is the actual source of the turbulence. Krumholz et al. (2018) argue that the only way to power dispersions $\gtrsim 10$ km s^{-1} is through bulk gas flows that are ubiquitous in interacting galaxies. Differences in the power sources for turbulence between interacting and disc galaxies may be manifesting themselves in the state of the gas as probed by Figure 2.7. It is not trivial to trace the sources of turbulence back from the gas dynamics in this way however since NGC 4038/9 lies along the PHANGS-ALMA main sample relation while NGC 3256 is offset from it. The individual properties of each interacting system may also change this offset, and the offset could change with time as the interactions evolve.

2.5.3   Virial diameter

Instead of asking if the gas is bound or not at the observed scales, we can ask at what size would the gas be in approximate free-fall collapse ($\alpha_{\mathrm{vir}} = 2$), given the measured surface densities and velocity dispersions. Figure 2.8 shows the Gaussian KDEs for these sizes. The all-pixel distributions peak around 300 to 400 pc between 55 and 120 pc resolution, respectively. Given the diameter at the peak of the distributions is roughly five beams across at 55 pc resolution, a cloud-decomposition analysis would be able to identify if most of the gas is grouped into clouds of this size.
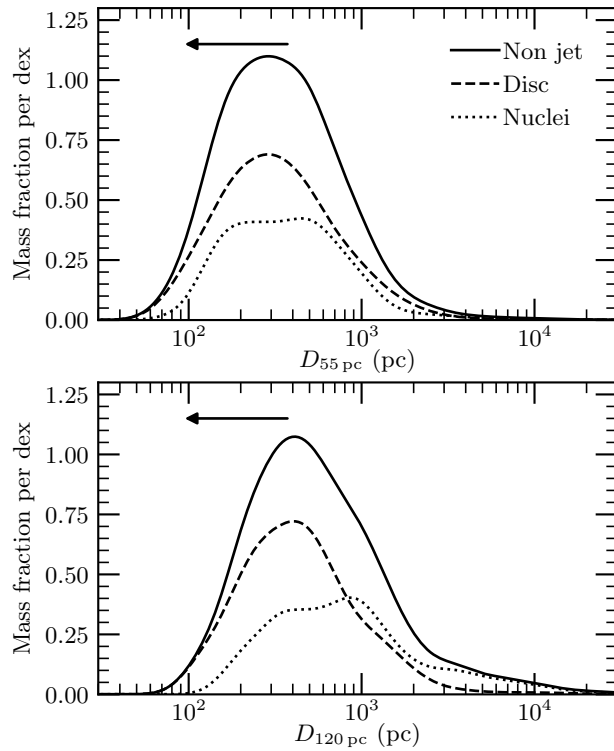
FIGURE 2.8: Cloud diameters calculated assuming a virial parameter of 2 for each pixel where surface density and velocity dispersion were measured in NGC 3256. Linestyles are the same as in Figure 2.2. Arrows show how values would shift if we adopt the Milky Way CO conversion factor of $6.25 \, \mathrm{M_\odot \, pc^{-2} (K \, km \, s^{-1})^{-1}}$ instead of the LIRG conversion factor of $1.38 \, \mathrm{M_\odot \, pc^{-2} (K \, km \, s^{-1})^{-1}}$.

If this interpretation is correct then it would imply that the molecular gas is mostly gravitationally bound, but on quite large scales of a few hundred parsecs. One alternative could be that the velocity dispersions are biased towards high values by multiple clouds along the line of sight, and removing that effect would drive these sizes down. It is also possible that even at our highest resolution there are multiple clouds within the beam and that the cloud-to-cloud velocity differences are driving up the dispersion (and the sizes in Figure 2.8). Without a good understanding of the cloud size and mass distributions in mergers like NGC 3256, this later alternative can only be explored with higher spatial resolution observations. Finally, it could be that the molecular gas is simply not bound at these scales and is behaving more similarly to the atomic gas traced by HI in spiral galaxies.

2.5.4 Expectations for a merger

High molecular gas surface densities, linked to enhanced quantities of molecular gas in interacting and merging galaxies, have been observed in many systems previously (e.g. Braine & Combes 1993; Kaneko et al. 2013; Violino et al. 2018). This has also been reproduced in numerical studies. Moreno et al. (2019), for example, measure a ~18 per cent increase in cold-dense gas ($n = 10 - 1000 \, \mathrm{cm}^{-3}$) and a ~240 per cent increase in cold ultra-dense gas ($n > 1000 \, \mathrm{cm}^{-3}$).

A possible origin of the extreme velocity dispersions in NGC 3256 is that the star formation rate was enhanced first, which then increased the velocity dispersion through stellar and supernova feedback. However, theoretical and numerical investigations into the sources of turbulent energy indicate that even at mass surface densities and turbulence levels replicating U/LIRG conditions and at the maximal limit of star formation rates for discs, the gas velocity dispersion can only reach ~$10 \, \mathrm{km \, s}^{-1}$ (Shetty & Ostriker 2012; Krumholz et al. 2018). Gas inflow was proposed by Krumholz et al. (2018) as the main mechanism to drive velocity dispersions above that limit. So while a portion of the measured velocity dispersion distribution can originate from star formation feedback, it is possible the highest dispersions are driven by gas flows.

Since the molecular gas at the scales observed in NGC 3256 appears smooth in comparison to disc galaxies and extreme external pressures are required to bind the gas, what are the actual sites of star formation like in this merger? It would seem that self-gravitating and collapsing overdensities must exist at scales smaller than 55 pc,

potentially like Galactic clumps and cores. Moreno et al. (2019) report that interactions dramatically increase the mass fraction of the densest cold gas in their simulations, indicating the source of enhanced star formation rates. However, this densest component only makes up ~0.2 percent of the cold gas mass. Overall they measure an enhancement in diffuse molecular gas that cannot collapse. These models could imply that we are observing the high surface densities of the enhanced cold gas reservoir, but only at the scales where the gas is too diffuse to directly contribute to star formation. Marginally-bound structures at the highest densities are driven to collapse by the interaction and thus the star formation rate increases, but the addition of turbulent energy from inflowing gas will act to over-pressurize the bulk of the molecular gas.

2.5.5 Caveats

We first consider the applicability of using a CO conversion factor to estimate molecular gas masses from integrated CO line intensities. Estimating mass from the optically thick CO emission with a conversion factor relies on the presence of virialized clouds which can relate their emitting surface area to the total mass in their volume. While the molecular gas in NGC 3256 is estimated to be well out of virial equilibrium due to self-gravity alone, it may be virialized when external pressure and gravitational terms (e.g. stars and the overall galactic potential) are included. If the molecular gas appears smooth on 55 pc scales because the majority of clouds are smaller than the beam, then the integrated line intensities would be proportional to the number of clouds within the beam. In lieu of optically thin emission, the collection of clouds within each beam may act optically thin such that each cloud contributes an average mass so the integrated intensity is still proportional to the total mass within the beam (the so-called "mist" model, Bolatto et al. 2013). Finally, beyond considering individual virialized clouds, the U/LIRG conversion factor used here has also been derived in the centres of U/LIRGs using CO spectra to estimate dynamical masses assuming smoothly distributed molecular gas (Downes & Solomon 1998).

The main assumption to be concerned with in the mist model when applying it to a system like NGC 3256 is that the sub-beam structure cannot be overlapping in spatial-spectral space. The high surface densities mean there is likely to be some degree of gas structures overlapping along the line of sight spatially, but the gas would also have to be Doppler shifted to the same velocities for the molecular mass to be underestimated. For

this effect to entirely account for the offset in Figure 2.7 would require ~4.5 clouds both along the line of sight and at the same velocity in most pixels. An average of 4.5 clouds along each line of sight seems excessively large.

We now consider the value we chose for the conversion factor. Molecular gas properties potentially present in NGC 3256 such as higher temperatures, larger velocity dispersions, low CO optical depths, and non-virialized gas have all been argued as sources of low conversion factors in various studies of U/LIRGs (e.g. Wild et al. 1992; Papadopoulos & Seaquist 1999; Zhu et al. 2003). However, by switching to the Galactic value, the surface densities would increase by a factor of ~4.5. This would result in the NGC 3256 non-nuclear sample overlapping considerably with the sample from NGC 4038/9, and it would also shift the bulk of the virial parameter distribution to ~2. Gas at these densities and scales being bound by self-gravity would call into question the findings of Moreno et al. (2019) where they argue the majority of the enhanced molecular gas is not participating in star formation. It could instead be that the offset of NGC 3256 is real and that NGC 4038/9 would be better described by the U/LIRG conversion factor which would shift NGC 4038/9 closer to where NGC 3256 appears in Figure 2.7. However, measurements of the conversion factor in NGC 4038/9 have actually come in either consistent with the Galactic value or even higher (Wilson et al. 2003; Schirm et al. 2014).

Differences in the proper conversion factor between NGC 3256 and NGC 4038/9 could originate from their differing merger stages as well as the regions analysed. Our observations of NGC 3256 cover the very centre of the system, where the conversion factor may be shifted to lower values (e.g. Weiß et al. 2001; Hitschfeld et al. 2008; Sliwa et al. 2013). It is also likely that the conversion factor varies significantly across different regions in this merger as Renaud et al. (2019) measure variations up to a factor of 2.2 in their simulation of a NGC 4038/9-like merger. They also expect spatial variations are even greater since they focused their analysis on actively star-forming regions. Directly estimating the conversion factor may be possible with these data but requires cloud decomposition in spatial and spectral dimensions. This will be investigated in a future paper.

Caution should be used when interpreting the velocity dispersions measured in both NGC 3256 and NGC 4038/9 due to the complex morphologies of interacting galaxies which makes it much more likely to observe multiple cloud structures along the line of

sight. This is a limitation of the current pixel-based analysis. The degree to which both mergers, and even each region within the two systems, are affected by cloud multiplicity is likely to result in a non-trivial rearrangement of their distributions in Figure 2.7. Our future cloud-decomposition analysis of NGC 3256 will help to eliminate this effect. We also note that while we attribute the spectral line widths to turbulence in our discussions, unresolved bulk motions also contribute to the measured dispersions. Given the high spatial resolution our observations however, an estimate of galactic rotation from the extrema of moment 1 maps contributes at most $5.5\,\mathrm{km\,s^{-1}}$ of dispersion across a single $120\,\mathrm{pc}$ beam. Bulk flow of gas from the merging process is also likely contributing in some regions of NGC 3256.

Interpretation of the virial parameters and internal turbulent pressures calculated for the mergers should also be made with caution. If the underlying assumptions are satisfied in NGC 3256 as well as in all of the galaxies presented by Sun et al. (2018), then using the same expressions for calculating these quantities should make the comparison of results straightforward. For the virial parameter, these assumptions include spherical clouds with density profiles of $\rho \propto r^{-2}$ that are the same size as the beam. The internal pressure relies on each beam being filled by one virialized cloud along each line of sight (Bertoldi & McKee 1992). Based on many previous studies of GMC properties in disc galaxies, these conditions are likely to hold in the main PHANGS-ALMA sample. However, without even higher resolution observations we cannot determine if these conditions hold in NGC 3256. The virial parameter distribution well above one indicates that the internal pressure would be underestimated, since the gas kinetic energy associated with bulk motions (like expansion) would not be accounted for in calculating the pressure. However, lines of sight with multiple components would overestimate the dispersion in the average cloud leading to an overestimation of the internal pressures.

2.6 Conclusions

We have observed the central $6\,\mathrm{kpc}$ of the closest LIRG, NGC 3256, in CO (2–1) with ALMA at GMC-scale resolution to obtain pixel-by-pixel distributions of mass surface density, velocity dispersion, peak brightness temperature, virial parameter, and internal turbulent pressure. From these distributions we find:

- Assuming the U/LIRG conversion factor of $1.38\,\mathrm{M_\odot\,pc^{-2}(K\,km\,s^{-1})^{-1}}$, molecular mass surface densities range between 8 to $5500\,\mathrm{M_\odot\,pc^{-2}}$. This range is similar to the overlap region of NGC 4038/9, but extends to lower surface densities. NGC 3256 has surface densities above the majority of the disc measurements from PHANGS-ALMA reported by Sun et al. (2018).

- Velocity dispersions range from 10 to $200\,\mathrm{km\,s^{-1}}$ in NGC 3256. The median outside the central kiloparsec radius is $25\,\mathrm{km\,s^{-1}}$. These velocity dispersions are well above the majority of the PHANGS-ALMA disc galaxies, and are consistent with NGC 4038/9.

- The vast majority of the gas appears unbound at 55 pc scales with virial parameters above 3, and medians even reaching 7 to 19. Coupled to this, we estimate very high turbulent pressures from 10^5 to $10^{10}\,\mathrm{K\,cm^{-3}}$. External pressure on GMCs may bind a fraction of the gas, but there is still likely a significant fraction of mass that is unbound.

- 50 per cent of the mass in the non-nuclear pixels of NGC 3256 has peak brightness temperatures significantly above almost all measurements in the main PHANGS-ALMA sample as well as the overlap region of NGC 4038/9. All measurements in the nuclei of NGC 3256 are above those in all other galaxies analysed here. This suggests the majority of molecular gas in NGC 3256 is significantly warmer than disc galaxies and even the most vigorously star forming region of NGC 4038/9.

- The observation of little or no trend in surface density, velocity dispersion, and peak brightness temperature with resolution indicates the molecular medium has a smoother structure at 55 pc scales than in the PHANGS-ALMA disc galaxies. A smooth molecular ISM appearing unbound on these scales could be consistent with FIRE-2 numerical results (Moreno et al. 2019). It may also be that gas at these scales in NGC 3256 more closely resembles the dynamics of giant molecular associations in disc galaxies.

An additional test of the boundedness of the gas in NGC 3256 will be carried out using a spatial and spectral decomposition of the CO emission in a future paper. Instead of assuming the beam size represents the relevant scale,this analysis will produce empirical estimates of the sizes of the molecular structures. We will also attempt

to estimate the CO conversion factor from the cloud size and linewidth catalogue. However, the virial parameter estimates reported in this work make it likely that this approach will produce at best an upper limit. Independent methods to estimate the conversion factor (e.g. estimating dust masses from the continuum or optically thin molecular line isotopologues) should also be investigated.

Applying both pixel-by-pixel and cloud-decomposition analyses to more merger systems at this resolution will help to determine if the apparent ISM dynamics and structure in NGC 3256 are general properties of these extreme systems. It can also further test the universality of gas dynamical state reported by Sun et al. (2018) across the PHANGS-ALMA main sample and overlap region in NGC 4038/9. In a forthcoming paper we will apply these analyses, at the same physical scales, to the entire NGC 4038/9 merger system in CO (2–1). This will also allow us to probe the nuclear regions for similarities with the nuclei of other galaxies.

Finally, higher resolution imaging of NGC 3256 in CO (2–1) would explore at what scale the molecular gas goes from a smooth medium to the clumpy one we assume must exist due to the presence of significant star formation. ALMA can observe down to ≈ 9 pc scales to search for significant changes in the physical quantities discussed here. Any trends with resolution would indicate a structured ISM like what is seen in the PHANGS-ALMA galaxies at 45 pc. Whether we will find clouds on scales smaller than 55 pc in NGC 3256 that are analogous to GMCs in nearby discs, or that the molecular gas remains unbound down to scales and densities that are more similar to Galactic clumps or cores is a question that awaits maximal resolution data from ALMA.

Acknowledgements

This research made use of Astropy, a community-developed core Python package for Astronomy (http://www.astropy.org, Astropy Collaboration et al. 2013, 2018). This research also made use of the Matplotlib (Hunter 2007), NumPy (van der Walt et al. 2011), scikit-learn (Pedregosa et al. 2011), Jupyter Notebook (Kluyver et al. 2016), and statsmodels (Seabold & Perktold 2010) Python packages. This research has made use of NASA's Astrophysics Data System. This research has made use of the VizieR catalogue access tool (Ochsenbein et al. 2000). This research has made use of the NASA/IPAC Extragalactic Database (NED), which is funded by the National Aeronautics and Space Administration and operated by the California Institute of Technology. This research has made use of the SIMBAD database, operated at CDS, Strasbourg, France (Wenger et al. 2000).

Data Availability

This paper makes use of the following ALMA data: ADS/JAO.ALMA#2015.1.00714.S (accessed from the ALMA Science portal at almascience.org). ALMA is a partnership of ESO (representing its member states), NSF (USA) and NINS (Japan), together with NRC (Canada), MOST and ASIAA (Taiwan), and KASI (Republic of Korea), in cooperation with the Republic of Chile. The Joint ALMA Observatory is operated by ESO, AUI/NRAO and NAOJ. The National Radio Astronomy Observatory is a facility of the National Science Foundation operated under cooperative agreement by Associated Universities, Inc.

The derived data generated in this research will be shared on reasonable request to the corresponding author.

2.A   Appendix: Estimating required external material

The virial parameters presented in Section 2.4.4 neglect the effect of external pressure on the cloud. We make a rough estimate of the pressure required to balance the internal turbulent pressure following a simplified form of that by Sun et al. (2020a). We aim to satisfy the criterion that the external pressure, P_{ext}, is equal to the internal pressure, P_{turb}. A simple expression for the gravitational pressure from mass external to the cloud

is

$$P_{\text{ext}} k_B = C G \Sigma_{\text{cloud}} \Sigma_{\text{tot}} \tag{2.1}$$

where k_B is the Boltzmann constant, C is a constant that contains normalizations for the assumed geometries of all of the material, G is the gravitational constant, Σ_{cloud} is the mass surface density of the molecular cloud, and Σ_{tot} is the surface density of all material along the line of sight.

Neglecting dark matter in the inner portion of this merger, Σ_{tot} is made up of

$$\Sigma_{\text{tot}} = \Sigma_{\text{cloud}} + \Sigma_{\text{ext,mol}} + \Sigma_{\star} + \Sigma_{\text{atom}} \tag{2.2}$$

$$= \Sigma_{\text{cloud}} + \Sigma_{\text{ext}} \tag{2.3}$$

where $\Sigma_{\text{ext,mol}}$ is the molecular gas surface density outside the cloud, $\Sigma_{\star}$ is the stellar surface density, Σ_{atom} is the atomic surface density, and Σ_{ext} is the sum of the components external to the cloud. Rewriting the external pressure with these separate terms gives

$$P_{\text{ext}} k_B = G \Sigma_{\text{cloud}} \left(C_1 \Sigma_{\text{cloud}} + C_2 \Sigma_{\text{ext}} \right) \tag{2.4}$$

where $C_1 \Sigma_{\text{cloud}}$ accounts for the self-gravity of the cloud and $C_2 \Sigma_{\text{ext}}$ the weight of material external to the cloud. C_1 and C_2 are again constants that depend on the geometry of these components. Assuming constant density within a spherical cloud, $C_1 = 3\pi/8$ (e.g. Equation A2 from Sun et al. 2020a).

Setting the external pressure equal to the measured internal pressure and rearranging Equation 2.4 we have an expression for the external mass surface density required to balance the internal turbulent pressure

$$\Sigma_{\text{ext}} = \frac{1}{C_2} \left(\frac{k_B P_{\text{turb}}}{G \Sigma_{\text{cloud}}} - \frac{3\pi}{8} \Sigma_{\text{cloud}} \right). \tag{2.5}$$

If we treat C_2 as tunable between $3\pi/8$ (spherical) and $\pi/2$ (disc with scale height much greater than the molecular disc scale height), then we can explore a reasonable range of external pressures given different combinations of relative geometries of the multiple components. This was the most useful approach considering that C_2 must encode the volumetric average of all three external components relative to the molecular clouds in a morphologically disturbed merger.

Calculating external surface densities, pixel-by-pixel using our measurements at 55 pc resolution, gives disc mass-weighted 16, 50, and 84 percentiles of (100, 1000, and $3000 \, M_\odot \, pc^{-2})/C_2$. The combined-nuclei percentiles are $(2 \times 10^3, \, 6 \times 10^3,$ and $20 \times 10^3 \, M_\odot \, pc^{-2})/C_2$. The same calculation for the PHANGS-ALMA sample results in most pixels having external surface densities of zero or less, which we interpret as the majority of gas being self-gravity dominated (Sun et al. 2020a). The remaining pixels in the PHANGS-ALMA sample appear around (50 to $100 \, M_\odot \, pc^{-2})/C_2$.

An important component this model neglects is the pressure contribution from self-gravity of the external material (e.g. the atomic term in Equation A9 from Sun et al. 2020a). This primarily depends on the surface density of the atomic gas, and acts to reduce the external surface density required to confine the molecular cloud. Galaxies in the PHANGS-ALMA sample are strongly impacted by this term, and so the full treatment by Sun et al. (2020a) is recommended to assess their pressure equilibrium. We do not expect the atomic surface density to provide a very substantial correction in a merger. Since we estimate NGC 3256 requires significantly higher external surface densities than the PHANGS-ALMA galaxies, it is unlikely the missing external self-gravity term would drastically alter our results.

Bibliography

Aalto S., Black J. H., Booth R. S., Johansson L. E. B., 1991a, A&A, 247, 291

Aalto S., Black J. H., Johansson L. E. B., Booth R. S., 1991b, A&A, 249, 323

Aalto S., Booth R. S., Black J. H., Johansson L. E. B., 1995, A&A, 300, 369

Astropy Collaboration et al., 2013, A&A, 558, A33

Astropy Collaboration et al., 2018, AJ, 156, 123

Bemis A., Wilson C. D., 2019, AJ, 157, 131

Bertoldi F., McKee C. F., 1992, ApJ, 395, 140

Blitz L., Thaddeus P., 1980, ApJ, 241, 676

Bolatto A. D., Leroy A. K., Rosolowsky E., Walter F., Blitz L., 2008, ApJ, 686, 948

Bolatto A. D., Wolfire M., Leroy A. K., 2013, ARA&A, 51, 207

Booth C. M., Agertz O., Kravtsov A. V., Gnedin N. Y., 2013, ApJ, 777, L16

Braine J., Combes F., 1993, A&A, 269, 7

Brandl B. R., et al., 2009, ApJ, 699, 1982

Brown T., Wilson C. D., 2019, ApJ, 879, 17

Calzetti D., et al., 2015, AJ, 149, 51

Catinella B., et al., 2018, MNRAS, 476, 875

Colombo D., et al., 2014, ApJ, 784, 3

Cormier D., et al., 2018, MNRAS, 475, 3909

Dale J. E., Bonnell I. A., 2008, MNRAS, 391, 2

Dame T. M., et al., 1987, ApJ, 322, 706

Downes D., Solomon P. M., 1998, ApJ, 507, 615

Engargiola G., Plambeck R. L., Rosolowsky E., Blitz L., 2003, ApJS, 149, 343

Farrah D., et al., 2001, MNRAS, 326, 1333

Federrath C., Klessen R. S., 2012, ApJ, 761, 156

Field G. B., Blackman E. G., Keto E. R., 2011, MNRAS, 416, 710

Fukui Y., et al., 1999, PASJ, 51, 745

Gao Y., Lo K. Y., Lee S. W., Lee T. H., 2001, ApJ, 548, 172

Genzel R., Stutzki J., 1989, ARA&A, 27, 41

Ginsburg A., et al., 2019, radio-astro-tools/spectral-cube: v0.4.4, doi:10.5281/zenodo.2573901

Girichidis P., et al., 2016, ApJ, 816, L19

Harada N., Sakamoto K., Martín S., Aalto S., Aladro R., Sliwa K., 2018, ApJ, 855, 49

He H., Wilson C. D., Sliwa K., Iono D., Saito T., 2020, MNRAS, 496, 5243

Heyer M. H., Carpenter J. M., Snell R. L., 2001, ApJ, 551, 852

Heyer M., Krawczyk C., Duval J., Jackson J. M., 2009, ApJ, 699, 1092

Hitschfeld M., et al., 2008, A&A, 479, 75

Howard C. S., Pudritz R. E., Harris W. E., 2017, MNRAS, 470, 3346

Howell J. H., et al., 2010, ApJ, 715, 572

Hunter J. D., 2007, Computing in Science & Engineering, 9, 90

Iono D., Yun M. S., Mihos J. C., 2004, ApJ, 616, 199

Jiménez-Donaire M. J., et al., 2019, ApJ, 880, 127

Jog C. J., Solomon P. M., 1992, ApJ, 387, 152

Johnson K. E., Leroy A. K., Indebetouw R., Brogan C. L., Whitmore B. C., Hibbard J., Sheth K., Evans A. S., 2015, ApJ, 806, 35

Kaneko H., Kuno N., Iono D., Tamura Y., Tosaki T., Nakanishi K., Sawada T., 2013, PASJ, 65, 20

Karachentsev I. D., Kudrya Y. N., 2014, AJ, 148, 50

Karl S. J., Naab T., Johansson P. H., Kotarba H., Boily C. M., Renaud F., Theis C., 2010, ApJ, 715, L88

Keller B. W., Kruijssen J. M. D., Wadsley J. W., 2020, MNRAS, 493, 2149

Keto E. R., Myers P. C., 1986, ApJ, 304, 466

Klaas U., Nielbock M., Haas M., Krause O., Schreiber J., 2010, A&A, 518, L44

Klassen M., Pudritz R. E., Peters T., 2012, MNRAS, 421, 2861

Kluyver T., et al., 2016, in Loizides F., Scmidt B., eds, 20th International Conference on Electronic Publishing. Positioning and Power in Academic Publishing: Players, Agents and Agendas. IOS Press, Netherlands, p. 87

Krumholz M. R., Dekel A., McKee C. F., 2012, ApJ, 745, 69

Krumholz M. R., Burkhart B., Forbes J. C., Crocker R. M., 2018, MNRAS, 477, 2716

Larson R. B., 1981, MNRAS, 194, 809

Law C. J., Zhang Q., Ricci L., Petitpas G., Jiménez-Donaire M. J., Ueda J., Lu X., Dunham M. M., 2018, ApJ, 865, 17

Lee M. G., Jang I. S., 2013, ApJ, 773, 13

Leroy A., Bolatto A., Walter F., Blitz L., 2006, ApJ, 643, 825

Leroy A. K., Walter F., Brinks E., Bigiel F., de Blok W. J. G., Madore B., Thornley M. D., 2008, AJ, 136, 2782

Leroy A. K., et al., 2015, ApJ, 801, 25

Leroy A. K., et al., 2016, ApJ, 831, 16

McKee C. F., Zweibel E. G., 1992, ApJ, 399, 551

McMullin J. P., Waters B., Schiebel D., Young W., Golap K., 2007, in Shaw R. A., Hill F., Bell D. J., eds, ASP Conf. Ser. Vol. 376, Astronomical Data Analysis Software and Systems XVI. Astron. Soc. Pac., San Francisco, p. 127

Michiyama T., et al., 2018, ApJ, 868, 95

Mihos J. C., Hernquist L., 1996, ApJ, 464, 641

Mizuno A., Onishi T., Yonekura Y., Nagahama T., Ogawa H., Fukui Y., 1995, ApJ, 445, L161

Mizuno N., Rubio M., Mizuno A., Yamaguchi R., Onishi T., Fukui Y., 2001, PASJ, 53, L45

Moreno J., et al., 2019, MNRAS, 485, 1320

Noguchi M., 1988, A&A, 203, 259

Ochsenbein F., Bauer P., Marcout J., 2000, A&AS, 143, 23

Ohyama Y., Terashima Y., Sakamoto K., 2015, ApJ, 805, 162

Padoan P., Haugbølle T., Nordlund Å., Frimann S., 2017, ApJ, 840, 48

Papadopoulos P. P., Seaquist E. R., 1999, ApJ, 516, 114

Papadopoulos P. P., van der Werf P. P., Xilouris E. M., Isaak K. G., Gao Y., Mühle S., 2012, MNRAS, 426, 2601

Pedregosa F., et al., 2011, Journal of Machine Learning Research, 12, 2825

Peng C. Y., Ho L. C., Filippenko A. V., Sargent W. L. W., 1998, in American Astronomical Society Meeting Abstracts. p. 06.07

Ptak A., Colbert E., van der Marel R. P., Roye E., Heckman T., Towne B., 2006, ApJS, 166, 154

Renaud F., Bournaud F., Agertz O., Kraljic K., Schinnerer E., Bolatto A., Daddi E., Hughes A., 2019, A&A, 625, A65

Rosolowsky E., 2007, ApJ, 654, 240

Rosolowsky E., Blitz L., 2005, ApJ, 623, 826

Rots A. H., 1978, AJ, 83, 219

Saintonge A., et al., 2017, ApJS, 233, 22

Saito T., et al., 2017, ApJ, 835, 174

Sakamoto K., Aalto S., Combes F., Evans A., Peck A., 2014, ApJ, 797, 90

Sanders D. B., Mirabel I. F., 1996, ARA&A, 34, 749

Sanders D. B., Mazzarella J. M., Kim D. C., Surace J. A., Soifer B. T., 2003, AJ, 126, 1607

Sargent M. T., et al., 2014, ApJ, 793, 19

Schirm M. R. P., et al., 2014, ApJ, 781, 101

Schweizer F., et al., 2008, AJ, 136, 1482

Seabold S., Perktold J., 2010, in van der Walt S., Millman J., eds, Python in Science Conf. Ser.. Available at: http://conference.scipy.org/proceedings/scipy2010/

Shetty R., Ostriker E. C., 2012, ApJ, 754, 2

Sliwa K., et al., 2013, ApJ, 777, 126

Sliwa K., Wilson C. D., Aalto S., Privon G. C., 2017, ApJ, 840, L11

Soida M., Urbanik M., Beck R., Wielebinski R., Balkowski C., 2001, A&A, 378, 40

Solomon P. M., Rivolo A. R., Barrett J., Yahil A., 1987, ApJ, 319, 730

Stierwalt S., et al., 2013, ApJS, 206, 1

Sun J., et al., 2018, ApJ, 860, 172

Sun J., et al., 2020a, ApJ, 892, 148

Sun J., et al., 2020b, ApJ, 901, L8

Tsuge K., Tachihara K., Fukui Y., Sano H., Tokuda K., Ueda J., Iono D., 2020b, preprint (arXiv:2005.04075),

Tsuge K., Fukui Y., Tachihara K., Sano H., Tokuda K., Ueda J., Iono D., Finn M. K., 2020a, PASJ, preprint (arXiv:1909.05240),

Utomo D., Blitz L., Davis T., Rosolowsky E., Bureau M., Cappellari M., Sarzi M., 2015, ApJ, 803, 16

Utomo D., et al., 2018, ApJ, 861, L18

Veilleux S., Kim D. C., Sanders D. B., 2002, ApJS, 143, 315

Violino G., Ellison S. L., Sargent M., Coppin K. E. K., Scudder J. M., Mendel T. J., Saintonge A., 2018, MNRAS, 476, 2591

van der Walt S., Colbert S. C., Varoquaux G., 2011, Computing in Science & Engineering, 13, 22

Watanabe Y., Sorai K., Kuno N., Habe A., 2011, MNRAS, 411, 1409

Weiß A., Neininger N., Hüttemeister S., Klein U., 2001, A&A, 365, 571

Wenger M., et al., 2000, A&AS, 143, 9

Whitmore B. C., et al., 2014, ApJ, 795, 156

Wild W., Harris A. I., Eckart A., Genzel R., Graf U. U., Jackson J. M., Russell A. P. G., Stutzki J., 1992, A&A, 265, 447

Wilson C. D., Scoville N., 1990, ApJ, 363, 435

Wilson C. D., Scoville N., Madden S. C., Charmandaris V., 2003, ApJ, 599, 1049

Wilson C. D., Elmegreen B. G., Bemis A., Brunetti N., 2019, ApJ, 882, 5

Wong T., et al., 2011, ApJS, 197, 16

Zhu M., Seaquist E. R., Kuno N., 2003, ApJ, 588, 243

3 | Extreme giant molecular clouds in the luminous infrared galaxy NGC 3256

This chapter contains the paper *Extreme giant molecular clouds in the luminous infrared galaxy NGC 3256*, submitted to *Monthly Notices of the Royal Astronomical Society* for peer review and publication. The full reference, as of now, is given below. The complete machine-readable table of cloud properties presented here has also been submitted to the journal and will be published alongside the paper.

Brunetti N., Wilson C. D., 2022, *submitted*
Department of Physics and Astronomy, McMaster University, Hamilton, ON L8S 4M1, Canada

Abstract

We present a cloud decomposition of ^{12}CO (2–1) observations of the merger and nearest luminous infrared galaxy, NGC 3256. 185 spatially and spectrally resolved clouds are identified across the central 6 kpc. Using a spatial resolution of 90 pc, we compare our cloud catalogue from NGC 3256 with recent cloud-finding results from ten galaxies observed in the PHANGS-ALMA survey. Distributions of cloud velocity dispersions, luminosities, CO-estimated masses, mass surface densities, virial masses, virial parameters, size-linewidth coefficients, and internal turbulent pressures in NGC 3256 are all significantly higher than measured in clouds in the PHANGS-ALMA galaxies. Cloud radii are slightly larger in NGC 3256 while free-fall times are shorter. The distribution of cloud eccentricities measured in NGC 3256 is generally indistinguishable from those of the PHANGS-ALMA sample. If the external pressures track the clouds' internal pressures in NGC 3256, like observed in spiral galaxies, then the average dynamical state of the clouds we identify and of those in nearby spiral galaxies may not be very different. However, the clouds in NGC 3256 appear to cover a narrower range of dynamical states than in nearby spiral galaxies. We also compare our cloud-finding results with a recent pixel-based analysis of these observations of NGC 3256 and find general agreement between the two methods.

Key words: ISM: clouds – ISM: kinematics and dynamics – ISM: structure – galaxies: interactions – galaxies: starburst – galaxies: star formation.

3.1 Introduction

Understanding the conditions which give rise to varying levels of star formation is an important part of fully describing galaxy evolution over cosmic time. Stellar feedback has dramatic morphological, kinematic, thermodynamic, and chemical impacts on the host galaxy, especially the interstellar medium (ISM). The injection of energy by stars into their surroundings contributes to the turbulent energy that supports the gas disc against gravity, setting the scale height of the atomic and molecular ISM (e.g. McKee & Ostriker 1977; Narayan & Jog 2002; Ostriker & Shetty 2011; Elmegreen 2011; Benincasa et al. 2016; Krumholz et al. 2018). Stellar radiation heats up pockets of the ISM around centres of active star formation through the far-ultraviolet photoelectric effect on polycyclic aromatic hydrocarbons and dust grains (Tielens & Hollenbach 1985; McKee 1989; Hollenbach & Tielens 1999). Mechanically driven shocks from stellar winds and supernovae also contribute to heating the surrounding ISM (McKee & Ostriker 1977; Krumholz et al. 2006; Hopkins et al. 2012). It has been widely shown that the typical rate of star formation within galaxies has dramatically changed over the age of the universe (see e.g. the review by Madau & Dickinson 2014). As the star-formation rate in a galaxy changes throughout its life, the dominance of star formation in driving morphological, kinematic, thermodynamic, and chemical changes will also evolve.

Since the majority of stars form in molecular gas, we focus on exploring the link between the conditions of the molecular gas and the resulting star formation rate. In particular, we aim to compare the molecular gas properties in nearby spiral galaxies with those within nearby merging galaxies. Mergers cause galaxies to enter a starburst phase (Larson & Tinsley 1978; Ellison et al. 2008, 2013; Hani et al. 2020) in which they exhibit elevated star formation rates relative to spiral galaxies as well as relative to their total amount of molecular gas (Daddi et al. 2010; Yamashita et al. 2017; Herrero-Illana et al. 2019; Wilson et al. 2019; Kennicutt & de los Reyes 2021). Comparing the molecular gas properties in starbursting mergers to spiral galaxies allows us to turn up the star formation rate and see what conditions in the molecular ISM lead to that more vigorous mode of star formation.

These merging systems may also recreate some of the conditions for star formation that existed in high-redshift galaxies. Local merging galaxies have star-formation rates that are similar to those in high-redshift galaxies (Zaragoza-Cardiel et al. 2018; Larson

et al. 2020; Elmegreen et al. 2021, 2009). Additionally, the galaxy merger fraction increases with redshift (e.g. see the compilation and comparison to literature merger fraction estimates spanning $z \lesssim 6$ by Romano et al. 2021). These similarities mean that since we can observe much smaller physical scales in nearby mergers than in high-redshift galaxies, we should be able to link the smaller-scale properties from nearby mergers to the larger scales at high redshift to build a more complete picture of star formation and ISM properties over cosmic time (for a review of the progress made in measuring the properties of the ISM in high-redshift systems see Tacconi et al. 2020).

At a distance of 44 Mpc (Table 3.1), NGC 3256 is the nearest luminous infrared galaxy (LIRG), forming stars at a rate of about $50 \, M_\odot \, \mathrm{yr}^{-1}$ (Sakamoto et al. 2014). It is a late-stage merger where the progenitor galaxies' nuclei are still separated but share a common envelope of gas, dust, and stars (Stierwalt et al. 2013). NGC 3256 also provides, within a single system, a fairly diverse set of environments in which to study molecular gas. The orientation of the northern nucleus appears to be nearly face-on, while the southern nucleus is nearly edge-on (for diagrams see figures 18 and 1 from Sakamoto et al. 2014; Harada et al. 2018; respectively). This edge-on orientation offers a clear view of the spectacular bipolar jet that extends 700 pc north and south of the southern nucleus while only being about 140 pc wide (Sakamoto et al. 2014). An analysis by Sakamoto et al. (2014) of the energy required to drive the jet indicates it must be at least partially driven by an active galactic nucleus (AGN), consistent with infrared (IR) and X-ray observations (Ohyama et al. 2015). There is also evidence for a red and blueshifted starburst-powered outflow being launched from the northern nucleus at an angle almost parallel with the line of sight (Sakamoto et al. 2014).

In this paper we compare clouds identified in carbon monoxide (CO) 2–1 observations of the LIRG NGC 3256 with clouds found in ten nearby spiral galaxies observed by the Physics at High Angular resolution in Nearby GalaxieS with ALMA (PHANGS-ALMA) survey (Rosolowsky et al. 2021). Details of the observations, imaging, and data preparation are summarized in Section 3.2. The cloud-finding procedure is described in Section 3.3, as well as the characterization of cloud-finding completeness. Section 3.4 covers the main results from comparing our cloud catalogue from NGC 3256 to those from PHANGS-ALMA, and in Section 3.5 we discuss physical implications of the similarities and differences as well as compare to a pixel-based analysis presented in Brunetti et al. (2021; Chapter 2). Finally, we summarize our results and conclusions in

Section 3.6.

3.2 Data

3.2.1 Observations

Observations of the CO $J = 2$–1 emission line were carried out towards NGC 3256 with the Atacama Large Millimeter/Submillimeter Array (ALMA) main array, the Morita Atacama Compact Array (ACA), and total-power array. See Brunetti et al. (2021) for a complete description of the observations, calibration, and imaging of the interferometric data. The results were cubes covering the central 6 kpc of NGC 3256 from 2004 to 3599 km s^{-1} with 5.131 km s^{-1} wide channels (using the radio convention) with a synthesized beam full width at half maximum (FWHM) of 0.25 arcsec (~53 pc). Note that the single-dish observations were not combined with the interferometric data (for details refer to Brunetti et al. 2021).

3.2.2 Matching resolution and producing uniform-noise cubes

There have been many studies on the biasing effects of differing resolutions and noise levels on cloud decompositions (Reid et al. 2010; Hughes et al. 2013; Rosolowsky et al. 2021). Theses studies clearly show that mitigating those differences is essential to making robust comparisons between data sets. Since our primary comparison in this work is to the homogenized cloud catalogue from Rosolowsky et al. (2021) we focus on replicating their procedures as closely as possible. The first step was to correct the cleaned CO cube for the primary beam response. We then convolved this cube to have a synthesized beam FWHM of 90 pc.

To simplify the effects that the noise level in the data has on things like completeness we produced uniform-noise CO cubes following the procedure described by Rosolowsky et al. (2021) and outlined here. We first estimated the noise in each pixel in spatial and spectral dimensions of the cleaned cube following the procedure and parameters used by Sun et al. (2018) [1] and Brunetti et al. (2021). We next produced a synthetic-noise cube

---

[1] The PYTHON script for producing noise cubes was obtained from https://github.com/astrojysun/Sun_Astro_Tools/blob/master/sun_astro_tools/spectralcube.py and we used the version at commit f444343.

of normally distributed random deviates with a mean of zero and standard deviation of one. The synthetic-noise cube had the same number of pixels in the x, y, and v dimensions as the CO cube. This synthetic-noise cube was convolved with a Gaussian with FWHM of 90 pc to replicate the spatial correlation of the original data, and the result was standardized to ensure a mean of zero and standard deviation of one. A noise-level target in Kelvins (σ_T) was chosen and a noise-adjustment cube (N^*) was calculated from the synthetic-noise cube (N) and the three-dimensional estimates of the CO-cube noise ($\sigma_{T,0}^2$) using equation 1 from Rosolowsky et al. (2021), reproduced here

$$N^*(x, y, v) = N(x, y, v)\sqrt{\sigma_T^2 - \sigma_{T,0}^2(x, y, v)}. \tag{3.1}$$

Finally, adding the noise-adjustment cube to the 90 pc resolution CO cube produced a cube with higher, but uniform, noise throughout.

While our observations of NGC 3256 were roughly the same sensitivity as those of the PHANGS-ALMA sample in Jy beam^{-1}, the greater distance meant we had about ten times higher noise in the Kelvin scale. Since we could not match the noise level of Rosolowsky et al. (2021) (0.075 K across all galaxies after noise homogenization), we tested several noise-level targets and chose to proceed with a value of 0.9 K as it was the lowest noise value that would not exclude clouds due to reducing the usable field of view (FoV). We also note that the observations of NGC 3256 have channels that are about a factor of two wider than the PHANGS-ALMA observations. We will need to be cautious when comparing NGC 3256 and PHANGS-ALMA data sets due to the different noise levels and channel widths.

3.3 Analysis

3.3.1 Cloud finding

To identify discrete molecular-gas structures in NGC 3256 we used the PYCPROPS[2] PYTHON package (Rosolowsky et al. 2021). This is a translation of the original Interactive Data Language (IDL) CPROPS package (Rosolowsky & Leroy 2006), that takes advantage

---

[2]https://github.com/PhangsTeam/pycprops

of the ASTRODENDRO[3] package for segmenting emission to increase speed as well as other changes to improve robustness for comparative analyses. Rosolowsky et al. (2021) provide a detailed description of the algorithm, which we briefly summarize here. We also provide our parameter choices and how they compare to Rosolowsky et al. (2021).

Local maxima are identified in the cube by ASTRODENDRO and tested for uniqueness from surrounding local maxima. Four metrics are used to reject maxima as unique structures and are 1) a minimum peak above the intensity at which the maximum merges with other maxima, 2) a minimum number of associated pixels, 3) a minimum separation from other maxima in spatial and spectral dimensions, and 4) a minimum change in properties when merged with nearby maxima. With a set of unique local maxima, the remainder of the pixels are assigned to maxima using a seeded compact watershed algorithm.

For the most direct comparison, we use the same criteria for finding maxima as Rosolowsky et al. (2021), which are 1) a minimum contrast between maxima of two times the noise in the cube, 2) a minimum number of pixels that corresponds to one quarter of the beam solid angle, 3) no minimum separation between maxima, and 4) no minimum change in properties from merging maxima. We also set the 'compactness' parameter to the same value as Rosolowsky et al. (2021), such that pixels were assigned to produce the most compact structures by the watershed algorithm. Specific arguments to the *fits2props* function are shown in Table 3.1.

In addition to choosing the same criteria for the closest comparison to PHANGS-ALMA as possible, we also believe these criteria are appropriate for the molecular ISM of a merger. Rosolowsky et al. (2021) describe their choice of criteria as being motivated by the expectation that they would find structures roughly the size of the beam and that they may sometimes be crowded together. We do not have strong prior constraints on the size of structures in NGC 3256 at the scale of our spatial resolution, so we are implicitly adopting the size of giant molecular clouds (GMCs) in the PHANGS-ALMA galaxies as that expected size. As for crowded molecular structures, we expect source crowding to be more prevalent in the merger than in spiral galaxies due to observations of mergers showing enhanced gas fractions (e.g. Ellison et al. 2015; Violino et al. 2018), as well as how the surface density map of NGC 3256 qualitatively appears more filled with

---

[3]http://www.dendrograms.org/

TABLE 3.1: Arguments to *fits2props*.

Argument name	Value
'distance'	44 Mpc[a]
'alphaCO'	$1.38\,M_\odot\,pc^{-2}(K\,km\,s^{-1})^{-1}$
'channelcorr'	0.185
'minpix'	29
'sigdiscont'	0
'compactness'	1000
'specfriends'	0
'friends'	0
'rmstorad'	$\sqrt{2\ln 2}$
'bootstrap'	100

[a] CMB-corrected redshift retrieved from NED, using *WMAP* five-year cosmology with $H_0 = 70.5\,km\,s^{-1}\,Mpc^{-1}$, $\Omega = 1$, and $\Omega_m = 0.27$.

Notes. Used version 1462ff4 of PYCPROPS. Arguments not listed here were left as their default values.

significant emission than many of the PHANGS-ALMA maps presented by Rosolowsky et al. (2021).

Despite attempting to flatten the noise throughout the CO cube to 0.9 K, as described in Section 3.2.2, we still calculated a noise cube from the flattened cube to account for any noise variations still present in the data. The median of all pixels in the noise cube was calculated to be 0.897 K and the minimum contrast between maxima was set to the default of two times this median noise. We also chose to use a signal mask when running PYCPROPS to limit the pixels assigned to maxima to only those with likely significant emission. This signal mask was produced from the flattened-noise cube with the same script used to make the noise cubes. We note that the procedure to generate the noise and signal-mask cubes was not identical to the PHANGS-ALMA pipeline, used by Rosolowsky et al. (2021), but they were designed by Sun et al. (2018) to be used for the same purposes (E. Rosolowsky, private communication).

With all pixels within the signal mask assigned to structures, PYCPROPS estimates integrated intensities, sizes, and line widths for each structure using moments calculated from the pixels of each structure in the emission cube. Moment zero along the spectral axis gives the integrated intensity, moment two along the spatial axes gives the intensity-weighted variances along those directions (the spatial covariance is calculated as well), and moment two along the spectral axis gives the intensity-weighted spectral-line variance (width). Diagonalizing the spatial variance-covariance matrix estimates the major and minor axes of the emission distribution, along with the position angle.

Next, PYCPROPS attempts to remove the effects of finite sensitivity and both spatial and spectral resolution from the properties above. The moments are repeatedly calculated for each cloud, including lower and lower intensity pixels. The sizes as a function of minimum included intensity are fit with a linear function, and the size at an intensity of 0 K is used to estimate the size if there was no noise in the emission cube. The extrapolated major and minor axes are deconvolved from the beam assuming both the cloud and beam are Gaussian. The same approach is used to extrapolate the spectral variance and then the finite channel response is removed, following Leroy et al. (2016) using the channel-to-channel correlation, to produce the final spectral-line width. We separately calculate the channel-to-channel correlation in emission-free channels with the Pearson correlation coefficient calculated from all pixel values between the i and $i + 1$ channels (the 'channelcorr' argument). PYCPROPS calculates integrated intensities

by fitting a quadratic function to the integrated intensities as a function of minimum-included intensity and extrapolating to an intensity of $0\,\mathrm{K}$.

From the extrapolated and deconvolved major and minor axes, PYCPROPS calculates a single radius for each structure as $R = \eta\sqrt{\sigma_{\mathrm{maj,d}}\sigma_{\mathrm{min,d}}}$ (equation 9 from Rosolowsky et al. 2021) where $\sigma_{\mathrm{maj,d}}$ and $\sigma_{\mathrm{min,d}}$ are the major and minor sizes, assumed to be the spatial standard deviations of Gaussian clouds, and η is a factor that depends on the mass distribution within the cloud. η corresponds to the 'rmstorad' argument to *fits2prop* in Table 3.1 and we note we have adopted the same value of $\sqrt{2\ln 2} \approx 1.18$ as used by Rosolowsky et al. (2021), corresponding to a Gaussian density profile and assuming R is the half width at half maximum (HWHM) of the cloud.

Cloud finding was carried out at $90\,\mathrm{pc}$ resolution to simplify comparisons to results from Rosolowsky et al. (2021), and we believe this resolution could also be compared to the $80\,\mathrm{pc}$ resolution pixel-based analysis from Brunetti et al. (2021). However, instead of using cubes regridded to have pixels that were half the beam FWHM, as done by Brunetti et al. (2021), we kept the original pixel grid from the original cleaned cube. This was because we found an unexpected trend of increasing cloud velocity dispersion distributions with decreasing pixel size. Tests where we regridded to various pixel sizes between 2 and ~12 pixels across the beam FWHM seemed to show this was because the boundaries between clouds produced by the watershed algorithm changed with changing pixel size. Visual inspection of the cloud boundaries within a small grouping of clouds with the smallest pixels showed each cloud remained spatially distinct over more velocity channels. In contrast, when larger pixels were used it was more typical for a boundary between two clouds to shift in the spatial dimensions while moving along the spectral dimension. These shifting boundaries resulted in the emission at one spatial location being split between two clouds along the velocity dimension, so that one cloud "wrapped around" a spatially adjacent one in velocity.

3.3.2 Estimating source-finding completeness

Interpretation of the cloud-property distributions measured in NGC 3256 depends on understanding the impact that the noise level, resolution, and choice of cloud-finding algorithm have on the types of clouds we are able to find. To empirically infer the completeness limits on our cloud finding we performed Monte Carlo tests by injecting 1200 synthetic sources with unique properties into our data, one at a time, and attempted

111

to find them with the same steps described in Section 3.3.1. We recorded if the injected sources were found as well as the cloud properties estimated by PYCPROPS.

We chose to inject sources into a subset of channels from the original emission cube that did not contain significant real emission at the high-velocity end of the spectrum. This process simplified the interpretation of the source-finding results since any clouds found would be attributed to the injection of the synthetic source. However, a limitation is that the effect of source blending is not incorporated in our completeness estimate. Blending of clouds likely plays a non-trivial role as most of the emission in NGC 3256 is interconnected through the cube with few instances of isolated "islands" of emission.

It is worth noting that the procedure for finding synthetic clouds was not exactly identical to cloud finding in the real emission. The difference was that instead of recalculating the noise cube after injecting each source, we used the noise cube from the original source finding, trimmed to the same channels as the emission cube. We found that recalculating the noise cube from just that subset of channels resulted in subtle noise structures across the FoV not appearing in the resulting noise cube. These structures appeared to be originating from channels with significant emission, which explained why they were missing in the recalculated synthetic-source noise cube. We chose to preserve the effects that the real emission was having on the noise cube over any that would be introduced when the synthetic sources were injected.

To choose the synthetic source properties, we followed Rosolowsky et al. (2021) by uniformly sampling (in log-space) cloud masses, surface densities, and virial parameters. The distributions of these properties were centred on $2 \times 10^7 \, \mathrm{M_\odot}$, $600 \, \mathrm{M_\odot \, pc^{-2}}$, and 7 with widths of 2.75, 2, and 2.25 dex, respectively. The ranges of synthetic properties were chosen such that the upper limits are about two times the largest values from our cloud catalogue and the lower limits are about half the smallest. Masses, surface densities, and virial parameters were used to calculate three-dimensional Gaussian parameters corresponding to the spatial and velocity standard deviations. These Gaussian parameters were then added, in quadrature, to the beam standard deviation or equivalent Gaussian channel width ($\sigma_{v,\mathrm{chan}}$ in equation 6 from Rosolowsky et al. 2021) to replicate the effects of resolution on the synthetic clouds' true properties. Peak brightness temperatures were then calculated from the mass and "convolved" spatial and spectral sizes still following the three-dimensional Gaussian cloud model of Rosolowsky et al. (2021). Position-position-velocity (PPV) Gaussians were calculated from these parameters and

were added to the emission cube.

For each of the 1200 choices of properties we also chose to separately inject and search for five identical sources that were centred at different right ascension (R.A.), declination (Dec.), and velocity positions. By injecting identical sources at different locations we reduce the stochastic nature of sources being more easily found (missed) if placed on a noise peak (trough). Five positions were uniformly drawn from ranges of R.A., Dec., and velocity, and each choice of cloud properties was injected at those five locations. The R.A. and Dec. ranges were limited to a region whose centre coincides with the centre of the FoV, with a width of 7.25 kpc in R.A. and height of 4.5 kpc in Dec.. Placing the synthetic sources within this region ensured the centres of the largest synthetic clouds were at least two spatial standard deviations from the mapped edges. Similarly, the number of channels that made up the subset of the cube in which synthetic sources were injected was chosen to cover a velocity range corresponding to $\sim 1\sigma_v$ for the largest synthetic cloud velocity width chosen, and the velocity centres were chosen to be ~0.4 velocity standard deviations from the edge channels.

Figures 3.1 and 3.2 summarize the results of our completeness estimation. Each point in Figure 3.1 represents a combination of cloud properties chosen in the mass-surface density-virial parameter space. In Figure 3.2 the results are shown converted to the observable peak brightness temperature-velocity dispersion-2D radius cloud property space (before applying the effects of resolution). The colours of the points indicate how many of the five unique positions were found by PYCPROPS such that regions of high and low completeness are the yellow and purple regions, respectively. The coupled nature of the properties shown in Figure 3.1 is apparent as no single property, or even pair of properties, straightforwardly determines the likelihood a cloud will be found. The observational constraints are clearer in Figure 3.2, primarily in the peak brightness temperature-radius plane, where it is either very likely a cloud is found or not depending on the part of parameter space in which it appears. The boundary between detectable and not-detectable clouds is similarly sharp in the mass-surface density-virial parameter space but is not as clear when the results are projected into the panels of Figure 3.1.
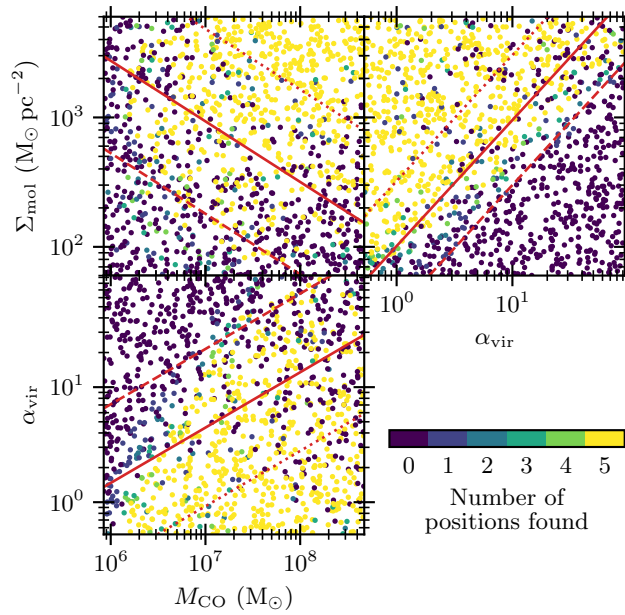
FIGURE 3.1: Results of Monte Carlo completeness tests from injecting synthetic sources with 1200 unique cloud properties chosen from log-uniform distributions of mass, surface density, and virial parameter. Each point represents one choice of cloud properties. Each choice of properties was injected five separate times into the cube at different R.A., Dec., velocity positions and PYCPROPS was run to attempt to find each source. The colours of the points indicate how many of the five different positions had at least one cloud found by PYCPROPS. Red lines indicate the predicted 80 (dotted), 50 (solid), and 20 (dashed) per cent completeness contours after averaging the three-dimensional fit along the axis not shown in each of the panels.
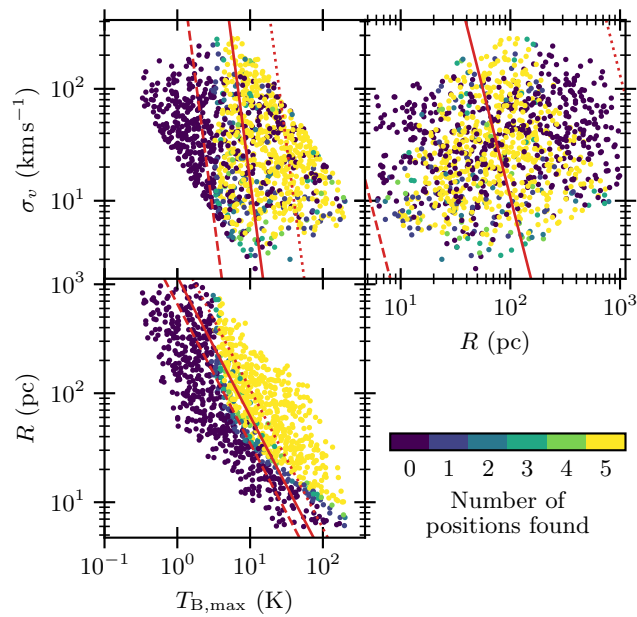
FIGURE 3.2: Same as Figure 3.1 but with the cloud properties converted to the observable properties of peak brightness temperature, velocity dispersion, and radius. To calculate the Gaussian PPV synthetic sources injected for the completeness tests, these values of R and σ_v are first combined with the beam and channel width, respectively, to emulate observational effects. Then the $T_{B,max}$ values are recalculated from these "observed" R and σ_v values, and finally the Gaussian source is calculated from these properties. The velocity dispersion vs. radius panel appears to have completeness-fit trends rising in the opposite direction to the scatter-point colours; see discussion in Section 3.3.2.

Following Rosolowsky et al. (2021), we perform a binomial logistic regression through maximum likelihood estimation to fit the completeness results with the function

$$P(M, \Sigma, \alpha_{\mathrm{vir}}) = \{ \tag{3.2}$$
$$1 + \exp\Big[$$
$$- c_0$$
$$- c_1 \log_{10}\left(\frac{M}{10^6\,\mathrm{M}_\odot}\right)$$
$$- c_2 \log_{10}\left(\frac{\Sigma}{150\,\mathrm{M}_\odot\,\mathrm{pc}^{-2}}\right)$$
$$- c_3 \log_{10}\left(\frac{\alpha_{\mathrm{vir}}}{2}\right)$$
$$\Big]$$
$$\}^{-1}$$

with the best-fitting parameters and 95 per cent confidence intervals (CIs) summarized in Table 3.2. To be clear, the fit is not done to the fraction of positions detected for each choice of cloud properties. Instead, for each combination of mass, surface density, and virial parameter (the independent variables) the dependent variable is either zero to mark no clouds found or one to mark at least one cloud found. With a functional form for the completeness we calculated a grid of completeness predictions over our range of synthetic source properties and plot the 80, 50, and 20 per cent completeness contours in Figures 3.1 and 3.2, averaged along the third axis not shown in each panel.

The velocity dispersion vs. radius panel in Figure 3.2 appears to have completeness-fit trends rising in the opposite direction to the scatter-point colours. However, this is due to different ranges of velocity dispersion and radius being probed by our completeness tests at different values of peak brightness temperature. If the scatter points are limited to a narrow range of temperatures then both the points and the fit trend show generally lower completeness for combined small radii and velocity dispersions and high completeness for large radii with high velocity dispersions. Ultimately, the combination of velocity dispersion and radius alone is not a strong predictor of completeness.

Properties estimated by PYCPROPS for the synthetic sources were compared to the known values used to inject the sources, over ranges similar to the range of properties

TABLE 3.2: Results of logistic regression fit to completeness results. Estimated parameters correspond to those in Equation 3.2.

Parameter	Best-fitting value	Lower 95% CI	Upper 95% CI
c_0	−2.8	−3.1	−2.6
c_1	1.8	1.7	2.0
c_2	3.9	3.7	4.1
c_3	−3.8	−4.0	−3.6

estimated for clouds found in the original CO cube. The ratio of total recovered luminosity to the input luminosity is about 0.7, on average, with a standard deviation near 0.2. When considering found clouds with the largest fraction of the luminosity, the ratio of estimated radii relative to input radii averages also around 0.7 with a standard deviation of about 0.2. The same comparison for velocity dispersions shows a ratio of about 0.8, on average, with a standard deviation around 0.3.

3.3.3 Cloud mass function

Figure 3.3 presents the cloud mass function for NGC 3256 in differential form; Figure 3.4 presents the cumulative mass function. The differential form shows the broad trend of a power law at high masses that turns over at low masses, while the cumulative form reveals some subtle features that are smoothed out in the differential binning. To aid comparison with other studies we fit the cumulative mass function with a double power law of the form

$$N(\geq M) = \begin{cases} AM_{\text{break}}^{(\alpha_{\text{high}}-\alpha_{\text{low}})}M^{(\alpha_{\text{low}}+1)} & M < M_{\text{break}} \\ AM^{(\alpha_{\text{high}}+1)} & M \geq M_{\text{break}} \end{cases} \qquad (3.3)$$

where α_{high} is the high mass power law index, α_{low} is the low mass power law index, M_{break} is the mass at which the power law index changes, and A is a normalization constant (Reid & Wilson 2006b). Best-fitting parameters are shown in Table 3.3. Following Reid & Wilson (2006a) (see their equation 6 and preceding discussion), the weight on each data point in the individual fits was set to $1/N(\geq M_{\text{CO}})^2$.

To incorporate the uncertainty on the mass of each cloud in the uncertainties on the best-fitting parameters we used a similar Monte Carlo approach to Reid & Wilson
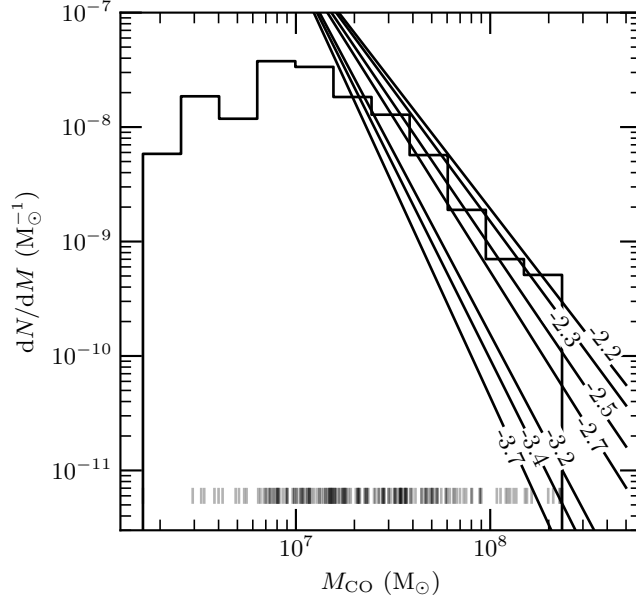
FIGURE 3.3: Differential mass function of clouds from NGC 3256 shown by the "step-wise" curve. Unbinned cloud masses are also shown as vertical lines near the bottom. Only resolved clouds are shown for consistency with the remaining figures and subsequent analysis. Straight lines indicate the range of pure power law indices from the PHANGS-ALMA galaxies fit by Rosolowsky et al. (2021).

TABLE 3.3: Results of fitting the cumulative cloud mass function with a double power law. Best-fitting parameters come from fitting the measured mass function directly with weights of $1/N(\geq M_{CO})^2$. The parameter uncertainties were estimated by fitting 10^5 synthetic mass functions derived from the mass uncertainties and finding the 5th, 16th, 84th, and 95th percentiles of the resulting parameter distributions, P_5 through P_{95}. Estimated parameters correspond to those in Equation 3.3.

Parameter	Best-fitting value	P_5	P_{16}	P_{84}	P_{95}
α_{low}	−1.41	−1.43	−1.42	−1.40	−1.39
α_{high}	−2.75	−2.77	−2.76	−2.70	−2.68
M_{break} (10^7 M$_\odot$)	3.06	2.88	2.95	3.11	3.17
$A/10^{15}$	1.1	0.3	0.5	1.2	1.7
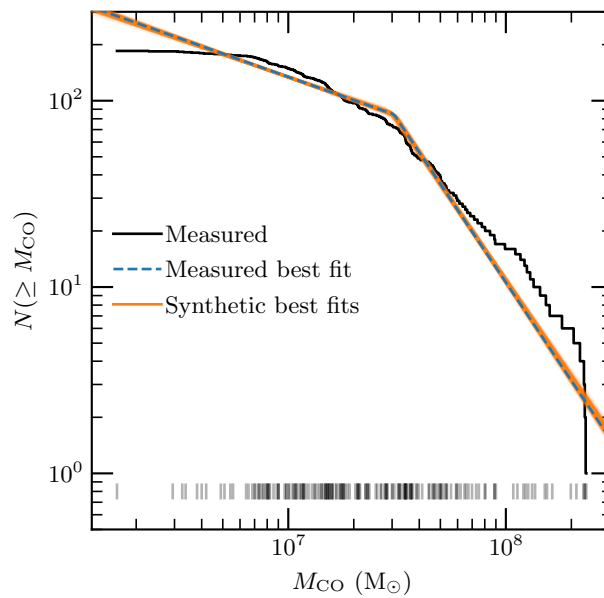
FIGURE 3.4: Cumulative mass function of resolved clouds from NGC 3256 shown by the "step-wise" curve. A one-dimensional view of the cloud masses is also shown as vertical lines near the bottom. The dashed blue curve shows the double power law best fit to the measured cloud masses. Orange curves show 200 of the 10^5 best fits to the synthetic cloud mass functions.

(2006a). We started by generating a new synthetic cloud-mass sample by drawing a random deviate from normal distributions centred at each measured cloud mass and with standard deviations equal to each mass uncertainty. With a new sample of 185 masses we recalculated $N(\geq M_{CO})$ and fit this synthetic mass function in the same way as the measured masses. We carried this out for 10^5 synthetic mass functions and report the inner 68 and 95 per cent of those best-fitting parameters in Table 3.3.

3.4 Results

3.4.1 Two-dimensional model of clouds

Figures 3.5 and 3.6 compare the distributions of cloud properties between NGC 3256 and each PHANGS-ALMA galaxy, estimated directly from the PYCPROPS measurements[4]. Distributions only include clouds that could be both spatially and spectrally deconvolved from the resolution of the observations. Note that all Gaussian kernel density estimator (KDE) bandwidths presented here were automatically calculated using the SCIPY implementation of Scott's Rule (Scott 1992), and that uniform weights were used for all clouds. Most properties are significantly larger in NGC 3256 than most or all of the clouds identified by Rosolowsky et al. (2021) (velocity dispersion, luminosity, CO-estimated mass, and mass surface density). Smaller differences are present for the distributions of on-sky radii, and no significant differences appear in the distributions of estimated cloud eccentricities. Medians and inner 68th percentiles are shown in Figure 3.5 but the means are very similar to the medians for all galaxies and properties. It is worth noting that the uncertainties on the means would appear smaller than the circles such that the mean for nearly every galaxy is significantly different from every other galaxy.

Radii: There is substantial overlap between the two-dimensional radii estimated for clouds in NGC 3256 and the PHANGS-ALMA galaxies, but the distribution for NGC 3256 extends to larger radii than most PHANGS-ALMA galaxies. The cloud-radius distribution in NGC 3256 is very similar to that in NGC 628, both of which exhibit the largest clouds shown here. The sizes of clouds in NGC 3256 are also noteworthy because nearly all radii are significantly larger than the beam HWHM, shown as the dotted lines

---

[4]The electronic table of clouds found by Rosolowsky et al. (2021) was retrieved from the journal website on 2021 July 31.
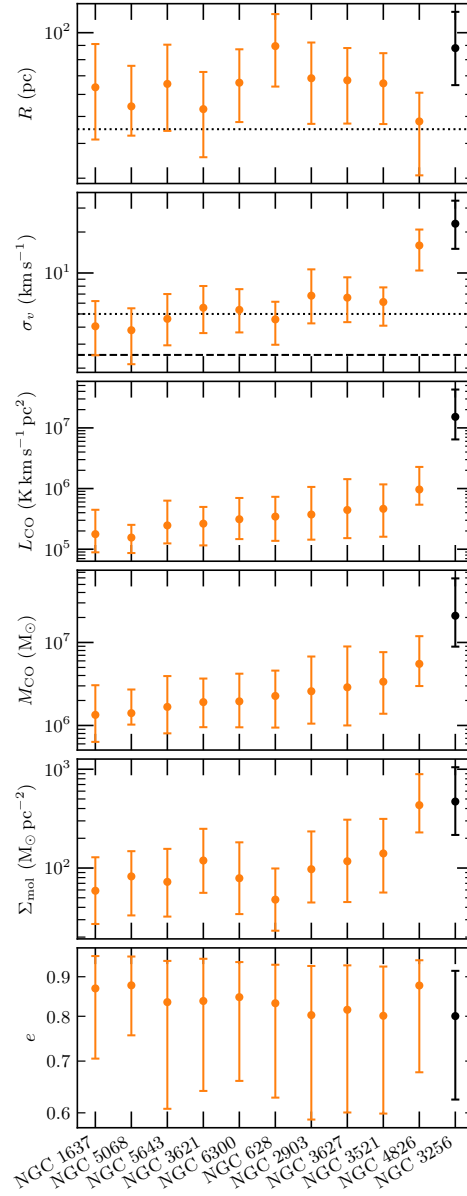
FIGURE 3.5: Resolved cloud-property distributions for NGC 3256 and the PHANGS-ALMA sample. Circles show medians and errorbars show 16th to 84th percentile ranges. Galaxies are sorted from low (left) to high (right) median cloud mass. The beam HWHM of 45 pc is shown with the dotted line in the R panel. Dotted and dashed lines in the σ_v panel show channel widths of $5\,\mathrm{km\,s^{-1}}$ for NGC 3256 and $2.5\,\mathrm{km\,s^{-1}}$ for PHANGS-ALMA, respectively. Mass and surface density in NGC 3256 were calculated with a ultra/luminous infrared galaxy (U/LIRG) α_{CO} (others with the Milky-Way value).
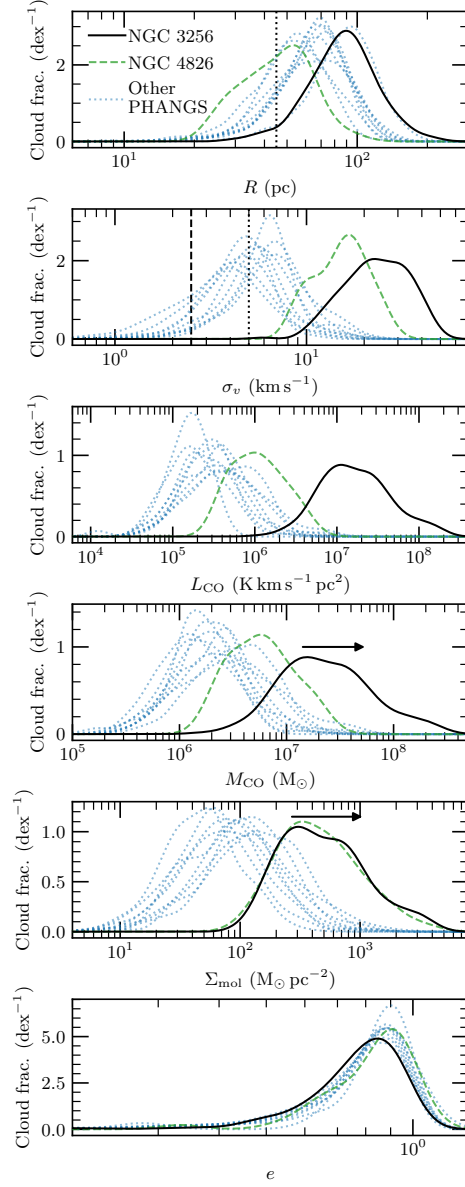
FIGURE 3.6: Same as Figure 3.5 but using Gaussian KDEs, with uniform weights for all clouds, to show the distributions of cloud properties. NGC 4826 is shown as a separate colour as it is usually the most different from the rest of the PHANGS-ALMA sample and often the most similar to NGC 3256. Vertical lines are the same as horizontal lines in Figure 3.5. Again, masses and mass surface densities in NGC 3256 are estimated with a U/LIRG α_{CO} of $1.38\,M_{\odot}\,pc^{-2}(K\,km\,s^{-1})^{-1}$; arrows indicate the direction and amount the distributions would shift if changed to a Milky Way conversion factor.

in Figures 3.5 and 3.6. Source-finding algorithms built on emission segmentation, such as PYCPROPS, typically identify peaks of emission near the size of the beam (Pineda et al. 2009; Hughes et al. 2013; Leroy et al. 2016; Reid et al. 2010; Rosolowsky et al. 2021), which is clearly apparent for many of the clouds in the PHANGS-ALMA galaxies. Given the matched resolution to the PHANGS-ALMA cloud-finding analysis, identical source-finding algorithm, and similar treatment of signal and noise portions of our cube it appears the difference in the sizes of molecular gas structures between NGC 3256 and most PHANGS-ALMA galaxies is real.

Velocity dispersions: Nearly all clouds in NGC 3256 have velocity dispersions well above our spectral resolution of $\approx 5\,\mathrm{km\,s^{-1}}$ (no clouds have velocity dispersions less than the channel width). The same is true for most galaxies from PHANGS-ALMA, except for NGC 5068 where ≈ 27 per cent of resolved clouds are estimated to have dispersions below their spectral resolution of $2.5\,\mathrm{km\,s^{-1}}$. The majority of clouds from NGC 3256 have velocity dispersions significantly larger than clouds from PHANGS-ALMA. However, the upper half of the distribution from NGC 4826 overlaps with the lower half of the distribution from NGC 3256.

Luminosities and masses: Given the larger cloud sizes and velocity dispersions found in NGC 3256, it is not surprising that its distribution of cloud luminosities is also significantly larger than all distributions from PHANGS-ALMA. When the luminosities are converted to estimates of the clouds' total molecular gas masses, the discrepancy between PHANGS-ALMA and NGC 3256 is not as pronounced due to the different CO conversion factors used. We used a single U/LIRG type conversion factor $\alpha_{\mathrm{CO(2-1)}} = 1.38\,\mathrm{M_\odot\,pc^{-2}(K\,km\,s^{-1})^{-1}}$ for NGC 3256 (see Brunetti et al. 2021; for a description of how we decided this was appropriate). For PHANGS-ALMA, a metallicity-dependent conversion factor was used based on radial metallicity gradients from Sánchez et al. (2014, 2019) and described in detail by Sun et al. (2020). All conversion factors for the PHANGS-ALMA clouds were larger than we used for NGC 3256, with a median of $\approx 6.75\,\mathrm{M_\odot\,pc^{-2}(K\,km\,s^{-1})^{-1}}$, such that all PHANGS-ALMA luminosities were scaled up by a larger factor to convert to masses than NGC 3256. Switching our choice of conversion factor to that of the Milky Way would result in the masses increasing by a factor of ~4.5, with the horizontal arrow in Figure 3.6 showing this change.

Mass surface densities: Molecular gas mass surface densities are even more consistent between NGC 3256 and PHANGS-ALMA than the total cloud masses. NGC 4826

has a very similar distribution of mass surface densities to NGC 3256, showing how its combination of small cloud radii but large masses results in surface densities similar to those in an ongoing major merger like NGC 3256. The top half of the distribution in NGC 3256 exceeds values from most of the PHANGS-ALMA clouds, but the lower half of the NGC 3256 distribution overlaps with NGC 3621, 2903, 3627, and 3521. NGC 628, 1637, 5068, 5643, 6300, and 628 on the other hand have most or all of their clouds at mass surface densities below all of the distribution from NGC 3256. These estimates again depend on the choice of H_2-to-CO conversion factor, and we again indicate the degree by which the NGC 3256 distribution would be shifted with the horizontal arrow in Figure 3.6.

Eccentricities: Distributions of estimated cloud eccentricities overlap across all galaxies. Medians are very similar across galaxies and the widths of the distributions are not too different. NGC 3256 has an average width among the sample shown in Figures 3.5 and 3.6. It is worth noting that the eccentricities are concentrated towards the upper limit of $e = 1$ with the median of clouds from all galaxies being $e \approx 0.8$. The median eccentricity corresponds to a ratio of minor to major axes of ≈ 0.6. Also, we note that while it appears the Gaussian KDE for eccentricity in Figure 3.6 shows values exceeding one, this is because the width of the smoothing kernel simply extends beyond the limit and there are no clouds with eccentricities greater than one.

Anderson-Darling tests: We performed two-sample Anderson-Darling tests (Scholz & Stephens 1987) between NGC 3256 and each PHANGS-ALMA galaxy for each of the cloud properties in Figures 3.5 and 3.6. The null hypothesis here is that both the sample from NGC 3256 and the PHANGS-ALMA galaxy come from the same distribution. The radius distributions between NGC 3256 and NGC 628 appear to originate from the same underlying distribution. Eccentricity distributions from NGC 628, 2903, 3521, and 3627 appear consistent with coming from the same underlying distribution as NGC 3256. Lastly, the mass surface density distributions from NGC 3256 and NGC 4826 also appear to come from the same parent distribution. For all other combinations of galaxies and cloud properties, the null hypothesis is rejected at the five per cent level. These properties for the first ten clouds found in NGC 3256 are reported in Tables 3.4 through 3.6, and the full machine readable catalogue will be published with the journal article.

Cloud orientations: Since the distribution of estimated cloud eccentricities is heavily skewed to elliptical clouds, we decided to inspect the spatial distribution of the estimated

124

position angles (PAs) to search for signs of cloud alignment. Given the presence of some spiral structure around the northern nucleus and the edge-on orientation of the southern nucleus, it seemed possible that signatures of cloud alignment may exist due to shear or viewing angle.

We checked the entire sample of resolved clouds across NGC 3256 as well as three regions chosen by eye that appeared to potentially contain clouds more aligned than the entire sample. Kolmogorov-Smirnov (KS) tests indicated that the distributions of PAs in those samples were not distinguishable from a uniform distribution of angles from 0° to 180° (randomly oriented clouds). Likewise, calculating the PA differences between all pairs of clouds within those samples and using KS tests to compare them to a uniform distribution of angles from 0° to 90° could not rule out the differences being uniformly distributed.

However, some small but statistically significant differences from uniform distributions were found when binning the PA differences by the separations between the pairs of clouds. For the entire sample, bins between 2.2 and 3 kpc showed fewer PA differences at 0° than expected from a uniform distribution. An excess of differences between 20° and 50° appeared in the entire sample in bins from 2.3 and 3.2 kpc and in the first two of the by-eye regions in bins of separation from 0.8 and 1.2 kpc. The second and third by-eye regions also showed a slight lack of differences around 55° in bins of separation from 0.3 and 1.2 kpc. These cases from the entire sample have velocity separations of $\pm 200\,\mathrm{km\,s^{-1}}$ while those from the by-eye regions have velocity separations of only about $\pm 100\,\mathrm{km\,s^{-1}}$. It appears the disturbed morphology of this merger system has prevented any strong signal of cloud alignment being present in these data. However, we hope these results will still be useful for future comparisons to other systems or theoretical studies.

3.4.2 Estimating three-dimensional cloud sizes

Additional properties of the clouds can be derived if the three-dimensional structure of the clouds can be approximated. Rosolowsky et al. (2021) make estimates of the three-dimensional cloud radius from the geometric mean in each dimension and with an adjustment made for clouds that exceed the characteristic molecular gas disc thickness. They assume a molecular disc FWHM of 100 pc for all galaxies in their sample. With that disc thickness they estimate the three-dimensional cloud radius, R_{3D}, to be either the

two-dimensional radius, R, if $R \leq \text{FWHM}/2$ or $\sqrt[3]{R^2\text{FWHM}/2}$ otherwise. We calculate R_{3D} for the clouds in NGC 3256 in the same way but we use a different molecular disc FWHM that we estimate empirically for NGC 3256 specifically. We take the median of the scale heights for NGC 3256 from Wilson et al. (2019), H_W, and calculate the median molecular disc $\text{FWHM} = 2\sqrt{\ln 2}H_W \approx 280\,\text{pc}$.

We calculate the three-dimensional radii for all of our clouds, shown in comparison with the PHANGS-ALMA clouds in Figure 3.7. Distributions only include clouds that could be both spatially and spectrally deconvolved from the resolution of the observations. Vertical lines, from left to right, show the beam HWHM, the PHANGS-ALMA molecular disc HWHM of 50 pc, and the disc HWHM for NGC 3256 of $\approx$140 pc. Since the piece-wise form of R_{3D} acts most strongly on the clouds with the largest R, and all of the PHANGS-ALMA clouds are limited by the same disc thickness, the difference between the NGC 3256 and PHANGS-ALMA distributions is more pronounced in R_{3D} than R. Only about seven per cent of the resolved clouds in NGC 3256 have $R \neq R_{3D}$ while this is true for 78 per cent of resolved PHANGS-ALMA clouds. Figure 3.8 compares the distributions of R and R_{3D} from NGC 3256 only.

3.4.3 Three-dimensional model of clouds

With an estimate for the three-dimensional radius of the NGC 3256 clouds we calculated several additional properties and compare the distributions from NGC 3256 to PHANGS-ALMA in Figures 3.9 and 3.10. Distributions only include clouds that could be both spatially and spectrally deconvolved from the resolution of the observations. Again, NGC 3256 clouds appear at or above the upper limits of clouds found by Rosolowsky et al. (2021) for most of these quantities (virial mass, size-linewidth coefficient, and internal pressure). However, the virial parameters for clouds in NGC 3256 are similar to the PHANGS-ALMA galaxies. Also, clouds in NGC 3256 have some of the shortest estimated free-fall times, with only NGC 4826 exhibiting shorter free-fall times.

Virial masses in NGC 3256 are understandably high given the high velocity dispersions and somewhat larger radii. Only the distribution from NGC 4826 significantly overlaps with the distribution from NGC 3256 (seen most clearly in Figure 3.10), with all other PHANGS-ALMA galaxies having much smaller virial masses.
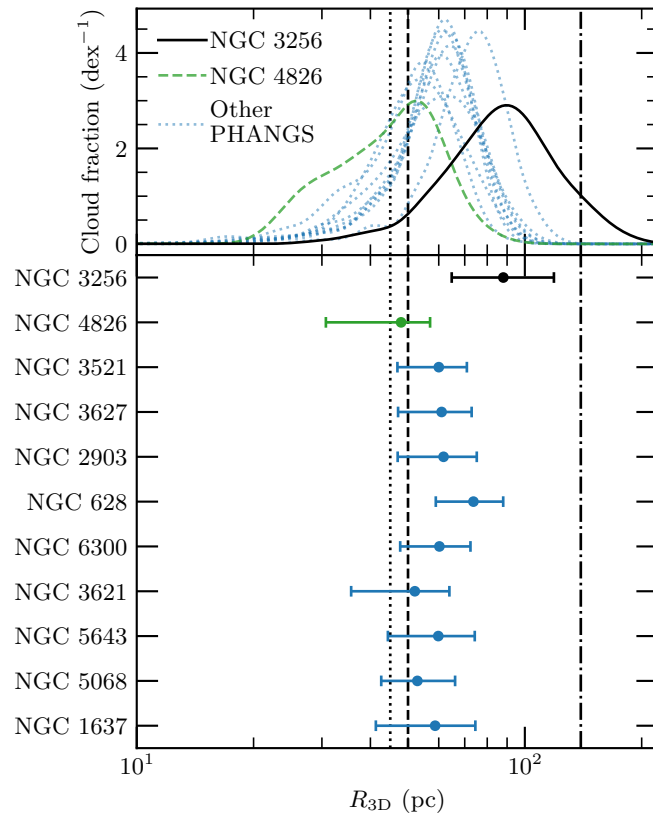
FIGURE 3.7: Distributions of estimated three-dimensional radii in resolved PHANGS-ALMA and NGC 3256 clouds shown with Gaussian KDEs, with uniform weights for all clouds, in the top panel and medians (circles) with inner 68th percentiles in the bottom panel. Galaxies are sorted from low (bottom) to high (top) median cloud mass. Vertical lines are, from left to right, the beam HWHM, molecular disc HWHM of 50 pc used for PHANGS-ALMA galaxies, and disc HWHM of 140 pc for NGC 3256.
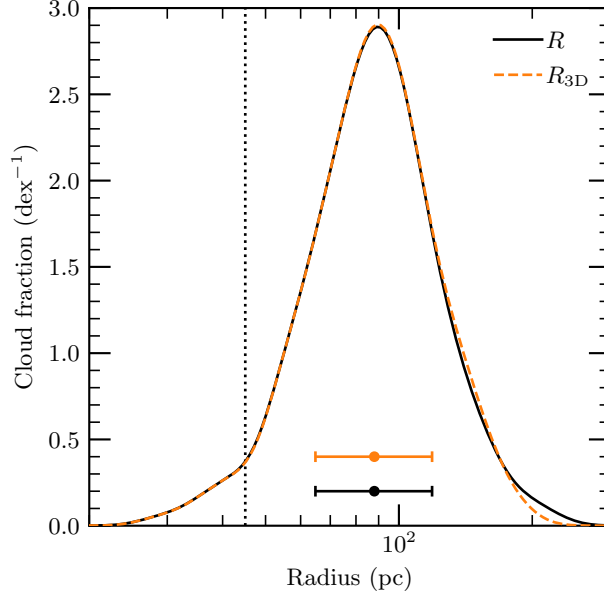
FIGURE 3.8: Gaussian KDEs, with uniform weights for all clouds, and medians with inner 68th percentiles of distributions of R (black solid line) and R_{3D} (orange dashed line) from NGC 3256 resolved clouds.

Virial parameters are also on the larger side in NGC 3256, even exceeding 10, though the lower half of the distribution from NGC 3256 overlaps with the upper halves from most of the PHANGS-ALMA galaxies. In virial parameter NGC 4826 is again very similar to NGC 3256. NGC 5068 has the lowest median virial parameter and some of the lowest values from PHANGS-ALMA so only a small portion of its distribution overlaps with the lowest portion of the distribution from NGC 3256.

In free-fall time, NGC 3256 appears at low values compared to the PHANGS-ALMA sample but the inner 68 per cent of its distribution does overlap with that from many of the PHANGS-ALMA galaxies. NGC 1637 and 628 are least consistent with NGC 3256 with most of their free-fall times above those in NGC 3256. In this comparison, it is really NGC 4826 that stands out with most of its distribution lying below the majority of the distributions from the other galaxies. These short free-fall times in NGC 4826 are driven by the very small cloud radii (compared to all galaxies discussed here) and higher masses (compared to the rest of the PHANGS-ALMA sample).

Interestingly, the distribution of size-linewidth coefficients (σ_v^2/R_{3D}) in NGC 3256 still exceeds most of the distributions from PHANGS-ALMA, showing that the increased
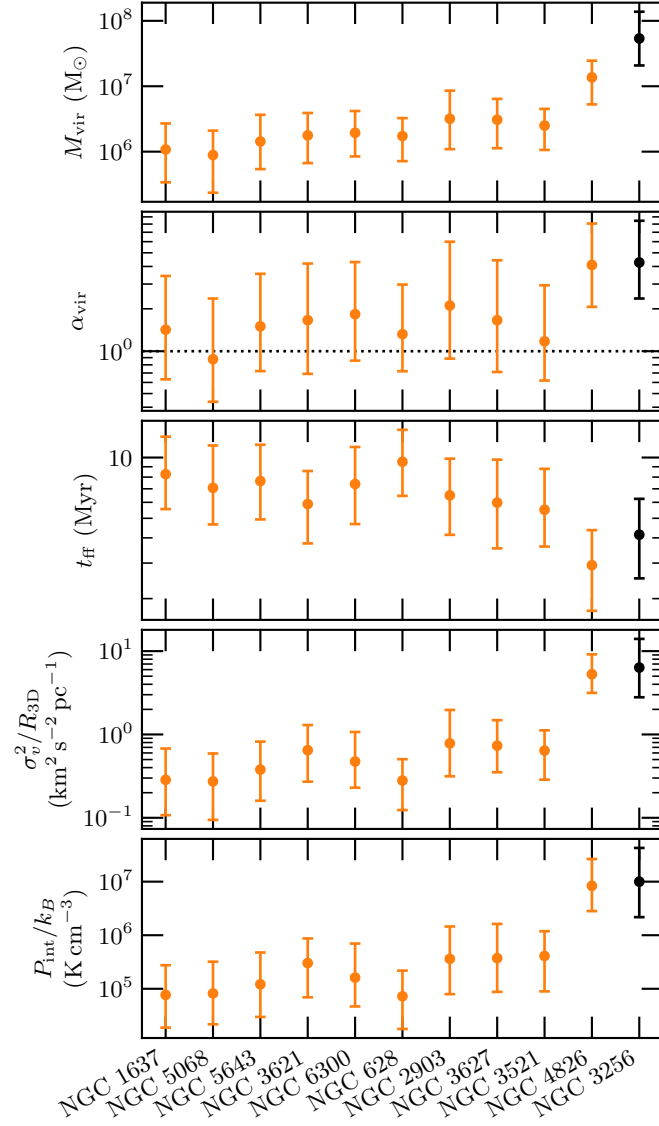
FIGURE 3.9: Same as Figure 3.5 but for properties derived using the three-dimensional radius estimates. Galaxies are sorted from low (left) to high (right) median cloud mass. The horizontal dotted line at $\alpha_{\mathrm{vir}} = 1$ indicates gravitational virial equilibrium. Calculations of the virial parameter, free-fall time, and internal pressures all depend on the choice of conversion factor. A U/LIRG conversion factor of $1.38\,\mathrm{M_\odot\,pc^{-2}(K\,km\,s^{-1})^{-1}}$ is used for NGC 3256. To change to a Milky Way conversion factor would require dividing the virial parameters by ~4.5, dividing the free-fall times by ~2, and multiplying the pressures by ~4.5.
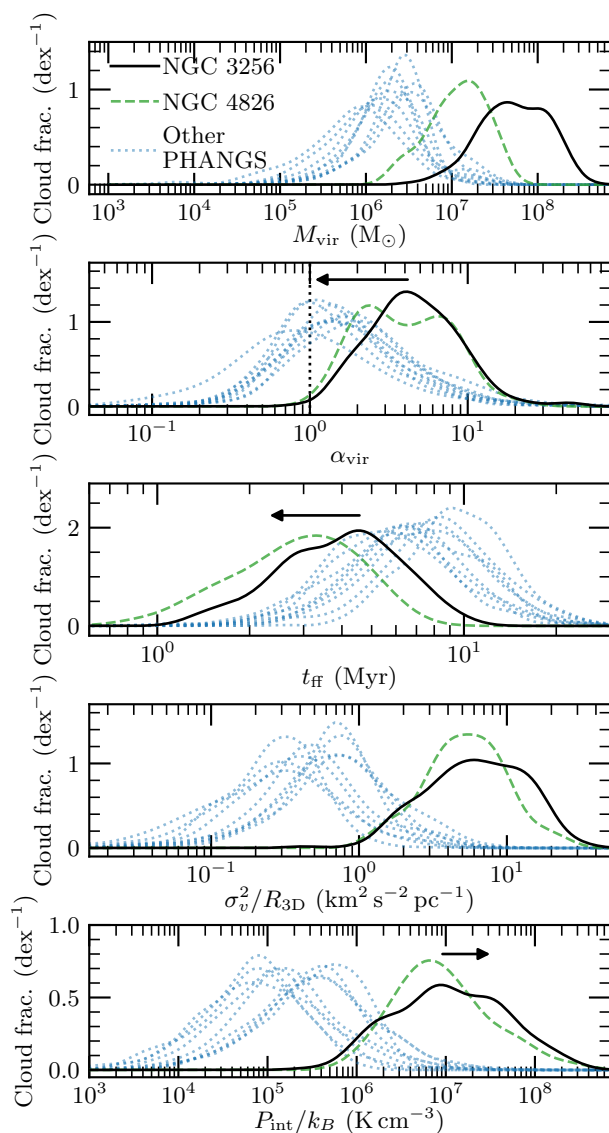
FIGURE 3.10: Same as Figure 3.9 but using Gaussian KDEs, with uniform weights for all clouds, to show the distributions of cloud properties. Horizontal arrows again show how the distributions from NGC 3256 that depend on the conversion factor would change if we switched from the U/LIRG value to the Milky Way value.

cloud sizes in NGC 3256 are outstripped by the larger linewidths. NGC 3256 also has the widest distribution, with a long tail to low coefficients that can be seen overlapping with some of the PHANGS-ALMA clouds in Figure 3.10. Most of the distribution of clouds in NGC 4826 is consistent with the distribution from NGC 3256, but the highest size-linewidth coefficients are still found in NGC 3256.

The comparison of internal pressures is also interesting since NGC 3256 again has the highest pressures shown here. The distributions of size-linewidth coefficient and internal pressure in NGC 3256 show that even though the identified clouds are somewhat larger relative to PHANGS-ALMA, the velocity dispersions are clearly significantly larger than expected for the sizes.

We performed two-sample Anderson-Darling tests for the properties presented in this section to test if the samples from NGC 3256 and each PHANGS-ALMA galaxy appear to be drawn from the same underlying distribution. The null hypothesis that the samples come from the same distribution was rejected at the 5 per cent level for all galaxies and properties except the virial parameters, size-linewidth coefficients, and internal pressures from NGC 4826. These properties for the first ten clouds found in NGC 3256 are reported in Tables 3.4 through 3.6, and the full machine readable catalogue will be published with the journal article.

TABLE 3.4: Example of cloud-property table showing the first ten rows and first seven columns for the clouds found in NGC 3256 with PYCPROPS. The full version, in machine-readable form, will be available in the published journal article.

Number	$T_{\mathrm{B,max}}$ (K)	$(S/N)_{\mathrm{max}}$[a]	N_{pix}	R.A. (°; J2000)	Dec. (°; J2000)	v (km s^{-1})
1	7.9	8.6	17 744	156.9706	−43.9034	2871
2	5.2	5.8	8507	156.9710	−43.9032	2872
3	9.0	10.0	48 931	156.9689	−43.9006	2847
4	6.8	7.9	5548	156.9674	−43.9002	2825
5	8.0	8.2	10 597	156.9616	−43.9016	2720
6	11.7	12.5	18 584	156.9624	−43.9059	2740
7	10.8	11.8	17 945	156.9665	−43.9036	2881
8	7.4	8.5	6381	156.9584	−43.9055	2660
9	6.1	6.2	13 402	156.9594	−43.9067	2723
10	8.7	9.5	6829	156.9643	−43.9039	2788

[a] Maximum signal-to-noise ratio over all signal and noise-cube pixels within each cloud.

TABLE 3.5: Continuation of the example cloud-property table from Table 3.4 for the first ten rows and the next ten columns. The cloud number is repeated as the left-most column for clarity.

No.	σ_v (km s^{-1})	$\delta\sigma_v$[a] (km s^{-1})	$\sigma_{maj,d}$ (pc)	$\delta\sigma_{maj,d}$[a] (pc)	$\sigma_{min,d}$ (pc)	$\delta\sigma_{min,d}$[a] (pc)	P.A. (°)	e	R (pc)	R_{3D}[b] (pc)
1	11.8	0.7	182	8	79	4	124	0.90	142	141
2	16.2	0.9	117	9	43	4	69	0.93	83	83
3	16.7	0.4	378	12	90	4	21	0.97	217	187
4	5.8	0.5	166	14	28	3	161	0.99	81	81
5	14.7	1.3	113	8	64	7	98	0.82	100	100
6	33.4	1.8	92	4	61	4	135	0.75	88	88
7	24.7	1.5	75	4	58	3	83	0.64	78	78
8	15.9	1.9	93	9	92	11	97	0.16	109	109
9	33.9	2.6	72	4	63	3	114	0.50	80	80
10	23.2	1.5	43	4	34	3	96	0.62	45	45

[a] Uncertainties were estimated by PYCPROPS through bootstrapping by resampling, with replacement, the pixels within each cloud 100 times, recalculating the cloud properties for each of those samples of pixels, and calculating the standard error on the mean of each property estimated from those samples. The relative uncertainties produced by PYCPROPS were converted to absolute uncertainties for this table.

[b] Calculated from the R column combined with the molecular disc scale height of NGC 3256 estimated by Wilson et al. (2019). See Section 3.4.2 for details.

TABLE 3.6: Same as Table 3.5 for the last nine columns.

No.	L_{CO} $(10^6 \, \mathrm{K \, km \, s^{-1} \, pc^2})$	δL_{CO}[a] $(10^6 \, \mathrm{K \, km \, s^{-1} \, pc^2})$	M_{CO} $(10^6 \, \mathrm{M_\odot})$	Σ_{mol} $(\mathrm{M_\odot \, pc^{-2}})$	M_{vir}[c] $(10^6 \, \mathrm{M_\odot})$	α_{vir}[c]	t_{ff}[c] (Myr)	P_{int}/k_B[c] $(10^6 \, \mathrm{K \, cm^{-3}})$	P_{comp}[d]
1	15.1	0.8	20.8	165	22.6	2.2	9	0.6	0.40
2	6.0	. . .[b]	8.2	190	25.2	6.1	6	2.2	0.07
3	46.8	1.3	64.5	219	60.7	1.9	7	1.6	0.77
4	5.4	0.5	7.4	180	3.2	0.9	6	0.3	0.60
5	8.8	0.6	12.1	191	25.2	4.2	7	1.5	0.16
6	24.9	1.3	34.3	705	114.0	6.6	3	32.8	0.64
7	28.3	1.2	39.0	1032	55.2	2.8	3	29.9	0.94
8	5.6	0.4	7.7	103	31.8	8.3	10	0.9	0.01
9	11.6	0.5	16.0	404	106.0	13.2	4	21.4	0.11
10	7.6	0.6	10.5	825	28.1	5.4	2	36.4	0.56

[a] Uncertainties were calculated the same as described in Table 3.5.

[b] Blank values indicate the value "Not A Number" was the result from PYCPROPS.

[c] Calculated using the R_{3D} column.

[d] Estimated with the logistic-function fit to the completeness results using the M_{CO}, Σ_{mol}, and α_{vir} columns. See Section 3.3.2 for details.

3.4.4 Correlations between cloud properties

In this section we plot several cloud properties against one another and compare any scaling relations found for clouds in NGC 3256 to PHANGS-ALMA. Generally, clouds found in NGC 3256 appear separated in these parameter spaces from the PHANGS-ALMA population of clouds, but it is important to keep in mind how a change in the adopted conversion factor would change the results shown here. Two additional versions of these scaling-relation plots are shown in Appendix 3.A. One version shows the NGC 3256 clouds coloured by their distance from the nuclei, and the other highlights the NGC 3256 clouds that are most consistent with the PHANGS-ALMA distributions for following clouds between parameter spaces.

Velocity dispersion vs. 3D radius: Figure 3.11 shows cloud velocity dispersions vs. estimated three-dimensional radii. Individual clouds are shown as circles for NGC 3256 and contours enclose 90, 80, 50, 20, and 10 per cent of the PHANGS-ALMA clouds, estimated from a two-dimensional Gaussian KDE. Using the fit to the completeness results and the PYCPROPS-estimated cloud mass, surface density, and virial parameter we predict the completeness for each cloud and show it as the colour of the circle. The directions of trends in completeness are generally the same between NGC 3256 and the PHANGS-ALMA galaxies.

The offset of clouds to higher velocity dispersions and radii in NGC 3256 compared to the total PHANGS-ALMA distribution is again apparent, with the offset being noticeably larger in velocity dispersion. There are some NGC 3256 clouds that overlap with the highest velocity dispersion and radius clouds from PHANGS-ALMA.

The orange-dashed line shows the fit to Milky Way clouds identified by Solomon et al. (1987) which nearly bisects the PHANGS-ALMA cloud distribution through the peak. The centre of the distribution from NGC 3256 appears about half a dex higher in velocity dispersions for their radii than expected when extending the Solomon et al. (1987) fit. Like the size-linewidth coefficients and internal pressures shown in Figures 3.9 and 3.10, this shows how the velocity dispersions measured in clouds within NGC 3256 exceed expectations from spiral galaxies, even given their larger sizes. Given the limited dynamic range covered in this parameter space relative to the scatter of the data, it is not really possible to say if the clouds from NGC 3256 are forming a separate trend that is somehow offset and/or rotated relative to the Milky Way relation. Even despite the large
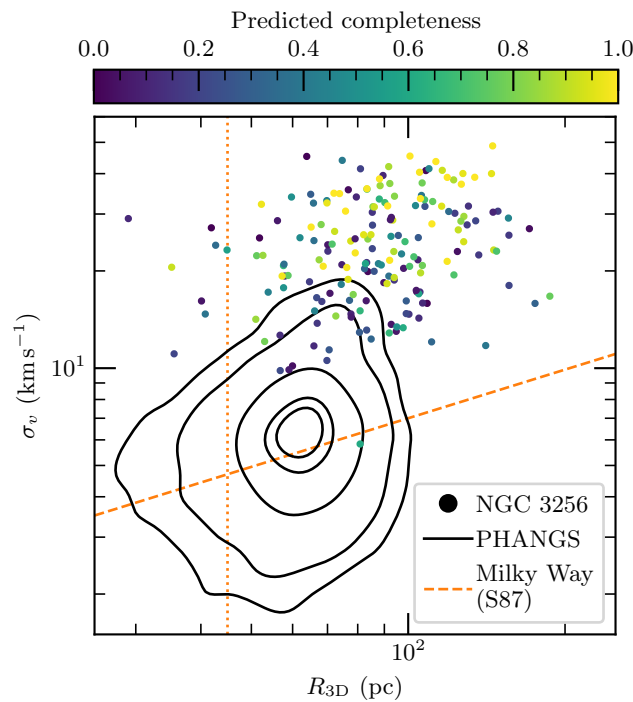
FIGURE 3.11: Velocity dispersion vs. three-dimensional radius. Each circle is a resolved cloud from NGC 3256, and black contours enclose 90, 80, 50, 20, and 10 per cent of the resolved PHANGS-ALMA clouds, determined by a Gaussian KDE with uniform weights for all clouds. Cloud circles from NGC 3256 are coloured by predicted completeness from the fit to the completeness test results and the cloud's estimated mass, surface density, and virial parameter. The orange-dashed line shows the fit to Milky Way clouds from Solomon et al. (1987). The vertical-dotted line shows the beam HWHM of 45 pc.

number of clouds identified by PHANGS-ALMA, their distribution of clouds does not show obvious evidence of a trend. Rosolowsky et al. (2021) do separate galaxies and then bin measurements by radius, which may indicate trends within galaxies that are offset between galaxies, but the significant scatter makes trends within galaxies hard to pin down.

Hughes et al. (2013) caution that trends within the size-linewidth space should be carefully inspected for spatial and spectral resolution origins. Given our matched spatial resolution with PHANGS-ALMA it appears real that the clouds in NGC 3256 are slightly larger. While our spectral resolutions are different by a factor of two, the difference between the median velocity dispersion and the channel width in PHANGS-ALMA is only about two while it is greater than a factor of four in NGC 3256. The higher velocity dispersions in NGC 3256 cannot be explained just by the wider channels.

CO-estimated mass vs. 2D radius: Figure 3.12 shows the CO-estimated masses vs. the two-dimensional estimated radii. Points are the same as Figure 3.11 but the contours now enclose 95, 90, 80, 50, and 20 per cent of the PHANGS-ALMA clouds. Clouds from NGC 3256 again exceed the masses and radii of the PHANGS-ALMA clouds. The orange-dashed lines show trends of constant mass surface density, with the PHANGS-ALMA distribution being centred on $100 \, M_\odot \, pc^{-2}$ and most of the clouds from NGC 3256 centred on $300 \, M_\odot \, pc^{-2}$. The highest-mass clouds in NGC 3256 actually scatter around mass surface densities of $1000 \, M_\odot \, pc^{-2}$, but at the same radii there are also clouds down around $300 \, M_\odot \, pc^{-2}$ making the NGC 3256 trend appear to fork at the largest radii. The sparseness of clouds at these most extreme masses and sizes makes it difficult to tell if this split in the trend is real, especially given the strong dependence of the completeness at constant radius but varying mass. Switching to the Milky Way conversion factor would move the NGC 3256 points up by ~0.6 dex.

Size-linewidth coefficient vs. mass surface density: The size-linewidth coefficients vs. mass surface densities are shown in Figure 3.13, with the same symbols and contours as Figure 3.12. At a given surface density, NGC 3256 clouds typically exhibit higher size-linewidth coefficients than many of the clouds from PHANGS-ALMA, but there is considerable overlap between the distributions at the low surface density end. However, the centre of the distribution from NGC 3256 does appear shifted to both higher size-linewidth coefficients and surface densities than PHANGS-ALMA. The orange-dashed line indicates where clouds in virial equilibrium would lie without considering external
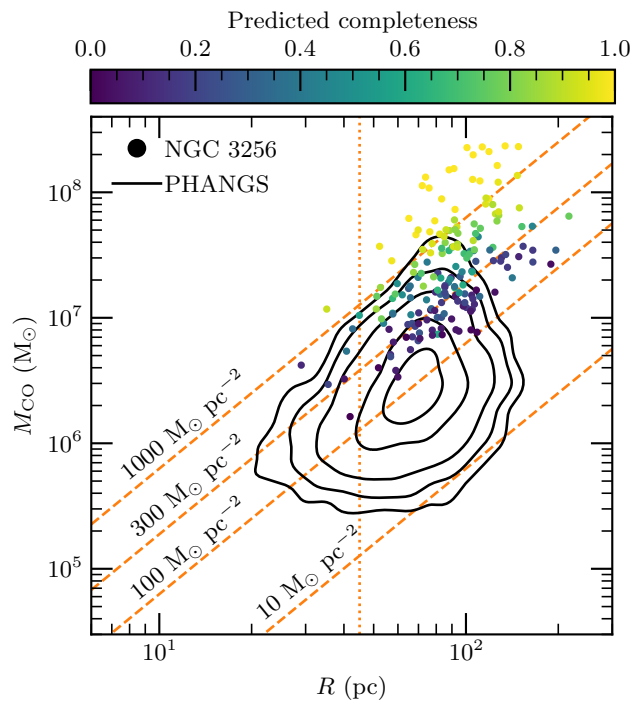
FIGURE 3.12: CO-estimated cloud mass vs. two-dimensional radius. Symbols are the same as in Figure 3.11, but contours here enclose 95, 90, 80, 50, and 20 per cent of the PHANGS-ALMA clouds. The orange-dashed lines indicate constant mass surface densities. The vertical-dotted line shows the beam HWHM of 45 pc. A U/LIRG conversion factor of $1.38\,\mathrm{M_\odot\,pc^{-2}(K\,km\,s^{-1})^{-1}}$ was used to calculate the CO masses in NGC 3256; changing to the Milky Way conversion factor would shift those points up by ~0.6 dex.

pressure confinement, and we can see that both the PHANGS-ALMA and NGC 3256 distributions are offset from that line (with the offset being greater for NGC 3256). The curving dotted-orange lines show where clouds in virial equilibrium within a constant external pressure environment would appear (Field et al. 2011). Generally higher pressures are needed for the NGC 3256 clouds to be kept in virial equilibrium. The external pressure confined picture from Figure 3.13 is important to consider when interpreting the distributions of virial parameters in clouds from NGC 3256 in Figures 3.9 and 3.10, since external pressure is not included in the calculation of α_{vir}. The clouds in NGC 3256 may appear far from virial equilibrium, with far too much kinetic energy; however with sufficient confining pressure they could be held together and even made to collapse. Clouds from NGC 3256 would shift to the right by ~0.6 dex if we switched from the U/LIRG conversion factor used here to the Milky Way factor.

Virial mass vs. CO-estimated mass: The relation between virial mass and CO-estimated mass is shown in Figure 3.14. Along with the higher CO-estimated masses for clouds in NGC 3256 compared to PHANGS-ALMA, the virial masses are also typically higher as well. There is some overlap for the lowest mass clouds from NGC 3256, but the majority of the distribution appears to form a trend that is offset to higher virial mass for a given CO mass. Both PHANGS-ALMA and NGC 3256 clouds are shifted to higher virial masses than expected for virial equilibrium, but the significantly higher velocity dispersions in NGC 3256 mean its clouds are shifted further. NGC 3256 points would move ~0.6 dex to the right if switched to the Milky Way conversion factor.

3.5 Discussion

3.5.1 Cloud properties that differ between NGC 3256 and PHANGS-ALMA

In Figure 3.6, the velocity dispersions of the clouds found in NGC 3256 stand out as most dissimilar to the clouds found in the PHANGS-ALMA sample by Rosolowsky et al. (2021). Figure 5 from Rosolowsky et al. (2021) shows clouds from the centres of galaxies have consistently the highest velocity dispersions, overlapping with the low end of the NGC 3256 distribution. In a pixel-based analysis, Brunetti et al. (2021) found that the centres of PHANGS-ALMA galaxies were most similar to the non-nuclear regions
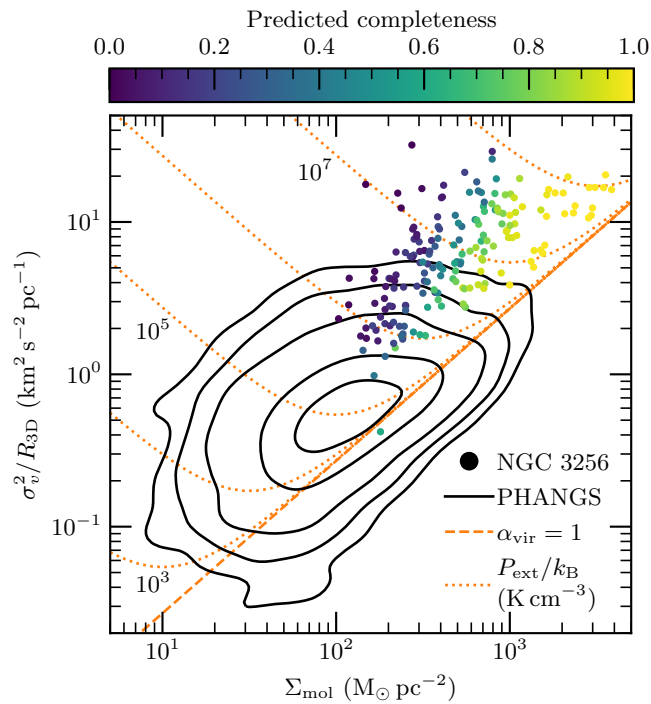
FIGURE 3.13: Size-linewidth coefficient vs. mass surface density. Symbols and contours are the same as in Figure 3.12. The orange-dashed line shows where clouds in virial equilibrium ($\alpha_{\mathrm{vir}} = 1$) would lie with no external pressure. Orange curving-dotted lines show where clouds would lie in virial equilibrium if instead they do experience external pressures, in units of $\mathrm{K\,cm^{-3}}\,k_{\mathrm{B}}^{-1}$. A U/LIRG conversion factor of $1.38\,\mathrm{M_\odot\,pc^{-2}(K\,km\,s^{-1})^{-1}}$ was used to calculate the mass surface densities in NGC 3256, and changing to the Milky Way conversion factor would shift those points to the right by ∼0.6 dex.
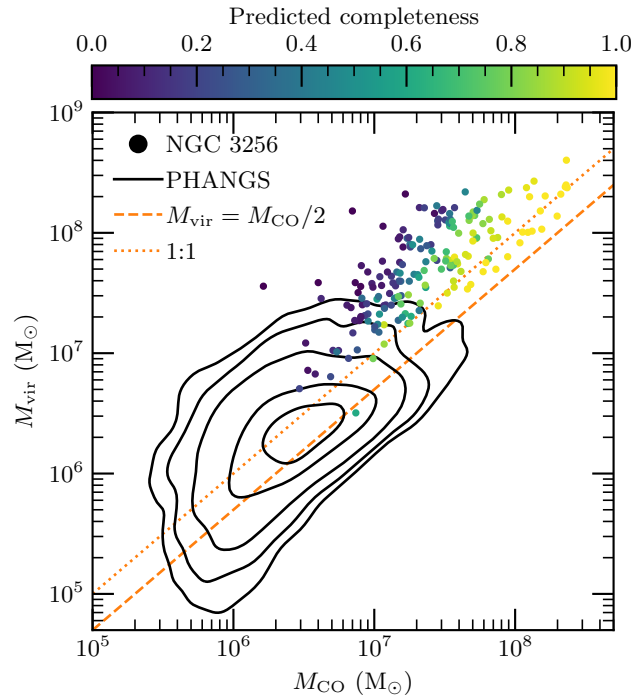
FIGURE 3.14: Virial mass vs. CO-estimated mass. Symbols and contours are the same as in Figure 3.12. The orange-dotted line shows where the virial mass is equal to the luminous mass and the dashed line shows where the virial mass is equal to half the luminous mass. The latter is expected for clouds in virial equilibrium when using two-dimensional Gaussian profiles for clouds, following Rosolowsky et al. (2021). A U/LIRG conversion factor of $1.38\,M_\odot\,pc^{-2}(K\,km\,s^{-1})^{-1}$ was used to calculate the CO masses in NGC 3256, and changing to the Milky Way conversion factor would shift those points to the right by $\sim0.6\,dex$.

in NGC 3256. The magnitude of the velocity dispersions measured across (most) of the PHANGS-ALMA sample are expected to originate primarily from star-formation driven turbulence (Shetty & Ostriker 2012; Krumholz et al. 2018). However, to reach the velocity dispersions measured in NGC 3256, Krumholz et al. (2018) suggest gas flows into the centres of galaxies are also needed. Interaction-induced torques drive the gas to flow towards the centres of merging systems (Noguchi 1988; Mihos & Hernquist 1996; Iono et al. 2004) which, in the model by Krumholz et al. (2018), likely explains the enhanced velocity dispersions in NGC 3256.

Gas flows driven by interactions may also explain the high velocity dispersions in NGC 4826, since it is thought to have undergone a merger in the past that drove most of the ISM into the centre of the galaxy (Braun et al. 1994). To a lesser extent this may also explain NGC 3627 having the third highest median velocity dispersion in the PHANGS-ALMA sample due to its likely interaction with NGC 3628 (Rots 1978; Soida et al. 2001).

It is interesting that most clouds in NGC 3256 appear with significantly larger velocity dispersions and many with slightly larger radii, compared to PHANGS-ALMA clouds. In a similar comparison at matched resolution (~53 pc with 5 km s^{-1} wide channels) and sensitivity, Hughes et al. (2013) found that clouds in the interacting NGC 5194 system have a distribution of radii very similar to NGC 598 and the Large Magellanic Cloud but elevated velocity dispersions. They observed that the regions of NGC 5194 that harboured higher velocity dispersions were also where the star formation rate was lower. They argued that non-transient clouds are likely to be in a state that balances their internal turbulence with external pressure as well as gravity (satisfying $\sigma_v \propto P_{\text{ext}}^{1/4} R^{1/2}$). They concluded that the elevated velocity dispersions at the same cloud sizes were driven more by differing external pressures between galaxies rather than different amounts of star-formation driven internal turbulence. However, in NGC 3256 we find a mix with clouds having both similar and larger radii to PHANGS-ALMA while almost always having larger velocity dispersions. In NGC 3256, enhanced external pressures alone could not simultaneously increase the velocity dispersions and radii, so there are likely additional sources of turbulence in NGC 3256 relative to PHANGS-ALMA.

If the external pressures were similar between NGC 3256 and PHANGS-ALMA and Larson's size-linewidth relation held, then increased velocity dispersions would result in larger radii that lie along the dashed line in Figure 3.11. The vertical offset of the clouds

in NGC 3256 from the dashed line to higher velocity dispersions may then indicate higher external pressures in NGC 3256. Shown another way, clouds from NGC 3256 are offset to higher internal pressures relative to PHANGS-ALMA in Figure 3.10. If the clouds are non-transient objects then the external pressures would have to be higher just to keep them bound, let alone collapse to form stars.

A qualitative comparison of the integrated-intensity maps of NGC 3256 (figure 1 from Brunetti et al. 2021) and NGC 4826 (figure 6 of the supplementary material from Rosolowsky et al. 2021) show both galaxies exhibit smoother emission across the FoV compared to the much more clumpy appearance of the rest of the PHANGS-ALMA maps. However, the FoV mapped in NGC 4826 only reaches a radius of about 1 kpc, the same radius used to define the central regions of PHANGS-ALMA galaxies by Sun et al. (2018). Thus, the clouds from NGC 4826 come solely from the central portion of the galaxy which Brunetti et al. (2021) found was the part of PHANGS-ALMA galaxies most similar to NGC 3256.

The CO luminosities of the clouds in NGC 3256 are also significantly larger than those in the PHANGS-ALMA galaxies, even compared to NGC 4826. Given the high peak-brightness temperatures (likely implying warm molecular gas) and large velocity dispersions in NGC 3256, it is not surprising the CO luminosities are extreme as well (Bolatto et al. 2013). From these luminosities, cloud masses are estimated to be significantly larger than in the PHANGS-ALMA sample, despite using a U/LIRG conversion factor that is between 3 and 11 times smaller than the values used by Rosolowsky et al. (2021). While the largest masses may originate from clouds blended in space and velocity near the nuclei, GMCs of masses $\sim 10^8 \, M_\odot$ are likely necessary to produce star clusters with masses similar to globular-cluster progenitors (Howard et al. 2017). Adamo et al. (2020) measured the upper-mass cutoff to the cluster mass function in NGC 3256 to be among the highest in local galaxies, which is consistent with this prediction of massive clouds resulting in the formation of massive star clusters.

Combining these mass estimates with the fairly similar cloud sizes seen in NGC 3256 and PHANGS-ALMA, we see the molecular gas mass surface densities in NGC 3256 exceed those measured in PHANGS-ALMA galaxies. Kruijssen (2012) predicts a correlation between the mass surface density of molecular gas and the cluster-formation efficiency (CFE). Adamo et al. (2020) find general agreement between this theoretical prediction and their observations of nearby mergers as well as nearby spiral galaxies

from the literature. Specifically, Adamo et al. (2020) estimate an upper limit on the CFE in NGC 3256 that is higher than most local galaxies. If the surface density-CFE correlation prediction by Kruijssen (2012) holds in general, then the extreme molecular gas mass surface densities in NGC 3256 relative to the PHANGS-ALMA galaxies would imply its CFE is high relative to the PHANGS-ALMA sample as well.

Virial mass comparisons are very similar to those for velocity dispersion, given the strong dependence of virial mass on the velocity dispersion of the cloud. Interestingly, the virial-mass distribution from NGC 3256 is one of the widest shown in Figure 3.10, potentially exhibiting blended double peaks. However, when the virial masses are combined with the CO masses to estimate the virial parameter, the resulting distribution from NGC 3256 is one of the narrowest. This implies most of the clouds in NGC 3256 have their mass closely tracking with their size and velocity dispersion so that a relatively narrow range of dynamical states is present, compared to some of the distributions of clouds found in the PHANGS-ALMA galaxies.

NGC 4826 has virial masses more closely approaching NGC 3256 than the other galaxies. The two galaxies have a similar median virial parameter, but NGC 4826 exhibits a different interplay between virial mass and virial parameter. Although there is a hint of a multi-modal distribution of virial masses in NGC 4826 with a peak clearly around $1.5 \times 10^7 \, \mathrm{M_\odot}$ and a possible second peak near $3 \times 10^6 \, \mathrm{M_\odot}$, it is clearly multi-modal in virial parameter. The lower virial-parameter peak in NGC 4826 around 2 could indicate collapsing or marginally unbound gas while the second peak near 7 is either very unbound or requires a significant external-pressure contribution to remain bound. Given the relatively broad distributions of the other virial-parameter distributions from the PHANGS-ALMA galaxies (easiest to see by comparing the heights of the peaks in Figure 3.10), perhaps we are seeing evidence that the ISM in these local spiral galaxies contains gas in a wider variety of dynamical states than the gas in NGC 3256.

The internal turbulent pressures in NGC 3256 not only appear significantly higher than PHANGS-ALMA (except NGC 4826) but also exhibit the widest distribution with about three blended but distinct peaks. If we assume most of the molecular gas is near pressure equilibrium, as Sun et al. (2020) found with a subset of the PHANGS-ALMA sample, then this would imply there is also a wider range of external pressures present in NGC 3256 than the nearby spiral galaxies. For example, the violent rearrangement of gas through the merger process with significant mass inflow towards the nuclei could

enhance external pressures. At the same time, gas in the outskirts of the progenitors of NGC 3256 would likely be less perturbed. It is intriguing that NGC 3256 has one of the narrowest distributions of virial parameter since the merger-driven rearrangement of the gas should also impact the state of the gas within clouds. Processes seem to be conspiring to take the morphological mess that has been made of the gas and make its dynamics conform to a smaller range of states.

3.5.2 Cloud properties similar between NGC 3256 and PHANGS-ALMA

The cloud radii are one of the more consistent quantities between NGC 3256 and PHANGS-ALMA galaxies. Given the matched resolution of all the observations, and the tendency of algorithms like PYCPROPS to identify structures near the resolution limit of the data, it is not too surprising how similar the distributions of radii between these galaxies are. On the other hand, NGC 3256 has the second largest median radius (second to NGC 628) and about 25 per cent of its clouds have radii exceeding most of the rest of the PHANGS-ALMA galaxies. While PYCPROPS attempts to remove observational effects in most of its estimates of cloud properties, our tests of the accuracy of the radius estimates (albeit without the effects of source blending; see Section 3.3.2) indicated it was systematically underestimating the true radii by about 30 per cent, meaning the true distribution of cloud radii may be shifted to even larger values. Rosolowsky et al. (2021) do not find a systematic bias in the estimates of the radii in the PHANGS-ALMA data, so a similar shift to the true cloud radii is not expected for the PHANGS-ALMA distributions. Finally, the higher noise level in our observations of NGC 3256 would likely truncate the full spatial extent of clouds since signal-to-noise (S/N) cuts are used to select significant emission. Better sensitivity would lead to more of the FoV being filled with significant emission, but it is ultimately difficult to predict how this would affect the radius distribution because PYCPROPS would likely still be identifying sources near the beam size.

Dobbs et al. (2011) presented a connection between the aspect ratios of simulated clouds and their estimated degree of binding by self-gravity. They found that their populations of simulated clouds with lower virial parameters appeared more spherical and regularly shaped than populations with elevated virial parameters in simulations with

greater levels of stellar feedback. Additionally, their simulations which best matched observed distributions of virial parameters in Galactic clouds also matched the observed distribution of Galactic cloud aspect ratios (with the majority between 1.5 to 2; e.g. Koda et al. 2006). Dobbs et al. (2011) gave an example of a long-lived and massive cloud which at first appeared fairly filamentary when its virial parameter was highest. At later times, it appeared much more round and its virial parameter had dropped by a factor of about three. In the observations presented here, we argue that the meaningful point to take away is that the molecular structures found in NGC 3256 appear slightly larger than PHANGS-ALMA but the distributions of shapes are indistinguishable. This may indicate that the enhanced velocity dispersions act to "puff up" the clouds in NGC 3256 but on average their dynamical state is similar to clouds in nearby spiral galaxies. It is important to note that at any instant an individual cloud's aspect ratio will not necessarily predict whether it will remain bound, but with a reasonable cloud sample size it may be possible to say if the size scale being probed is the primary size of objects that are bound.

3.5.3 Free-fall times

A noteworthy feature of the free-fall times in NGC 3256 is that they are actually not as different as might be expected given the higher surface densities compared to the PHANGS-ALMA galaxies. Since the free-fall time is proportional to the inverse of the volume density it appears the slightly larger cloud radii overcome some of the differences in mass so that the distributions of free-fall times overlap considerably.

Wilson et al. (2019) estimated free-fall times ranging from 2.5 to 14 Myr in NGC 3256 at 512 pc resolution. Despite our linear resolution being almost 6 times smaller than those observations (or 32 times smaller in area) we estimate free-fall times ranging from 1 to 10 Myr. These similar free-fall times would imply similar average molecular gas volume densities between 90 and 512 pc scales. Fairly constant gas properties across these size scales are also consistent with the minimal changes in pixel-based estimates of molecular gas surface density, velocity dispersion, and peak brightness temperature found by Brunetti et al. (2021) in NGC 3256 at scales from 55 to 120 pc. The interpretation that the molecular ISM in NGC 3256 may be relatively smooth on the scales analysed by Brunetti et al. (2021) may also extend up to scales of about 500 pc, since otherwise differing filling factors would result in measured gas densities changing

with resolution. For example, Sun et al. (2018) find more significant trends in these properties in their pixel-based analysis of PHANGS-ALMA galaxies at scales from 45 to 120 pc, indicative of the clumpy nature of the ISM in nearby spiral galaxies.

The efficiency per free-fall time is set by the ratio of the free-fall time to the gas depletion time ($\epsilon_{\mathrm{ff}} \equiv t_{\mathrm{ff}}/t_{\mathrm{dep}}$ where $t_{\mathrm{dep}} = \Sigma_{\mathrm{mol}}/\Sigma_{\mathrm{SFR}}$). While the distribution of free-fall times in NGC 3256 reaches much smaller values than most of the PHANGS-ALMA clouds from Rosolowsky et al. (2021), about half the distribution overlaps with most of the PHANGS-ALMA free-fall times. It seems that it is the difference in depletion times between NGC 3256 and the PHANGS-ALMA galaxies that plays the dominant role in producing values of ϵ_{ff} that are almost an order of magnitude larger in NGC 3256 compared to spiral discs at 500 pc scales (Wilson et al. 2019).

At 90 pc resolution, it may be that the difference in ϵ_{ff} between U/LIRGs and spirals is not as large as at ~500 pc resolution. Unfortunately, a comparison of ϵ_{ff} between spiral galaxies and starbursts on the scale of GMCs is complicated by the stochastic nature of star formation at those physical scales. However, it does raise the interesting possibility that the degree of stochasticity at a given scale may depend on the absolute level of the star formation rate in the system. For example, if the star formation rate surface density were ten times higher in a particular galaxy, then about ten times the number of star-forming sites per unit area would be present. In this situation, the area that would have to be averaged over to fully sample all star-formation stages to obtain an accurate estimate of ϵ_{ff} could be about ten times smaller than in a galaxy with a lower star formation rate surface density.

3.5.4 Pixel-based vs. cloud-based emission decomposition

Figure 3.15 shows that there is general agreement between the cloud-finding results presented here and the pixel-based decomposition of these observations from Brunetti et al. (2021)[5]. This comparison also highlights the complementary nature of these two analyses. The pixel-based method removes the requirement of choosing what conditions indicate boundaries between clouds, and therefore eliminates differences

---

[5]To avoid lines of sight with multiple spectral components, Brunetti et al. (2021) excluded pixels west of an R.A. of approximately $10^{\mathrm{h}}27^{\mathrm{m}}50^{\mathrm{s}}.3$. Additionally, two polygonal regions around the jet originating from the southern nucleus were excluded based on enhanced velocity dispersions along linear features extending roughly north-south of the southern disc. These regions have not been excluded from the cloud finding analysis.

between analyses originating from the chosen definition of a cloud. However, the pixel-based analysis assumes that each beam is filled with roughly one GMC that is the same size as the beam. The cloud-finding analysis identifies relevant physical size scales so that properties like average surface density, mass, virial parameter, and internal pressure can be calculated using sizes determined from the data. Also, the ability of the cloud-finding decomposition to automatically analyse lines of sight made up of multiple spectral components allows us to potentially extract more information from the observations.

To facilitate comparison with Sun et al. (2018), Brunetti et al. (2021) calculated percentiles and Gaussian KDEs of the pixel-based distributions using mass weighting, while Figures 3.6 through 3.14 in this chapter use uniform weights for all clouds. We compared pixel and cloud distributions with both mass and uniform weighting and found that the comparisons were similar in both cases. Figure 3.15 shows the mass-weighted Gaussian KDEs comparing several properties of the molecular gas estimated with the pixel and cloud-based methods.

Qualitatively, the distributions of mass surface density and internal pressure are quite consistent between the pixel and cloud-based analyses. Distributions of peak brightness temperatures from the cloud identification peak at higher values than those of the pixel-based analysis, and the clouds reach somewhat higher temperatures. Conversely, velocity dispersion, virial parameter, and free-fall time distributions peak at lower values from the cloud measurements than pixels. Velocity-dispersions measured in clouds are more consistent with pixels that exclude the nuclei (i.e. pixels whose distances from both nuclei are >1 kpc after accounting for the inclination angles of the nuclei). The mass-weighted inner 68th percentiles for distributions from both methods are reported in Table 3.7.

The fact that the velocity-dispersion distributions from non-nuclear pixels and clouds are so similar despite the western region not being included in the pixel distributions likely indicates the spectral decomposition of clouds was successful at separating components along the line of sight. The multiple spectral components likely arise from independent gas features along the line of sight (e.g. gas from the two progenitor galaxies overlapping in projection) rather than gas with significantly different turbulent motions. The automatic spectral decomposition provided by cloud finding in the full PPV cube is especially useful in morphologically disturbed merger systems where the line of sight can be very complex due to gas overlapping in projection.

148
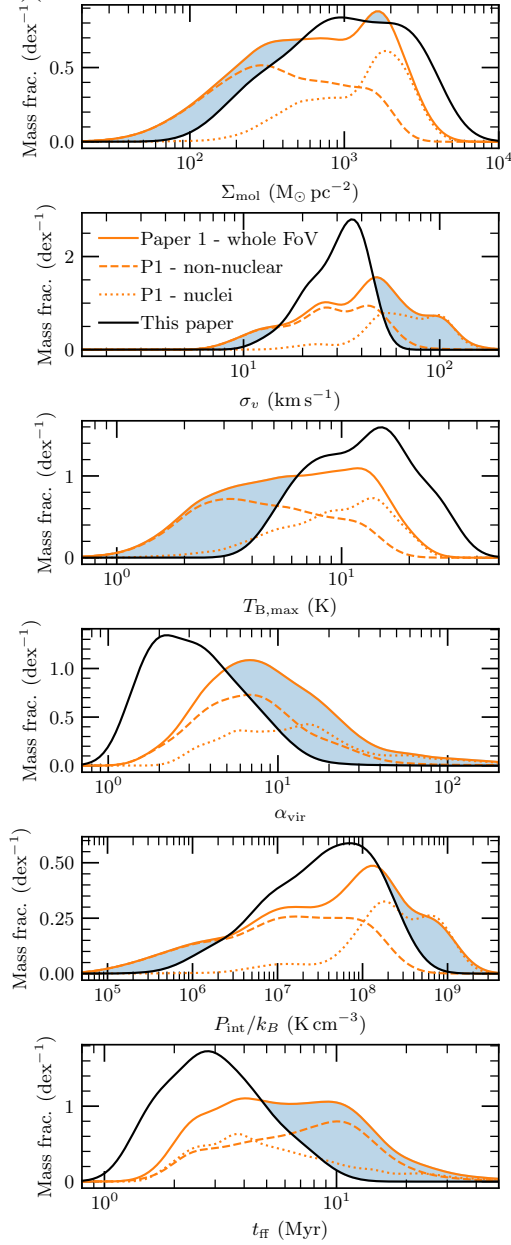
FIGURE 3.15: Mass-weighted Gaussian KDEs comparing molecular gas properties measured in clouds at 90 pc resolution (black) to those measured from the pixel-based analysis from Brunetti et al. (2021) at 120 pc resolution (orange). Distributions from the pixel analysis are also broken into the non-nuclear (dashed) and nuclear (dotted) components. Blue-shaded regions show where the pixel distribution is above that from the clouds, to highlight where the distributions are most different. The same U/LIRG CO-to-H_2 conversion factor was used in both analyses.

TABLE 3.7: Mass-weighted inner 68th percentiles for the cloud and pixel-based distributions.

Quantity (units)	Cloud		Nuclear pixels		Non-nuclear pixels	
	P_{16}	P_{84}	P_{16}	P_{84}	P_{16}	P_{84}
Σ ($M_\odot$ pc^{-2})	360	2800	500	2400	140	1200
σ_v (km s^{-1})	21	40	45	100	14	47
$T_{B,max}$ (K)	7	20	5	16	2	10
α_{vir}	2	6	5	34	3	15
P_{int}/k_B (10^6 K cm^{-3})	7	120	75	720	1	93
t_{ff} (Myr)	2	5	3	11	3	13

While the pixel and cloud distributions are generally consistent, some of the larger differences appear to be related to limitations in the pixel-based analysis. For example, the higher peak brightness temperatures measured in the cloud distribution are mainly found in regions associated with the jet in the cloud analysis that are not in the pixel-based analysis. The higher peak temperatures were excluded from the pixel method to ensure a thorough removal of the jets, but that exclusion could have been too aggressive, allowing the cloud analysis to retain more pixels closer to the jet in spatial projection but spectroscopically distinct from it. Related to the fixed pixel size, the distribution of cloud pressures does not extend as high as estimated in individual pixels. The internal pressure goes as $P_{int} \propto R^{-1}\Sigma_{mol}\sigma_v^2$ where R is the pixel size in the pixel-based analysis (Sun et al. 2018) or the three-dimensional radius for clouds (Rosolowsky et al. 2021). Thus, the constant pixel size appears to overestimate the pressures for the largest clouds more than it underestimates it for the smallest clouds. Although some care needs to be taken when comparing the extrema of distributions between the pixel and cloud-based methods, if the beam size is close to the median cloud radius then the bulk of the molecular gas properties appear to agree between methods.

3.5.5 Mass function comparisons

Previous cloud decomposition

The observations presented here have also been independently imaged and analysed through cloud finding with cpropstoo by Mok et al. (2020). We adjust the masses from Mok et al. (2020) to use our choices of distance to NGC 3256, CO 2–1 to 1–0 ratio, and CO-to-H_2 conversion factor. Unlike in our analysis, Mok et al. (2020) do not convolve the observations, retaining the full resolution they achieve of 95×60 pc (adjusted from their adopted distance to NGC 3256 of 36 Mpc to 44 Mpc used here) or about 70 per cent the beam area of our 90 pc FWHM beam. Their noise root-mean-square (RMS) is also likely different than ours, because of the different beam sizes and the addition of noise in our data cube to homogenize the RMS throughout the cube. Despite these differences, they found 123 GMCs above their completeness limit of 1.5×10^7 $M_\odot$ where we found 120 above that limit (all resolved spatially and spectrally). Their completeness limit mass is also near where our differential and cumulative mass functions both deviate from high-mass power laws. Finally, their maximum cloud mass of 2.9×10^8 $M_\odot$ is about 20 per cent higher than ours.

To characterize the shape of the GMC mass function in NGC 3256, Mok et al. (2020) fit both a Schechter function and pure power law. The Schechter function results do not place strong constraints on the characteristic cutoff mass and there is not a strong preference for either the Schechter or power law functional form. Mok et al. (2020) report a pure power law index of -2.10 (with a 1σ confidence interval from -2.20 to -2.00), which is almost exactly halfway between our low and high mass indices. Since their low-mass cutoff in fitting the mass function is about a factor of two smaller than our break mass, we would expect their slope to be intermediate between our low and high-mass slopes as it tries to account for some of the curvature in the mass distribution.

Simulated and actual observations of star forming regions analysed at different angular resolutions, with beam-area ranges of about a factor of 100, show very little or no variation in the high-mass slope of source mass functions (Reid et al. 2010; Louvet et al. 2021). Therefore, our mass function may be more consistent with that from Mok et al. (2020) than initially anticipated from the differing resolutions, especially considering how close the beam sizes in these analyses of NGC 3256 are. Less easy to predict is the effect of the differing noise levels between the analyses due to the

noise level varying throughout the cube used by Mok et al. (2020). While Reid et al. (2010) generally found that increasing the noise at fixed resolution resulted in somewhat shallower high-mass slopes in their mass-function fits, the noise difference in the two analyses of NGC 3256 depends on where in the cube (position and velocity) each cloud was found. Since most of our clouds were found near the central velocity of the galaxy, where the original noise is worst, it seems reasonable that the resulting mass function slopes would not be wildly different.

PHANGS-ALMA

Rosolowsky et al. (2021) performed similar fits to Mok et al. (2020) on the GMC mass functions from their sample of 10 galaxies, with the addition of attempting to also fit for the effect of completeness causing the turnover at low masses. Four of the mass functions show significant preference for Schechter-function fits over a pure power law (NGC 628, 2903, 3521, and 3627) but the remainder do not show evidence for a preference. The pure power-law indices are shown in Figure 3.3 as the straight lines overplotted on our differential mass function from NGC 3256, ranging from −2.2 to −3.7. Our high-mass slope is near the middle of the distribution of slopes from PHANGS-ALMA. The index fits for NGC 1637 and NGC 6300 are consistent with the high-mass index in NGC 3256. NGC 628, NGC 2903, and NGC 3621 have significantly steeper (more negative) indices than NGC 3256. Conversely, NGC 2903, 3627, 4826, and 5643 all have significantly shallower indices than the high-mass index from NGC 3256, but still steeper than its low-mass index. The confidence interval from NGC 3627 overlaps with the pure power-law fit from Mok et al. (2020), and the interval from NGC 4826 overlaps with both the fit from Mok et al. (2020) and the midpoint between our low and high-mass indices. It is worth noting that robust comparisons over the same mass range cannot be made between NGC 3256 and the PHANGS-ALMA galaxies due to the majority of our most-complete clouds being at or above the most-massive PHANGS-ALMA clouds.

Some of the same limitations are present in our mass function for NGC 3256 as those from PHANGS-ALMA. Blending of sources in crowded regions due to coarse spatial resolution will alter the measured mass function shape from the true underlying distribution, and this effect is likely worse in NGC 3256 than in the galaxies from PHANGS-ALMA. The result of source blending on the shape of a mass function can be difficult to predict since small but not necessarily low-mass clouds will be most blended,

blending is worst for the higher-mass clouds for which crowding is worst, and low-mass clouds can be artificially formed by the combination of neighbouring noise peaks or low-mass clouds below the detection threshold (Reid et al. 2010). Also, Rosolowsky et al. (2021) note that their estimates of mass completeness indicate they are only able to measure the mass-function shape over a relatively small mass range (a factor of about ten between the lowest and highest robust masses). Our rough estimates of where the mass completeness is significantly impacting the shape of the mass function in NGC 3256 are where the differential mass function begins to turn over ($\sim 10^7 \, M_\odot$) and the double power law break mass ($3 \times 10^7 \, M_\odot$). Thus, we are also limited to a mass range of about a factor of ten where our mass function is most robust.

As in our comparison with the mass function derived by Mok et al. (2020), our comparisons to the PHANGS-ALMA mass functions are complicated by different noise levels. If the broad trend of worsening noise causing shallower mass functions (Reid et al. 2010) is at play here then perhaps the true slope for NGC 3256 should be steeper, more like NGC 628, NGC 2903, or NGC 3621. Another way to view this is that the slope in NGC 3256 (with worse noise) from Mok et al. (2020) is shallower than most of the PHANGS-ALMA fits. Again, it is possible more sensitive data will reveal the slope from NGC 3256 to be more in line with PHANGS-ALMA, but the trend of mass function slope with noise is not a strong one. We note that the fitting procedures between Mok et al. (2020) and Rosolowsky et al. (2021) still differ in that Rosolowsky et al. (2021) fits clouds of all masses by including terms to account for low completeness at low mass. Also, the pure power-law fits by Mok et al. (2020) do not include the effects of mass uncertainties while those from Rosolowsky et al. (2021) do.

Again, these comparisons must be made with caution due to the differing noise levels in our observations of NGC 3256 and those from PHANGS-ALMA. A lack of clouds in our sample with similar luminosities or masses to PHANGS-ALMA is predominantly an observational effect, such that the full distribution of clouds in NGC 3256 likely includes low-luminosity or mass PHANGS-ALMA-like clouds. However, it is not straightforward to predict how improved-sensitivity observations of NGC 3256 would alter the cloud distribution. First, we would detect gas down to lower surface densities, which would reveal new low-mass clouds as well as add low surface-density gas to the outer extents of already-identified clouds. Whether this new gas is assigned to new or pre-existing clouds would depend on the S/N contrast of the new emission. The second effect is the tendency

for algorithms like PYCPROPS to break emission up into roughly beam-sized structures, so the spatial extent of the new emission would also impact how it was assigned to new or existing clouds. It is clear, though, that a population of clouds on scales of 90 pc in NGC 3256 is significantly more luminous (and likely also more massive) than in the PHANGS-ALMA galaxies.

3.6 Conclusions

We have performed molecular-cloud identification on observations of the nearest LIRG, NGC 3256, at a matched resolution of 90 pc to the PHANGS-ALMA cloud-finding results presented by Rosolowsky et al. (2021). In these ^{12}CO (2–1) observations we have identified 185 spatially as well as spectrally resolved clouds, which in almost all properties analysed are extreme relative to the PHANGS-ALMA sample. Properties from the first ten clouds in our catalogue are provided in Tables 3.4 through 3.6, and the full machine-readable catalogue will be published with the journal article.

Cloud velocity dispersions, luminosities, CO-estimated masses, mass surface densities, virial masses, virial parameters, size-linewidth coefficients, and internal turbulent pressures are all significantly higher than values measured in clouds in the PHANGS-ALMA galaxies. Radii are slightly larger in NGC 3256 and free-fall times slightly shorter. However, the distribution of cloud eccentricities measured in NGC 3256 is often indistinguishable from those from the PHANGS-ALMA sample. Explanations for the similarities and differences across these properties are discussed in Section 3.5.

Despite differences in how the data were prepared, the mass function of clouds in NGC 3256 measured here appears roughly consistent in power-law slope with the independent analysis of these observations by Mok et al. (2020). Compared to the mass function shapes derived from the PHANGS-ALMA galaxies by Rosolowsky et al. (2021), the high-mass portion from NGC 3256 appears near the middle of their distribution of slopes.

Comparison of this analysis with a pixel-based approach used by Brunetti et al. (2021) shows general agreement between the measured molecular-gas properties. Cloud and pixel-based analyses appear to be complementary in this case as the pixel analysis naturally does not require choosing what defines the edge of a "cloud", while the cloud analysis can include more observed regions because of its ability to decompose multiple

spectral components along the line of sight. Given the median cloud radius found here is 100 pc and the pixel analysis was performed with resolutions of 55, 80, and 120 pc, the pixel analysis was potentially resolving the clouds more than initially expected. The largest differences between the two methods appear to be related to the limitations imposed by the pixel-based analysis assuming clouds of a fixed size or having to avoid spectrally complex lines of sight.

The question of how the molecular-gas depletion times in NGC 3256 compare at cloud scales to previous observations around 500 pc remains open. While the molecular mass surface densities measured here at 90 pc resolution are comparable to those at 512 pc resolution (Wilson et al. 2019), measurements of the star-formation rate surface density at 90 pc resolution are lacking. In principle, continuum measurements from these observations could give an estimate of the star formation rates in the regions of highest molecular gas surface density. However, continuum measurements using solely these ~230 GHz observations will include significant contamination from dust emission. The addition of observations at 100 GHz would help extract just the free-free component for estimating the star-formation rate.

With direct estimates of the free-fall times from this work and depletion times from the continuum, it would be possible to estimate the efficiency per free-fall time (ϵ_{ff}) on cloud scales. While there is significant scatter in ϵ_{ff} at cloud scales in spiral galaxies, due to poorly sampling the various stages of star formation at such small scales, it would be possible to test if this effect is present at the same scales in a starbursting merger. Imaging the CO and continuum observations at a range of resolutions and recalculating free-fall times, depletion times, and ϵ_{ff} would allow us to explore the scatter in these quantities as a function of physical scale.

Finally, observations of CO at even higher-resolution could begin to probe the gas properties within individual clouds. We could first search for signatures of the ISM becoming clumpier than it appeared from 55 to 120 pc. Given the high star-formation rate in NGC 3256 there must eventually be a scale where the molecular gas decouples from its surroundings and would be observed to be collapsing. Observing gas within individual clouds would also likely reveal the small-scale properties that set the self-gravitating threshold density of the gas as well as the fraction of self-gravitating gas.

Acknowledgements

Data Availability

The derived data generated in this research will be shared on reasonable request to the corresponding author.

3.A Appendix: Additional scaling-relation views

Presented here are the same scaling relations shown in Figures 3.11 through 3.14 but highlighting some additional features. In Figure 3.16, the colour of the points from NGC 3256 now indicates the distance from the cloud centre to one of the progenitor nuclei. The distance to both nuclei was calculated for each cloud and the smaller distance is used to colour the points. Positions of the nuclei are the same as used by (Brunetti et al. 2021) and are R.A. $10^{\mathrm{h}}27^{\mathrm{m}}51^{\mathrm{s}}.226$ Dec. $-43°54'13''.942$ for the northern nucleus and R.A. $10^{\mathrm{h}}27^{\mathrm{m}}51^{\mathrm{s}}.221$ Dec. $-43°54'19''.168$ for the southern nucleus. Generally, clouds with the highest values for any of the properties shown are found closer to the nuclei while most of the rest of the distributions are at a mix of distances.

To explore if it is always the same clouds in NGC 3256 that are most consistent with PHANGS-ALMA throughout Figures 3.11 through 3.14, we have highlighted clouds either with the smallest values of velocity dispersion or two-dimensional radius in Figure 3.17. The criteria are easiest to see in the top-left panel as clouds that had $\sigma_v < 17\,\mathrm{km\,s}^{-1}$ are in green and $R < 60\,\mathrm{pc}$ are in red. The colour for clouds that met both of the criteria was chosen by the quantity with the larger per cent difference from the corresponding threshold. For example, a cloud with a velocity dispersion of $2\,\mathrm{km\,s}^{-1}$ and two-dimensional radius of $40\,\mathrm{pc}$ would be shown in green. Broadly, those two groups are typically the clouds that are most similar to PHANGS-ALMA or their trends. This is not true, however, for small-radius clouds in the velocity dispersion vs. radius and size-linewidth coefficient vs. mass surface density plots, where clouds from NGC 3256 appear where there are no clouds from PHANGS-ALMA.
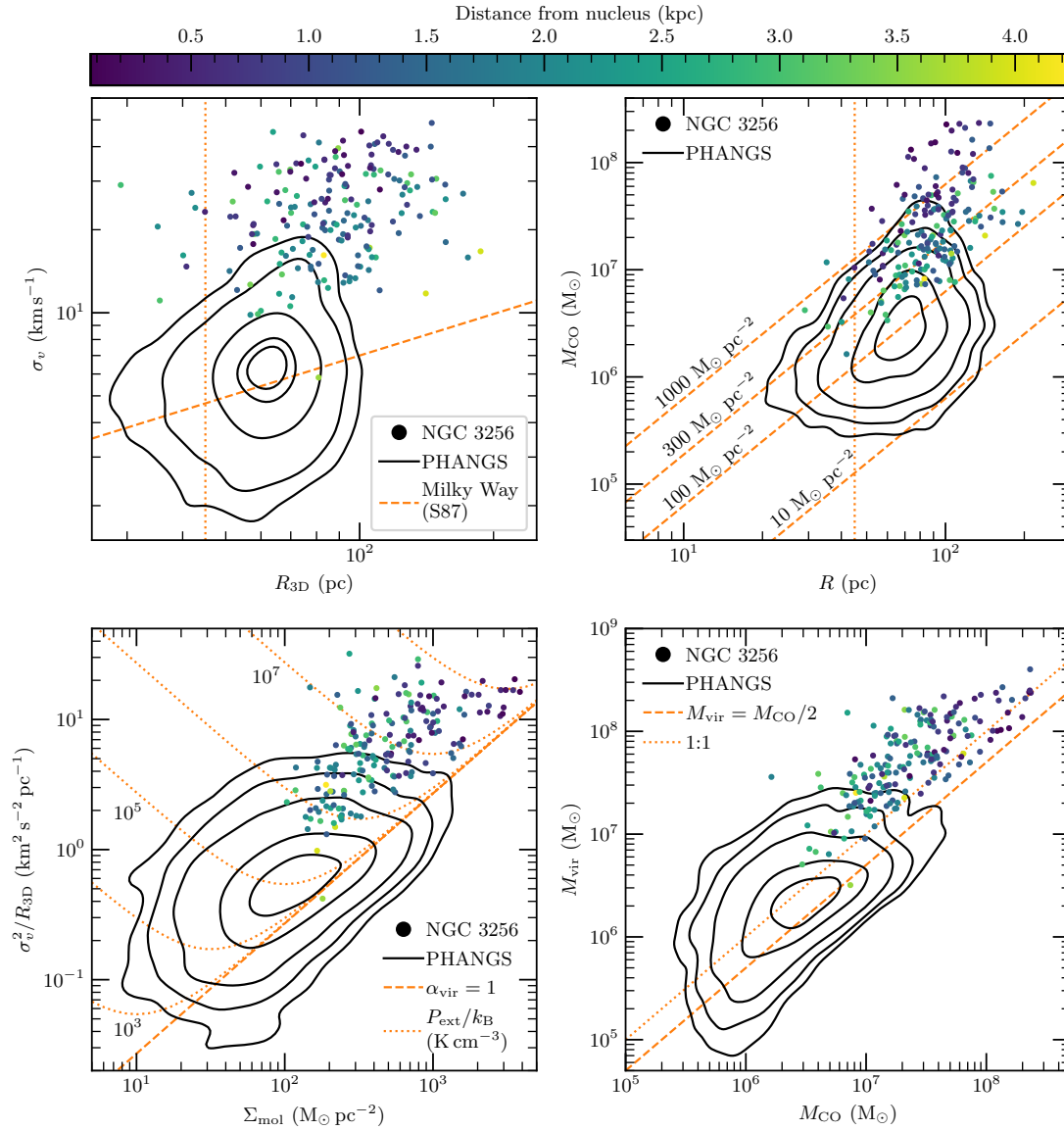
FIGURE 3.16: Same as Figures 3.11 through 3.14 but now the points from the NGC 3256 clouds are coloured by their distance from one of the progenitor nuclei. The smaller of the two distances from the northern or southern nucleus is shown. Positions of the nuclei are R.A. $10^h27^m51^s.226$ Dec. $-43°54'13''.942$ for the northern nucleus and R.A. $10^h27^m51^s.221$ Dec. $-43°54'19''.168$ for the southern nucleus.
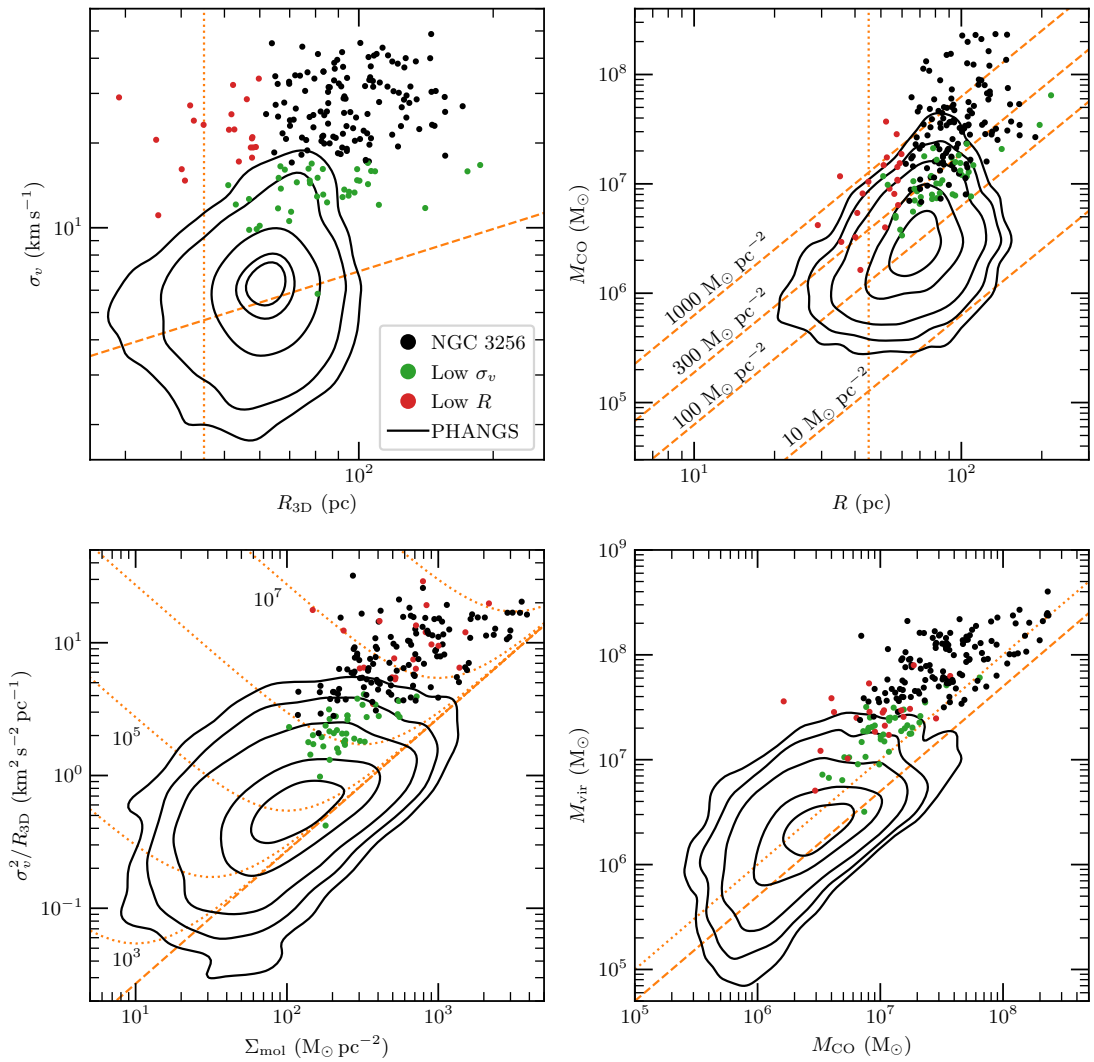
FIGURE 3.17: Same as Figures 3.11 through 3.14 but clouds with small velocity dispersions or radii marked with colour in each panel. Green points show clouds with $\sigma_v < 17\,\mathrm{km\,s^{-1}}$ and red points show clouds with $R < 60\,\mathrm{pc}$. If a cloud met both of the criteria then the colour was chosen based on which property has the largest per cent difference from the threshold.

Bibliography

Adamo A., et al., 2020, MNRAS, 499, 3267

Astropy Collaboration et al., 2013, A&A, 558, A33

Astropy Collaboration et al., 2018, AJ, 156, 123

Benincasa S. M., Wadsley J., Couchman H. M. P., Keller B. W., 2016, MNRAS, 462, 3053

Bolatto A. D., Wolfire M., Leroy A. K., 2013, ARA&A, 51, 207

Braun R., Walterbos R. A. M., Kennicutt Robert C. J., Tacconi L. J., 1994, ApJ, 420, 558

Brunetti N., Wilson C. D., Sliwa K., Schinnerer E., Aalto S., Peck A. B., 2021, MNRAS, 500, 4730

Comrie A., et al., 2021, CARTA: The Cube Analysis and Rendering Tool for Astronomy, doi:10.5281/zenodo.4905459

Daddi E., et al., 2010, ApJ, 714, L118

Dobbs C. L., Burkert A., Pringle J. E., 2011, MNRAS, 413, 2935

Ellison S. L., Patton D. R., Simard L., McConnachie A. W., 2008, AJ, 135, 1877

Ellison S. L., Mendel J. T., Patton D. R., Scudder J. M., 2013, MNRAS, 435, 3627

Ellison S. L., Fertig D., Rosenberg J. L., Nair P., Simard L., Torrey P., Patton D. R., 2015, MNRAS, 448, 221

Elmegreen B. G., 2011, ApJ, 737, 10

Elmegreen D. M., Elmegreen B. G., Marcus M. T., Shahinyan K., Yau A., Petersen M., 2009, ApJ, 701, 306

Elmegreen D. M., et al., 2021, ApJ, 908, 121

Field G. B., Blackman E. G., Keto E. R., 2011, MNRAS, 416, 710

Hani M. H., Gosain H., Ellison S. L., Patton D. R., Torrey P., 2020, MNRAS, 493, 3716

Harada N., Sakamoto K., Martín S., Aalto S., Aladro R., Sliwa K., 2018, ApJ, 855, 49

Herrero-Illana R., et al., 2019, A&A, 628, A71

Hollenbach D. J., Tielens A. G. G. M., 1999, Reviews of Modern Physics, 71, 173

Hopkins P. F., Quataert E., Murray N., 2012, MNRAS, 421, 3488

Howard C. S., Pudritz R. E., Harris W. E., 2017, MNRAS, 470, 3346

Hughes A., et al., 2013, ApJ, 779, 44

Hunter J. D., 2007, Computing in Science & Engineering, 9, 90

Iono D., Ho P. T. P., Yun M. S., Matsushita S., Peck A. B., Sakamoto K., 2004, ApJ, 616, L63

Kennicutt R. C., de los Reyes M. A. C., 2021, ApJ, 908, 61

Kluyver T., et al., 2016, in Loizides F., Scmidt B., eds, 20th International Conference on Electronic Publishing. Positioning and Power in Academic Publishing: Players, Agents and Agendas. IOS Press, Netherlands, p. 87

Koda J., Sawada T., Hasegawa T., Scoville N. Z., 2006, ApJ, 638, 191

Kruijssen J. M. D., 2012, MNRAS, 426, 3008

Krumholz M. R., Matzner C. D., McKee C. F., 2006, ApJ, 653, 361

Krumholz M. R., Burkhart B., Forbes J. C., Crocker R. M., 2018, MNRAS, 477, 2716

Larson R. B., Tinsley B. M., 1978, ApJ, 219, 46

Larson K. L., et al., 2020, ApJ, 888, 92

Leroy A. K., et al., 2016, ApJ, 831, 16

Louvet F., Hennebelle P., Men'shchikov A., Didelon P., Ntormousi E., Motte F., 2021, A&A, 653, A157

Madau P., Dickinson M., 2014, ARA&A, 52, 415

McKee C. F., 1989, ApJ, 345, 782

McKee C. F., Ostriker J. P., 1977, ApJ, 218, 148

McKinney W., 2010, in Stéfan van der Walt Jarrod Millman eds, Python in Science Conf. Ser.. Available at: http://conference.scipy.org/proceedings/scipy2010/, p. 56

Mihos J. C., Hernquist L., 1996, ApJ, 464, 641

Mok A., Chandar R., Fall S. M., 2020, ApJ, 893, 135

Narayan C. A., Jog C. J., 2002, A&A, 394, 89

Noguchi M., 1988, A&A, 203, 259

Ochsenbein F., Bauer P., Marcout J., 2000, A&AS, 143, 23

Ohyama Y., Terashima Y., Sakamoto K., 2015, ApJ, 805, 162

Ostriker E. C., Shetty R., 2011, ApJ, 731, 41

Pedregosa F., et al., 2011, Journal of Machine Learning Research, 12, 2825

Pineda J. E., Rosolowsky E. W., Goodman A. A., 2009, ApJ, 699, L134

Reid M. A., Wilson C. D., 2006a, ApJ, 644, 990

Reid M. A., Wilson C. D., 2006b, ApJ, 650, 970

Reid M. A., Wadsley J., Petitclerc N., Sills A., 2010, ApJ, 719, 561

Romano M., et al., 2021, A&A, 653, A111

Rosolowsky E., Leroy A., 2006, PASP, 118, 590

Rosolowsky E., et al., 2021, MNRAS, 502, 1218

Rots A. H., 1978, AJ, 83, 219

Sakamoto K., Aalto S., Combes F., Evans A., Peck A., 2014, ApJ, 797, 90

Sánchez S. F., et al., 2014, A&A, 563, A49

Sánchez S. F., et al., 2019, MNRAS, 484, 3042

Scholz F. W., Stephens M. A., 1987, Journal of the American Statistical Association, 82, 918

Scott D. W., 1992, Multivariate Density Estimation: Theory, Practice, and Visualization. Wiley Series in Probability and Statistics, John Wiley & Sons, New York

Seabold S., Perktold J., 2010, in van der Walt S., Millman J., eds, Python in Science Conf. Ser.. Available at: http://conference.scipy.org/proceedings/scipy2010/

Shetty R., Ostriker E. C., 2012, ApJ, 754, 2

Soida M., Urbanik M., Beck R., Wielebinski R., Balkowski C., 2001, A&A, 378, 40

Solomon P. M., Rivolo A. R., Barrett J., Yahil A., 1987, ApJ, 319, 730

Stierwalt S., et al., 2013, ApJS, 206, 1

Sun J., et al., 2018, ApJ, 860, 172

Sun J., et al., 2020, ApJ, 892, 148

Tacconi L. J., Genzel R., Sternberg A., 2020, ARA&A, 58, 157

Tielens A. G. G. M., Hollenbach D., 1985, ApJ, 291, 722

Violino G., Ellison S. L., Sargent M., Coppin K. E. K., Scudder J. M., Mendel T. J., Saintonge A., 2018, MNRAS, 476, 2591

Virtanen P., et al., 2020, Nature Methods, 17, 261

van der Walt S., Colbert S. C., Varoquaux G., 2011, Computing in Science & Engineering, 13, 22

Wenger M., et al., 2000, A&AS, 143, 9

Wilson C. D., Elmegreen B. G., Bemis A., Brunetti N., 2019, ApJ, 882, 5

Yamashita T., et al., 2017, ApJ, 844, 96

Zaragoza-Cardiel J., Smith B. J., Rosado M., Beckman J. E., Bitsakis T., Camps-Fariña
A., Font J., Cox I. S., 2018, ApJS, 234, 35

4 | ALMA observations of the Antennae: effects of merger stage on cloud-scale molecular gas

Brunetti N., Wilson C. D., 2022, *in preparation*

Department of Physics and Astronomy, McMaster University, Hamilton, ON L8S 4M1, Canada

Abstract

We present ALMA observations of the central 9 kpc of the Antennae merger at 55 pc resolution in CO (2–1). Maps of molecular-gas mass surface density, velocity dispersion, peak brightness temperature, virial parameter, and internal turbulent pressure are derived from these data at a range of spatial resolutions. A pixel-based analysis is used to compare, at matched spatial resolution, the gas properties in the Antennae to those in nearby spiral galaxies from the PHANGS-ALMA survey and the nearest LIRG NGC 3256. The molecular gas in the Antennae exhibits some of the highest surface densities, velocity dispersions, peak brightness temperatures, and turbulent pressures compared to PHANGS-ALMA galaxies. Only the centres of the more massive nearby spirals have similar gas properties to those in the Antennae. However, the virial parameters in the Antennae are consistent with many of the PHANGS-ALMA galaxies. NGC 3256 has higher nuclear velocity dispersions as well as system-wide peak brightness temperatures and virial parameters than the Antennae, potentially as a result of the different stages at which the two mergers are observed. We find general consistency between gas properties estimated from these CO (2–1) observations and previous CO (3–2) data, but small differences motivate the need for future CO (3–2) observations that measure emission on all spatial scales as our CO (2–1) observations do to enable a better-matched comparison of the two CO transitions.

167

4.1   Introduction

Through the spatial correlation of molecular gas and recent star formation seen in galaxies throughout the universe, we know that stars form from molecular gas. The efficiency with which molecular gas is converted into stars has been observed to be fairly similar across many nearby spiral galaxies (Utomo et al. 2018). However, estimates for the star-formation efficiency (SFE) in the most actively star-forming galaxies deviate from what is observed in more quiescent spiral galaxies (e.g. Kennicutt & de los Reyes 2021). Comparable observations of these different star-formation regimes will allow us to understand what causes this SFE difference.

Kiloparsec-scale observations of both spiral galaxies and starbursts have revealed the difference in SFEs but not the cause (de los Reyes & Kennicutt 2019; Wilson et al. 2019; Kennicutt & de los Reyes 2021), so observations at smaller scales are the natural next step. Many nearby spiral galaxies have been observed in molecular gas at scales around 100 pc and even smaller, but the relative rarity of and distance to starbursting galaxies has precluded similar observations. Brunetti et al. (2021) and Chapter 3 present the highest spatial-resolution observations of the luminous infrared galaxy (LIRG) and actively star-forming merger NGC 3256 at physical scales around 100 pc. Analysis with matched-resolution and methods to the Physics at High Angular resolution in Nearby GalaxieS with ALMA (PHANGS-ALMA) homogeneous survey of 70 nearby spiral galaxies (Sun et al. 2018, 2020; Rosolowsky et al. 2021) reveals the molecular gas in the merger reaches some of the highest mass surface densities, velocity dispersions, peak brightness temperatures, virial parameters, and internal turbulent pressures. However, a single merger that happens to be the nearest LIRG cannot be expected to be representative of all merging and starbursting systems. To extend the sample of mergers, we have observed NGC 4038/9 (Arp 244, "the Antennae") at the same spatial resolution to add it to these comparisons of molecular-gas properties.

At a distance of 22 Mpc (Schweizer et al. 2008), NGC 4038/9 is the nearest gas-rich major merger, with $\sim 2 \times 10^{10}\,M_{\odot}$ of molecular gas in the central region (Stanford et al. 1990; Wilson et al. 2000; Gao et al. 2001; Wilson et al. 2003; Brandl et al. 2009; Schirm et al. 2014). Based on a significant body of numerical work on reproducing the morphology and kinematics of the interaction, the system is currently either just before or just after the second pericentre passage (e.g. Toomre & Toomre 1972; Barnes 1988;

Mihos et al. 1993; Karl et al. 2010; Privon et al. 2013; Renaud et al. 2015). Its central region hosts the two progenitor nuclei, still separated by about 7 kpc. Given these orbital details, NGC 4038/9 is likely at an earlier merger stage than NGC 3256, and so offers a chance to probe how the molecular-gas properties depend on the time in the merging process.

The total star-formation rate (SFR) is between $11\,\mathrm{M}_\odot\,\mathrm{yr}^{-1}$ (separately estimated from far ultra violet probing ~1 to 100 Myr and 24 μm probing ~1 to 400 Myr) and $20\,\mathrm{M}_\odot\,\mathrm{yr}^{-1}$ (from Hα probing ~1 to 10 Myr; Chandar et al. 2017). Separated from the nuclei is the starbursting "overlap region" which alone exhibits a SFR of about $4\,\mathrm{M}_\odot\,\mathrm{yr}^{-1}$ over the last $\lesssim$100 Myr from mid through far infrared observations (Brandl et al. 2009; Klaas et al. 2010; Bemis & Wilson 2019). The remainder of the central part of the merger has a SFR totaling about $2.6\,\mathrm{M}_\odot\,\mathrm{yr}^{-1}$ (Bemis & Wilson 2019).

NGC 4038/9 also hosts plentiful young massive star clusters, with an estimated population of at least 10^4 clusters (Whitmore et al. 2010; Chandar et al. 2015; Mok et al. 2020). Several stellar populations of different ages have also been identified throughout the system with a young starburst population in the overlap region (~3 to 10 Myr; Mengel et al. 2001, 2005; Whitmore et al. 2010) and older post-starburst populations in the nuclei (~65 Myr; Mengel et al. 2001). Exploring the molecular-gas properties of this system will provide the details on what conditions are necessary to form the most massive star clusters. Our understanding of nearby mergers like NGC 4038/9 should also fill in the small-scale information on how star and cluster formation occurred at high redshift, where mergers were much more common (e.g. Romano et al. 2021) and when the progenitors of globular clusters had to form.

In this chapter we present giant molecular cloud (GMC)-scale Atacama Large Millimeter/Submillimeter Array (ALMA) observations of the central ~9 kpc of NGC 4038/9 in carbon monoxide (CO) *J*=2–1. These observations are used to probe the molecular-gas properties across the diverse interstellar medium (ISM) conditions of NGC 4038/9. Section 4.2 details the observations presented here, along with our calibration and imaging procedure for the CO (2–1) data. In Section 4.3 we describe the pixel-based method used to measure the molecular-gas properties in NGC 4038/9 at a range of spatial resolutions. Results are laid out in Section 4.4, comparing NGC 4038/9 to the PHANGS-ALMA results presented by Sun et al. (2018, 2020), and a discussion of the implications is in Section 4.5. Finally, Section 4.6 summarizes the results and conclusions of this work.

4.2 Data

4.2.1 Observations

ALMA mosaicked observations of the central ~9 kpc of NGC 4038/9 were obtained in Cycle 6 between 16 October, 2018 and 11 January, 2019. The main 12 m-array was used in both a compact and extended configuration. The Morita Atacama Compact Array (ACA) was included for sensitivity to larger-scale emission, and the total power (TP) array was also included to capture the largest-scale emission. Band 3 and 6 observations were carried out with spectral setups designed to cover the J=2–1 and 1–0 rotational transitions of ^{12}CO, ^{13}CO, and $C^{18}O$, as well as $C^{17}O$ (1–0) and the cyanide radical (CN) (1–0). Sufficient bandwidth was covered to also allow detection of continuum emission in both Bands. The spectral resolution of the ^{12}CO (2–1) spectral window is 1.953 MHz, or approximately 2.5 km s^{-1}.

4.2.2 Calibration and imaging

Calibration of all interferometric data was carried out using the ALMA Common Astronomy Software Applications (CASA) pipeline by observatory staff as part of data quality assurance. CASA versions 5.4.0-68 and 5.4.0-70 along with 42030M CASA54-P1-B and 42254M CASA54-P1-B of the ALMA pipeline were used, and after downloading the raw data from the archive, the same versions were used to reapply the calibration prior to our imaging.

We inspected the diagnostic plots in the observatory weblogs to search for problematic data that were not properly calibrated or left unflagged by the ALMA pipeline. This search included viewing system temperature plots, water vapour radiometer corrections, bandpass calibration tables and amplitude calibrator models. Calibrated amplitudes and phases for the bandpass, phase, and amplitude calibrators were also inspected as well as ALMA-pipeline images of the calibrator sources. Nothing was identified that was serious enough to warrant changes to the calibration or additional flagging.

Given the complex morphology of molecular line emission expected in the Antennae at the resolution of our observations and the number of lines to be imaged, we requested access to an early version of the PHANGS-ALMA imaging pipeline for CASA (Leroy

et al. 2021). We also hoped this pipeline would simplify imaging the various combinations of arrays and configurations used in these observations. When we began the process of imaging, version one of this pipeline had reached a stable point and active development was ongoing on a separate version-two branch of the code. We started with the version-one code (at commit 5ef53d3) and began making modifications for imaging all combinations of arrays and configurations used to observe NGC 4038/9, as well as several additional spectral lines. Details of these modifications are given in Appendix 4.A. The modified version of the interferometric imaging pipeline used here will be shared on reasonable request to the corresponding author, with a fully annotated GIT change history starting from the PHANGS-ALMA version-one code.

The overall procedure followed by the imaging pipeline has not changed dramatically between version one and version two, described in detail by Leroy et al. (2021), so we only briefly summarize the steps here. With calibrated interferometric data ready, the pipeline begins preparing the data for imaging by making copies of the relevant measurement sets (MSs) for the requested spectral lines and array combinations. The continuum level is fit to channels without spectral line emission, defined by a user-specified recession velocity and spectral line width for each spectral line, and the continuum is subtracted from the visibilities. Spectral windows (SPWs) containing only the lines being imaged are split out, spectral regridding to desired channel widths is applied, and each constituent array-MS is concatenated into new MSs containing each spectral line and unique combination of arrays; e.g. ^{12}CO (2–1) ACA plus compact main array, ^{12}CO (2–1) ACA plus compact and extended main arrays, etc.

Imaging begins by producing dirty cubes from each of the spectral line and array combination MSs. A shallow multi-scale clean is then performed, without any clean regions specified, down to a threshold of four times the standard deviation estimated from the median absolute deviation from the entire dirty cube's median value. Angular sizes of model components used in the ACA plus two main-array configuration cubes are point sources, 0.5, 1, 2.5, 5, and 10 arcsec. A signal mask is produced through binary dilation, in spatial and spectral dimensions, of a mask of pixels above four times the standard deviation of the multi-scale residuals into pixels above two times the standard deviation. Cleaning is continued from the multi-scale results, using only point-source model components within the signal mask, down to a threshold equal to the standard deviation of the multi-scale residuals. All cleaning steps also include an additional

stopping criterion based on periodic checks that the fractional change in the total model flux is greater than 1 per cent. At this point, visual inspection of all cubes was carried out to search for artefacts related to calibration and cleaning errors.

TP data processing was carried out with the PHANGS-ALMA TP calibration and imaging pipeline for CASA[1] in CASA version 4.7.2-REL (r39762). Herrera et al. (2020) describe the full details of the pipeline procedure so we only highlight differences in our procedure and explicit settings used. We used a modified version that does not perform any spectral binning. Also, we note that all continuum subtraction was carried out using order-one polynomial (linear) fits to the continuum levels.

At this point, the interferometric and TP cubes were combined with the PHANGS-ALMA imaging pipeline to produce the complete measurements of the spectral-line emission in NGC 4038/9. Interferometric cubes corrected for the primary beam response were made by dividing by the primary beam cubes, and the corrected cubes were convolved to have circular synthesized beams. The interferometric cubes were padded with masked pixels to cover at least the entire TP field of view (FoV), and the TP cubes were regridded on to the same astrometric and spectral grid as the interferometric cubes. Using the *feather* task in CASA, the TP cubes were combined with both main-array configurations plus the ACA. The feathered cubes still contain the primary beam response applied to the interferometric data (and the inherent response in the TP data) so another copy of the cubes was made which is multiplied by the interferometric primary beam response, to produce flat-noise cubes.

4.3   Analysis

4.3.1   Measuring molecular-gas properties

At the stage when the cleaned interferometric cubes were convolved to have circular synthesized beams, the beam full widths at half maximum (FWHMs) were made to have physical sizes of 55, 80, 90, 120, and 150 pc. These beam sizes facilitate direct comparisons to the fixed-scale pixel analyses of Sun et al. (2018) and Brunetti et al. (2021) (55,

---

[1]PHANGS-ALMA TP calibration and imaging pipeline scripts obtained from `https://github.com/PhangsTeam/TP_ALMA_data_reduction` at commit ca9f82c.

80, and 120 pc) as well as Sun et al. (2020) and Brunetti et al. (in preparation; Chapter 3; 90 and 150 pc). After feathering the TP data with the convolved interferometric cubes, each cube was spatially regridded such that the pixels were half the synthesized beam FWHM on a side to roughly Nyquist sample the beams. Moment zero (integrated intensity) and two (intensity-weighted velocity dispersion, σ_v) maps were calculated from the regridded cubes using the SPECTRALCUBE package. Only significant-emission pixels were included in the moment calculations, with the pixel masks generated in the same way as by Sun et al. (2018; see also Brunetti et al. 2021). Maps of peak brightness temperature in each pixel were also produced from within the significant-emission masks.

Integrated-intensity maps were converted to mass surface density maps using a CO-to-H_2 conversion factor (α_{CO}) and an intensity ratio between CO (2–1) and CO (1–0) (R_{21}). We adopted a single Milky-Way like conversion factor of $\alpha_{CO(2-1)} = 6.25\,M_\odot\,pc^{-2}(K\,km\,s^{-1})^{-1}$ for all measurements from NGC 4038/9, following Sun et al. (2018). Using the same conversion factor as Sun et al. (2018) reduces any differences in the estimated mass surface densities to originating from different integrated intensities. The conversion factor in NGC 4038/9 is not yet well constrained (see Section 4.5 for further discussion) but previous investigation has estimated it may be similar to the typical Milky-Way value (Wilson et al. 2003). This conversion factor includes a contribution from helium and other heavy elements. We also applied a correction to the velocity dispersion measurements for the finite channel width of the observations, in the same way as Brunetti et al. (2021) (using equations 15 through 17 from Leroy et al. 2016).

From our measurements of Σ_{mol} and σ_v we also estimate the virial parameter and internal turbulent pressure in each pixel, following Sun et al. (2020) with

$$\alpha_{vir} \approx 3.1 \left(\frac{\Sigma_{mol}}{10^2\,M_\odot\,pc^{-2}} \right)^{-1} \left(\frac{\sigma_v}{10\,km\,s^{-1}} \right)^2 \left(\frac{D_{beam}}{150\,pc} \right)^{-1} \tag{4.1}$$

and

$$\frac{P_{turb}}{k_B} \approx 3.3 \times 10^4\,K\,cm^{-3} \left(\frac{\Sigma_{mol}}{10^2\,M_\odot\,pc^{-2}} \right) \left(\frac{\sigma_v}{10\,km\,s^{-1}} \right)^2 \left(\frac{D_{beam}}{150\,pc} \right)^{-1}. \tag{4.2}$$

D_{beam} is the FWHM of the synthesized beam. These are equivalent to equations 13 and 15 from Sun et al. (2018) and used by Brunetti et al. (2021). As described in Sun et al.

173

(2018), these equations assume roughly a single cloud fills each synthesized beam along with the equation for the virial parameter assuming a cloud density profile that goes as $\rho(r) \propto r^{-1}$. The resulting maps of molecular-gas properties at 55 and 150 pc resolution are shown in Figures 4.1 and 4.2, respectively. We note that while we use square pixels, following Sun et al. (2018) and Brunetti et al. (2021), Sun et al. (2020) instead resample their maps to have hexagonal pixels that match the beam size before measuring the gas properties.

4.3.2 Separating measurements by region

To examine the impact that the location of the molecular gas within NGC 4038/9 has on the gas properties, we separate our measurements into sub-samples that are close to the nuclei and farther away. Following Sun et al. (2018) and Brunetti et al. (2021), all pixels that are less than 1 kpc from either nucleus (shown as gray circles with radii of 1 kpc in Figures 4.1 and 4.2) are included in the nuclear-pixel sample, and all pixels farther from the nuclei than 1 kpc make up the non-nuclear sample. Sun et al. (2020) separate their aperture measurements[2] into central and disc regions within each galaxy based on distinct structures identified in near-infrared images (the full description of this methodology is given by Querejeta et al. 2021). Finally, since the CO (3–2) observations of NGC 4038/9 analysed by Sun et al. (2018) only covered the overlap region, we also identify pixels in our CO (2–1) data that are in the same overlap region for direct comparisons (gray polygons in Figures 4.1 and 4.2). We traced a region out to a primary-beam response of 0.2 in the original Whitmore et al. (2014) observations from which the moment maps used by Sun et al. (2018) were derived, and identified all pixels in our CO (2–1) moment maps within that region. This region corresponds roughly to a right ascension (R.A.) range from $12^{\mathrm{h}}01^{\mathrm{m}}56\overset{\mathrm{s}}{.}5$ to $12^{\mathrm{h}}01^{\mathrm{m}}53\overset{\mathrm{s}}{.}5$ and a declination (Dec.) range from $-18°53'16\overset{''}{.}9$ to $-18°52'5''$.

---

[2]Table of measurements from Sun et al. (2020) was retrieved from the journal website on 2021 September 6.
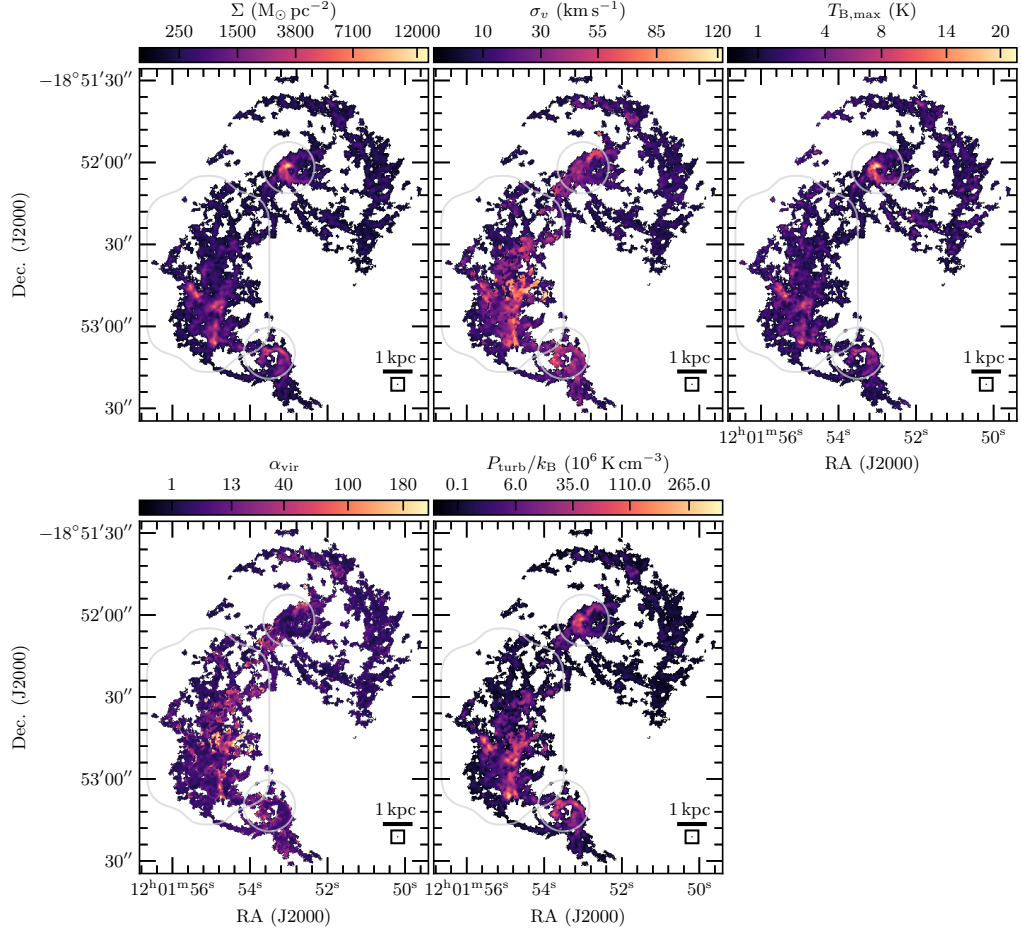
FIGURE 4.1: Maps of molecular-gas properties in NGC 4038/9 at 55 pc resolution, calculated from CO (2–1) moment maps as described in Section 4.3.1. The top row shows, from left to right, mass surface density, velocity dispersion, and peak brightness temperature. The bottom row shows the virial parameter on the left and the internal turbulent pressure on the right. Pixels are half of the beam FWHM on a side. The gray circles indicate the regions within 1 kpc radius of the nuclei, denoting the nuclear and non-nuclear regions discussed in later sections. The gray polygons in the lower-left indicate the overlap-region FoV observed in CO (3–2) by Whitmore et al. (2014) and analysed by Sun et al. (2018), and pixels in these polygons make up our overlap-region sub-sample. The squares in the bottom-right corner of each panel contain a circle with diameter equal to the beam FWHM. A scale bar indicating 1 kpc at the distance of NGC 4038/9 is also shown in the bottom-right corner of each panel. A CO-to-H_2 conversion factor of $6.25\,M_\odot\,pc^{-2}(K\,km\,s^{-1})^{-1}$ was used to convert integrated-intensities to mass surface densities, which also affects the estimates of the virial parameter and internal turbulent pressure (see Equations 4.1 and 4.2).
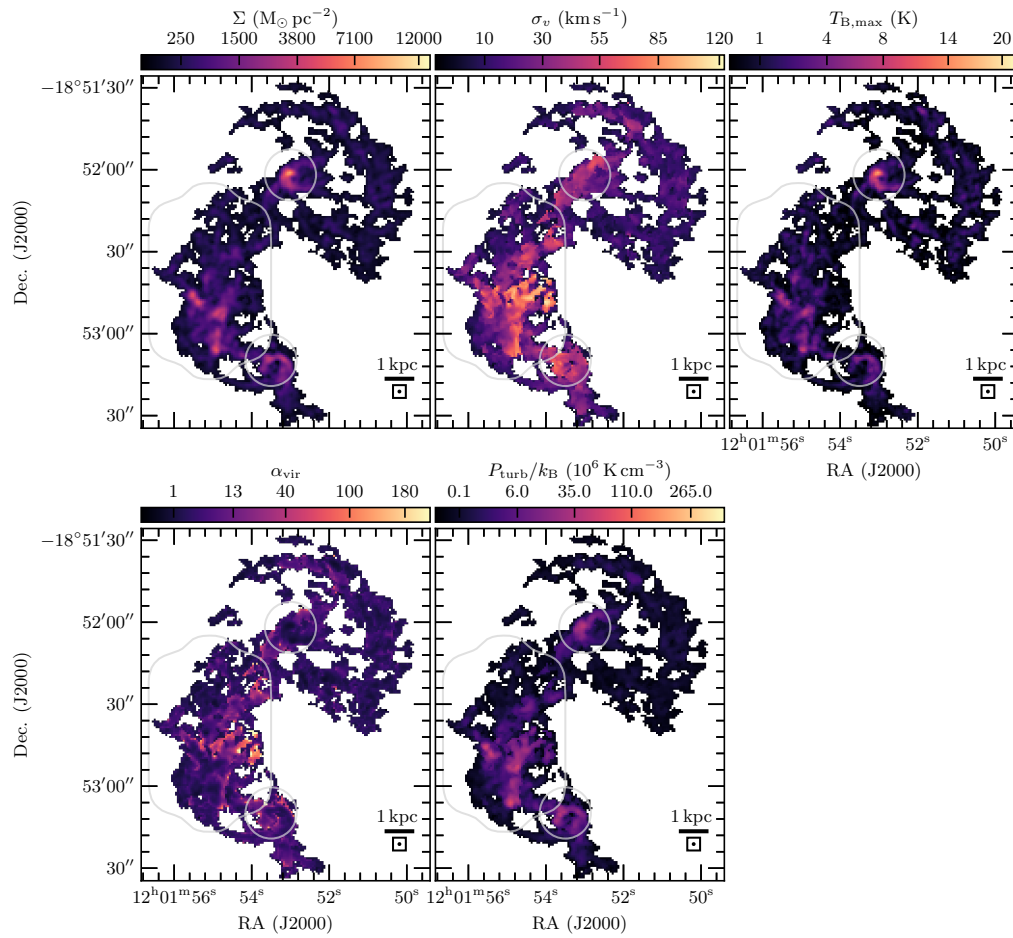
FIGURE 4.2: The same as Figure 4.1 but showing the molecular-gas properties at 150 pc resolution. Versions at 80, 90, and 120 pc resolution were also analysed. See the Figure 4.1 caption for more details.

4.4 Results

4.4.1 Gas-property percentiles

Qualitative comparisons between NGC 4038/9, NGC 3256, and the PHANGS-ALMA galaxies presented by Sun et al. (2018) are shown as mass-weighted medians (symbols) and inner 68th percentiles (errorbars) in Figure 4.3. Galaxies are also split between nuclear (triangles) and non-nuclear (circles) sub-samples, with the Whitmore et al. (2014) overlap region FoV also included for NGC 4038/9 (stars). Measurements at 120 pc resolution are shown but comparisons at 80 pc and 55 pc resolution were also made with generally the same results as seen in Figure 4.3. There is considerable overlap between sub-samples in NGC 4038/9 from the nuclear and non-nuclear pixels, with the medians from one overlapping with the inner 68th percentiles from the other.

NGC 4038/9 exhibits higher mass surface densities measured in CO (2–1) than almost all other galaxies in Figure 4.3. The CO (3–2) measurements from NGC 4038/9 exceed even our values, but see Section 4.5.3 for a discussion of the caveats in comparing to the CO (3–2) observations. PHANGS-ALMA galaxies overlap with NGC 4038/9 most significantly in the samples from their central regions, but the upper halves of samples from several disc regions also overlap with NGC 4038/9. The nuclear and non-nuclear samples from NGC 4038/9 and NGC 3256 are similar, with those from NGC 4038/9 being wider, having slightly higher medians, and extending to higher surface densities at all resolutions.

The results from the velocity dispersion, peak brightness temperature, and internal turbulent pressure comparisons are similar to those seen in mass surface density. NGC 4038/9 exhibits some of the highest values, although the centres of NGC 3256 and NGC 3627 often reach significantly higher values. On the other hand, M 33, NGC 2835, NGC 5068, and M 31 typically have values for all of these properties significantly below all of those measured in NGC 4038/9.

The comparison of virial parameters in NGC 4038/9 is quite different from the other gas properties. With median virial parameters less than half of those in NGC 3256, the broad samples from NGC 4038/9 overlap at least partially with all PHANGS-ALMA galaxies at all resolutions. The nuclear medians from NGC 4038/9 also appear lower than those from the non-nuclear pixels, similar to what is seen in the centres and discs
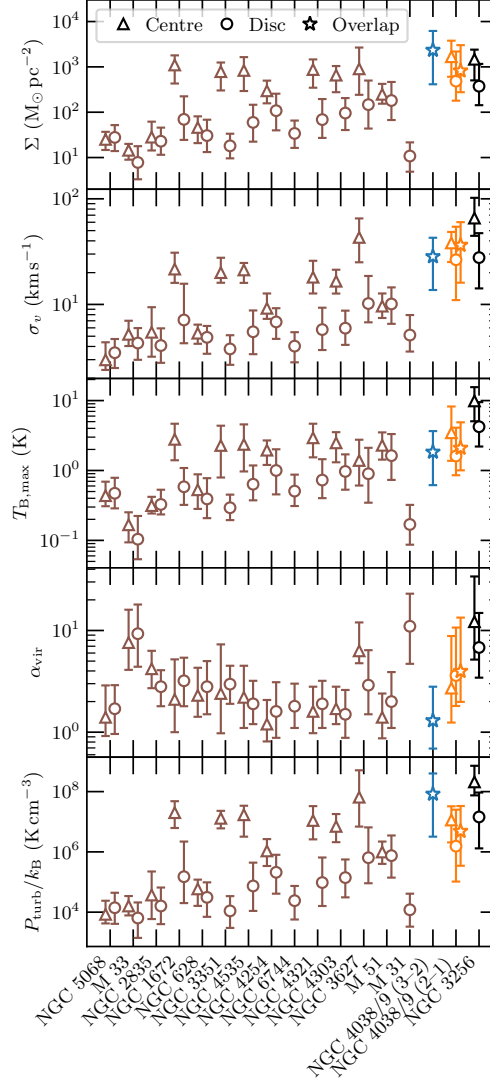
FIGURE 4.3: Comparisons of mass-weighted pixel-sample percentiles at 120 pc resolution from NGC 4038/9, NGC 3256, and Sun et al. (2018) for mass surface density, velocity dispersion, peak brightness temperature, virial parameter, and internal turbulent pressure. Medians are shown as symbols and the inner 68th percentiles as errorbars. Samples are split between centre (triangle) and non-centre/disc (circle) pixels. NGC 4038/9 also has pixel samples from the Whitmore et al. (2014) overlap region FoV, shown as stars. Percentiles from our CO (2–1) observations of NGC 4038/9 are in orange, from the CO (3–2) observations in blue, NGC 3256 is in black, and the remainder of the galaxies analysed by Sun et al. (2018) are in brown. Galaxies from Sun et al. (2018) are ordered along the x axis from low stellar mass at the left to high stellar mass at the right. Stellar masses are from Sun et al. (2020), where available, and from Sun et al. (2018) otherwise (i.e. M 31, M 33, and M 51).

of the PHANGS-ALMA galaxies but contrary to NGC 3256. However, the spread of the samples from both NGC 4038/9 and NGC 3256 do result in considerable overlap between the two. Virial-parameter samples from the CO (3–2) measurements are much lower than in CO (2–1), with the medians from the former at the lower edge of the inner 68th percentile range of the latter.

The same comparisons are made in Figures 4.4 through 4.8 but the samples from NGC 4038/9 are now shown with the full PHANGS-ALMA list of galaxies analysed by Sun et al. (2020). The resolutions of the measurements are 150 and 90 pc for these comparisons. Note that the separation of pixels in the PHANGS-ALMA galaxies was made in the same manner as for NGC 4038/9, not using the centre and disc designations from Sun et al. (2020). We chose this approach to reduce variability in the comparison with NGC 4038/9 potentially brought on by differences in how pixels are assigned to the different regions. Using the simple 1 kpc radius also has the benefit of often increasing the number of pixels within the centres of galaxies, resulting in less stochastic inner 68th percentiles for less massive and/or more distant galaxies. However, given the size-stellar mass relation of galaxies, the fraction of a galaxy included in the central region will increase as stellar mass decreases. For example, across the stellar-mass range of the PHANGS-ALMA galaxies shown in Figures 4.4 through 4.8 of 1.2×10^9 to 83.1×10^9 M$_\odot$, a range of stellar radii of about 6 to 30 kpc is expected (Trujillo et al. 2020; Sánchez Almeida 2020). This effect will likely result in the percentiles from the centres of low stellar mass galaxies being underestimated since contaminating disc pixels will make up a larger fraction of pixels in their central 1 kpc.

Trends in the medians and inner 68th percentiles with resolution are not very strong in NGC 4038/9 so the data do not appear very different compared to Figure 4.3. General trends between NGC 4038/9 and PHANGS-ALMA disc galaxies observed in Figure 4.3 appear in these comparisons as well. The centres of PHANGS-ALMA galaxies are the most similar to NGC 4038/9, regardless of spatial scale. Similarities are greater at higher stellar masses, even to the point that some of the disc samples from the highest stellar mass PHANGS-ALMA galaxies overlap with the samples from NGC 4038/9. NGC 4038/9 exhibits some of the highest mass surface densities, velocity dispersions, and peak brightness temperatures compared to the PHANGS-ALMA galaxies. Virial parameters and internal turbulent pressures measured in NGC 4038/9 are much more similar to those measured in PHANGS-ALMA galaxies, though for the pressures it is
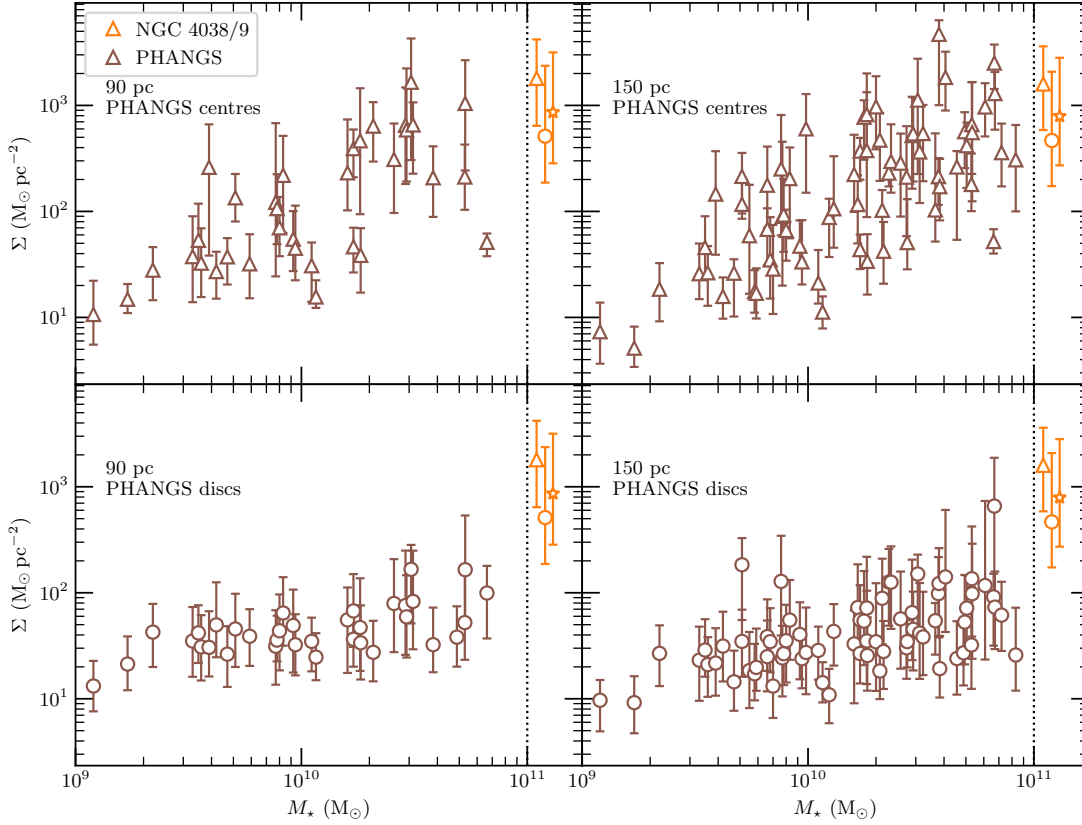
FIGURE 4.4: Mass-weighted pixel-sample percentiles vs. stellar mass from NGC 4038/9 (orange) and Sun et al. (2020) (brown) for mass surface density. Medians are shown as symbols and the inner 68th percentiles as errorbars. The top row shows PHANGS-ALMA samples from galaxy centres (triangles) and the bottom row shows samples from outside the centres (circles; based on being within a 1 kpc radius of the centre, not the centre and disc designations from Sun et al. 2020). NGC 4038/9 samples from the nuclei, outside the nuclei (including the overlap region), and just the overlap region are shown in both rows. The left column shows measurements at 90 pc resolution and the right columns at 150 pc. Note that the position of NGC 4038/9 along the x axis is arbitrary.
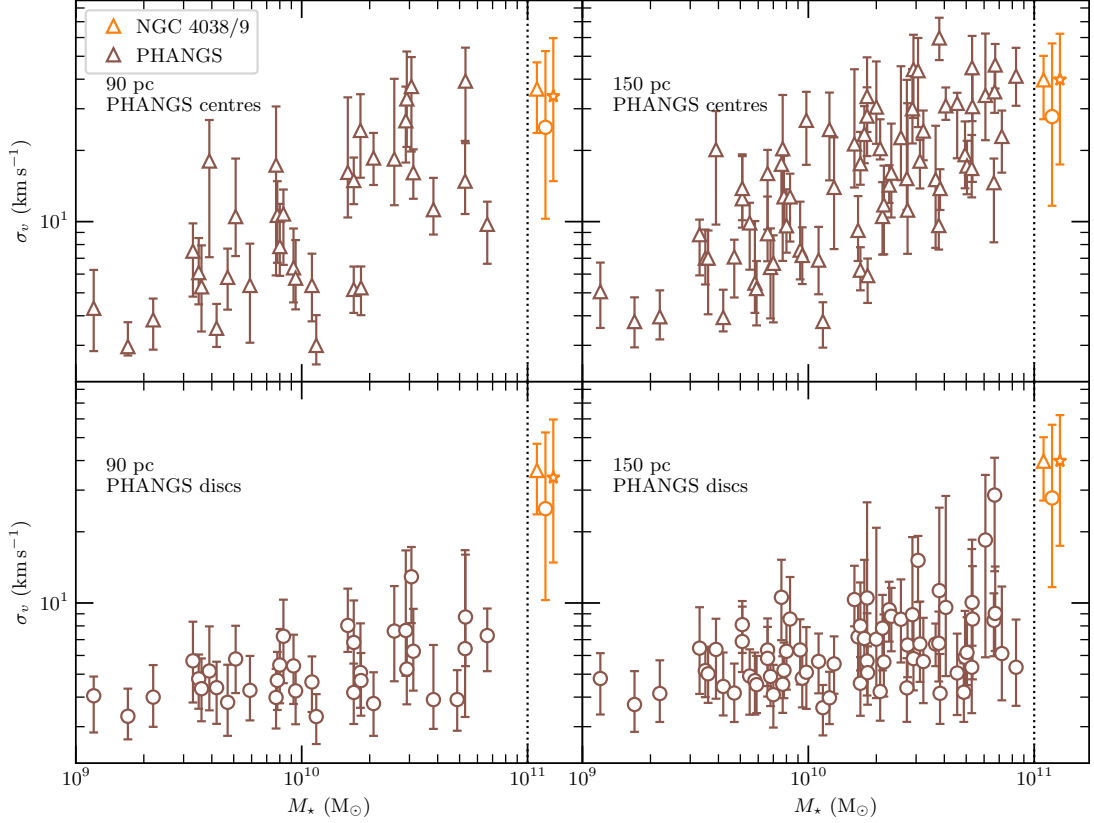
FIGURE 4.5: Same as Figure 4.4 but showing samples of velocity dispersion.

still mainly true only for the centres of PHANGS-ALMA galaxies. Finally, there are usually at least a few PHANGS-ALMA galaxies that have more extreme gas properties than NGC 4038/9 across all properties shown in Figures 4.4 through 4.8.

4.4.2 Anderson-Darling tests

We performed a series of two-sample Anderson-Darling (AD) tests (Scholz & Stephens 1987) to compare quantitatively the samples of molecular-gas measurements from NGC 4038/9, NGC 3256, and galaxies observed in the PHANGS-ALMA survey. The null hypothesis, H_0, is that both samples originate from the same underlying distribution and by calculating the AD statistic we estimate whether this appears true at the five per cent level. Specifically, we take the measurements from pixels in the CO map of NGC 4038/9 as the first sample and the measurements from another galaxy at the
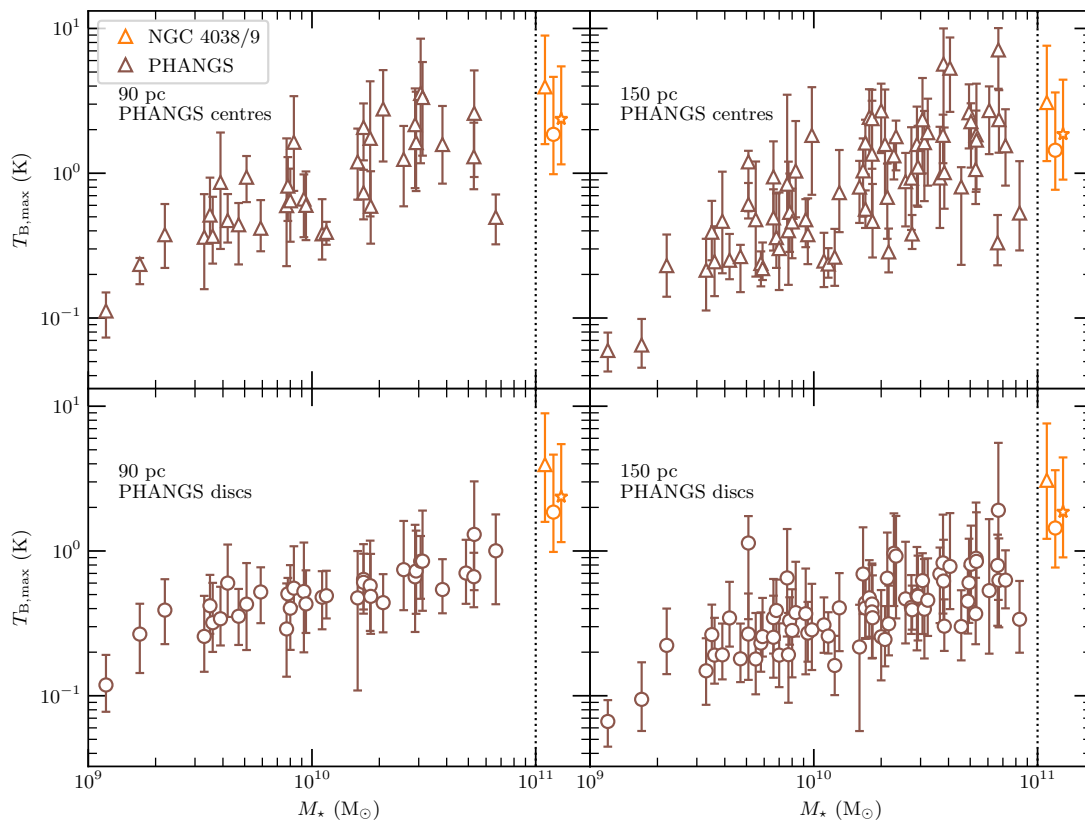
FIGURE 4.6: Same as Figure 4.4 but showing samples of peak brightness temperature.
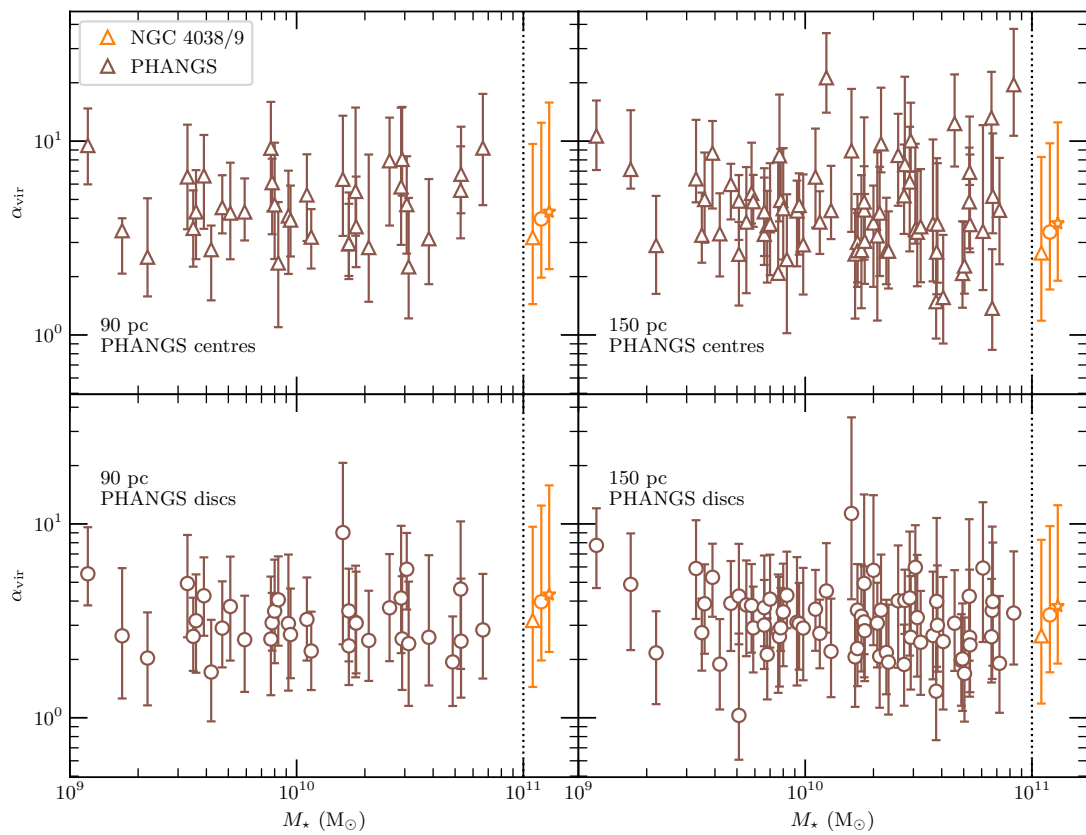
FIGURE 4.7: Same as Figure 4.4 but showing samples of virial parameter.
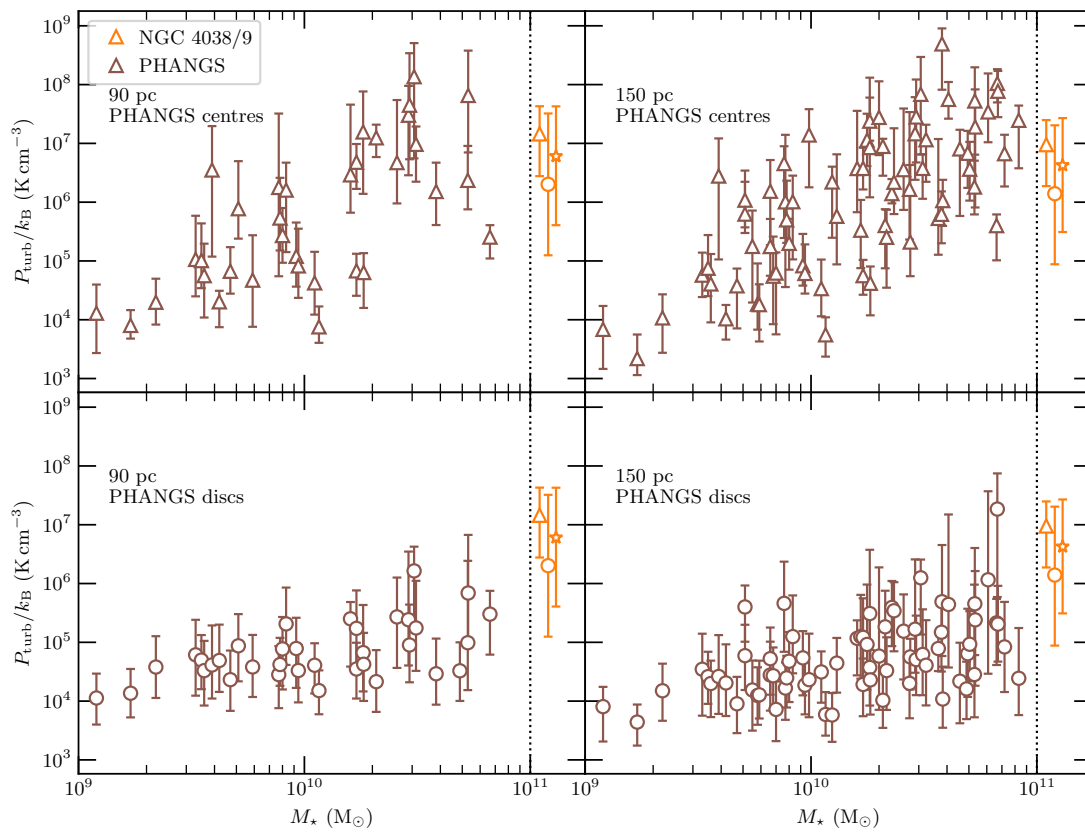
FIGURE 4.8: Same as Figure 4.4 but showing samples of internal turbulent pressure.

same resolution (e.g. NGC 3256) as the second sample. Measurements of mass surface density, velocity dispersion, peak brightness temperature, virial parameter, and internal turbulent pressure are all individually tested. One set of samples consists of all measurements made within significant pixels or hexagonal apertures from the CO maps towards each galaxy. Sub-samples from the centres and outside the centres of each galaxy are also tested, along with the overlap region in NGC 4038/9 defined by the mapped FoV from Whitmore et al. (2014). All possible pairs between the whole FoV, centre, non-centre, and overlap region samples between each pair of galaxies, at matched resolution, were tested.

All tests between NGC 4038/9 and NGC 3256 reject H_0 at the five percent level, indicating the molecular-gas properties originate from different underlying distributions. Visual inspection of the sample distributions from these two galaxies clearly show differences across all gas properties. The differences between the mass surface density samples are the least obvious but the centres, widths, and strengths of tails to low or high densities are consistent with the AD test results.

Similarly, all tests between NGC 4038/9 and each galaxy presented by Sun et al. (2018) reject H_0 at the five percent level. The differences between the sample distributions are often obvious, with gas properties in NGC 4038/9 typically appearing at more extreme (i.e. higher) values than most measured in the PHANGS-ALMA galaxies.

Sun et al. (2018) did include CO (3–2) observations of the overlap region in NGC 4038/9 in their analysis and our tests also always reject H_0 when comparing those data to our CO (2–1) observations. Even when the CO (2–1) sample is limited to the same region of NGC 4038/9 the samples appear to come from different distributions. There are limitations to comparing these CO (3–2) and CO (2–1) observations in this way, however. The inclusion of ACA and TP observations in the CO (2–1) data make it sensitive to much larger-scale emission than the CO (3–2) data which only consisted of only a single configuration of the main 12 m array. Recovering more of the large-scale emission would increase the total mass detected, mainly by adding low surface density measurements since the larger structures are likely to be less dense than the compact emission picked up by the main array.

The AD test results between NGC 4038/9 and the galaxies presented by Sun et al. (2020) were mixed. One clear pattern is that H_0 was rejected at the five per cent level in (almost) all cases when regions from NGC 4038/9 were compared with the whole

FoV or non-central regions of the PHANGS-ALMA galaxies. This pattern was present both when the central pixels of the PHANGS-ALMA galaxies were chosen to be those within 1 kpc of the centre and with the designations from Sun et al. (2020). In addition, H_0 could not be rejected when comparing NGC 4038/9 to the centres of many of the PHANGS-ALMA galaxies, also regardless of how the centres were defined. For a given galaxy, the properties for which H_0 was not rejected is usually the same across the different regions in NGC 4038/9 it was compared to. No galaxy accepted H_0 for all properties across all regions compared with its central samples. An important caveat is that often the galaxies that have the most tests where H_0 cannot be rejected also have a small number of pixels in their centres, so the ability to distinguish the underlying distributions from the measurement samples may be limited in those cases. There are more tests where H_0 is rejected when using the 1 kpc definition of the centres and there are usually many more pixels in the central regions of the PHANGS-ALMA galaxies with that definition. Details at the galaxy-by-galaxy and region-by-region levels are given in Appendix 4.B.

4.4.3   Correlations between molecular-gas properties

Figures 4.9 through 4.12 show mass-weighted probability density functions (PDFs) of several of the molecular-gas properties plotted against each other. All PDFs here are made from Gaussian kernel density estimators (KDEs), with bandwidths automatically chosen using the scipy implementation of Scott's Rule (Scott 1992).

Figure 4.9 shows the molecular-gas velocity dispersion vs. molecular-gas mass surface density PDFs of all significant pixels from NGC 4038/9 and NGC 3256 or apertures from all galaxies presented by Sun et al. (2020). The shift of most of the mass to both higher surface densities and velocity dispersions in NGC 4038/9 and NGC 3256 is visible, but the lower values from the merger samples overlap with the higher values from the PHANGS-ALMA galaxies. The apertures from the centres of (primarily barred) spiral galaxies populate a very similar part of the parameter space to NGC 4038/9 and NGC 3256. These central PHANGS-ALMA values make a dispersion-surface density trend that is slightly offset to higher velocity dispersion for a given surface density from the rest of the PHANGS-ALMA sample. The dispersion-surface density trends in the merger samples are more consistent with this offset PHANGS-ALMA trend. There may also be evidence for the merger-sample trends broadening at high surface densities,

extending to higher velocity dispersions at a given surface density than the PHANGS-ALMA sample. However, the sensitivity limit in this space roughly follows the upper-left edge of the contours (see figure 1 from Sun et al. 2020) and is likely truncating the extent of the scatter along the trends seen in NGC 4038/9 and NGC 3256. To explore if the trends in the mergers truly broaden at high surface densities or are possibly broader than the PHANGS-ALMA trend at all surface densities will require both more sensitive and higher spectral-resolution observations.

Figure 4.10 shows the same contours for NGC 3256 and the PHANGS-ALMA galaxies, but now the sample from NGC 4038/9 is split into pixels within 1 kpc of either nucleus and those beyond. As seen in Figures 4.3 through 4.4, pixels near the nuclei of NGC 4038/9 exhibit higher surface densities and velocity dispersions. The two-dimensional view also emphasizes the split between regions is not perfect as there is considerable overlap between the two sub-samples. The nuclear regions of NGC 4038/9 are generally most consistent with the centres of (mostly barred) PHANGS-ALMA galaxies, and the non-nuclear regions are more consistent with the upper limits of the PHANGS-ALMA discs and the centres of unbarred spirals. A similar separation by nuclear and non-nuclear regions was seen in NGC 3256. The wider peak in the PDF from NGC 3256 in Figure 4.10 is near the peak of its nuclear measurements, and the narrower peak is near the non-nuclear peak (see figure 7 from Brunetti et al. 2021). We also note that the trend of velocity dispersion with surface density appears stronger in the non-nuclear sample from NGC 4038/9 than the nuclear sample, such that a majority of the mass in the nuclear sample actually appears with nearly constant velocity dispersion with surface density. This feature may indicate our choice of CO-to-H_2 conversion factor is not appropriate for regions near the nuclei of NGC 4038/9, and we discuss this possibility further in Section 4.5.

In Figure 4.11 we compare the velocity dispersions and surface densities measured in the Whitmore et al. (2014) overlap region from our CO (2–1) observations to the CO (3–2) observations analysed by Sun et al. (2018). This comparison highlights the slight offset to higher velocity dispersions measured in the CO (2–1) data and conversely the slightly higher mass surface densities measured in the CO (3–2) data. The bulk of the mass in the CO (2–1) measurements thus appears to follow a slightly steeper trend. Also obvious here is the much broader range of velocity dispersions measured at a given surface density in the CO (2–1) data compared to the CO (3–2) data. We discuss both

FIGURE 4.9: Mass-weighted Gaussian KDEs of molecular-gas velocity dispersion vs. molecular-gas mass surface density measured in all significant pixels or hexagonal apertures from NGC 4038/9 (orange filled contours), NGC 3256 (black dotted contours), and all PHANGS-ALMA galaxies presented by Sun et al. (2020) (brown contours). Contours enclose 99.5, 90, 50, and 20 per cent of the mass from each data set. The top (bottom) panel shows measurements made at 90 pc (150 pc) resolution in NGC 4038/9 and PHANGS-ALMA and 80 pc (120 pc) resolution in NGC 3256.
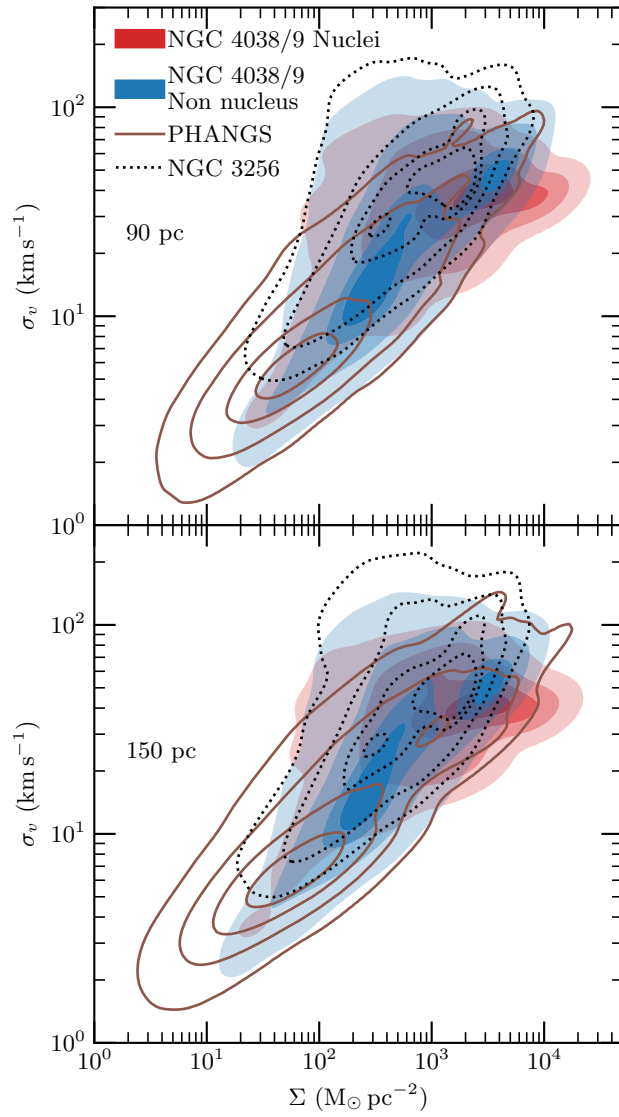
FIGURE 4.10: Same as Figure 4.9 but now the sample from NGC 4038/9 is separated into pixels within 1 kpc of the nuclei (red) and those beyond (blue).

potential physical and methodological sources of these differences in Section 4.5.

Figure 4.12 now shows the internal turbulent pressure measured in the overlap region in both CO (2–1) and CO (3–2) vs. the mass surface density and velocity dispersion. Viewed in this way, it is obvious how the higher turbulent pressures estimated from the CO (3–2) data are driven by the higher surface densities. A similar absolute range of velocity dispersions is measured in the two transitions, but the CO (3–2) pressures are consistently higher at all velocity dispersions. The range of surface densities is similar but the maximum reached in CO (3–2) is noticeably higher, and combined with the offset to higher surface densities at fixed velocity dispersion pushes the pressures above those from the CO (2–1) data.

4.5 Discussion

4.5.1 Comparison of mergers

It appears the differences in the molecular-gas properties in NGC 4038/9 and NGC 3256 can be explained by their different merger stages. Previous numerical work on replicating the morphology and kinematics of NGC 4038/9 seems to point towards it being sometime around second pericentre passage (Toomre & Toomre 1972; Barnes 1988; Mihos et al. 1993; Karl et al. 2010; Privon et al. 2013; Renaud et al. 2015). NGC 3256 is a late-stage merger, likely entering the point of coalescence, due to its disturbed morphology and closely separated nuclei that share a common envelope (Stierwalt et al. 2013). Moreno et al. (2019) show that after first pericentre passage, the SFR relative to an isolated control galaxy increases by a factor of about five for about 25 Myr before settling to a more moderate enhancement of a factor of about two. After second pericentre passage and during coalescence, a second dramatic enhancement persists for about 500 Myr at a rate ~10 to 30 times higher than the control, before more gradually reducing. Comparing the SFR of NGC 4038/9 of around $6.6 \, M_\odot \, yr^{-1}$ (Brandl et al. 2009; Bemis & Wilson 2019) and NGC 3256 of $50 \, M_\odot \, yr^{-1}$ to the simulated SFR enhancements fits their inferred merger stages.

Our observations of higher molecular gas surface densities in NGC 4038/9 than NGC 3256 but lower SFR may also fit into the evolution of dense gas in the simulations presented by Moreno et al. (2019). After the first pericentre passage and until just after
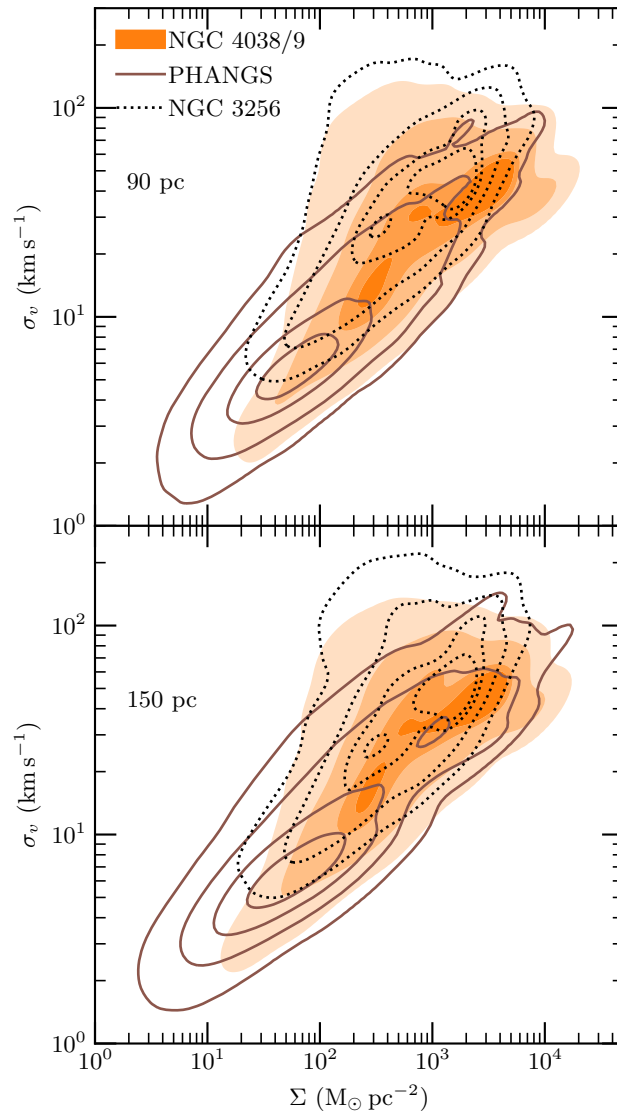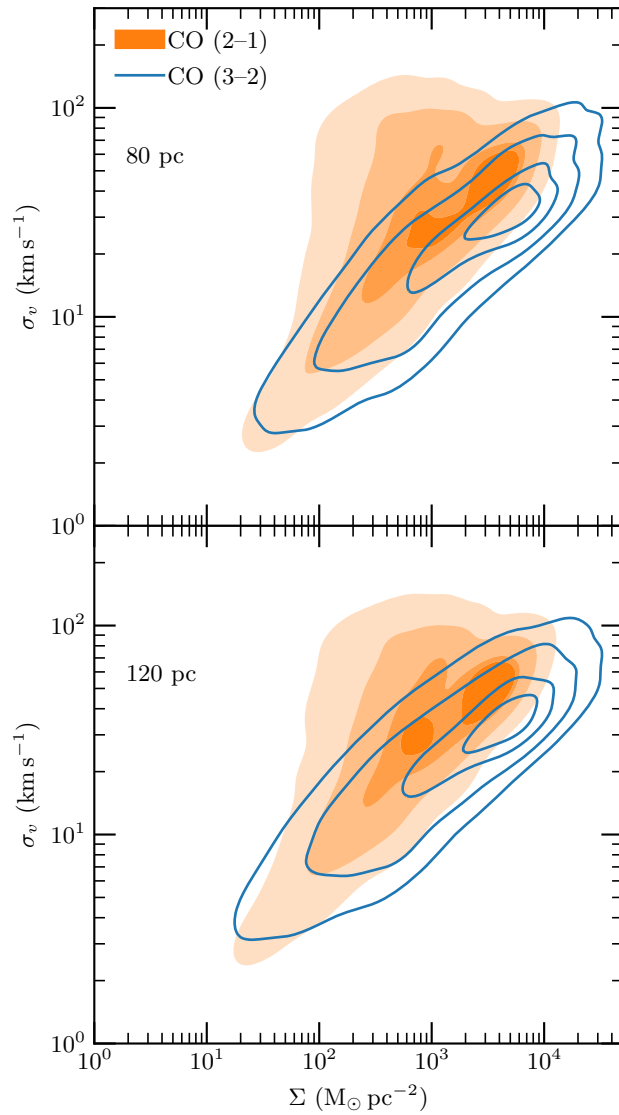
FIGURE 4.11: Mass-weighted Gaussian KDEs of molecular-gas velocity dispersion vs. molecular-gas mass surface density measured in significant pixels within the Whitmore et al. (2014) overlap region FoV of NGC 4038/9. CO (2–1) measurements are again shown in orange filled contours and CO (3–2) is in blue contours. Contours enclose 99.5, 90, 50, and 20 per cent of the mass from each data set. The top panel shows measurements made at 80 pc resolution in both transitions, and the bottom panel shows 120 pc resolution.
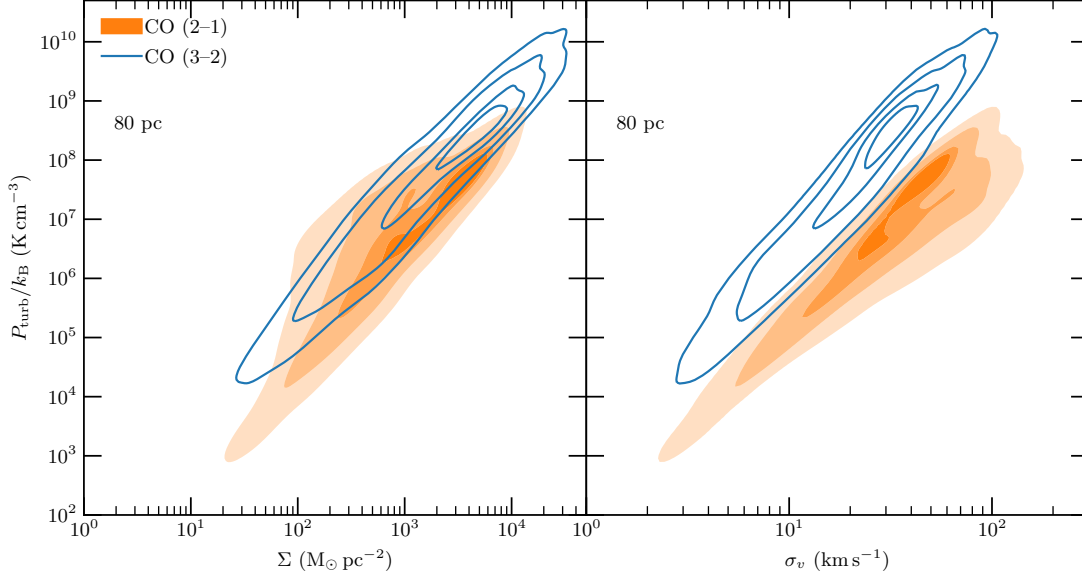
FIGURE 4.12: Mass-weighted Gaussian KDE of the molecular-gas internal turbulent pressure vs. molecular-gas mass surface density (left) and velocity dispersion (right) measured in the Whitmore et al. (2014) overlap region FoV of NGC 4038/9. Colours and contour levels are the same as Figure 4.11.

the second passage, the mass of cold-dense gas ($n > 10\,\mathrm{cm}^{-3}$, $T < 300\,\mathrm{K}$) in their fiducial merger simulation is enhanced to almost twice that in their isolated galaxy control (their figure 7). The dense-gas mass then becomes depleted relative to the isolated galaxy before rebounding to about the same mass just before coalescence, and then slowly depleting to below the mass in the isolated galaxy. We may be catching NGC 4038/9 close enough to its second encounter that the molecular gas mass is still maximally enhanced whereas NGC 3256 is showing signs of the subsequent reduction of molecular gas. To explain the higher SFR in NGC 3256 despite the lower molecular-gas surface density we turn to the behaviour of the densest gas in their simulations. While Moreno et al. (2019) found the total mass of molecular gas decreased after second passage, the mass in cold ultra-dense gas ($n > 1000\,\mathrm{cm}^{-3}$, $T < 300\,\mathrm{K}$) increased by a factor of about 100. The fraction of cold-dense gas in the ultra-dense regime increased from about 0.1 per cent to around 30 per cent, leading to the dramatic increase in the SFR after second passage. Thus, it could be that the total mass of very dense gas is significantly higher in NGC 3256 than in NGC 4038/9. If however the increase in ultra-dense gas comes from compression increasing the highest densities while reducing the filling fraction, rather

than from an overall increase in the amount of molecular gas, our resolution may not be as well matched to the bulk of the gas from which stars are forming in NGC 3256 as NGC 4038/9. Surface density measurements are subject to beam dilution that can artificially depress the density if the emitting structures do not completely fill each beam. Higher resolution observations are necessary to continue to probe how the molecular-gas properties change (or do not) with spatial scale.

While the velocity dispersions in the non-nuclear regions of NGC 4038/9 and NGC 3256 are quite similar, the nuclear velocity dispersions in NGC 3256 are significantly higher than in NGC 4038/9. Higher velocity dispersions near the nuclei of NGC 3256 may also be driven by the different merger stages. Star formation is predicted to produce at most about $10\,\mathrm{km\,s^{-1}}$ of turbulent velocity dispersion (Shetty & Ostriker 2012; Krumholz et al. 2018), with gas flows required to power larger velocity dispersions (Krumholz et al. 2018). The later merger stage of NGC 3256, resulting in more morphological disruption and likely more significant tidal flows of gas towards the nuclei, could result in the larger velocity dispersions compared to NGC 4038/9.

Combining higher surface densities but similar velocity dispersions (in the non-nuclear regions) in NGC 4038/9 compared to NGC 3256 results in lower virial parameters for some of the gas. While we might expect the higher SFR in NGC 3256 to imply lower virial parameters than in NGC 4038/9, we may be seeing the combination of enhanced turbulence and ultra-dense gas in NGC 3256 making the gas appear unbound at the scales probed. Perhaps in the more violent coalescence stages only the densest (and therefore smaller-volume) portions of the molecular gas in NGC 3256 will even approach being gravitationally bound. In contrast, the so-far weaker tidal flows in NGC 4038/9 may not have transformed its ISM away from appearing largely near virial equilibrium or collapse like many of the PHANGS-ALMA galaxies. The ISM in NGC 4038/9 still being in a transitional stage may explain the wide range of virial parameters compared to PHANGS-ALMA and the non-nuclear regions of NGC 3256. It could also be that the methods to measure SFR observationally lag behind the properties of the molecular gas we measure. The dynamical state of the molecular gas may now be unfavorable for widespread star formation but our SFR indicators rely on a currently-existing population of stars that are the result of past gas conditions. We must also caution that the virial parameters shown in Figures 4.3 and 4.7 do not account for pressure confinement contributing to binding the observed molecular gas. Brunetti et al. (2021) roughly estimate that stellar surface

densities and cloud-cloud collisions between GMCs could provide enough external pressure to balance the internal pressure for some of the gas in NGC 3256.

Assuming the CO emission is optically thick in both NGC 4038/9 and NGC 3256 would imply the peak brightness temperature is roughly equal to the kinetic temperature of the molecular gas. Higher peak brightness temperatures in NGC 3256 would then indicate the kinetic temperature of the gas is also higher than in NGC 4038/9. Given the higher SFR in NGC 3256 is producing more stars that are heating the molecular gas, it is not surprising the molecular gas appears hotter in NGC 3256 than NGC 4038/9. A similar radiative transfer analysis of NGC 3256 to what we have planned for NGC 4038/9, spanning several CO transitions as well as optically thin and thick isotopologues, would be necessary to further investigate differences in the temperatures and densities of the molecular gas in the two mergers at GMC scales.

4.5.2 Conversion-factor considerations

Since the CO-to-H_2 conversion factor influences many of the molecular-gas properties presented here, we now discuss the appropriateness of our choice to use a single value throughout NGC 4038/9 and of using the Milky Way value. A single conversion factor has the benefit that changes to the factor result in shifting the sample of quantities all together. However, it is likely an oversimplification to assume all regions within NGC 4038/9 truly have the same conversion factor as radial gradients in the conversion factor of nearby spirals are clearly measured (Blanc et al. 2013; Sandstrom et al. 2013). While regional changes in the conversion factor in mergers are less constrained, it is likely that these effects are also at play in NGC 4038/9, since the velocity-dispersion samples differ between the nuclear and non-nuclear regions and the overlap region dominates the total star formation. As for the choice of the Milky-Way value itself, this choice first helps in simplifying comparisons with other work like Sun et al. (2018) and Galactic studies. A single conversion factor across NGC 4038/9 and the PHANGS-ALMA galaxies from Sun et al. (2018) means that Figures 4.3, 4.4, and 4.11 at the least indicate that the surface brightness of CO emission is systematically higher in NGC 4038/9. However, there is evidence that indicates the Milky-Way conversion factor may not be far off for the bulk of the CO emission in NGC 4038/9, even given the typical differences between spiral galaxies and starbursts/mergers (Narayanan et al. 2011, 2012; Renaud et al. 2019a,b). Wilson et al. (2003) estimated $\alpha_{CO(1-0)} \approx 6.5 \, M_\odot \, pc^{-2} (K \, km \, s^{-1})^{-1}$ in NGC 4038/9 from

virial-mass estimates of resolved super giant molecular complexes, or a factor of ≈ 1.5 larger than the Milky-Way value we use here. Schirm et al. (2014) performed non-local thermodynamic equilibrium radiative transfer modeling of NGC 4038/9 with the RADEX code on eight transitions of CO and two transitions of [CI]. To make their mass estimate consistent with that of Brandl et al. (2009) they had to assume a starburst-like CO abundance and arrived at a conversion factor of $\alpha_{CO(1-0)} \approx 7 \, M_\odot \, pc^{-2} (K \, km \, s^{-1})^{-1}$, consistent with Wilson et al. (2003). Converting this conversion factor to CO (2–1), with the same R_{21} we adopted, gives a value of $\alpha_{CO(2-1)} \approx 10 \, M_\odot \, pc^{-2} (K \, km \, s^{-1})^{-1}$. Given the observed spread in the conversion factor within starbursts of factors of ~ 3 to 4 (Bolatto et al. 2013), we opted to simplify comparisons to previous works over adding another complication by assuming an offset in the factor that is well within the spread.

It is tantalizing with such high resolution and sensitive observations to attempt an estimate of the conversion factor through estimates of the virial mass. However, as shown in Figures 4.3 and 4.7, our estimates of the virial parameter of the molecular gas from 55 to 150 pc scales shows assuming the gas is in virial equilibrium is not necessarily true. The molecular gas may not be as unbound as the virial parameters indicate because our estimates of the virial parameter do not include the external pressures and gravitational potential the molecular gas is likely subject to from external stellar, atomic gas, and molecular gas material. Still, it is not clear from this analysis alone which pixels are likely to truly be near virial equilibrium and thus capable of rendering accurate estimates of the virial mass and therefore the conversion factor.

The situation may improve if we turn from this pixel-based analysis to a cloud-finding approach, since it may be more likely we could identify coherent and therefore marginally-bound molecular gas structures. However, comparisons of the pixel-based analysis by Sun et al. (2018) to the cloud-finding analysis by Rosolowsky et al. (2021) in PHANGS-ALMA galaxies and the pixel analysis of NGC 3256 by Brunetti et al. (2021) with the cloud analysis from Chapter 3 find general agreement between the molecular-gas properties measured with both techniques. Specifically, the very high virial parameters estimated in NGC 3256 by Brunetti et al. (2021) persisted in the cloud-finding analysis in Chapter 3 such that it is not obvious that a virial-mass estimate of the conversion factor is appropriate. Another way to view this is that if the range of virial parameters we estimate in NGC 4038/9 is correct (about an order of magnitude) then the result would be an equally-large spread in estimated conversion factors, and so

no better than the factor of ~3 to 4 spread mentioned above. Just to match that spread would require assuming two-thirds of the molecular gas observed had additional factors contributing to its boundedness, and with the present analysis there is no justification for that assumption or indication of which gas is bound or not. We plan to address the question of what conversion factor is appropriate for NGC 4038/9 by combining all CO data in the present observations with forthcoming ALMA observations in a radiative transfer analysis of several transitions and optically thin and thick CO isotopologues, at similar spatial resolution to the observations presented here.

There may actually be a signature in these data of the conversion factor in NGC 4038/9 changing in the gas closer to the nuclei. While a trend between the velocity dispersion and surface density in NGC 4038/9 is obvious up to about $10^3 \, \mathrm{M_\odot \, pc^{-2}}$, at surface densities above this there is a flattening of the trend that is most easily seen in Figure 4.10. Since this flattening is strongest in the nuclear sub-sample from NGC 4038/9, and is not seen in any of the sub-samples from Sun et al. (2020) who adopt a radially variable conversion factor, our choice of a single conversion factor for NGC 4038/9 is likely the cause. If the conversion factor in fact decreases towards the nuclei in NGC 4038/9 then the nuclear surface densities would be shifted to the left in Figure 4.10, by an amount that would depend on how close each pixel is to the nuclei. An interesting consequence of this interpretation is that for pixels with surface densities below about $10^3 \, \mathrm{M_\odot \, pc^{-2}}$, the conversion factor may not vary as much as when comparing the nuclear and outer regions. The limits of sensitivity and resolution should be kept in mind for the low velocity dispersion and surface density portion of this space. The censoring function derived by Sun et al. (2020) (see their figure 1 and appendix C) shows that at low surface density the detection probability for all velocity dispersions is reduced, but at high surface densities it is mostly the high velocity dispersions pixels that have poorer detection probablities. In other words, the censoring function rises steeply at low surface densities and flattens out somewhat at higher surface densities, potentially making the spread in the trend from the non-nuclear sub-sample at low surface densities appear smaller than it truly is.

4.5.3   Comparison of CO (2–1) and CO (3–2) in the overlap region

Preliminary insight into the excitation conditions for CO in NGC 4038/9 is possible through comparison of the measurements of CO (2–1) and CO (3–2) emission. Starting

with properties that do not depend on the choice of conversion factor, the peak brightness temperatures measured in the two transitions of CO in the overlap region are quite similar, though the sample from CO (3–2) is shifted to slightly lower temperatures. If both spectral lines are optically thick then their peak brightness temperatures would be roughly equal to the gas kinetic temperature, and so the simplest explanation for the difference in the observed peak temperatures would be the emission is coming from gas at different temperatures. The sense seems backwards however, since the J=3 level is a higher energy above the ground state than the J=2 level. It could be that the different spectral lines are emitted by gas at the same temperature but that the volume of emitting gas is different between the transitions such that the filling factor and thus the beam dilution is different. Having less gas emitting the CO (3–2) transition so beam dilution reduces the observed peak brightness temperature is plausible given the need for warmer and denser gas to excite the transition compared to CO (2–1).

The comparison of the velocity-dispersion samples is similar, with the CO (3–2) sample shifted to lower values than CO (2–1), but to a larger degree than the peak brightness temperatures. If the same gas was emitting the bulk of both transitions, we would expect the velocity dispersions to be the same since the velocities of the random motions within the beam should be of the same magnitude leading to the same broadening of the spectral lines. An important caveat to this comparison is that Sun et al. (2018) estimated their values from CO (3–2) using $\sigma_v = I_{CO}/(\sqrt{2\pi}T_{B,max})$ while we used the moment two, or intensity-weighted velocity dispersion, for CO (2–1). In the case of Gaussian spectral profiles, the two methods converge to the same accurate estimate of the width of the spectral line. However, when multiple spectral components are present (e.g. from distinct molecular-gas structures at different velocities along the line of sight) the methods can diverge from each other and will overestimate the velocity dispersion of each of the components. The disturbed nature of NGC 4038/9 and overlapping molecular gas, in projection, due to the placement of the progenitor galaxies means there is a fair fraction of pixels in both transitions that have multiple spectral components. Both methods will overestimate the velocity dispersion most when the spectral components have similar widths and peaks, and less when one component dominates the integrated intensity. The moment method has the added complexity that the degree it will overestimate the line-of-sight mass-weighted mean velocity dispersion also depends on the velocity separation of the spectral components. It is likely that

some of the increased scatter in Figures 4.9, 4.10, and 4.11 originates from the added variability of moment-two velocity dispersions depending on the velocity separation of spectral components along the line of sight. Techniques that decompose the spectral emission along the line of sight (e.g. cprops) will be necessary to estimate the velocity dispersion within spectrally distinct molecular-gas structures. A final caveat here is that the velocity resolution of the CO (3–2) observations is $5\,\mathrm{km\,s^{-1}}$ compared to $2.5\,\mathrm{km\,s^{-1}}$ for CO (2–1), which could mean the velocity dispersions may extend even lower in the CO (3–2) emission if observed at similar resolution.

As for the mass surface densities estimated from the two transitions, the sample from CO (3–2) is actually shifted to higher values than CO (2–1), despite the lower peak brightness temperatures and velocity dispersions. Since the integrated intensity is roughly proportional to the product of the peak brightness temperature and the velocity dispersion, it is surprising the surface densities are often higher from CO (3–2). The details of how the peak brightness temperatures combine with the velocity dispersions to make the surface densities are not obvious through this comparison of summary statistics, but the general trend should carry through for the bulk of the mass. Instead, the higher-than-expected surface densities from CO (3–2) may indicate the conversion of integrated intensity to mass is incorrect. Since both CO (2–1) and CO (3–2) use the Milky-Way conversion factor it would be specifically the intensity ratio of CO (3–2) to CO (1–0) or CO (2–1) to CO (1–0) that would be incorrect. The higher surface densities in CO (3–2) even outweigh the lower velocity dispersions resulting in lower virial parameters and higher internal turbulent pressures compared to CO (2–1). A more comprehensive comparison of these transitions, spanning the entire FoV covered here in CO (2–1), will be made using new ALMA observations of NGC 4038/9 as part of the conversion-factor analysis mentioned above.

As mentioned in Section 4.4.1, the changes in the median molecular-gas properties with resolution in NGC 4038/9 are typically small relative to PHANGS-ALMA measured by Sun et al. (2018, 2020). If you start with a beam that is roughly the size of a typical GMC and increase the size of the beam, it is expected that e.g. the measured surface density and peak brightness temperature would decrease as a result of beam dilution as less of the beam is filled with emission from clouds. That trend would be particularly obvious if the molecular ISM is clumpy, as observed in nearby spiral galaxies. If the beam you start with is smaller than the typical GMC size, then increasing the size of the

beam would likely not result in very much change in e.g. the measured surface density. In the second scenario, if the beam size eventually was made larger than a typical GMC then you would transition to the first scenario. Even weaker trends in median molecular-gas properties than those seen in NGC 4038/9 were measured in NGC 3256 by Brunetti et al. (2021), and a subsequent cloud finding analysis resulted in cloud radii slightly larger in NGC 3256 than PHANGS-ALMA galaxies (see Chapter 3). The weak trends measured in NGC 4038/9 imply it is also in the second scenario and that the typical size of GMCs may again be larger than those in PHANGS-ALMA galaxies. The clouds in NGC 4038/9 may not be as large as in NGC 3256 given the slightly stronger trends in NGC 4038/9. An interesting investigation would be to calculate the "clumping factor" defined by Leroy et al. (2013) for NGC 4038/9 and NGC 3256 and compare to those calculated by Sun et al. (submitted) for the PHANGS-ALMA galaxies. If the mergers exhibit lower clumping factors than the PHANGS-ALMA galaxies, then a shortcut for estimating the clumping and typical GMC size would be to calculate the changes in molecular-gas property medians over a fairly modest change in resolution.

4.6 Conclusions

We have presented GMC-scale observations of the central 9 kpc of NGC 4038/9 in CO (2–1). Maps of molecular-gas mass surface density, velocity dispersion, peak brightness temperature, virial parameter, and internal turbulent pressure have been derived from these data at a range of spatial resolutions from 55 to 150 pc. Comparisons of the pixel-by-pixel distributions of these gas properties from NGC 4038/9 have been made at matched spatial resolution to the PHANGS-ALMA sample of 70 nearby spiral galaxies (Sun et al. 2018, 2020), the overlap region of NGC 4038/9 observed in CO (3–2) (Whitmore et al. 2014; Sun et al. 2018), and the merger and nearest LIRG NGC 3256 (Brunetti et al. 2021).

Relative to the PHANGS-ALMA galaxies, NGC 4038/9 has some of the highest molecular gas surface densities, velocity dispersions, peak brightness temperatures, and turbulent pressures. These gas properties measured in the discs of the PHANGS-ALMA galaxies are often significantly lower than those measured in NGC 4038/9. The centres of the PHANGS-ALMA galaxies with the highest stellar masses do show some overlap with the gas properties in NGC 4038/9. Virial parameters measured in NGC 4038/9,

while spanning a large range, are much more similar to the PHANGS-ALMA galaxies than any other gas property. Differences by region in NGC 4038/9 (nuclei vs. non-nuclear) are similar to those seen in PHANGS-ALMA galaxies, with the most extreme gas properties near the nuclei.

Gas surface densities are similar between NGC 4038/9 and NGC 3256, though velocity dispersions near the nuclei of NGC 3256 and peak brightness temperatures throughout the system are significantly higher than in NGC 4038/9. Higher peak brightness temperatures may be caused by higher kinetic temperatures caused by the higher SFR in NGC 3256. Some of the higher velocity dispersions in the nuclei of NGC 3256 may be due to contamination from the jet in the southern nucleus and/or the outflow in the northern nucleus. However, larger line widths from more intense merger-driven gas flows to the nuclei of NGC 3256, that are producing more turbulence, could be a result of its later merger stage than NGC 4038/9. The wider, but systematically lower, range of virial parameters in NGC 4038/9 compared to NGC 3256 could also be a consequence of the differing merger stages. NGC 3256 may be leaving the starburst phase as coalescence of the progenitor galaxies increases the turbulence and suppresses further star formation, but NGC 4038/9 may be caught in the transition between bursts of enhanced star formation.

Comparisons of the molecular-gas properties of the overlap region in NGC 4038/9 estimated from the CO (2–1) presented here and CO (3–2) from Sun et al. (2018) show general agreement. Surface densities appear slightly lower and peak brightness temperatures slightly higher in CO (2–1), leading to higher virial parameters and lower turbulent pressures than CO (3–2). The difference in peak brightness temperature may be a result of different kinetic gas temperatures being traced by the different transitions, but this possibility cannot currently be distinguished from differences in filling factors and/or the degree of excitation. The higher surface densities derived from the CO (3–2) line are unexpected given the fairly similar velocity dispersions and lower peak brightness temperatures, and may indicate the conversion from integrated intensity to mass is not consistent between the two transitions.

Next steps will include applying a cloud-finding analysis to these observations of NGC 4038/9. The pixel-based analysis presented here is most accurate when one molecular cloud is along the line of sight and relies on assuming roughly one cloud is within each beam. A cloud analysis, which includes both spatial and spectral identification

of clouds, will allow us to verify the pixel-based velocity-dispersion measurements and directly measure the sizes of the clouds. Comparisons will also be possible with the cloud-finding results for PHANGS-ALMA galaxies by Rosolowsky et al. (2021) and NGC 3256 (Chapter 3).

Another line of investigation will focus on comparisons of several CO isotopologues and transitions across the entire region observed in this work. J=2–1 transitions of ^{13}CO and C^{18}O as well as the J=1–0 transition of ^{12}CO were also observed in this project and will allow for exact matching of *uv* coverage as well as spatial and spectral resolutions. Resolved intensity-ratios between transitions and relative abundances of the isotopologues can be estimated in this merging system for comparison with the Milky Way and nearby spiral galaxies. Additional observations are being obtained with ALMA, mapping the same field of view with the same array combinations in CO (3–2), extending the area probed by this transition at cloud scales beyond the overlap region for the first time. With three transitions of ^{12}CO a radiative transfer analysis will be possible to constrain the densities and temperatures of the molecular gas in NGC 4038/9, and help to estimate the CO-to-H$_2$ conversion factor at cloud scales.

Acknowledgements

This research has made use of the NASA/IPAC Extragalactic Database (NED), which is funded by the National Aeronautics and Space Administration and operated by the California Institute of Technology. This research has made use of the SIMBAD database, operated at CDS, Strasbourg, France (Wenger et al. 2000).

Data Availability

This paper makes use of the following ALMA data: ADS/JAO.ALMA#2018.1.00272.S (accessed from the ALMA Science portal at `almascience.org`). ALMA is a partnership of ESO (representing its member states), NSF (USA) and NINS (Japan), together with NRC (Canada), MOST and ASIAA (Taiwan), and KASI (Republic of Korea), in cooperation with the Republic of Chile. The Joint ALMA Observatory is operated by ESO, AUI/NRAO and NAOJ. The National Radio Astronomy Observatory is a facility of the National Science Foundation operated under cooperative agreement by Associated Universities, Inc.

The primary-beam cube from project ADS/JAO.ALMA#2011.0.00876.S was retrieved from the JVO portal (`http://jvo.nao.ac.jp/portal`) operated by the NAOJ.

The derived data generated in this research will be shared on reasonable request to the corresponding author.

4.A   Appendix: Modifications to the PHANGS-ALMA interferometric imaging pipeline

Starting from commit 5ef53d3, we made modifications to handle the additional array configurations and spectral lines present in the NGC 4038/9 observations compared to the bulk of the PHANGS-ALMA observations and to address some code bugs. The first change was to automate the continuum subtraction step based on the user-defined spectral-line centre and width parameters. Since the PHANGS-ALMA observations consisted of only one main-array configuration combined with the ACA and TP, the ability to combine two main-array configurations had to be added. This modification also included adding angular scales to use in Band 6 multi-scale cleaning of our extended main-array configuration data. Additionally, PHANGS-ALMA data consisted of only

Band 6 observations, primarily focused on ^{12}CO (J=2–1). Steps like channel binning had to be made to handle additional lines in the NGC 4038/9 observations, e.g. ^{12}CO (1–0), ^{13}CO (2–1), CN (1–0), etc. This modification also included the addition of angular scale specifications for the Band 3 multi-scale cleaning. Coding bugs were fixed that prevented clean masks from being used in the single-scale clean step and from manually specifying image and pixel sizes. At this stage we also added the ability to manually specify the "robust" argument to *tclean*.

Given the volume of data and computing resources available, we had to switch to setting "chanchunks" to −1 in *tclean* since our highest resolution cubes could not fit in memory all at once. To further improve memory management and processing speed, we removed additional image padding in R.A. and Dec. during imaging and instead added padding of the interferometric cubes before feathering to ensure the angular coverage was at least as large as the TP cubes. The final change related to the cube size was adding a check during writing masks to disk that would do the writing in batches of channels to avoid memory issues on our largest cubes that were about 16 GB in size. Since the pre-imaging regridding would not guarantee exactly the same spectral channels would be filled with data across all arrays, we added a call to the *split* task to remove one channel at each end of the imaging SPWs to avoid blank channels being included in the cube for cleaning. Finally, substantial effort was also spent on properly capturing all CASA logging output and redirecting it to output files. This message capturing was missing in version one and made it difficult to ensure each step was performed correctly as well as verifying adjustments to the code for the Antennae observations.

4.B Appendix: Anderson-Darling tests for NGC 4038/9 and Sun et al. (2020) galaxies

Summaries of the AD tests between NGC 4038/9 and PHANGS-ALMA galaxies from Sun et al. (2020), as described in Section 4.4.2, are shown in Figures 4.13 through 4.16 and Tables 4.1 and 4.2. Figures 4.13 and 4.14 and Table 4.1 show the results when the PHANGS-ALMA central pixels are those within a 1 kpc radius of the centre. Figures 4.15 and 4.16 and Table 4.2 show the results when the PHANGS-ALMA central pixels come from the designations by Sun et al. (2020).
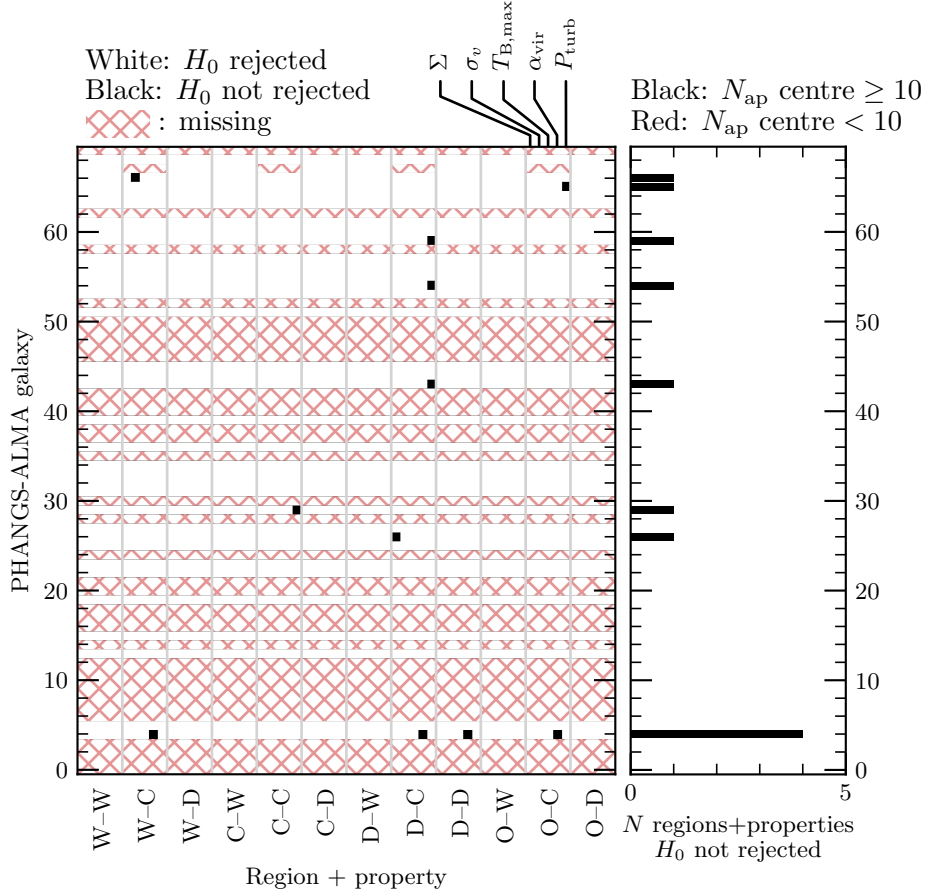
FIGURE 4.13: *Left:* A summary of which samples from the Sun et al. (2020) PHANGS-ALMA galaxies have H_0 rejected (white squares) or not rejected (black squares) from the 90 pc resolution measurements. Red hatches indicate where measurements were not available. Each row (y axis) is a separate galaxy, and each column is a different molecular-gas property (indicated at the top right). Vertical gray lines group the five gas properties tested for each region pair (e.g. whole FoV from NGC 4038/9 compared with the centre from PHANGS-ALMA galaxies). Region pairings are NGC 4038/9–PHANGS-ALMA where W = whole FoV, C = centre, D = disc, and O = overlap region (NGC 4038/9 only). Central pixels for the PHANGS-ALMA galaxies are those within a 1 kpc radius of the centre. *Right:* For each PHANGS-ALMA galaxy, the number of tests in which H_0 could not be rejected are shown by the horizontal bars. These are sums across all molecular-gas properties and region pairs. The bars are coloured red if there are less than ten apertures in the central region of the PHANGS-ALMA galaxy, and black otherwise.
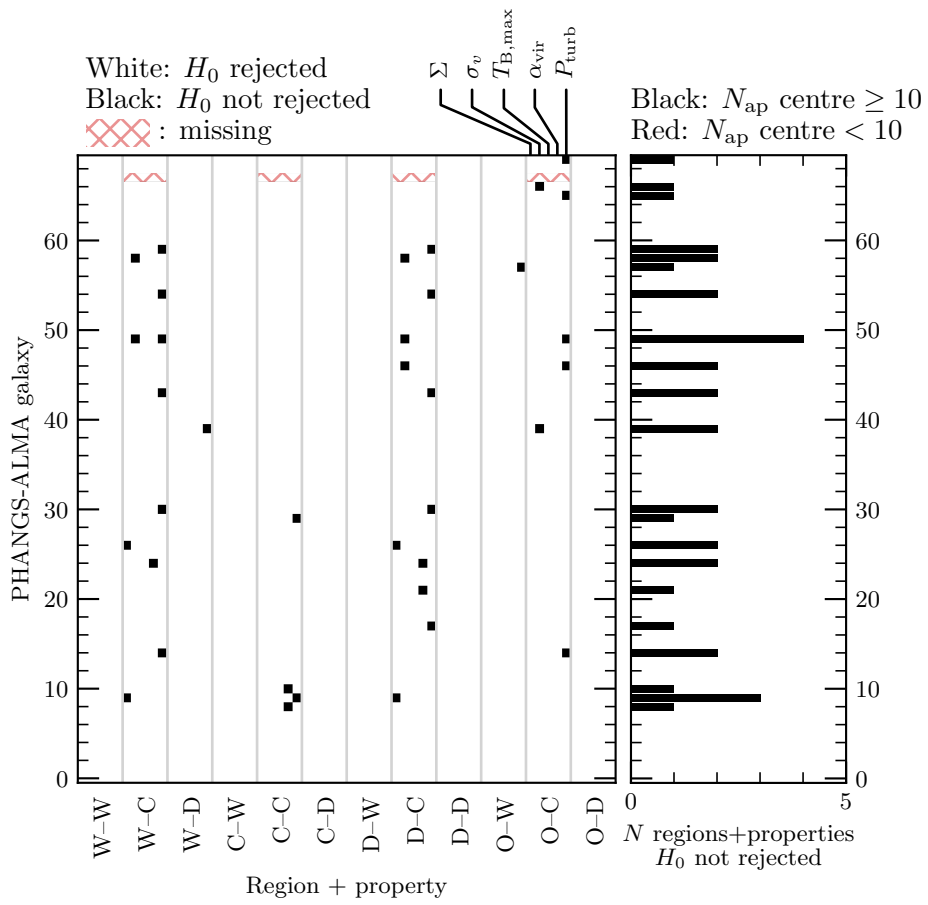
FIGURE 4.14: Same as Figure 4.13 but for the measurements made at 150 pc resolution.
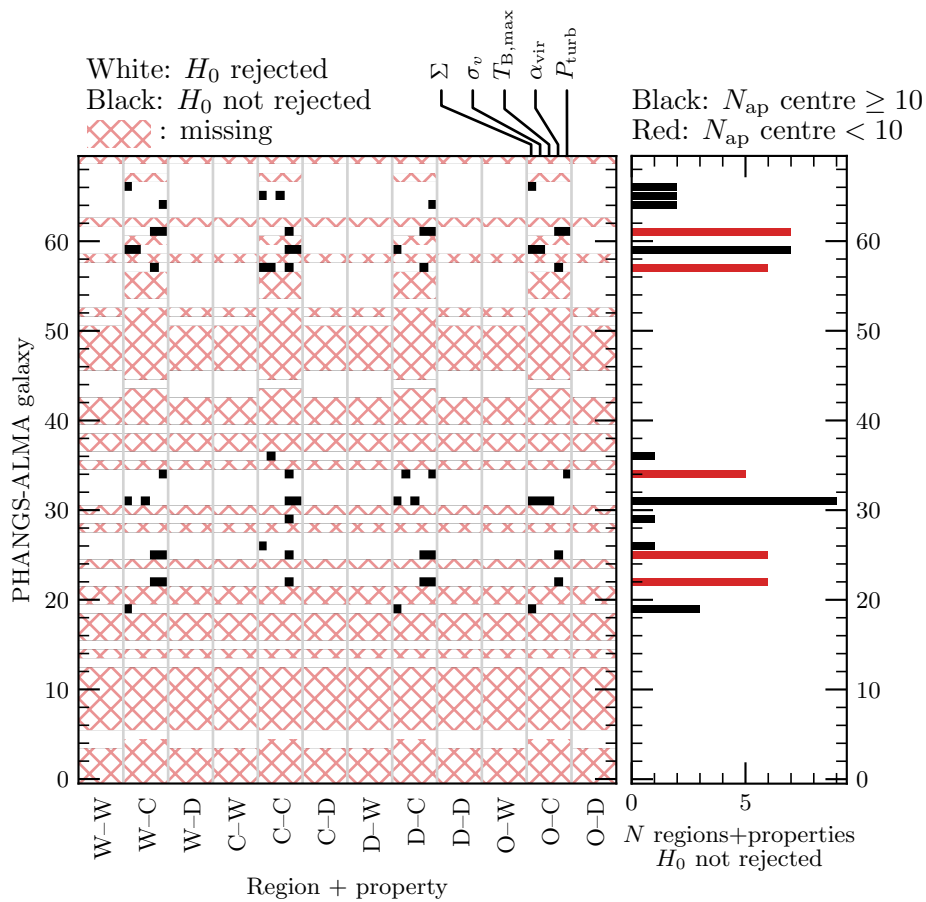
FIGURE 4.15: Same as Figure 4.13 but when the central pixels for the PHANGS-ALMA galaxies are based on the designations from Sun et al. (2020).

FIGURE 4.16: Same as Figure 4.15 but for the measurements made at 150 pc resolution.

TABLE 4.1: Summary of AD tests, aggregated by PHANGS-ALMA galaxy, when central pixels are within 1 kpc radius of the centre.

Galaxy	Figure ID[a]	$H_{0,150}$[b]	$H_{0,90}$[b]	$N_{ap,150}$		$N_{ap,90}$		$M_\star$[e]	SFR[e]	i[e]
				centre[c]	disc[d]	centre[c]	disc[d]	$(10^9\,M_\odot)$	$(M_\odot\,yr^{-1})$	(°)
NGC 4548	49	4	. . .	45	982	. . .	. . .	45.6	0.53	38.3
NGC 1300	9	3	. . .	118	919	. . .	. . .	71.9	2.06	31.8
NGC 2566	24	2	. . .	100	1878	. . .	. . .	40.6	8.47	48.5
NGC 4535	46	2	. . .	82	2351	. . .	. . .	32.3	2.07	42.1
NGC 3507	30	2	. . .	71	1019	. . .	. . .	27.3	0.75	24.2
NGC 4941	58	2	. . .	56	1140	. . .	. . .	12.4	0.36	53.1
NGC 1511	14	2	. . .	43	735	. . .	. . .	7.6	2.27	73.5
NGC 2903	26	2	1	63	2327	170	5292	28.9	2.08	67.0
NGC 4424	43	2	1	55	68	129	118	8.3	0.31	58.2
NGC 4694	54	2	1	37	39	71	58	7.8	0.15	60.7
NGC 4951	59	2	1	52	162	119	250	3.9	0.21	70.5
NGC 4293	39	2	0	51	113	122	195	30.6	0.60	65.0
NGC 1097	8	1	. . .	103	2990	. . .	. . .	60.8	5.08	48.6
NGC 1317	10	1	. . .	153	422	. . .	. . .	36.6	0.40	24.5
NGC 1792	21	1	. . .	59	1409	. . .	. . .	23.3	2.21	64.7
NGC 1559	17	1	. . .	67	2151	. . .	. . .	21.3	3.72	58.7
NGC 7496	69	1	. . .	107	1450	. . .	. . .	9.8	2.16	34.7

Continued on next page

Galaxy	Figure ID[a]	$H_{0,150}$[b]	$H_{0,90}$[b]	$N_{ap,150}$ centre[c]	$N_{ap,150}$ disc[d]	$N_{ap,90}$ centre[c]	$N_{ap,90}$ disc[d]	$M_\star$[e] $(10^9\,M_\odot)$	SFR[e] $(M_\odot\,yr^{-1})$	i[e] (°)
NGC 6300	66	1	1	89	2031	209	4007	29.2	2.39	49.3
NGC 3351	29	1	1	61	930	126	1327	20.8	1.09	45.1
NGC 5643	65	1	1	132	2535	313	4772	18.2	2.14	29.9
NGC 4826	57	1	0	83	64	226	82	16.0	0.20	58.6
NGC 300	4	0	4	29	98	13	80	1.7	0.14	39.8

[a] Index corresponding to the y axis of Figures 4.14 and 4.13.

[b] Number of tests that H_0 could not be rejected. This can be at most 60.

[c] Number of apertures in the centre sub-sample.

[d] Number of apertures in the disc sub-sample.

[e] Values from Sun et al. (2020).

Notes. Only galaxies with at least one test in which H_0 could not be rejected are shown. Rows are sorted first by $H_{0,150}$, then by $H_{0,90}$, and finally by $M_\star$.

TABLE 4.2: Same as Table 4.1 but instead using the centre and disc pixel designations from Sun et al. (2020).

Galaxy	Figure ID[a]	$H_{0,150}$	$H_{0,90}$	$N_{ap,150}$		$N_{ap,90}$		$M_\star$	SFR	i
				centre	disc	centre	disc	$(10^9\,M_\odot)$	$(M_\odot\,yr^{-1})$	(°)
NGC 3511	31	17	9	4	765	14	1656	5.1	0.42	75.0
NGC 1546	16	16	...	4	968	...	...	22.8	0.80	70.1
NGC 3621	34	16	5	1	1486	7	3375	9.2	0.79	65.4
NGC 4826	57	14	6	1	146	7	301	16.0	0.20	58.6
IC 1954	1	13	...	5	1049	...	...	6.6	0.48	57.2
NGC 5068	61	12	7	1	221	2	332	2.2	0.28	27.0
NGC 7456	68	12	0	1	132	7	182	1.2	0.06	63.7
NGC 4540	48	10	...	5	423	...	...	6.8	0.19	38.3
NGC 1511	14	9	...	10	768	...	...	7.6	2.27	73.5
NGC 2835	25	9	6	3	179	7	238	5.9	0.76	41.1
NGC 1637	19	8	3	7	1353	20	2786	7.7	0.66	31.1
NGC 1792	21	7	...	8	1460	...	...	23.3	2.21	64.7
NGC 4298	40	7	...	19	2309	...	...	13.0	0.56	59.6
NGC 4951	59	7	7	9	205	18	351	3.9	0.21	70.5
NGC 4535	46	5	...	7	2426	...	...	32.3	2.07	42.1
NGC 3626	35	5	...	15	135	...	...	27.5	0.23	46.6
NGC 7496	69	5	...	19	1538	...	...	9.8	2.16	34.7

Continued on next page

TABLE 4.2: *continued*

Galaxy	Figure ID[a]	$H_{0,150}$	$H_{0,90}$	$N_{ap,150}$		$N_{ap,90}$		$M_\star$	SFR	i
				centre	disc	centre	disc	$(10^9\,M_\odot)$	$(M_\odot\,yr^{-1})$	(°)
IC 5273	2	5	. . .	12	738	. . .	. . .	5.5	0.56	48.5
NGC 2283	23	5	0	6	281	17	543	3.6	0.26	44.2
NGC 4321	42	4	. . .	142	4781	. . .	. . .	49.4	3.41	39.1
NGC 3507	30	4	. . .	20	1070	. . .	. . .	27.3	0.75	24.2
NGC 5643	65	4	2	17	2650	38	5047	18.2	2.14	29.9
NGC 5042	60	4	0	2	298	. . .	364	4.7	0.33	51.4
NGC 4569	50	3	. . .	76	2468	. . .	. . .	67.2	1.54	70.0
NGC 1566	18	3	. . .	26	3918	. . .	. . .	53.3	4.49	30.5
NGC 253	3	3	. . .	13	2190	. . .	. . .	38.0	4.90	75.0
NGC 1317	10	3	. . .	35	540	. . .	. . .	36.6	0.40	24.5
NGC 3137	28	3	. . .	7	481	. . .	. . .	5.8	0.41	70.1
NGC 6300	66	3	2	32	2088	84	4132	29.2	2.39	49.3
NGC 5530	64	3	2	8	790	14	1488	9.4	0.31	61.9
NGC 2903	26	3	1	15	2375	49	5413	28.9	2.08	67.0
NGC 1433	13	3	0	78	606	221	772	52.9	0.81	28.6
NGC 2997	27	3	0	42	5338	113	11 598	31.2	2.79	31.9
NGC 4579	52	2	. . .	28	3050	. . .	. . .	83.1	1.08	37.3
NGC 5134	62	2	. . .	27	511	. . .	. . .	21.6	0.37	22.7

TABLE 4.2: *continued*

Galaxy	Figure ID[a]	$H_{0,150}$	$H_{0,90}$	$N_{ap,150}$		$N_{ap,90}$		$M_\star$	SFR	i
				centre	disc	centre	disc	$(10^9\,M_\odot)$	$(M_\odot\,yr^{-1})$	(°)
NGC 4536	47	2	. . .	31	1994	. . .	. . .	20.0	2.99	64.8
NGC 1672	20	2	. . .	44	1247	. . .	. . .	17.7	2.73	43.8
NGC 3627	36	2	1	21	2912	73	6898	53.1	3.24	56.5
NGC 3351	29	2	1	40	951	92	1361	20.8	1.09	45.1
NGC 4571	51	2	0	7	704	. . .	563	11.6	0.30	31.9
NGC 3596	33	2	0	15	480	35	891	3.5	0.23	21.6
NGC 1300	9	1	. . .	88	949	. . .	. . .	71.9	2.06	31.8
NGC 4548	49	1	. . .	37	990	. . .	. . .	45.6	0.53	38.3
NGC 4293	39	1	0	71	93	154	163	30.6	0.60	65.0
NGC 2090	22	0	6	. . .	516	3	1101	11.1	0.32	64.4

[a] Index corresponding to the y axis of Figures 4.16 and 4.15.

Bibliography

Astropy Collaboration et al., 2013, A&A, 558, A33

Astropy Collaboration et al., 2018, AJ, 156, 123

Barnes J. E., 1988, ApJ, 331, 699

Bemis A., Wilson C. D., 2019, AJ, 157, 131

Blanc G. A., et al., 2013, ApJ, 764, 117

Bolatto A. D., Wolfire M., Leroy A. K., 2013, ARA&A, 51, 207

Brandl B. R., et al., 2009, ApJ, 699, 1982

Brunetti N., Wilson C. D., Sliwa K., Schinnerer E., Aalto S., Peck A. B., 2021, MNRAS, 500, 4730

Chandar R., Fall S. M., Whitmore B. C., 2015, ApJ, 810, 1

Chandar R., Fall S. M., Whitmore B. C., Mulia A. J., 2017, ApJ, 849, 128

Comrie A., et al., 2021, CARTA: The Cube Analysis and Rendering Tool for Astronomy, doi:10.5281/zenodo.4905459

Gao Y., Lo K. Y., Lee S. W., Lee T. H., 2001, ApJ, 548, 172

Ginsburg A., et al., 2019, radio-astro-tools/spectral-cube: Release v0.4.5, doi:10.5281/zenodo.3558614

Herrera C. N., et al., 2020, A&A, 634, A121

Hunter J. D., 2007, Computing in Science & Engineering, 9, 90

Karl S. J., Naab T., Johansson P. H., Kotarba H., Boily C. M., Renaud F., Theis C., 2010, ApJ, 715, L88

Kennicutt R. C., de los Reyes M. A. C., 2021, ApJ, 908, 61

Klaas U., Nielbock M., Haas M., Krause O., Schreiber J., 2010, A&A, 518, L44

Kluyver T., et al., 2016, in Loizides F., Scmidt B., eds, 20th International Conference on Electronic Publishing. Positioning and Power in Academic Publishing: Players, Agents and Agendas. IOS Press, Netherlands, p. 87

Krumholz M. R., Burkhart B., Forbes J. C., Crocker R. M., 2018, MNRAS, 477, 2716

Leroy A. K., et al., 2013, ApJ, 769, L12

Leroy A. K., et al., 2016, ApJ, 831, 16

Leroy A. K., et al., 2021, ApJS, 255, 19

McKinney W., 2010, in Stéfan van der Walt Jarrod Millman eds, Python in Science Conf. Ser.. Available at: http://conference.scipy.org/proceedings/scipy2010/, p. 56

Mengel S., Lehnert M. D., Thatte N., Tacconi-Garman L. E., Genzel R., 2001, ApJ, 550, 280

Mengel S., Lehnert M. D., Thatte N., Genzel R., 2005, A&A, 443, 41

Mihos J. C., Bothun G. D., Richstone D. O., 1993, ApJ, 418, 82

Mok A., Chandar R., Fall S. M., 2020, ApJ, 893, 135

Moreno J., et al., 2019, MNRAS, 485, 1320

Narayanan D., Krumholz M., Ostriker E. C., Hernquist L., 2011, MNRAS, 418, 664

Narayanan D., Krumholz M. R., Ostriker E. C., Hernquist L., 2012, MNRAS, 421, 3127

Ochsenbein F., Bauer P., Marcout J., 2000, A&AS, 143, 23

Privon G. C., Barnes J. E., Evans A. S., Hibbard J. E., Yun M. S., Mazzarella J. M., Armus L., Surace J., 2013, ApJ, 771, 120

Querejeta M., et al., 2021, A&A, 656, A133

Renaud F., Bournaud F., Duc P.-A., 2015, MNRAS, 446, 2038

Renaud F., Bournaud F., Daddi E., Weiß A., 2019a, A&A, 621, A104

Renaud F., Bournaud F., Agertz O., Kraljic K., Schinnerer E., Bolatto A., Daddi E., Hughes A., 2019b, A&A, 625, A65

de los Reyes M. A. C., Kennicutt R. C., 2019, ApJ, 872, 16

Romano M., et al., 2021, A&A, 653, A111

Rosolowsky E., et al., 2021, MNRAS, 502, 1218

Sánchez Almeida J., 2020, MNRAS, 495, 78

Sandstrom K. M., et al., 2013, ApJ, 777, 5

Schirm M. R. P., et al., 2014, ApJ, 781, 101

Scholz F. W., Stephens M. A., 1987, Journal of the American Statistical Association, 82, 918

Schweizer F., et al., 2008, AJ, 136, 1482

Scott D. W., 1992, Multivariate Density Estimation: Theory, Practice, and Visualization. Wiley Series in Probability and Statistics, John Wiley & Sons, New York

Shetty R., Ostriker E. C., 2012, ApJ, 754, 2

Stanford S. A., Sargent A. I., Sanders D. B., Scoville N. Z., 1990, ApJ, 349, 492

Stierwalt S., et al., 2013, ApJS, 206, 1

Sun J., et al., 2018, ApJ, 860, 172

Sun J., et al., 2020, ApJ, 901, L8

Toomre A., Toomre J., 1972, ApJ, 178, 623

Trujillo I., Chamba N., Knapen J. H., 2020, MNRAS, 493, 87

Utomo D., et al., 2018, ApJ, 861, L18

Virtanen P., et al., 2020, Nature Methods, 17, 261

van der Walt S., Colbert S. C., Varoquaux G., 2011, Computing in Science & Engineering, 13, 22

Wenger M., et al., 2000, A&AS, 143, 9

Whitmore B. C., et al., 2010, AJ, 140, 75

Whitmore B. C., et al., 2014, ApJ, 795, 156

Wilson C. D., Scoville N., Madden S. C., Charmandaris V., 2000, ApJ, 542, 120

Wilson C. D., Scoville N., Madden S. C., Charmandaris V., 2003, ApJ, 599, 1049

Wilson C. D., Elmegreen B. G., Bemis A., Brunetti N., 2019, ApJ, 882, 5

5 | Summary and future work

5.1   Summary of this work

Major galaxy mergers significantly alter many properties of the progenitor galaxies and produce some of the most extreme star-forming environments. While not common in the local universe, the nearest mergers act as crucial laboratories for the study of starburst activity and the conditions within the interstellar medium (ISM) that produce such vigorous star formation. High spatial resolution observations of these nearby systems allow us to resolve the molecular-gas structures from which stars and stellar clusters are born. These observations provide the constraints necessary for refining models of star formation and galaxy evolution under some of the most extreme conditions a galaxy experiences. By extension, studying local galaxy mergers also helps us probe the conditions in the early universe when mergers were much more common and star formation was ocurring much more rapidly. In this thesis, I have presented the highest spatial resolution observations to date of the giant molecular cloud (GMC)-scale carbon monoxide (CO) J=2–1 spectral line in two local mergers, NGC 3256 and NGC 4038/9, with detailed comparisons to nearby spiral galaxies.

In Chapter 2 we presented our observations of NGC 3256 with a pixel-by-pixel analysis at a range of spatial resolutions, from 120 to 55 pc. We calculated molecular-gas properties including mass surface density, velocity dispersion, peak brightness temperature, virial parameter, and internal turbulent pressure in all pixels with significant emission detected. We then compared the mass-weighted distributions of these properties in NGC 3256 to an early sample from the Physics at High Angular resolution in Nearby GalaxieS with ALMA (PHANGS-ALMA) survey of 14 nearby spiral galaxies, and found that all properties are high in NGC 3256. High mass surface densities imply larger quantities of molecular gas in the merger (and at higher densities). The large velocity dispersions indicate greater levels of turbulence in the ISM from the high star-formation rate (SFR) and tidally-driven gas flowing towards the nuclei. High peak brightness temperatures are likely associated with higher kinetic temperatures of the molecular gas also from the elevated SFR. The molecular gas appears largely unbound by self gravity as indicated by high virial parameters. We estimated that for clouds in NGC 3256 to be bound under their own gravity, they would either need to have radii of 150 to 500 pc or an order of magnitude more external mass surface density than PHANGS-ALMA galaxies to produce enough external pressure to balance the very high

internal pressures of the molecular gas. Finally, we argued that the small changes with resolution measured in the mass-weighted median surface densities, velocity dispersions, and peak brightness temperatures relative to the PHANGS-ALMA galaxies are a signature of a smoother molecular ISM in NGC 3256 compared to "normal" spiral galaxies.

In Chapter 3 we presented the analysis of 185 molecular clouds identified in our NGC 3256 observations, with a comparison to cloud-finding results from PHANGS-ALMA galaxies. We carefully matched spatial resolutions and analysis methods to maximize the robustness of these comparisons. The molecular-cloud properties in NGC 3256 again appeared extreme relative to the properties measured in the PHANGS-ALMA galaxies: larger mass-weighted median cloud mass surface density, velocity dispersion, CO luminosity, CO-estimated mass, virial mass, virial parameter, size-linewidth coefficient, and internal turbulent pressure. A slightly larger mass-weighted median cloud radius in NGC 3256, despite matched 90 pc resolution to the PHANGS-ALMA observations, indicates the difference in cloud sizes is real. While shorter free-fall times were expected in clouds within NGC 3256 because of the significantly higher surface densities, the differences in free-fall times were not as significant due to the larger cloud sizes.

Samples of cloud properties in NGC 3256 were shown to likely be originating from different underlying distributions than all PHANGS-ALMA galaxies through two-sample Anderson-Darling (AD) tests. We found the most extreme clouds (e.g. largest masses, radii, surface densities, velocity dispersions) were typically found closer to the nuclei. Also, we showed that clouds with the smallest radii and lowest velocity dispersions are usually the ones most consistent with clouds in PHANGS-ALMA galaxies, with the exception that small-radii clouds can be quite different from PHANGS-ALMA clouds in the size-linewidth vs. surface density plane. Two-sample AD tests on the sample of cloud eccentricities in NGC 3256 showed it is indistiguishable from several samples from PHANGS-ALMA galaxies, potentially indicating the average dynamical state of clouds in the merger is not much different from that in some nearby spiral galaxies. Using Kolmogorov-Smirnov (KS) tests on the distributions of cloud position angles (PAs), we found almost no evidence for the alignment of the projected orientations of the clouds in NGC 3256. We fit the mass function of clouds in NGC 3256, finding the shape was roughly consistent with both an independent analysis of the data as well

as many of the cloud mass functions from PHANGS-ALMA galaxies. Camparing the samples of cloud-based properties to our pixel-based properties from Chapter 2 showed general consistency between the methods, but also highlighted their complementary nature. We carried out completeness estimation on our cloud-finding results through false-source injection and retrieval, and we used three-dimensional logistic regression to fit the completeness test results to estimate the completeness for each cloud found in the real data. We also expanded the visualization of the completeness and logistic-regression results to be shown in terms of the "observable" cloud properties.

In Chapter 4 we presented our observations of NGC 4038/9 and a pixel-based analysis using the same method as on NGC 3256 in Chapter 2. We calculated the same set of molecular-gas properties as in Chapter 2 and at a variety of spatial resolutions, this time from 55 to 150 pc. Using two-sample AD tests we compared the samples of molecular-gas properties in NGC 4038/9 to those from NGC 3256 from Chapter 2, the early PHANGS-ALMA sample used in Chapter 2, the full PHANGS-ALMA sample of 70 nearby spiral galaxies, and estimates made in the overlap region of NGC 4038/9 from previous CO (3–2) observations. Comparisons were made between all permutations of the entire mapped field of views (FoVs), centres/nuclei of galaxies, outside the centres, and the overlap region of NGC 4038/9. We found NGC 4038/9 appeared similarly extreme relative to the PHANGS-ALMA galaxies as NGC 3256, with the centres of only the most massive spiral galaxies approaching the properties measured in NGC 4038/9. However, the virial parameters measured in NGC 4038/9 are consistent with those measured in many of the PHANGS-ALMA galaxies (while spanning the largest range of any of the galaxies presented), and they are significantly lower than in NGC 3256. Combining the higher virial parameters in NGC 3256 with its higher peak brightness temperatures and nuclear velocity dispersions, we argued that approaching coalescense has produced greater levels of turbulence through stronger tidally-driven gas flows as well as the higher measured SFR, which in turn has heated the gas to higher temperatures. We compared the samples of molecular-gas properties in just the overlap region estimated from our CO (2–1) with those from CO (3–2) and found general agreement despite the significant differences in sensitivity to large spatial scales.

5.2 Implications

5.2.1 Molecular-gas properties in mergers are extreme

Throughout this thesis we have shown that the molecular-gas properties in local merging galaxies are generally extreme relative to nearby spiral galaxies. Given the high SFRs, especially in NGC 3256, it is not surprising the molecular gas mass surface densities and peak brightness temperatures are higher in the mergers studied here compared to spiral galaxies. Large quantities of rapid star formation require large reservoirs of dense fuel (e.g. Kennicutt & de los Reyes 2021), and the young massive stars produced will influence their gas environments resulting in a hotter ISM (e.g. Tielens & Hollenbach 1985; Draine 2003).

However, it is important to keep in mind that the extragalactic observational tracers of SFR are not instantaneous, but instead use the quantity of currently existing young stars to estimate the SFR averaged back in time. On the other hand, measurements of gas properties *are* current so that there is a time lag between the initial conditions for star formation determined by the molecular-gas properties and the observed SFR. This time lag could help reconcile the high SFR in NGC 3256 with the high velocity dispersions (and thus high virial parameters) we have measured. We have shown that the velocity dispersions measured in the molecular gas within these mergers appear high enough that we expect the clouds to be largely unbound under their own self gravity (again especially in NGC 3256). Complicating the explanation for both high SFRs and virial parameters, however, is the caveat that our virial parameter estimates are made under the simplification of not accounting for mass external to the molecular clouds (i.e. binding contributions beyond self gravity). So it may be that the strongest conclusion we can make about the dynamical state of the molecular gas in these mergers with the current observations is that a more complete estimate of the confining forces is needed. It may even be more important to include this complete account of binding forces in mergers than in spiral galaxies since the simple estimates of boundedness in spiral galaxies (i.e. Sun et al. 2018) give broadly the same answer as a more complete dynamical modelling that includes various massive components of the galactic disc (i.e. Sun et al. 2020). Through our simple estimate of the amount of external mass surface densities required to bind the gas observed in NGC 3256 we can only say that it is likely that some of

the gas is bound given the broad range of requisite surface densities. So the question becomes: is enough molecular gas bound and destined to collapse to maintain the high SFRs in NGC 3256 or are we seeing the conditions that will precede the decline of its SFR?

5.2.2 The extremity of molecular-gas properties depends on merger stage

In Chapter 4 we showed that, while the two mergers NGC 3256 and NGC 4038/9 exhibit some of the most extreme molecular-gas properties in nearby galaxies, there are differences in those properties between the two systems. Simulations have shown that enhancements in SFR and gas properties throughout the process of two galaxies merging are not constant and not identical across differing progenitors (e.g. Dubinski et al. 1996; Boylan-Kolchin et al. 2005; Moreno et al. 2019; Hani et al. 2020). So when galaxy mergers are observed, at whichever snapshot of the merging process we happen to catch them, their gas properties will not be altered relative to nearby spiral galaxies in exactly the same ways. In NGC 3256 and NGC 4038/9 we are seeing how coalescense and pericentre passages impact molecular gas, respectively. Close passages lead to both bursty and long-lived (~1 Gyr) enhancements in the SFR, caused by tidal torques driving gas flows to the centres of the progenitors where high gas densities are formed (e.g. Hernquist 1989; Barnes & Hernquist 1991; Blumenthal & Barnes 2018). Coalescense takes that process to an even more extreme level, where SFR can be enhanced by another factor of five, and then decline to non-merger levels over 500 to 1000 Myr (Moreno et al. 2019; Hani et al. 2020). The longer time scale for the SFR to return to non-merger levels after pericentre passages may be appearing in the lower virial parameters in NGC 4038/9 compared to NGC 3256. We do caution that this interpretation is based on observations of mergers at only two points in the process, where *any* differences in properties could be ascribed to a trend.

5.2.3 Smoother molecular ISM in mergers

Our identification of clouds with larger radii and very weak trends with spatial resolution in surface density, velocity dispersion, and peak brightness temperature imply a molecular ISM in some mergers that is made of larger structures and possibly even

smoother than in nearby spiral galaxies. Increased gas fractions in mergers have been observed on large scales (e.g. Ellison et al. 2015; Violino et al. 2018) and appear in simulations of mergers, with evidence for mass enhancements of the densest gas being the most dramatic (Moreno et al. 2019). A ubiquitous molecular medium would result in cloud identification schemes (that must segment emission into chunks) finding larger clouds. It could also reduce the apparent clumpiness if GMCs are embedded in a diffuse molecular reservoir rather than being high-density "islands" in an atomic-gas-filled medium. The smaller change in median properties we measure in NGC 3256 compared to NGC 4038/9 may again be a result of their different merger stages, where the more-advanced merger has a larger molecular-gas volume filling fraction due to more intense tidal and morphological disturbances further compressing the gas. All else held constant, the degree of clumpiness/smoothness in the molecular ISM may be related to the strength of interaction-induced gas compression.

5.2.4   Analysis methods

We believe the general consistency our pixel and cloud-based analyses of NGC 3256 in Chapters 2 and 3 shows the complementary nature of the methods. The pixel analysis has the shortcomings of needing to assume a size for the molecular clouds and being most accurate when only a single cloud is along the line of sight. Carrying out the cloud analysis directly determines the sizes of the clouds from the data and is able to separate clouds along the line of sight whose velocity separations are resolved. However, the cloud analysis relies on a particular definition of cloud boundaries that is largely arbitrary, but worst of all, means the boundaries depend on the resolution and noise of the data. Measuring properties on a regular spatial grid with a pixel-based analysis puts all emitting regions on the same footing, mitigating most of the influence of the quality of the particular data. Consistency between these two methods means the assumed sizes, number of clouds along the line of sight, and cloud boundaries are representative of the molecular-gas structures and the method is not strongly altering the results.

However, this consistency in sizes and velocity dispersions in NGC 3256 should not be taken as proof that all mergers would exhibit consistent results when analysed with these two methods. We emphasize that these morphologically disturbed systems, where expectations for molecular-cloud sizes are not well constrained and gas components from

the progenitor systems can overlap in projection, are the most likely places for pixel-based analyses to suffer. In addition, if the molecular ISM is more ubiqitous in mergers on average, then cloud boundaries may not be well defined resulting in cloud analyses being even more dependent on resolution and noise levels. Carrying out both analyses on cloud-scale observations of molecular gas in mergers will help mitigate assumptions of size, the number of clouds along the line of sight, and definitions of cloud boundaries.

We also believe it is important to emphasize the need for homogenization of data and procedures in analysing observations like those presented in this thesis. Many studies have shown the importance of matching spatial resolution, spectral resolution, spatial filtering, noise levels, etc. in cloud-finding analyses of observations (e.g. Reid et al. 2010; Hughes et al. 2013; Rosolowsky et al. 2021). The carefully-constructed and described procedure for homogenizing molecular-gas observations for cloud finding by Rosolowsky et al. (2021) and our work replicating it with our observations are necessary strides in making molecular-cloud comparison studies robust against systematic uncertainties. While some of our analysis was not identical to that by Rosolowsky et al. (2021), the mass function fitting in particular, we hope that by publishing our cloud catalogue in an accessible electronic form as they did means the results from NGC 3256 can be incorporated into subsequent analyses in as robust a way as possible.

5.3 Moving forward

Looking to the future, the analyses of the data sets presented in this thesis are not exhaustive. We have plans for several additional investigations on the data we already possess, and we have plans for acquiring further observations of these merging systems to probe deeper.

In Chapter 3 we showed the utility in carrying out a cloud-identification analysis on the CO spectral-line observations of NGC 3256, both for verifying our results from the pixel-based analysis from Chapter 2 and for comparisons to previous cloud results in other galaxies. We plan to perform a cloud analysis on our observations of NGC 4038/9 from Chapter 4 to complement the pixel analysis presented there. We will investigate the impact of clouds overlapping along the line of sight, especially in the overlap region, on our estimates of molecular-gas velocity dispersions. Using the same methods as we did on NGC 3256 will allow us to explore if cloud radii are generally larger in galaxy

mergers or whether cloud radii also potentially depend on the merger stage. Estimates of the CO-luminous masses and virial masses of clouds in NGC 4038/9 are also of interest given the significantly lower virial parameters we estimated pixel-by-pixel. We also plan to measure the cloud mass function and its shape in NGC 4038/9, which can be compared to studies measuring the young-massive cluster mass function (e.g. Mok et al. 2020). This comparison can be used to understand the star and cluster formation efficiencies at very high molecular gas mass surface densities, potentially probing the formation environments of globular clusters.

Accompanying the ^{12}CO (2–1) observations of NGC 4038/9 are ^{13}CO (2–1), C^{18}O (2–1), and ^{12}CO (1–0), all at the same spatial and spectral resolutions. Also, a new Atacama Large Millimeter/Submillimeter Array (ALMA) observing program has been accepted and is underway to add ^{12}CO (3–2), ^{13}CO (1–0), and C^{18}O (1–0) at cloud scales to this data set. All of these different isotopologues and rotational transitions will be combined in a large velocity gradient (LVG) analysis to model and constrain the molecular-gas densities and temperatures throughout NGC 4038/9. We will also be able to estimate the CO-to-H$_2$ conversion factor at cloud scales. Finally, a much more direct comparison of the molecular-gas properties derived from CO (2–1) and CO (3–2), matching spatial scale sensitivity across both nuclei and the overlap region, will be carried out beyond that presented in Chapter 4.

We also have plans to propose for even higher spatial resolution ALMA observations of the molecular gas in NGC 3256 and NGC 4038/9. Adding the most extended configurations to attain the highest possible resolution possible with ALMA will allow us to probe down to 12 pc scales in NGC 3256, for example, and search for evidence of the molecular ISM transitioning from smooth to clumpy. We expect that at some point the substructure within the molecular clouds (e.g. clumps and cores) will be resolved since those are the sites of immediate cluster and star formation. Attempting to measure the demographics of the largest clumps in a luminous infrared galaxy (LIRG) and galaxy merger would be very informative for the types of environments where the most intense star formation occurs. With these new observations it will also be possible to jointly image all of the data together with those presented in this thesis so that all spatial scales down to sub GMCs are captured. Then it would be possible to investigate the structure of the ISM from kpc down through ∼10 pc, all within merger systems.

Regardless of if we acquire higher-resolution observations of NGC 3256 and/or

NGC 4038/9, we plan to calculate the "clumping factor" introduced by Leroy et al. (2013) in both systems for comparison with the factors calculated across the entire PHANGS-ALMA galaxy sample. This quantitative comparison should help us test if the molecular ISM is actually smoother/ubiquitous on cloud scales, along with searching for galactic properties that drive spiral galaxies and mergers to be smoother or more clumpy. The inclusion of several interacting spiral galaxies in the PHANGS-ALMA sample also offers the possibility to search for a continuous transition of the ISM in galaxies from clumpy to smooth.

We also feel it would be useful to further explore the dynamical state of the molecular gas in NGC 3256 and NGC 4038/9 through the balance of internal and external pressures arising from all components of the galactic potential, similar to Sun et al. (2020). The applicability of the simple virial parameter that neglects external pressure terms is likely limited in major mergers that are experiencing violent relaxation and intense gas flows, but we need quantitative estimates of the importance of external forces. This will necessitate a similar multi-wavelength analysis of these systems, to make spatially-resolved estimates of the atomic gas, stellar, and molecular gas masses. Long wavelength stellar-mass tracers will be especially important to include dust-obscured stars in these dusty mergers. Finally, modeling the distributions of matter will require special attention as the typical assumptions of vertical hydrostatic equilibrium in a well-behaved disc are likely violated in mergers.

There are also important avenues of investigation that extend beyond the two mergers analysed in this thesis. Previously targeted observations of other mergers as well as future surveys that begin to homogeneously build a sample of cloud-scale merger observations akin to PHANGS-ALMA for nearby spiral galaxies should both be leveraged.

The first place we plan to look is to the public ALMA archive for cloud-scale observations of other galaxy mergers that can be analysed similarly and compared to NGC 3256 and NGC 4038/9. While matching all observational parameters like spatial and spectral resolution, sensitivity, spatial scales probed, etc. will not likely be possible across all existing observations, we can begin to fill out the demographics of molecular gas and clouds this way. Larger samples of merging galaxies will allow us to explore trends with merger stage like the molecular-gas densities, velocity dispersions, temperatures, dynamical states, and degree of clumping. The diversity of viewing angles, orbital parameters, and merger-progenitor properties means there is a significant

parameter space possible in merging galaxies that needs to be constrained at high spatial resolution. Archival studies have proven not only possible but fruitful given the wealth of precision data sets in the archive (e.g. Wilson et al. 2019; Brunetti & Wilson 2019; Ledger et al. 2021; Sánchez-García et al. 2021). Preliminary results, despite the data heterogeneity, could also add to the scientific case for future large proposals to survey mergers homogeneously with ALMA.

While it may seem obvious that a significant improvement to our understanding of merging galaxies would be made through a PHANGS-ALMA-type survey of mergers, this will be an expensive task to undertake. The relative rarity of galaxy mergers in the local universe means large distances to a sizeable sample of systems would require very high spatial resolution which in turn makes the surface-brightness sensitivity very costly to achieve (even pushing the limits of ALMA and the generosity of their proposal reviewers). To take the same approach as PHANGS-ALMA would mean carefully selecting systems for observing efficiency as well as to attempt wide coverage of different merger stages, progenitor properties, etc. The next major steps in constraining molecular-gas properties in merging galaxies will rely on making this kind of survey a reality, however, as there is only so much that can be learned about the general process of merging through detailed studies of one or two systems.

Another crucial direction for future work is through collaboration with the community of simulators that is producing high-resolution predictions for the molecular ISM in interacting and merging galaxies (e.g. the Feedback In Realistic Environments-2 suite; Hopkins et al. 2018). Approaching the analysis of simulations as we do observations would help develop effective metrics and statistics to use in both cases that can be easily compared. Such synergy has been demonstrated in comparisons of interacting galaxies in Sloan Digital Sky Survey (SDSS) observations and cosmological simulations from IllustrisTNG (e.g. Patton et al. 2013, 2020; Hani et al. 2020). Specific criteria for matching interacting galaxies with robust control galaxies were developed and refined over hundreds of thousands of observed and simulated galaxies. While the high-resolution approach of our observations and the simulations presented by e.g. Moreno et al. (2019) means we cannot explore sample sizes that large, we need to begin working towards the most important properties of the molecular gas for teasing out differences between observations and simulations. These kinds of simulations can also help put our observations into better context, by making estimates of the merger stage and progenitor

properties that are observationally inaccessible. The ideal workflow is one where observers and simulators work together to find where our models for galaxy evolution and star formation are incomplete, formulate the questions we believe will help us improve those models, design our observations to retrieve those answers, and through analysis produce more complete models and the next set of questions.

Bibliography

Barnes J. E., Hernquist L. E., 1991, ApJ, 370, L65

Blumenthal K. A., Barnes J. E., 2018, MNRAS, 479, 3952

Boylan-Kolchin M., Ma C.-P., Quataert E., 2005, MNRAS, 362, 184

Brunetti N., Wilson C. D., 2019, MNRAS, 483, 1624

Draine B. T., 2003, ARA&A, 41, 241

Dubinski J., Mihos J. C., Hernquist L., 1996, ApJ, 462, 576

Ellison S. L., Fertig D., Rosenberg J. L., Nair P., Simard L., Torrey P., Patton D. R., 2015, MNRAS, 448, 221

Hani M. H., Gosain H., Ellison S. L., Patton D. R., Torrey P., 2020, MNRAS, 493, 3716

Hernquist L., 1989, Nature, 340, 687

Hopkins P. F., et al., 2018, MNRAS, 480, 800

Hughes A., et al., 2013, ApJ, 779, 46

Kennicutt R. C., de los Reyes M. A. C., 2021, ApJ, 908, 61

Ledger B., Wilson C. D., Michiyama T., Iono D., Aalto S., Saito T., Bemis A., Aladro R., 2021, MNRAS, 504, 5863

Leroy A. K., et al., 2013, ApJ, 769, L12

Mok A., Chandar R., Fall S. M., 2020, ApJ, 893, 135

Moreno J., et al., 2019, MNRAS, 485, 1320

Patton D. R., Torrey P., Ellison S. L., Mendel J. T., Scudder J. M., 2013, MNRAS, 433, L59

Patton D. R., et al., 2020, MNRAS, 494, 4969

Reid M. A., Wadsley J., Petitclerc N., Sills A., 2010, ApJ, 719, 561

Rosolowsky E., et al., 2021, MNRAS, 502, 1218

Sánchez-García M., et al., 2021, preprint (arXiv:2111.03876),

Sun J., et al., 2018, ApJ, 860, 172

Sun J., et al., 2020, ApJ, 892, 148

Tielens A. G. G. M., Hollenbach D., 1985, ApJ, 291, 722

Violino G., Ellison S. L., Sargent M., Coppin K. E. K., Scudder J. M., Mendel T. J., Saintonge A., 2018, MNRAS, 476, 2591

Wilson C. D., Elmegreen B. G., Bemis A., Brunetti N., 2019, ApJ, 882, 5

A | Cleaning the NGC 3256 CO (2–1) ALMA cube

A.1 Multi-scale clean (step 1)

We began with multi-scale clean to prevent modeling the largest-scale, diffuse emission with point sources. This approach avoids cleaning "holes" into the diffuse emission which could happen with small point-source clean masks. Scales were chosen through trial-and-error to satisfy the criteria of cleaning the large-scale structures with as few scales as possible and not cleaning too deeply too quickly. These criteria prevented the creation of negative features 2 to 3 times the size of the synthesized beam arising from cleaning large amounts of emission in one major cycle. We settled on scales of 15, 20, and 25 pixels, using square pixels that were $0\rlap{.}''0416$ on a side. The resulting synthesized beam full width at half maximum (FWHM) was $0\rlap{.}''25 \times 0\rlap{.}''22$. We ran five major cycles with these scales before one roughly -13σ feature appeared in a single channel, about the size of the synthesized beam.

Masks were manually drawn or edited at each major cycle to broadly encompass most of the emission present. We began with large masks to give the large-scale model components room to fit the large-scale emission. Masks were extended as we cleaned deeper and more real emission was revealed. This approach differs slightly from a typical point-source clean that starts by masking only the brightest regions of emission and is extended as emission is cleaned. The output cube had a significant amount of the diffuse emission cleaned. This processing left the residual cube with primarily just significant point sources and filamentary structures up to a few synthesized beams in width.

A.2 Supervising the automultithresh algorithm during point-source cleaning (step 2)

Since the remaining emission was on the scale of the synthesized beam, we continued cleaning from where the multi-scale clean finished, but using only point-source model components. The automultithresh algorithm satisfactorily masked about 90 per cent of the remaining emission at this step, using the set of parameters recommended[1] for imaging combined 12 m and 7 m observations. These settings are listed in Table A.1.

---

[1] https://casaguides.nrao.edu/index.php/Automasking_Guide

TABLE A.1: Settings for automultithresh used during point-source cleaning.

Argument name	Value
'sidelobethreshold'	2.0
'noisethreshold'	4.25
'minbeamfrac'	0.3
'lownoisethreshold'	1.5
'negativethreshold'	0.0

automultithresh struggled in places where 1) faint, diffuse emission in the southern region of the galaxy was not included in clean masks and 2) the mask was expanded too far out from the peaks in the faint northern arm near the edge of the map. Since automultithresh resulted in both too little and too much masking, but the majority of the masking appeared to be reasonable, we decided to interactively edit the automatically generated masks at each major cycle. This editing allowed us to prevent over-cleaning (e.g. around the northern arm). Note that when running *tclean* interactively, 'cycleniter' must be set to the same value as 'niter' to make the automultithresh algorithm behave as it would in non-interactive mode.

In a majority of major cycles we added to the mask, extending it over the diffuse emission sooner than the algorithm would have naturally done. We could do this because we had seen how far the emission went in some of our previous clean attempts, as well as being able to see how emission persisted over multiple channels. This expansion was done primarily in the southern part of the field of view (FoV). We also removed masking around the northern arm once the brightest ridge of emission was cleaned. automultithresh continued to mask a large elliptical region around the arm, ~3 to 4 times the width of the arm, which was difficult to distinguish from an imaging artefact. This portion of the mask was removed for several cycles until it appeared clear there was no further strong emission coming from the centre of the arm. The remaining emission appeared real so we let the mask extend around the centre of the arm by a few widths. It did not take long for this feature to be cleaned so we then removed the mask again for subsequent major cycles. Finally, we removed mask regions at the edge of the valid pixels in the map which were clearly artefacts.

Eventually, the mask appeared to cover the majority of emission that would be in the map and did not need to be extended further. We allowed *tclean* to continue with this

mask until it reached our 2σ threshold.

A.3   Final non-interactive point source clean (step 3)

This step was a reproduction of the point-source clean (or step 2) so that given our final clean mask, anyone else could run the exact same cleaning as we did.

After trimming the outermost masks around map-edge artefacts, this final mask represented our carefully edited choices for where the emission needed to be cleaned. Using the union of each major-cycle mask, separately for each channel, we created a mask cube encompassing all of the pixels we wished to clean. This mask cube was fed into a non-interactive *tclean*, with the auto-masking algorithm turned off (so the mask would not be modified), the threshold set to 2σ, and starting from where the multi-scale clean (step 1) finished. This cleaning proceeded until it reached the threshold.

Visual inspection of the resulting cube showed very similar results, on most channels, to the final image produced in step 2. Around the northern arm it appeared to be cleaned more deeply, leaving a slight depression around the central ridge of the arm. This effect was similar to when the auto-masking algorithm was run without supervision but not as severe.

The residual cube looked very much like noise across the entire extent of the map in the fainter emission channels, and most of the obvious emission was removed in the brighter channels. The result was a dramatic reduction in sidelobe artefacts. The final emission cube appeared reasonable, with a hint of the mask boundaries only around the northern arm. This procedure gave us the flexibility in modeling the wide range of spatial scales present in the cube while also preventing the introduction of most of the potential cleaning artefacts.

B | Deriving synthetic-source properties for GMC completeness tests

B.1 Introduction

This appendix works through how the synthetic-source properties from Rosolowsky et al. (2021) are converted to the Gaussian parameters that are used to actually create and inject the sources into the emission cubes for cloud-finding completeness testing. Then we work those results backwards to find expressions for the source properties in terms of the observable properties. This process allows calculations of completeness estimations in the observable parameter space. A brief summary of the procedure carried out by Rosolowsky et al. (2021) and that we follow in Chapter 3 precedes the derivations.

For clarity, synthetic-source properties refer to mass (M_{CO}), mass surface density (Σ), and virial parameter (α_{vir}). Gaussian or observable properties refer to the amplitude or peak brightness temperature ($T_{B,max}$), on-sky two-dimensional radius (R), and the velocity standard deviation (σ_v).

B.2 Procedure for creating synthetic sources

This procedure was used by Rosolowsky et al. (2021) and followed in Chapter 3 to create samples of synthetic sources for cloud-finding completeness tests. We start by drawing cloud masses, mass surface densities, and virial parameters from log-uniform distributions. These are the synthetic-source properties.

From those properties, Rosolowsky et al. (2021) explicitly state the relations to two of the Gaussian parameters that are used to create the synthetic sources for adding to the emission cubes. Those relations were for the on-sky two dimensional radius $R = \left(\frac{M}{2\pi\Sigma}\right)^{1/2}$ and the velocity standard deviation $\sigma_v = \left(\frac{\alpha_{vir}G}{5}\right)^{1/2}\left(\frac{\pi M\Sigma}{2}\right)^{1/4}$. While explicitly provided, we still derive these expressions here in Sections B.3.1 and B.3.2 to understand how Rosolowsky et al. (2021) arrived at them. Also required is a Gaussian amplitude ($T_{B,max}$) calculated from the mass, surface density, and virial parameter choices, which was not given by Rosolowsky et al. (2021) but is derived here in Section B.3.3.

With the three Gaussian parameters, we calculate the function on a three-dimensional grid that is identical to the emission cube and add the Gaussian source to the original emission cube.

B.3 Gaussian parameters in terms of source properties

B.3.1 Radius

The size relation comes from the equation for the surface density in the last paragraph of section 3.4 from Rosolowsky et al. (2021).

$$\Sigma = \frac{M_{\mathrm{CO}}}{2\pi R^2} \tag{B.1}$$

$$\boxed{R(M_{\mathrm{CO}}, \Sigma) = \left(\frac{M_{\mathrm{CO}}}{2\pi\Sigma}\right)^{1/2}.} \tag{B.2}$$

The extra factor of two comes from assuming R is the HWHM of a two-dimensional Gaussian, which contains half of the mass.

B.3.2 Velocity standard deviation

We start with the definition of the virial mass

$$M_{\mathrm{vir}} = \frac{5\sigma_v^2 R}{G} \tag{B.3}$$

and substitute in the relation for the radius giving

$$M_{\mathrm{vir}} = \frac{5\sigma_v^2}{G}\left(\frac{M_{\mathrm{CO}}}{2\pi\Sigma}\right)^{1/2}. \tag{B.4}$$

Next we use the "simple virial parameter" expression from Rosolowsky et al. (2021) $\alpha_{\mathrm{vir}} = 2M_{\mathrm{vir}}/M_{\mathrm{CO}}$ to eliminate the virial mass

$$\frac{M_{\mathrm{CO}}\alpha_{\mathrm{vir}}}{2} = \frac{5\sigma_v^2}{G}\left(\frac{M_{\mathrm{CO}}}{2\pi\Sigma}\right)^{1/2} \tag{B.5}$$

which can finally be rearranged for σ_v as

$$\sigma_v^2 = \frac{GM_{\text{CO}}\alpha_{\text{vir}}}{(2)(5)}\left(\frac{2\pi\Sigma}{M_{\text{CO}}}\right)^{1/2} \tag{B.6}$$

$$= \frac{G\alpha_{\text{vir}}}{5}\left(\frac{\pi M_{\text{CO}}\Sigma}{2}\right)^{1/2} \tag{B.7}$$

$$\boxed{\sigma_v(M_{\text{CO}}, \Sigma, \alpha_{\text{vir}}) = \left(\frac{G\alpha_{\text{vir}}}{5}\right)^{1/2}\left(\frac{\pi M_{\text{CO}}\Sigma}{2}\right)^{1/4}.} \tag{B.8}$$

B.3.3 Peak brightness temperature

Starting with the Gaussian function

$$f(x,y,v) = A\exp\left\{-\frac{1}{2}\left[\frac{(x-x_0)^2}{\sigma_x^2} + \frac{(y-y_0)^2}{\sigma_y^2} + \frac{(v-v_0)^2}{\sigma_v^2}\right]\right\} \tag{B.9}$$

we will simplify it by assuming it is circular in the x-y plane and note that the amplitude, A, will be the peak brightness temperature, $T_{\text{B,max}}$,

$$f(x,y,v) = T_{\text{B,max}}\exp\left\{-\frac{1}{2}\left[\frac{(x-x_0)^2 + (y-y_0)^2}{\sigma_x^2} + \frac{(v-v_0)^2}{\sigma_v^2}\right]\right\}. \tag{B.10}$$

The triple integral of that function over all space would be $(2\pi)^{3/2}T_{\text{B,max}}\sigma_x^2\sigma_v$. Multiplying that by the conversion factor and equating it to the mass lets me solve for the amplitude in terms of quantities we have

$$M_{\text{CO}} = (2\pi)^{3/2}\alpha_{\text{CO}}T_{\text{B,max}}\sigma_x^2\sigma_v \tag{B.11}$$

$$T_{\text{B,max}} = \frac{M_{\text{CO}}}{(2\pi)^{3/2}\alpha_{\text{CO}}\sigma_x^2\sigma_v}. \tag{B.12}$$

We do not derive σ_x above, but instead R, which is the on-sky HWHM. So using HWHM $= R = \sqrt{2\ln 2}\sigma_x$, the amplitude becomes

$$T_{\text{B,max}} = \frac{M_{\text{CO}}}{(2\pi)^{3/2}\alpha_{\text{CO}}\sigma_v}\frac{2\ln 2}{R^2} \tag{B.13}$$

$$= \frac{\ln 2 M_{\text{CO}}}{2^{1/2}\pi^{3/2}\alpha_{\text{CO}}R^2\sigma_v}. \tag{B.14}$$

Substituting in the expressions above for R and σ_v we get

$$T_{\text{B,max}} = \frac{\ln 2M}{2^{1/2}\pi^{3/2}\alpha_{\text{CO}}} \frac{2\pi\Sigma}{M} \left(\frac{5}{G\alpha_{\text{vir}}}\right)^{1/2} \left(\frac{2}{\pi M\Sigma}\right)^{1/4} \tag{B.15}$$

$$= \frac{2^{3/4}\ln 2}{\pi^{3/4}\alpha_{\text{CO}}} \left(\frac{5}{G\alpha_{\text{vir}}}\right)^{1/2} \left(\frac{1}{M}\right)^{1/4} \Sigma^{3/4} \tag{B.16}$$

$$\boxed{T_{\text{B,max}}(M_{\text{CO}}, \Sigma, \alpha_{\text{vir}}) = \frac{\ln 2}{\alpha_{\text{CO}}} \left(\frac{2\Sigma}{\pi}\right)^{3/4} \left(\frac{5}{G\alpha_{\text{vir}}}\right)^{1/2} \left(\frac{1}{M}\right)^{1/4}.} \tag{B.17}$$

B.4 Source properties in terms of Gaussian parameters

It is informative to look at the completeness fitting results in the parameter space that the synthetic Gaussian sources were directly calculated in. These parameters also happen to be observable properties of the sources. To do this, we create grids of the Gaussian parameters, calculate the source properties from those grids, and calculate the completeness on that grid with the completeness fit.

B.4.1 Mass

The mass relation is a good place to start since the intermediate Equation B.14 above offers the simple rearrangement

$$T_{\text{B,max}} = \frac{\ln 2M_{\text{CO}}}{2^{1/2}\pi^{3/2}\alpha_{\text{CO}}R^2\sigma_v} \tag{B.18}$$

$$\boxed{M_{\text{CO}}(T_{\text{B,max}}, R, \sigma_v) = \frac{2^{1/2}\pi^{3/2}\alpha_{\text{CO}}T_{\text{B,max}}R^2\sigma_v}{\ln 2}.} \tag{B.19}$$

B.4.2   Mass surface density

We can then replace the mass in the surface density relation as follows:

$$\Sigma = \frac{M_{CO}}{2\pi R^2} \tag{B.20}$$

$$= \frac{2^{1/2}\pi^{3/2}\alpha_{CO}T_{B,max}R^2\sigma_v}{\ln 2}\frac{1}{2\pi R^2} \tag{B.21}$$

$$\boxed{\Sigma(T_{B,max}, \sigma_v) = \left(\frac{\pi}{2}\right)^{1/2}\frac{\alpha_{CO}T_{B,max}\sigma_v}{\ln 2}.} \tag{B.22}$$

Note that the surface density does not depend on R! This is because we are using the amplitude and volume of the Gaussian to calculate the mass, which carries a factor of R^2. However, the dilution of that mass over the two-dimensional area that gives the mass surface density has a factor of R^{-2}. Thus there is no dependence on the radius when Σ is expressed this way.

B.4.3   Virial parameter

Finally, we substitute the new expressions above into the equation for σ_v to solve for α_{vir}:

$$\sigma_v = \left(\frac{G\alpha_{\mathrm{vir}}}{5}\right)^{1/2} \left(\frac{\pi M_{\mathrm{CO}}\Sigma}{2}\right)^{1/4} \tag{B.23}$$

$$= \left(\frac{\alpha_{\mathrm{vir}}G}{5}\right)^{1/2} \left(\frac{\pi}{2} \frac{2^{1/2}\pi^{3/2}\alpha_{\mathrm{CO}}T_{\mathrm{B,max}}R^2\sigma_v}{\ln 2} \frac{\pi^{1/2}\alpha_{\mathrm{CO}}T_{\mathrm{B,max}}\sigma_v}{2^{1/2}\ln 2}\right)^{1/4} \tag{B.24}$$

$$= \left(\frac{\alpha_{\mathrm{vir}}G}{5}\right)^{1/2} \left[\frac{\pi^3\alpha_{\mathrm{CO}}^2}{2\left(\ln 2\right)^2}T_{\mathrm{B,max}}^2 R^2\sigma_v^2\right]^{1/4} \tag{B.25}$$

$$= \left(\frac{\alpha_{\mathrm{vir}}G}{5}\right)^{1/2} \frac{\pi^{3/4}\alpha_{\mathrm{CO}}^{1/2}}{2^{1/4}\left(\ln 2\right)^{1/2}}T_{\mathrm{B,max}}^{1/2} R^{1/2}\sigma_v^{1/2} \tag{B.26}$$

$$\sigma_v^{1/2} = \left(\frac{\alpha_{\mathrm{vir}}G}{5}\right)^{1/2} \frac{\pi^{3/4}\alpha_{\mathrm{CO}}^{1/2}}{2^{1/4}\left(\ln 2\right)^{1/2}}T_{\mathrm{B,max}}^{1/2} R^{1/2} \tag{B.27}$$

$$\sigma_v = \frac{\alpha_{\mathrm{vir}}G}{5} \frac{\pi^{3/2}\alpha_{\mathrm{CO}}}{2^{1/2}\ln 2}T_{\mathrm{B,max}}R \tag{B.28}$$

$$\boxed{\alpha_{\mathrm{vir}}(T_{\mathrm{B,max}}, R, \sigma_v) = \frac{5\left(2^{1/2}\right)\ln 2}{\pi^{3/2}G\alpha_{\mathrm{CO}}} \frac{\sigma_v}{T_{\mathrm{B,max}}R}.} \tag{B.29}$$

Bibliography

Rosolowsky E., et al., 2021, MNRAS, 502, 1218

C | Miovision data-science internship

C.1 Introduction

As part of the NSERC-CREATE New Technologies for Canadian Observatories (NTCO) program, I completed a six month placement at the traffic-data company Miovision. My role was data science intern, working full time within the data science team with Maximilien Schirm and Kazimierz Sliwa. The placement started on June 10, 2019 and finished on December 13.

This report serves as a summary of the work I accomplished, divided chronologically into five sections. After a brief overview of the company, Section C.2 describes my first project working on searching for wasted green time in coordinated intersections, I then discuss a novelty prediction machine learning project in Section C.3, Section C.4 covers work on estimating intersection saturation flow rates, Section C.5 reviews a project to cluster Miovision web application users based on browser tracking-data, and Section C.6 describes my work forecasting time-series vehicle volume data with machine learning techniques.

C.1.1 Overview of Miovision

Miovision provides data to customers (e.g. municipalities) on the performance of traffic flow at intersections across North America and beyond. At every signalized intersection, there is a controller that causes the signals to change, switches between signal timing plans throughout the day, uses pedestrian buttons to allow safe pedestrian crossing, uses induction loop-detectors built into the road to determine which lanes need green signals, and handles special signal plans for events such as emergency vehicles moving through the intersection. The state of all of these signals is recorded as a function of time and stored in the cloud by Miovision. This first set of services Miovision provides are built upon making information about the state of existing intersection hardware accessible remotely.

In addition to hardware that was previously installed at intersections, Miovision also provides streamable video cameras. These cameras have a 360° overhead view of the intersection, giving customers access to a live feed of the conditions at their intersections from anywhere that has an internet connection. Using these cameras, Miovision provides another service. Computer vision is used on the live video for identification,

classification, and counting of vehicles as well as pedestrians at intersections. While video is not stored long-term, the counts of vehicles and pedestrians from the video are stored in the cloud for later analysis.

Finally, Miovision leverages the wealth of continuously recorded data for traffic analysis and optimization. Tools are provided to customers for characterizing their intersections for efficiency and safety. The work I carried out took place at this level; we analysed traffic and signal data measured over time at a wide variety of intersections. Projects involved a mixture of algorithm development (Sections C.2, C.4, and C.5) and machine learning investigations (Sections C.3 and C.6). All of the projects presented here were carried out using PYTHON for the majority of the analysis as well as SNOWFLAKE SQL[1] for data retrieval and some minor analysis.

C.2 Wasted green time on minor movements in coordinated intersections

C.2.1 Motivation

Coordinated intersections are ones that are part of a corridor of high vehicle volume intersections. The signal timing is set at each intersection such that vehicles traveling along the corridor, at the speed limit, will arrive at green lights for each intersection, for each signal cycle. Coordination is used to maximize the throughput of vehicles along the directions with greatest volume through the corridor, with the signals for the remaining directions showing red most of the time. We will refer to the directions of greatest volume as major directions and the directions perpendicular to the majors as minor directions.

A low-level optimization of coordination is to ensure the major-direction signals spend as much time green as possible, or conversely that the minor directions are allotted the minimum green-signal time needed to empty a typical vehicle queue. If the amount of green time on the minor directions is too long, resulting in a green signal when no vehicles are moving through those directions, then vehicles along the major directions may end up waiting at red signals unnecessarily. By optimizing for maximal

---

[1] snowflake.com

green time on the majors it is possible to have the opposite occur. However, priority is still given to maximizing green signals on the majors because their higher volumes of vehicles means it is more likely there will be cars waiting at any given major red signal than a minor red.

Green occupancy ratio (GOR) is defined as the fraction of the green-signal duration in which vehicles are present in the intersection. It can be used to identify cases where green signals are unnecessarily long on minor directions. It could be as straightforward as ensuring all minor movements have a high GOR, since a low GOR indicates vehicles are not using all of the green-signal time.

A subtlety in finding places where this optimization can be made is that low GORs have to be occurring across all minor movements that have green signals simultaneously. For example, an intersection could be set up to have the eastbound and westbound directions as the minors and for each cycle both of those directions have green signals starting and ending at the same time. If there is a low GOR on the eastbound direction but the westbound direction has a consistently high GOR, it would not be beneficial to simply reduce the green time for the minors. The higher volume headed westbound requires the longer duration to avoid vehicles getting stuck at multiple red lights when trying to move through the intersection. Not all directions and movements have green signals overlapping with others so it is possible that a single movement occurs alone (e.g. a T-intersection). This means that any search for low GOR must be able to handle both overlapping and non-overlapping green-signal cases.

Most intersections that Miovision handles have the GOR data available to carry out this type of search, but the process was entirely manual prior to my arrival. A traffic engineer would first have to determine if the intersection was even coordinated. Since the intersection is setup to allow vehicles through in a fixed time for each signal cycle (set by the travel time through the corridor at the speed limit), all of the cycles will be identical in duration. This means one of the quickest ways to manually identify if an intersection is coordinated is by plotting the duration of each cycle versus time to see if the cycles are all the same length. Figures C.1 and C.2 show examples of this type of plot for a coordinated and uncoordinated intersection, respectively. The left panels show the duration of each cycle, broken down by signal colour duration, versus time for a single day.

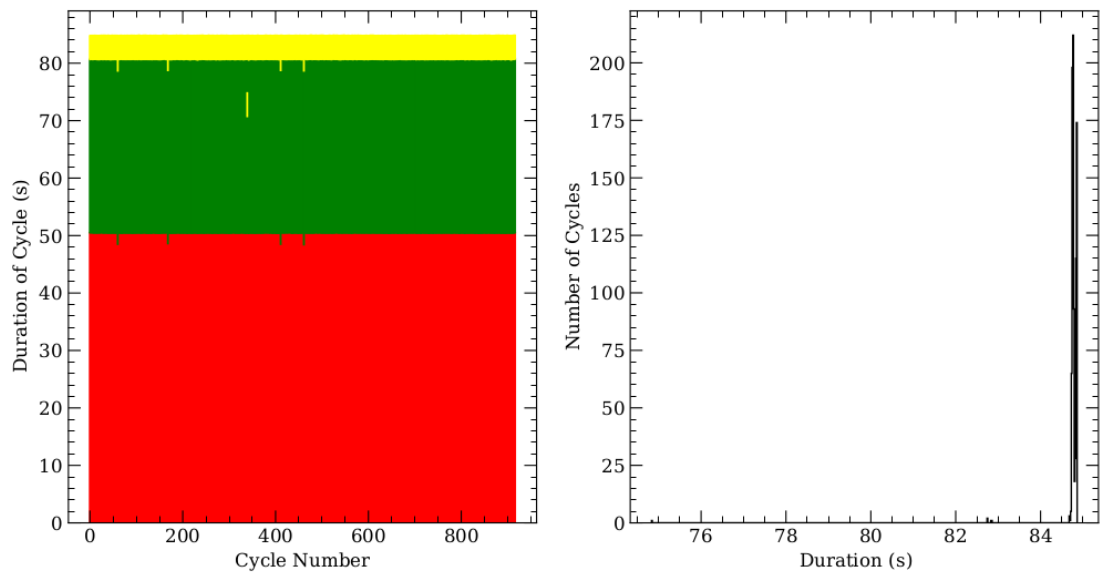If the intersection was coordinated, the traffic engineer would then have to plot

FIGURE C.1: *Left:* Cycle durations as a function of time with time increasing to the right. One day of data for a single movement in a single intersection is shown, broken down into the three signal colours. Since almost all cycles have the same duration it is clear this intersection is coordinated at all times. *Right:* Histogram of cycle durations for the same data shown on the left. The narrow distribution is characteristic of coordinated movements.
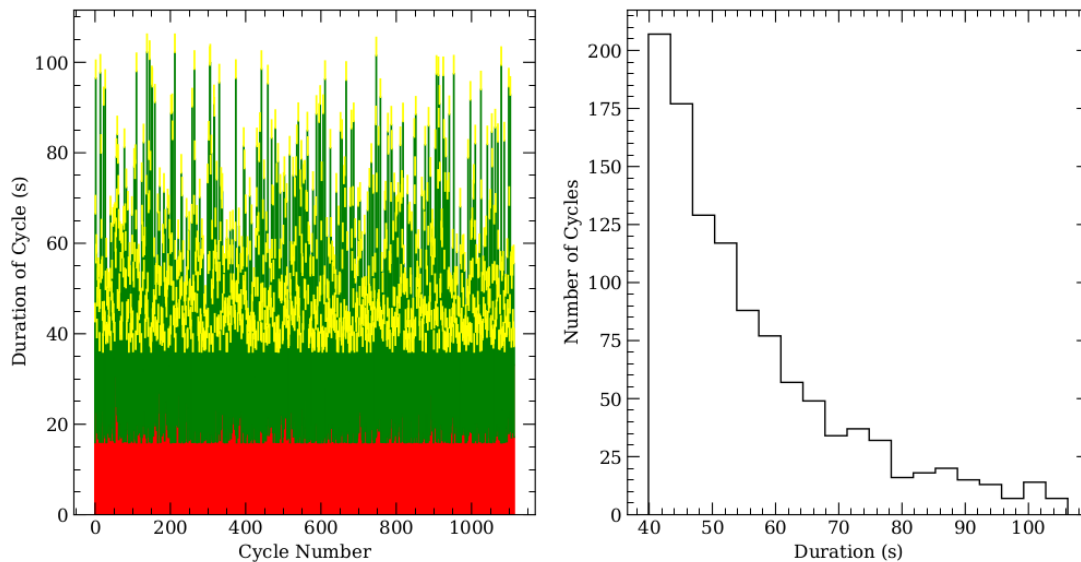
FIGURE C.2: Same as Figure C.1 but for an intersection that is not coordinated. The phase interval plot shows large variations in the duration of each cycle resulting in a significantly wider distribution. This indicates an uncoordinated movement.

distributions of the GORs for the minor movements. To find movements that were simultaneously green, they would watch real-time recordings of the signals changing. Finally, they would decide if there was wasted green time that could be optimized by searching for recurring occurrences of low GORs in plots of GOR versus time.

We set out to automate this labour intensive but relatively low skill process to increase the efficiency of Miovision's only traffic engineer. Our first goal was to automate this process for ~90 per cent of intersections. This would allow the traffic engineer to focus their time on investigating *how* to optimize problematic intersections rather than *which* intersections needed optimization. This first version could be made relatively quickly and immediately start making the process more efficient for most intersections. Then with some test intersections run through our automated method, we could identify improvements and increase the fraction of intersections the method worked for.

C.2.2 Implementation

We approached automating the identification of wasted green time on minor movements in a manner similar to the manual process outlined above. We first needed to determine

if the intersection was coordinated. In the simplest case where an intersection has only one signal timing plan throughout the entire day, the major directions should have phase durations that are all approximately the same. Uncoordinated signals would have phases that vary in duration, potentially between every cycle. Figures C.1 and C.2 show cycle durations from single timing plans for the two cases. Also shown are histograms of the total phase durations for each cycle. As expected, the coordinated intersection has a much narrower distribution of cycle durations compared to the uncoordinated example and so we can use the distributions to automatically distinguish between the two cases.

The actual algorithm for determining if a major movement is coordinated consisted of four steps. We take the cycle durations for a single day from a single movement in one intersection and discount the top 10 per cent of the cycle durations. This helps to remove outliers, due to hardware glitches and other external phenomena impacting the signal timing (e.g. a train or emergency vehicle passing through the intersection). We then used the NUMPY (Oliphant 2006) histogram function on the remaining distribution with the automatic bin width setting, storing the bins and the number of cycles in each bin. Bins that had less than one percent of the number of cycles in the highest duration bin were then discarded, which helped remove bins with very few cycles that were not representative of the timing plan. Finally, we classified the movement as coordinated if the remaining lowest duration bin was smaller than the remaining highest duration bin by less than a factor of 2.1 and as uncoordinated otherwise. This last check picks out the narrower distributions from coordinated intersections, but it also handles the case where a fraction of cycles are an integer multiple of the lowest duration bin. While the thresholds described here were chosen to properly classify a small sample of test intersections, we did not have the opportunity to do a complete investigation into optimal thresholds that would work on a large number of different intersections.

The natural complication that we have not addressed yet is that most intersections do not have a single timing plan in a day, but multiple timing plans that try to optimize for the peaks and valleys in demand (see Figure C.3). This includes intersections that are coordinated for parts of the day, while uncoordinated otherwise. So if a single distribution of phase durations is calculated for the entire day then there will be a combination of all the coordinated and uncoordinated cycles. Ideally, we would be able to first identify when each timing plan is in effect or obtain this information from the traffic signal controller. Unfortunately, we do not have that information. Thus we did
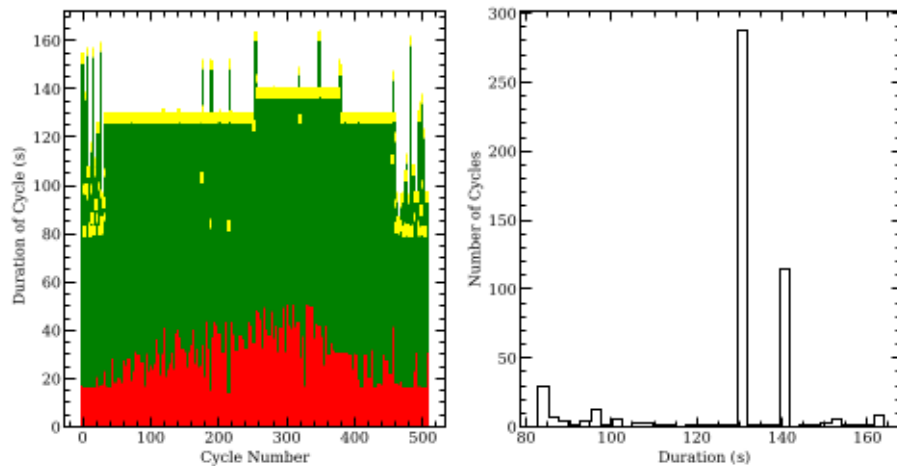
FIGURE C.3: Same as Figures C.1 and C.2 but for an intersection where there are multiple timing plans throughout the day. This movement starts uncoordinated but switches to being coordinated for the morning rush. The timing plan remains coordinated for the evening rush but the cycle duration increases. The cycle duration then returns to the same as during the morning rush. Finally, the timing plan switches to being uncoordinated through the middle of the night until the next morning rush. The distribution of durations shows the signature of all these timing plans combined, making it obvious that intersections like these require timing plan labels as a function of time.

not include this check in the first version of our implementation.

Once an intersection was identified as coordinated, we determined which movements had simultaneously occurring green signals. For this prototype, we chose to search only for cases of exact overlap in time, i.e. movements that had green signals with both the same start and end times. This was done for every cycle in an intersection for a single day's worth of data so that all concurrent cycles would be considered together, and any cycles that did not overlap with other movements would be considered on their own. All combinations of movements were searched for concurrency so that not only were cases of concurrent pairs of movements identified but also triplets, quartets, etc.

With concurrent and non-concurrent cycles identified, we finally applied thresholds to determine if the intersection was wasting green time on its minor movements. If greater than 10 per cent of cycles had GOR less than 0.8, we labelled the intersection as wasting green time. We also did not have an opportunity to fully investigate these thresholds. Figures C.4 and C.5 show histograms of the GORs for concurrent movements and non-concurrent movements, respectively. Both show cases where green time is likely

being wasted.

As a proof of concept, PYTHON was adequate as it allowed us to quickly prototype the algorithm. To ensure this tool would scale to working on data from many intersections over many days, it would be ideal to translate at least a portion of the process to the SNOWFLAKE warehouse or another scalable solution.

Due to a lack of support infrastructure and to have the chance to explore projects with greater learning potential, we decided to stop work on the wasted green time investigation and focus on the other projects described here. Once a more complete development environment had been created, another team member later revisited this project. This attempt took a time-aggregated approach directly within SNOWFLAKE. It was proving to be useful in identifying optimization problems in intersections and was likely the way forward for the project, at the time of writing. While the work described here was not used in the later SNOWFLAKE solution, it demonstrated that the problem could be addressed in an automated way. This work also exposed information on potential pitfalls and opportunities for improvement that were folded in to the later attempt. Finally, this project provided a good first problem for me to address to become familiar with Miovision's data and to begin learning how to use SNOWFLAKE SQL.

C.3 Predicting novelty of newly recorded data

C.3.1 Motivation

Anomaly detection aims to identify measurements that do not follow the distribution produced by the process of interest. Novelty detection, on the other hand, assumes previous measurements are drawn solely from that distribution and aims to determine if new measurements also belong to that distribution. This means that anomaly detection is an unsupervised learning process where the algorithm must determine two classes (inlier and outlier) without labelled training data. Novelty detection is instead a semi-supervised learning process where labelled training data exists for measurements labelled "normal." The algorithm then determines if new measurements belong to the "normal" class or not, and we call the "not" measurements "novel."

Novelty detection can be used to monitor measurements for changes that manifest as new distributions in the measured values. In the context of data that Miovision
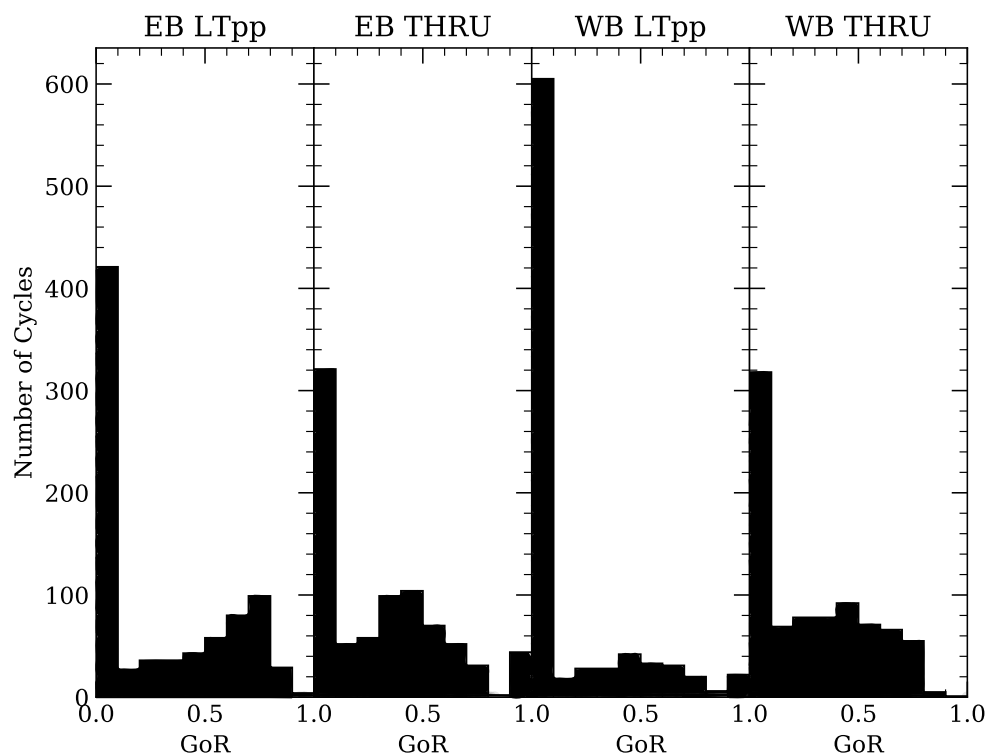
FIGURE C.4: Histograms of GOR for each cycle in a 24 hour period from a single coordinated intersection. The four minor movements with cycles that exactly overlap in time are shown. Considering all of these movements together is necessary to ensure changes to the timing plan only act to remove low GOR cycles. This example shows that a significant number of cycles across all of these movements have very low occupancy, indicating that there are no vehicles moving through those movements during those cycles. Some reduction in green phase durations on these movements would likely be beneficial.
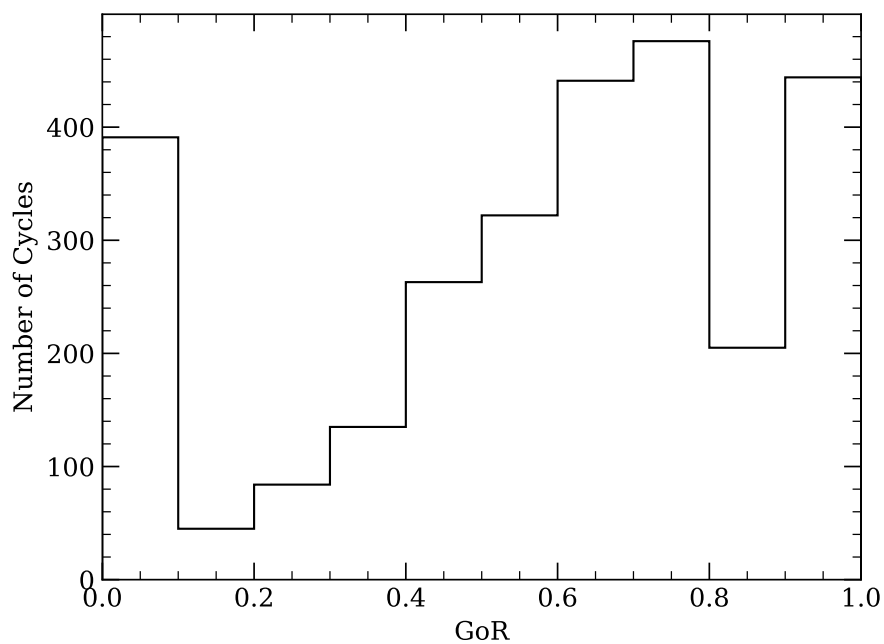
FIGURE C.5: Same as Figure C.4 but for a movement that has green signals that do not occur at the same as other movements. In this case, identifying low occupancy ratios on this one movement would be sufficient to identify times to remove wasted green time. This movement actually has a fair fraction of its cycles with high GOR but there is certainly a population of cycles with very low ratios. Investigating the timing plan for the times of day where those low GOR cycles originate could reveal opportunities to reallocate green time in a way that would optimize throughput.

currently records we had two initial ideas for where to use novelty detection however, we only investigated one. The use case we investigated was identifying newly added intersections that were misconfigured. Here misconfigured meant the labels for directions and movements (e.g. northbound, eastbound, through, left turn, etc.) were mixed up. The use case we did not investigate was to automatically identify hardware failures or changes in traffic patterns through continuous monitoring of all intersections.

To search for misconfigured intersections we could make a training set of normal labels from a list of intersections where the configurations were validated by-hand. Then new intersections could be deemed misconfigured or not based on the fraction of novel-classified measurements that were recorded in a short period of time. New intersections could mean ones that are already in the Miovision database but were simply not included in the training set, or they could be ones where Miovision hardware is installed in the future. The former case would help ensure all current customer intersections are recording data properly, and the later case would allow us to quickly alert all future new customers to misconfigurations so their data would be accurate from very early on.

The benefits of this technique over simple thresholding on individual measured parameters is that the boundaries between normal and novel classes are automatically learned from all input historical data. This means it is possible for those boundaries to take complex paths through the N-dimensional space of input features. Simple thresholds can pick out normal and novel cases in each feature with all other features held constant, but machine-learned novelty detection can take the distributions of all features into account simultaneously.

C.3.2   Implementation

Training with a single week versus seven Thursdays

An early test we carried out was investigating the impact of having a model trained on data from all days of the week compared to data from multiple instances of the same day of the week. Simply, would a model trained on Monday through Sunday be more accurate at identifying misconfigured intersections? The data used here were day of the week, hour of the day, minute of the hour, direction, movement, priority, durations of each signal colour, occupancy ratios for each signal colour, and the simple delay for each

TABLE C.1: Fraction of cycles, from the single Thursday prediction day, predicted novel from models trained on seven days in a single week or trained on seven Thursdays in a row. Novelty fractions are calculated for the original data (correctly configured) and with the labels on directions and movements swapped in the prediction data set (simulating a misconfigured intersection).

Training set	Original	Misconfigured
1 Week	0.314	0.325
7 Thursdays	0.398	0.411

cycle (the time between the first vehicle arriving on a red signal and when the signal turns green).

A total of eight intersections were used: seven intersections were included in the training set, while a single intersection was used for validation of the novelty prediction model. None of the intersections was chosen for being particularly novel or normal, as all were picked at random. The one-class support vector machine algorithm as implemented in SCIKIT-LEARN (Pedregosa et al. 2011) was used to produce these models. An aggregate novelty score was calculated for each model by making the normal/novel class predictions for all cycles from one day of data and calculating the fraction of all cycles that were classified novel.

The "Original" column of Table C.1 shows the comparison of training on seven days in a single week and seven Thursdays in a row (the prediction day was also a Thursday). The difference is noticeable at about 27 per cent, with seven Thursdays of training data producing a higher novelty fraction. This can be understood by realizing that differing traffic patterns on each day of a week would result in data populating more of the feature space. When the feature distributions from the prediction day were compared to the training distributions, it is not likely that the prediction data contains something previously unseen in the training data. On the other hand, if multiple Thursdays appear quite similar, then smaller differences between the prediction and training distributions could appear more significant, thus resulting in the higher novelty fraction.

Novelty measured from simulated misconfigurations

Our next test aimed to measure how much the novelty fraction changes when an intersection is deliberately misconfigured. To do so, we swapped labels for pairs of movements

257

such that the resulting configuration did not match the actual intersection (e.g. data from the northbound through movement is relabelled eastbound left turn). By simulating misconfiguration in this way, we could directly measure the change in novelty predictions that arise from the movements being mislabelled. Comparing the "Original" and "Misconfigured" columns in Table C.1 shows how the novelty fractions change when going from properly labelled to mislabelled movements. In this case, only about a three percent difference arises from the mislabeling. It appears that the information used to train these models is not adequate to produce a strong change in the novelty fraction of this intersection. The broader applicability of these results is limited however, because this test was only carried out on a single intersection predicted from a week of training data from only seven intersections.

Including the day of week as features

We wanted to directly test the effect that the day of week has on the models. In particular, we examined the difference in novelty fractions predicted when the day of week was encoded as input features to the model and when it was not. Separate models for each day of the week were trained on data from 42 intersections. We also trained ten separate models where the particular calendar day was varied to estimate the variation in results from the day that was chosen for training. Novelty predictions were always made on one Thursday of data from a single validation intersection (the same day and intersection as previous tests).

Figure C.6 shows the novelty fraction predicted by all models trained where the day of week is encoded as features. Thursday models predicted the lowest novelty fraction, Wednesday and Friday show an increased novelty fraction over the Thursday models, while the remaining days predicted all cycles as novel. This behaviour is built into the models however, since the day of week feature forces data from differing days of the week to be more distant in feature space.

When we performed the same test but without the day of week encoded as features in the models, we found the results summarized in Figure C.7. Novelty fractions are all consistent around 40 per cent for weekdays. Models that were trained on Saturdays and Sundays show about twice the novelty fraction as models trained on weekdays. This indicates that signal durations, occupancy ratios, and simple delays are intrinsically different on the weekend compared to weekdays. While this is not surprising from
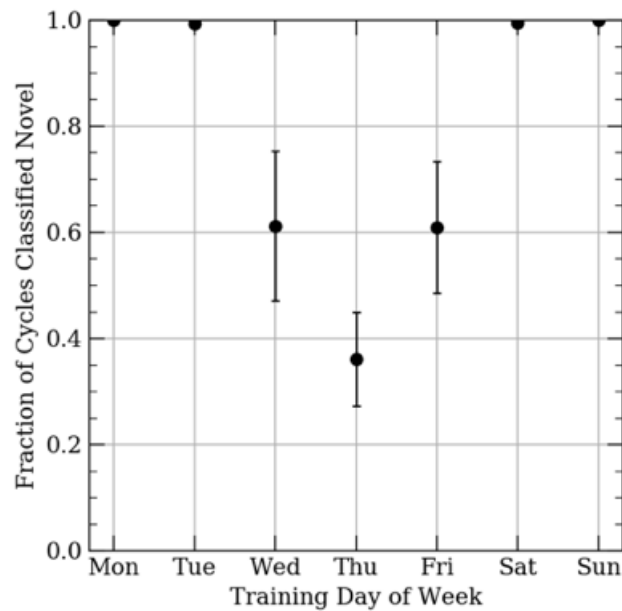
FIGURE C.6: Fraction of cycles classified as novel as a function of model, where each model is trained on the day of week specified. Prediction data are from a single intersection during a single Thursday, and the day of the week is encoded as features to the model. Each model is trained on data measured from 42 intersections during the given day of the week. The points show the mean of ten separate realizations and error bars show the standard error of the mean.
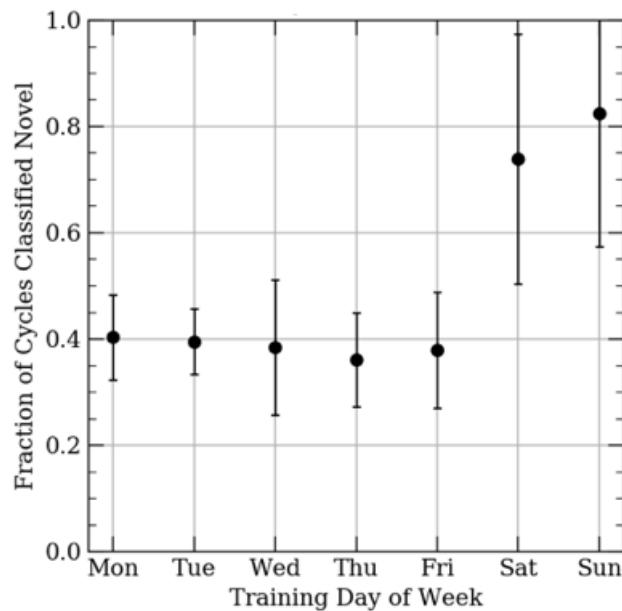
FIGURE C.7: Same as Figure C.6 but without the day of week included as features. This can be thought of as "not telling" the models that the data from different days of the week are intrinsically different. However, the models still find significant differences between novelty predictions from weekday-trained models and weekend-trained models.

anecdotal experience, it is important to have shown this occurs for novelty detection. We now know it must be taken into consideration when building these models and drawing conclusions from them.

Number of training days for prediction convergence

The last test we worked on was trying to estimate the appropriate amount of training data necessary to produce stable novelty predictions. Training data was collected in batches of between one and fourteen days. Days within each batch were sampled ten different times to probe the variability coming from the particular days used in training. For example, the batch with two days of training data could have its first set include January 15 and June 4 while the second set could have March 27 and July 16, etc.

Seven intersections had the novelty of each cycle predicted on data spanning a 24 hour period, from midnight to midnight on August 1, 2019. Each prediction intersection

had its own models where the prediction intersection was held out of the training set. This setup should give insight into the requisite training set size for accurately estimating the novelty fraction of a new intersection after just one day of data are recorded.

Figure C.8 shows the results of this test with the novelty fraction versus the number of days of data included in the training sets. Points are the mean novelty fraction from the ten realizations and error bars are the standard error on the mean. Interestingly, all intersections converge after about four or five training days, without significant changes up to 14 days.

The two intersections with consistently high novel fractions (9c0b814 and 58246c5a) are both odd cases. 9c0b814 has only a small number of cycles from that 24 hour period and would do better by having just another day of data measured. 58246c5a has significant scatter in all of its novelty fraction estimates and so requires closer inspection to understand the cause of this considerable variation. The result for the other five intersections are consistent with our expectations, where the novelty fraction converges as more data are included and the scatter decreases as well. This shows that fairly stable predictions can be made from relatively lightweight models that are trained on data from only a handful of days.

C.4   Automatic saturation flow rate estimation

C.4.1   Motivation

During our first "hack day" event, I partnered with traffic engineer Sajad Shiravi and traffic analytics software development manager Mark Fennema. Our goal was to create a prototype that automatically estimated the saturation flow rate at an intersection. The saturation flow rate is the number of vehicles that move through an intersection per unit time in a dense flow of traffic (Bester & Meyers 2007). Knowing this for different movements in an intersection is a crucial part of optimizing the performance of an intersection. The saturation flow rate is the result of the physical constraint imposed by the geometry and configuration of an intersection on moving traffic.

The automated method we set out to prototype uses two traffic flow data sets, which Miovision currently measures continuously. These are the GOR, and number of vehicles that pass through a single movement per unit time (the vehicle volume). This method
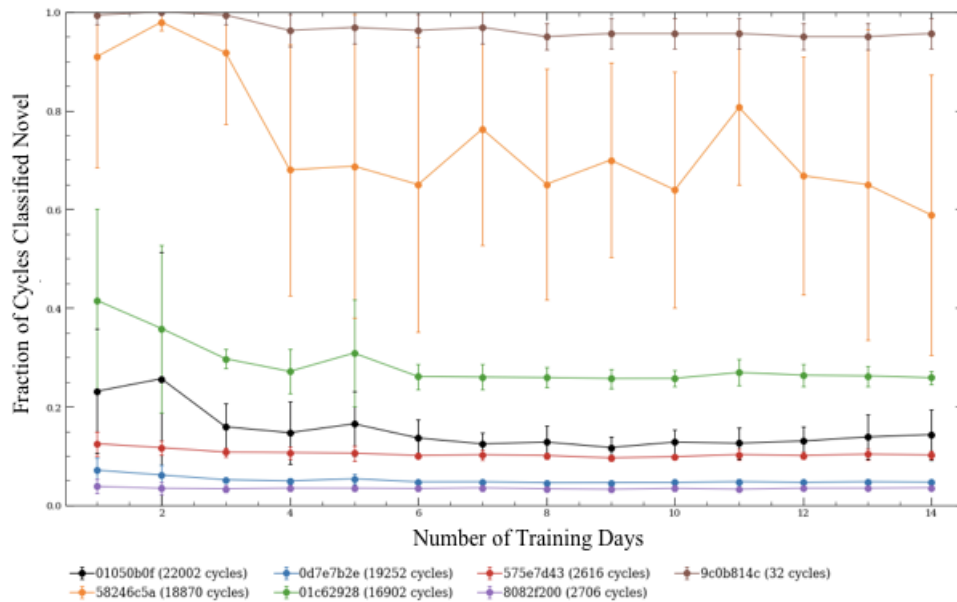
261

FIGURE C.8: Novelty fraction from a 24 hour period as a function of the number of days used to train the model. Points and error bars are the mean and standard error of the mean, respectively, for ten realizations of each number of days included in training each model. The list of intersections used to train the models for each prediction intersection are the same except that the prediction intersection is held out in each case.

greatly improves upon both the standard empirical method for estimating saturation flow rates as well as the standard method for modeling the saturation flow rate, both of which are still used by most cities to optimize their signal timing plans.

Here I summarize the current standard empirical method, but see other sources (e.g. Bester & Meyers 2007; Shao & Liu 2012; etc.) for more detail. The current method involves sending two workers to the intersection of interest where they must time vehicle movements manually. One person is typically located at the stop bar of the movement being measured and the second person tries to stand halfway down the usual queue length, upstream of the intersection. A queue building up on the red light is necessary to replicate dense traffic flow. Once the light turns green, the two workers must coordinate timing the interval between each vehicle passing the worker at the stop bar. They must also ensure only vehicles that were part of the original queue are timed so the rate estimate comes from the densest traffic flow. With these timings, the saturation flow rate is calculated as

$$s = 3600\bar{h}^{-1} \tag{C.1}$$

where s is the saturation flow rate in vehicles per hour (vph) and $\bar{h}$ is the average of the times between vehicles crossing the stop bar in seconds (Bester & Meyers 2007).

This method is clearly limited by the workers' ability to communicate the timing of each vehicle and the potential for vehicles to be missed by-eye, limiting the sample size. It is also impossible to validate the results after timings have been carried out. Finally, the measurements are necessarily taken over a short time period to limit financial cost at the cost of limiting the generality of the results (e.g. different times of day, different weather, different timing plans, etc.). While it is a straightforward technique, it is not very robust in practice.

Another common method for estimating saturation flow rates relies upon analytical modeling of traffic moving through the intersection. This is typically done through an exhaustive (and therefore complex) combination of many parameters that can impact the flow. The typical model used is from the Highway Capacity Manual (Transportation Research Board 2016) and is made up of 13 parameters, all used to estimate the flow rate. With so many parameters it is difficult to measure each one with enough certainty to prevent propagated errors from overwhelming the final estimate for the flow rate.

For our method, we used vehicle count data combined with measured signal phase durations to automatically estimate the saturation flow rate. Count data was collected

using Miovision's SmartSense product, which uses computer vision to detect and track vehicles as they move through the intersection. Signal phase durations were obtained directly from the signal controller. It is the same principle as the empirical method above except we use continuously collected data from the SmartSense device, with known accuracy, allowing us to average the flow rate over multiple green signals. To make sure we are measuring the rate during dense traffic flow we simply ignore cycles where vehicles are not passing through the movement during the majority of the green signal. This is easily accomplished by only considering cycles with high GOR.

C.4.2 Implementation

Previously, there had been modeling done at an intersection where we had all of the requisite Miovision data sources recorded so we decided to do a bootstrap comparison of the three methods. First, saturation flow rates were estimated with the existing analytical model. Next, Sajad estimated the flow rates with the empirical method by manually counting vehicles in Miovision-recorded video of that intersection. Sajad found that the industry standard estimates agreed within a few percent so we knew we had them measured as well as any city would have done with either method.

Finally, Mark and I wrote a Python script to estimate the flow rate using our proposed method. We first took the cycles in which the movement of interest had both a GOR greater than or equal to 80 per cent, and a red occupancy ratio for the first five seconds greater than or equal to 80 per cent. This ensures that there were likely vehicles queued up waiting for the signal to turn green as well as having vehicles traveling through the movement for at least 80 per cent of the green signal, achieving dense traffic flow.

For those cycles, we obtained the vehicle volume measurements for that movement from the SmartSense count data. With green signal durations and the vehicle volumes for high capacity cycles we calculated the saturation flow rates as

$$s = (3.6 \times 10^6)\frac{V}{g} \tag{C.2}$$

where V is the vehicle volume for that movement during that cycle and g is the green signal duration in milliseconds. Figure C.9 shows the histograms of saturation flow rates calculated in this way for a single movement (westbound through) for each day of a week. Some days have fewer cycles because there is less traffic resulting in less cycles

with high GOR (i.e. Saturday and Sunday), so the rates are not as well constrained. Mean saturation flow rates are between 1775 and 2750 vph. Comparing this with the manual and modelled rate of 3000 vph shows a significant difference between the methods. Aggregating all of the estimates from our method over the full week, shown in Figure C.10, results in a rate of 2200 ± 400 vph, which is still inconsistent with both the manual and modelled methods.

There are three main causes for this discrepancy that we identified. First was that both the vehicle volume and occupancy ratio measurements were for two lanes that were making the westbound through movement. The empirical video measurement that Sajad did by-hand was only taking one lane into account, so this means that our method was a form of average between the target lane and another lane. While relying on in-ground loop detectors, it would be costly to fix this since a detector for each lane would have to be installed at the intersection. However, since there is already a Miovision camera at the intersection for the volume measurements, it would be straightforward to start using the computer vision application for measuring occupancy at the intersection. It would then be straightforward to configure volume and occupancy measurements for each lane independently. This would align the estimates from our method with those from Sajad's by-hand estimates.

The second source of the inconsistency between our method and the industry standard methods is the inclusion of vehicles that are still accelerating to saturation-rate speed in our method. This would naturally decrease the flow rate relative to a stream of vehicles that is already up to speed, consistent with the difference that we see between our method and the other methods. This effect could be mitigated by ignoring the first few seconds after the signal has turned green so that most of the vehicles moving through are then up to saturation-rate speed.

Finally, our current method is limited by the inclusion of vehicles that arrive after a queue has passed through the intersection. The time it takes these later vehicles to move through the intersection will not represent the flow rate during high vehicle density. Flow rates estimated from these vehicles would likely be higher than the true saturation rate and so will bias our estimate high. Contamination from this case could be removed by comparing the timestamps for when each vehicle crossed the intersection and limiting the calculation to only short intervals between vehicles.
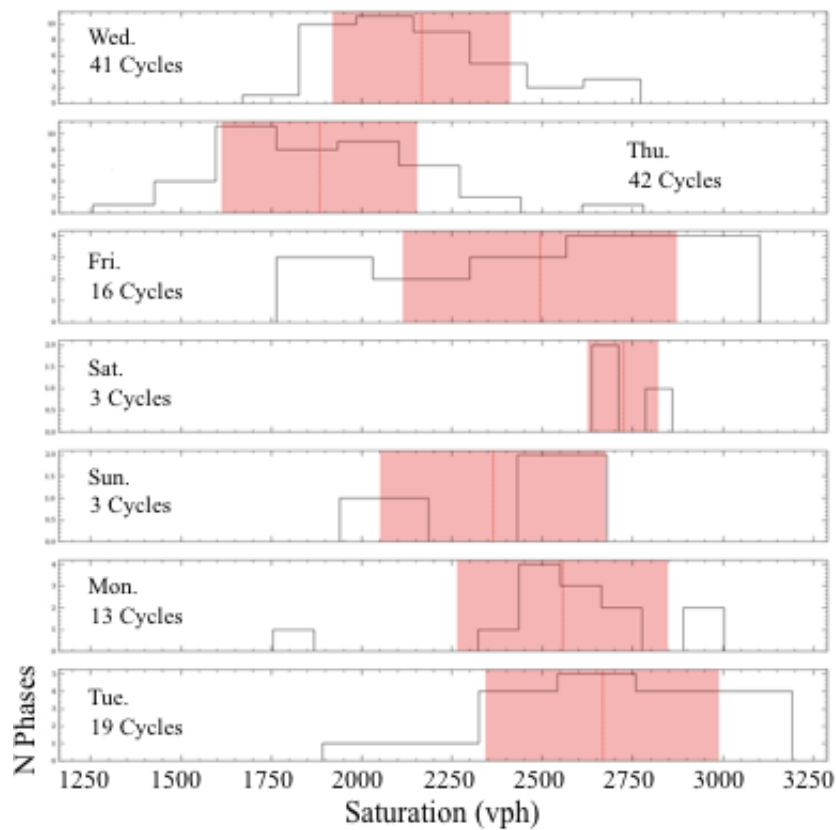
FIGURE C.9: Histograms of automatically estimated saturation flow rates for each day of a week for a single movement in a single intersection. Vertical dashed lines indicate means for each day and shaded regions show one standard deviation above and below the means. To include a cycle in this calculation, there had to high occupancy ratios for both the green signal and first five seconds of the red signal. Therefore, on days with lower volumes there are less cycles used.
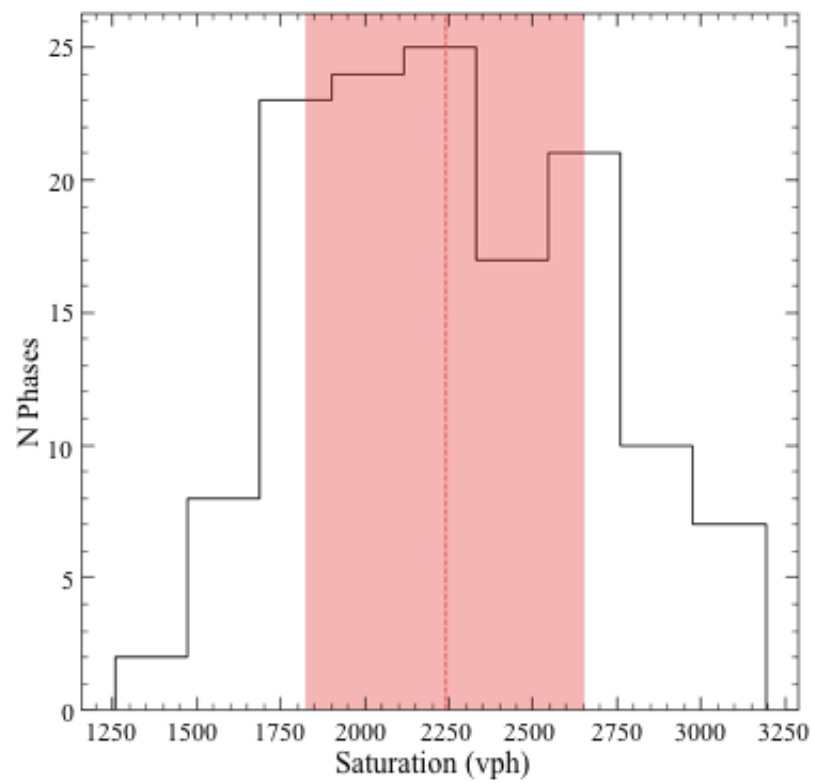
FIGURE C.10: Same as Figure C.9 but showing all measurements in a single distribution. The estimated mean and standard deviation for this distribution is 2200 ± 400 vph.

C.5   Clustering TrafficLink user behaviour

C.5.1   Motivation

Miovision collects information about the actions that users of its TrafficLink web application take as well as information related to the hardware and software used to access the site. While the data was still in a preliminary state, with plans to improve the granularity and specificity of the tracked information, data scientist Kazimierz Sliwa and I attempted to find groupings of users in these data as part of our second hack day event.

Event information used for this task includes actions like opening pages, querying and analysing data, viewing archived video from cameras at intersections, and viewing plots. From this we calculated the fraction of all possible tracked events that a user carried out during each session. Information on how the web site was accessed was also used in these tests such as if the user connected with a desktop or mobile device, if they were using a Windows, Mac, or Linux operating system, and which browser they were using. Even information on how each user was directed to the TrafficLink website for each session (e.g. through a Google search, an email, directly going to the URL manually) is tracked and so we tested using it in this analysis.

We used data that were recorded between June 2019 and the hack day in November. Data prior to June 2019 was not available. For consistency we decided to include users' measured actions starting from the date they first logged into TrafficLink in the time period we had data, to 28 days after that first login. So if a user only logged in once in those first 28 days then their data would consist of only that one session. If a user logged in multiple times a day for all 28 days then their data would be the sum of all actions for all of those sessions. This meant we could add a feature that was the fraction of days in their 28 day interval in which they logged in. Another feature derived from this was the average number of sessions per day, normalized by 28 days (called "% Sessions" in Figure C.15).

There are two limitations to note about our dataset and analysis. First, we are unable to identify whether a users' first login event corresponded to a new user, or a returning user. We can only discern whether it was the first login event during the time period of the data. We hoped looking at the first 28 days for each user in the same way would standardize the data enough to identify clusters. The other limitation was that the data

did not include any indicators for each new session a user started (i.e. when they had to log back in and start everything fresh). Since we knew users would be prompted to re-enter their login credentials after 15 minutes of inactivity (but not actually have to restart their work from scratch), we simply designated a new session starting if there was greater than 15 minutes between recorded events.

With these data in hand, and the limitations they presented, the initial goal was to try identifying two types of users: beginners and experts. One potential application of such a system would be to suggest targeted help and recommendations to users based on their experience level with TrafficLink. This could also be extended to identify features of the website that were underused and to suggest ways those features could be incorporated into users' work. For the hack day event, we were aiming only to search for clusters of users in the preliminary data, and qualitatively identify clusters as beginner and expert users.

C.5.2   Implementation

Our initial list of features consisted of 47 features. We used principal component analysis (PCA) to reduce the dimensionality of our feature space, while retaining most of the variance. Figure C.11 shows the cumulative explained variance of the principal components using all 47 features. This shows that 90 per cent of the variance comes from the top ~20 components. We tested clustering using the *k-means*, *DBSCAN*, and *OPTICS* scikit-learn algorithms, but we settled on *k-means* because of its simplicity due to its shorter list of parameters. For this set of features, no obvious clusters were apparent by-eye and applying the clustering algorithm did not make any clusters obvious, as shown in Figure C.12.

Upon inspection of the full list of features we found that several were always recorded as zero. Since those features would not add any information to differentiate users we excluded them from further testing. We also recognized there were some feature groups based on name such as analysed, opened, and queried. We made aggregate features from these groups from the sum of all events in each group. These two steps reduced the number of features from 47 to 9, drastically reducing the dimensionality of the feature space.

The new cumulative explained variance is shown in Figure C.13 and this results in ~90 per cent of the variance being explained by only six components. The three
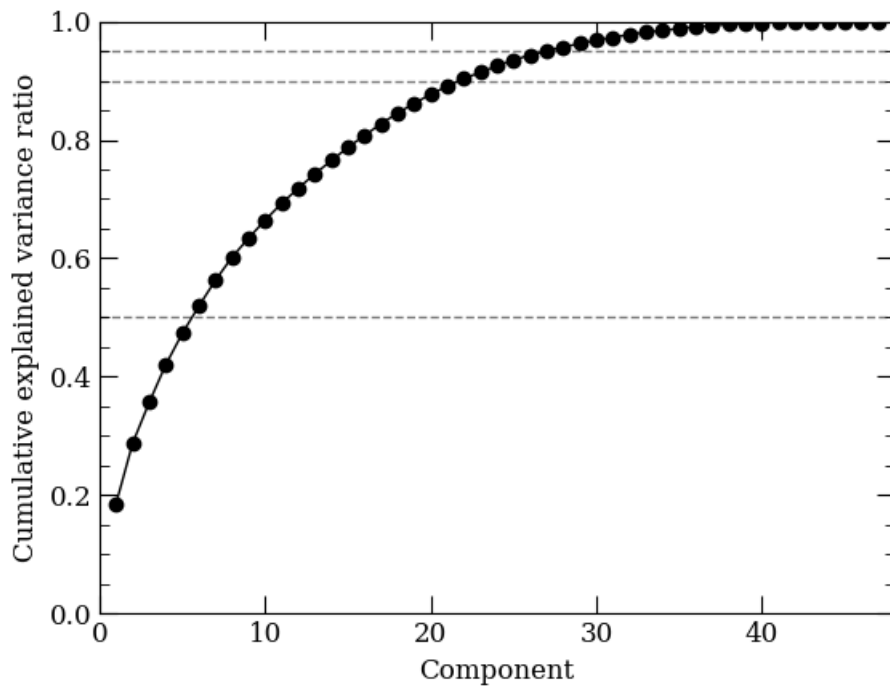
FIGURE C.11: Cumulative explained variance from PCA using all 47 features. Horizontal dashed lines indicate 50, 90, and 95 per cent explained variance. Features are ordered from those that contain the most to the least variance, from left to right.
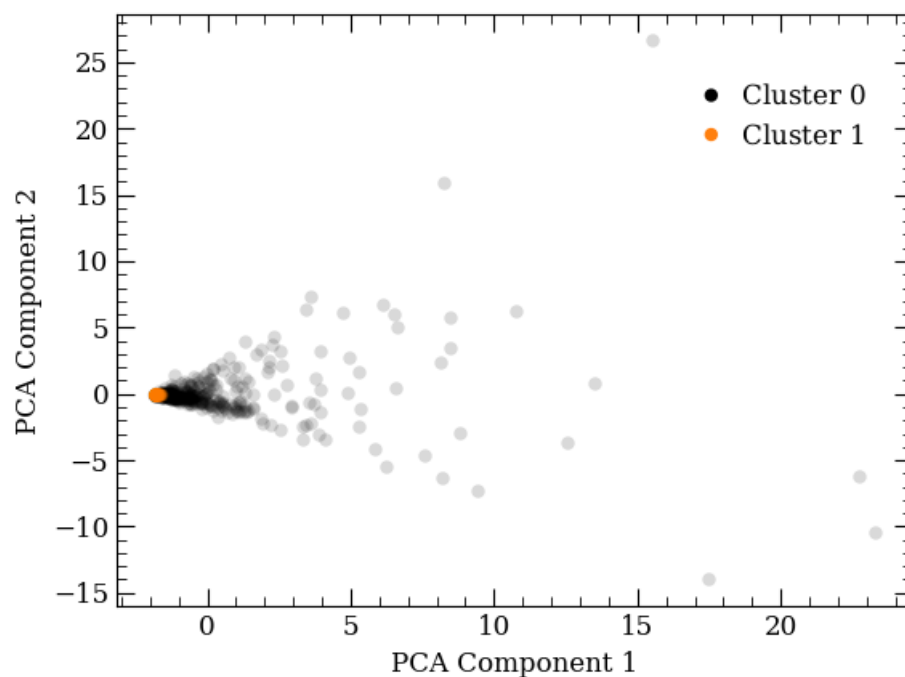
FIGURE C.12: TrafficLink usage data projected along the two highest variance components from PCA with all 47 features included. Clustering was performed on these data with the SCIKIT-LEARN *k-means* algorithm which found one cluster shown in black points and another in orange points. There is almost no clear separation amongst users viewed with these features, even when the data are projected on to the plane that encapsulates the most variance.
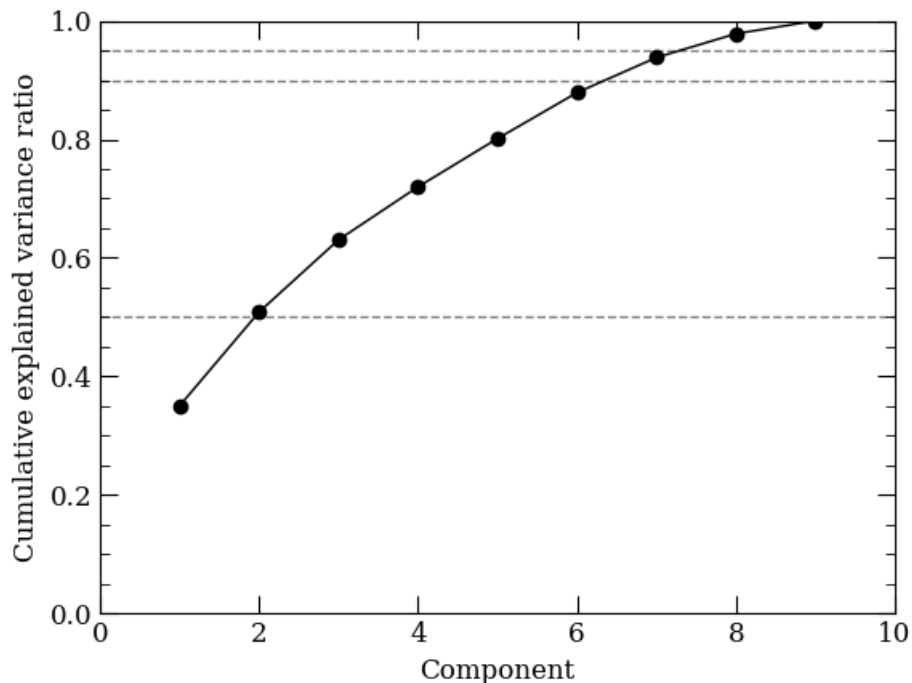
FIGURE C.13: Same as Figure C.11 but instead using aggregated features and excluding features which were always zero. Having 90 per cent of the variance encoded in only six features is a vast improvement over the previous example that needed about 20 features to achieve the same.

components with the highest variance are plotted against each other in Figure C.14. Points are coloured by the cluster they belong to as determined by the *k-means* algorithm, set to identify two clusters. There is a fairly noticeable cluster that is tightly arranged in a line spanning component two while a second cluster is made up of more diffuse points that flare away from the line of the first cluster. While it is a subtle distinction in those visualizations, boxplots of the original features with the two clusters split out shown in Figure C.15 reveal differences between clusters for some of the features. Examples are the opened, viewed, and percent of events features.

We succeeded in our first goal of identifying clusters of users, but did we find clusters that correspond to beginners and experts like we wanted? There is at best tentative evidence that cluster zero may be beginners while cluster one may be more experienced users. In most features, cluster zero generally has fewer events recorded compared to cluster one which could indicate cluster zero is doing fewer different tasks
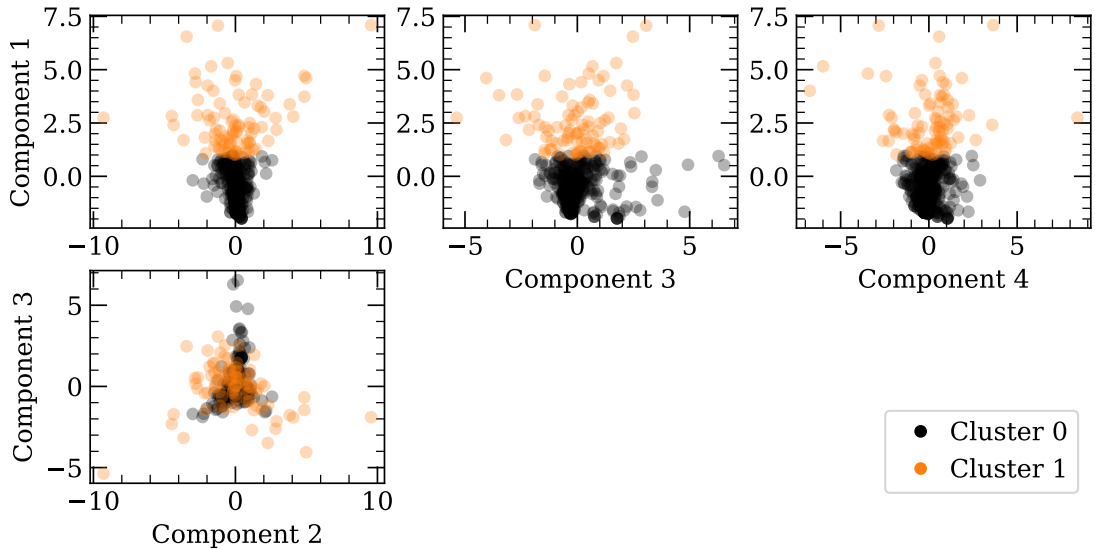
FIGURE C.14: Several projections of the final PCA components for the TrafficLink user data along with the final two clusters we identified. Cluster zero is quite compact and linear while cluster one is more diffuse and farther from zero along the component-one axis. In the component three versus component two plane it even appears that cluster zero has three tight linear features while cluster 1 is arranged in a more round cloud.

in TrafficLink because they have not become familiar with much of the website yet. Importantly, the fraction of all tracked events recorded for cluster zero is less than cluster one. This could indicate cluster one is more familiar with a wider range of features in the site. However, it is interesting that the distribution of recalled events (related to viewing archived video recorded at intersections) for cluster zero has a tail to higher numbers than cluster one. This would appear to indicate cluster zero users are watching more video. So instead of finding beginner and expert users, we may have actually found users who primarily use TrafficLink for watching video and another group that uses the other portions of the website, without watching much video. Further investigations are certainly required to solidify the conceptual meanings of these user groupings.
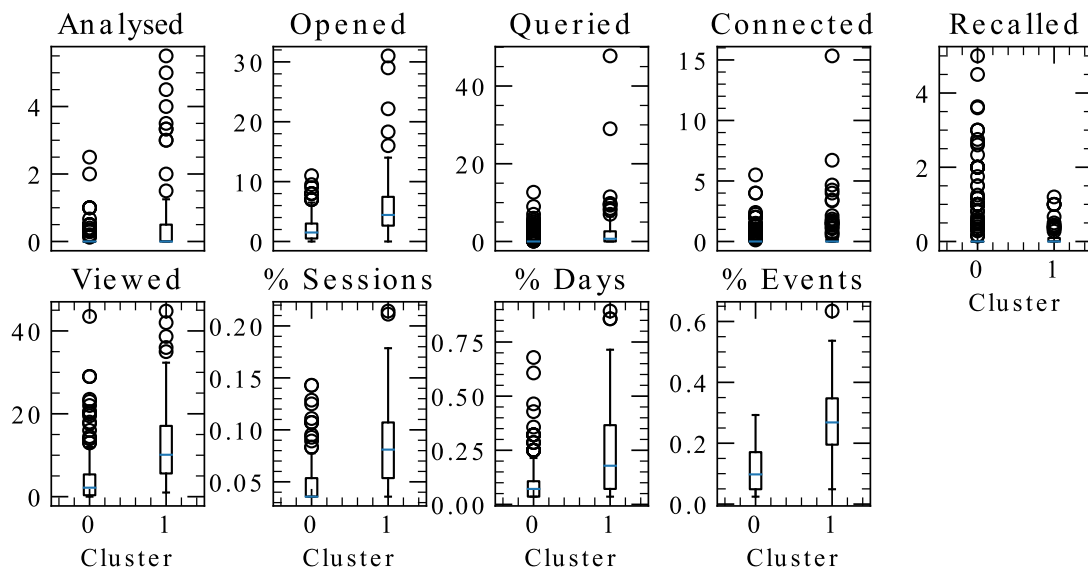
FIGURE C.15: Box plots of all aggregated features for our final two clusters. Some features show noticeable differences in the cluster distributions (e.g. opened, viewed, and percent of events). Since cluster one typically has distributions to higher numbers of actions and fractions of events, it may be that cluster one is a group that is more experienced with TrafficLink than cluster zero. Interestingly, the opposite is hinted at in the long tail of the recalled feature distribution, indicating heavy video users.

C.6   Vehicle volume forecasting

C.6.1   Motivation

Vehicle volumes are measurements of the number of vehicles arriving at an intersection over a given time interval. It can be measured for each movement within an intersection and during each signal colour. At its simplest, these measurements indicate the flow of vehicles through an intersection and the demand the signal plan must accommodate.

Time-series forecasting of vehicle volumes builds on the tremendous amount of historical data Miovision currently has and is continuing to gather. It opens up new possible avenues of analysis and thus customer value. There are several potential applications for volume forecasting.

Long-term trends can be identified through forecasting that can then be used to characterize changes in demand at an intersection. These trends can also be used to predict when problems may arise due to significant changes in volumes. For example, gradually increasing volumes could eventually lead to saturation at the intersection causing congestion and possibly increased rates of dangerous incidents.

Rapidly occurring changes in volumes can also be compared to forecasted values. Depending on the nature of these changes, improvements to the model may be useful (e.g. incorporating when a nearby school lets students out for the day) or impractical (e.g. when a collision will occur and in what way that will affect volumes). Both cases expose additional information on the processes that shape the flow of vehicles through the intersection of interest, and this is only possible when prior knowledge and data can be used to produce expectations for the future.

Changes can be either expected or unexpected. A skillful model will incorporate a variety of changes we expect based on prior knowledge to simplify. Both slow trends and rapid changes can be produced in scheduled or predictable ways. An example of a slow increase in volumes could be one where a new residential region is developed near an intersection, so a gradual increase in vehicles could be expected as new people move into the area and begin driving. Examples of rapid expected changes such as daily school end times, summer breaks starting and ending, and sporting events.

Having an expectation of what volumes you will record at a particular time means that when the actual measurement is made, the accuracy of the prediction can indicate

our level of understanding for vehicle flow through that intersection. Poor predictive skill could indicate that the information used to make predictions is incomplete or irrelevant. Investigating additional information would likely be useful as well as possibly re-engineering existing data into forms that more directly connect to volume forecasts.

While changes to volumes could be identified manually, a significant gain in efficiency, completeness, and consistency can be made through automation of these forecasts. Miovision tracks over 1000 intersections with ~20 per cent of these intersections equipped to measure vehicle volumes in five minute bins, 24/7. These volume measurements will be for each signal colour (phase) from each movement at each intersection. This presents a tremendous amount of data to routinely forecast manually as well as searching for differences between measurements and forecasts. In addition, Miovision hardware is installed at new intersections all the time. For any useful amount of forecasting and analysis to be done this process must be automated.

C.6.2 Infrastructure

We chose to implement our forecasting using SCIKIT-LEARN (Pedregosa et al. 2011) in PYTHON for model training, testing, and prediction. In addition to being a widely used package with mature documentation, this framework also allows for most of the data collection and engineering pipeline to be built agnostic of the particular algorithm used to produce models. The interface to most algorithms is relatively consistent in SCIKIT-LEARN such that switching algorithms can be as straightforward as switching out the name of the function.

Data are stored by Miovision within cloud-based SNOWFLAKE SQL databases that are updated with new measurements nightly (note that this was in place before my internship). All data are queried and downloaded with PYTHON using the pandas module (McKinney 2010) with a database connection provided by SNOWFLAKE. We chose to use the Data Version Control (DVC)[2] package for version controlling training data, models, and some model metrics. We also used DVC to automate some of the process of producing those artefacts through directed acyclic graph pipelines. Additional automation was accomplished with Bash scripting. All training data storage, model training, model assessment, and forecasting was carried out on a Kubernetes[3] cluster running in the

---

[2]dvc.org
[3]kubernetes.io

Amazon Elastic Kubernetes Service (an Amazon Web Services Product[4]). A significant amount of investigation and prototyping was carried out on that Kubernetes cluster using JupyterLab notebooks (Kluyver et al. 2016) for interactive data manipulation and analysis. However, the final code framework for producing forecasts was designed to be non-interactive, running through a set of scripts.

C.6.3 First models

While some investigative models were produced before this stage, they were used to forecast at most a handful of intersections for only a week or two. This section will describe the first major iteration of models we prepared on a sizeable sample of intersections.

A sample of 45 intersections was chosen to forecast. The only requirements to make this list were that they had vehicle volumes recorded on January 1, 2019 and November 11, 2019. In practice, this meant that these intersections had at least 11 months of data. We chose this to balance between having a significant amount of historical measurements along with providing a sample of around 50 intersections that actually had enough data. With this list of intersections we then used all available volumes starting from January 1, 2018. Additionally, volumes were only used that were recorded with the same intersection configuration as the intersections had on November 11, 2019.

For simplicity, we will first describe the feature engineering and model training for the volumes arriving during the green phase on an example northbound through movement. Our models sought to predict the number of vehicles that would arrive in the next hour at each intersection during the green light of that northbound through movement. The only inputs to the models were the number of vehicles that arrived at those intersections, on a green signal, for the northbound through, for each hour in the last week (i.e. the previous 168 measurements of volume). Note that a separate model is trained for each intersection so that there are 45 intersections and thus 45 corresponding models. So the inputs ($\vec{x}$) to the model were the previous 168 volume measurements and the output (y) was the volume in the next hour. All models were trained on up to 1 year and 11 months of volumes in which the previous 168 hours predicted the next hour.

While the model predicts a single hour ahead of its inputs, it can be used recursively to produce a forecast that extends indefinitely into the future. To do this, we start by using

---

[4] aws.amazon.com

the last week of measured volumes to predict one hour into the future. The predicted value is then added to the end of our input vector, $\vec{x}$. The oldest measurement in $\vec{x}$ is dropped so that it consists of 167 measured volumes and the one predicted volume. Finally, this updated $\vec{x}$ is used as the input to the model again, now predicting two hours after the last measurement. This procedure can technically be repeated indefinitely, but there is a point in which feeding purely forecasted volumes into the model as inputs will lead to divergent forecasts. For our initial tests we chose to only forecast one week (168 hours) beyond our last measurement, resulting in no forecasts being made with solely forecasted volumes as inputs.

Up to this point we have been describing forecasting volumes on just a single phase of the signal for a single movement in each intersection. However, we chose algorithms that intrinsically handle multivariate outputs (discussed below) for a reason. This was because we trained each model to forecast all phases of the signal as well as each movement at the intersection (e.g. northbound through, northbound left turn, northbound right turn, southbound through, southbound right turn, etc.). Once again, we trained a separate model for each of the 45 intersections where their inputs (X) are 168 volume measurements for each combination of movement and signal phase. Their outputs ($\vec{y}$) are one volume prediction for each combination of movement and signal phase.

We used two regression algorithms from the SCIKIT-LEARN module: *LinearRegression* and *RandomForestRegressor*. The main constraints on choosing these algorithms were to allow for multivariate inputs and outputs, to create models that took up modest amounts of disk space (e.g. $\lesssim 1\,\text{MB}$ each), and that would not take longer than a day to complete both the cross-validation and final model training steps on our initial sample. With our initial compute resources, we could run both algorithms through cross-validation training, evaluation of the validation set, and training on all historical data in about 16 hours.

Starting with the *LinearRegression* algorithm allowed for fast and light (both in terms of memory and disk usage) models, and provided a straightforward baseline of comparison for any of the more complex algorithms we chose to experiment with. We selected the *RandomForestRegressor* due to its computational efficiency as well as the ability to handle many model features of various types and structures (e.g. real numbers, integers, categorical data, etc.). The *RandomForestRegressor* algorithm's flexibility would allow us to experiment with nearly any feature we would consider helpful in

producing accurate volume forecasting models.

Figure C.16 shows an example of the last week of measured volumes in a training set from a single movement at a single intersection as well as one week forecasts produced by linear regression. The model reproduces the general features of volumes in this intersection in its predictions: peaks and troughs in the numbers of vehicles corresponding to local day and night, weekdays showing more peaks throughout the day than weekends, lower maxima on weekends than weekdays, steeper slopes during the morning than the evening, and peaks during the week in the morning, noon, and evening. All of these features appear across most of the intersections in our sample as well as almost all of the movements. There are variations across our sample of intersections and there can be quite a bit of variation between volumes on different signal phases of movements. For example, Figure C.16 shows most vehicles arrive when the signal is green for the westbound through movement. However, for the westbound left turn movement, most vehicles arrive when the signal is red. How the total volumes are distributed between movements at each intersection is dependent on the timing plans implemented and the location of the intersection relative to homes, workplaces, schools, highways, etc.

Forecasts can be validated by waiting for the forecasted period to elapse and comparing the actual measurements during that time with the original forecast. Figure C.17 shows the same forecast period as Figure C.16, including the measured volumes for the forecasted week. Residuals are also shown to emphasize the largest differences. While both algorithms produce fairly accurate forecasts, this example highlights that there is still room for improvement in choosing the features to include and in algorithm hyperparameter tuning.

Figures C.18 and C.19 show estimates of the importance of each feature in models for both algorithms from the same intersection and movement as Figure C.16. Only the first 44 features are shown in Figure C.18 (out of all 7392) from the linear regression model due to the significant importance of those features. These features correspond to the last hour of historical data for each signal phase and each movement used to predict just one signal phase and movement. Interestingly, this is showing that the model has found that historical data from many combinations of signal phases and movements in the intersection have predictive power in forecasting the volume for an individual pair of signal phase and movement. Figure C.19 shows all features used with the random forest
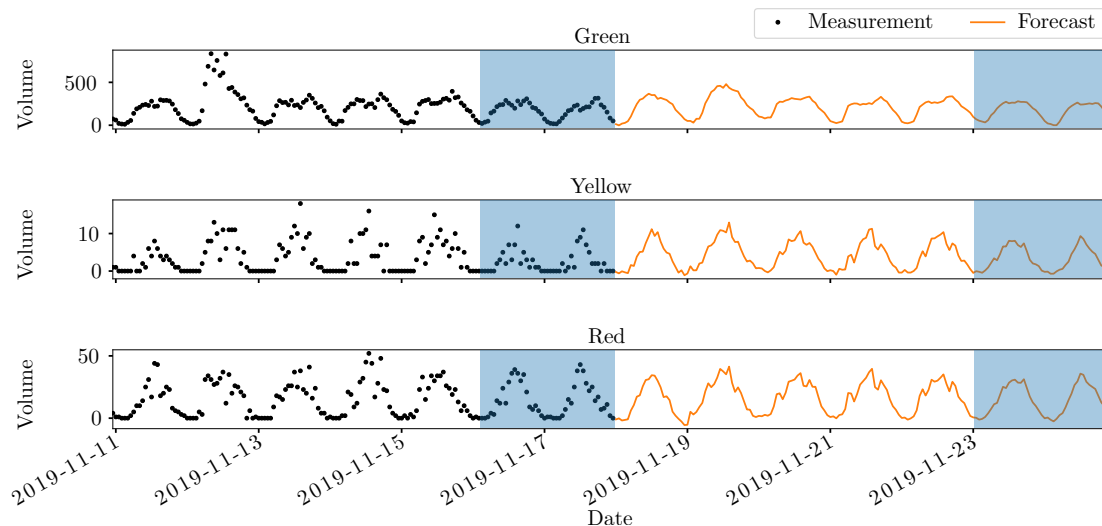
FIGURE C.16: The number of vehicles passing through a single movement in a single intersection as a function of time. Measurements (black points) are binned in one hour intervals. Only the last week of training data are shown. The orange lines are forecasted volumes, while the blue regions indicate weekends. Peaks occur during the day, troughs at night, and the most extreme peaks occur during the morning and evening rush.

used to produce a forecast of all signal phase and movement combinations. Unlike the linear regression models, this model gives significant importance to features using much older volumes (the age of the input historical volume increases to the right in this plot). This may indicate why, for some intersections, one algorithm produces significantly better forecasts than the other.

While comparing measurements and forecasts for each intersection can reveal insights into traffic behaviour, a major goal of this work is to forecast as many intersections as possible, and to automate that process. Figure C.20 shows aggregated forecast errors for all 45 intersections and the two algorithms we have worked with. Intersections are sorted by the mean absolute errors (MAEs) of the linear regression models. There is a gradual increase in the errors across intersections until the three very worst for the linear regression models. The worst linear regression models actually exhibit forecasts that drastically diverge from the measured volumes, showing there exists some potential for instability in models made with that algorithm on these data. The random forest models do not exhibit any such extreme divergence for any intersection and so appear to be a more stable option for forecasting these volume data from these features.
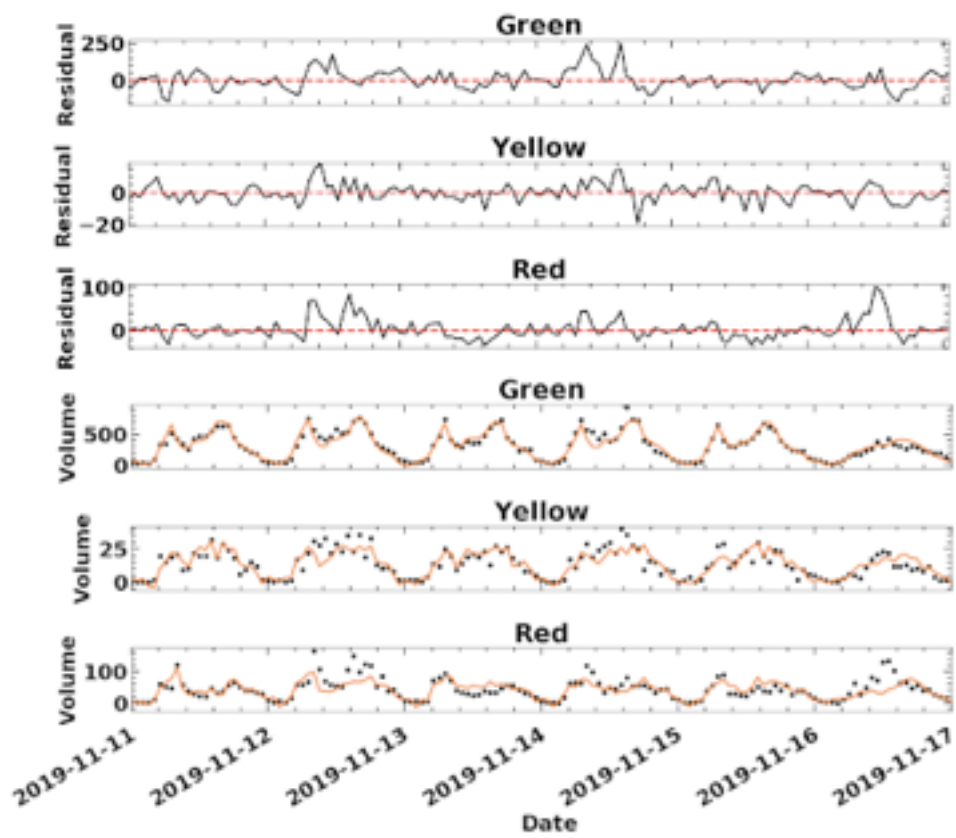
FIGURE C.17: The bottom three panels show the same forecasts as in Figure C.16 (orange lines) compared to the measured volumes (black points) that were not included in training this model. The top three panels show the residuals for each of the signal phases as a function of time.
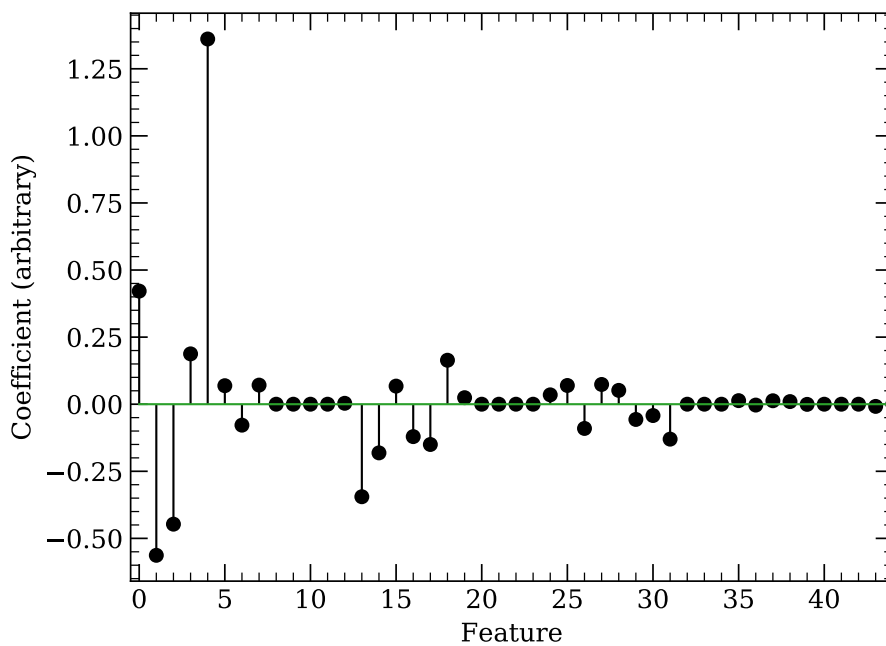
FIGURE C.18: The first 44 model coefficients from the linear regression algorithm for a single intersection corresponding to a single movement. These features correspond to the last hour of historical data for all signal phases and movements in the intersection used to forecast an individual signal phase and movement. Importantly, this is showing that the models are using volumes from multiple movements in the intersection to predict a single movement.
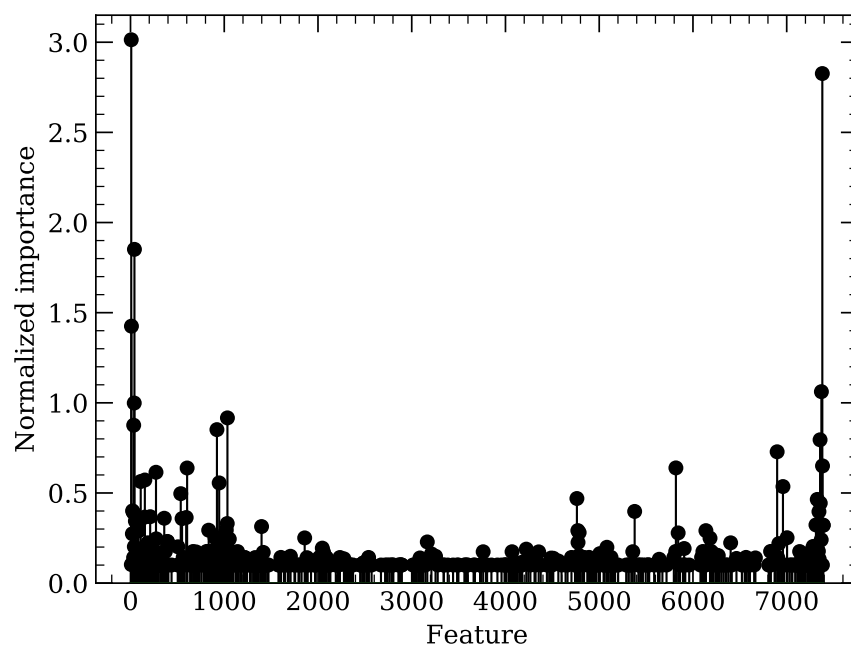
FIGURE C.19: Mean decrease in impurity importance metrics for all features from the random forest model for the same intersection as Figure C.18, normalized by the standard deviation of the importances for all constituent tree estimators. The ordering of features is the same as in Figure C.18. There is significant importance in features that are nearly a week old relative to the hour to predict, which is very different from the linear regression model.
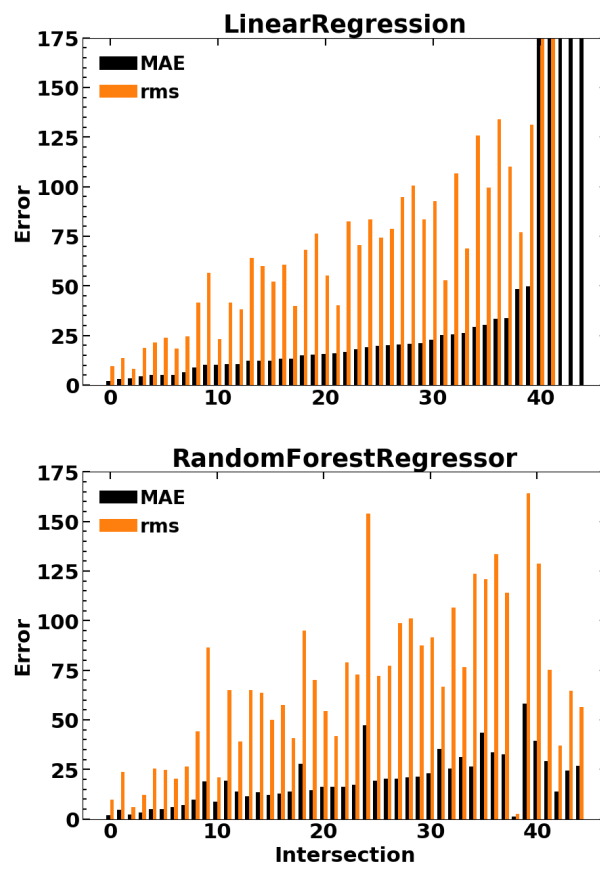
FIGURE C.20: Aggregated errors in forecasts for our initial sample of 45 intersections, with intersections ordered by the MAE (black bars) of the linear regression forecasts. Root mean square errors are shown as orange bars. The last three intersections on the right exhibited forecasts from the linear regression models that diverged from the measured volumes.
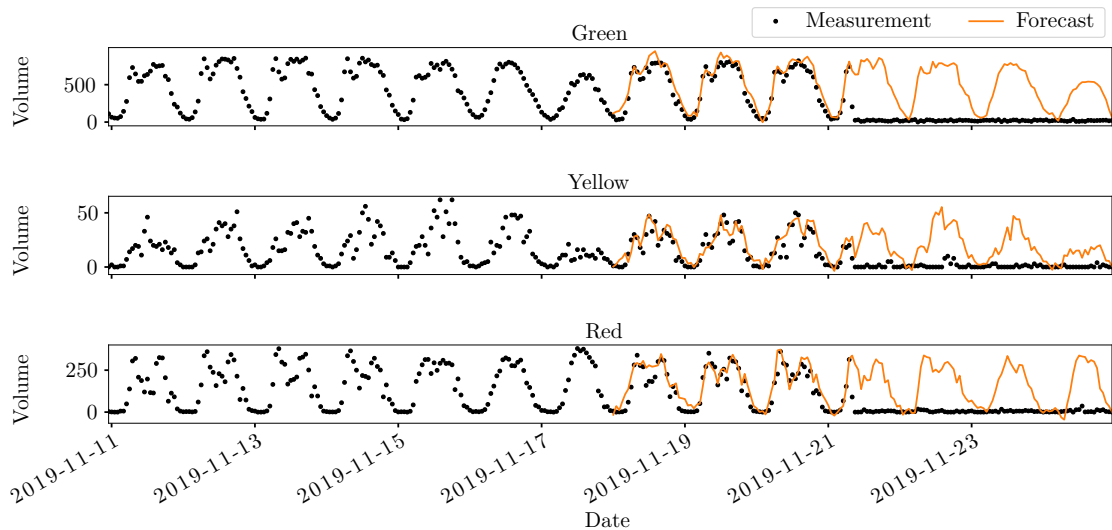
FIGURE C.21: Volume versus time for all signal phases in a single movement at a single intersection, again with measurements show as black points and forecasts as orange lines. The model was trained on data up to November 11, 2019 and the forecast was made for the following week. The forecasted week of data was measured and aggregated errors were calculated (this intersection has the highest errors from both algorithms where the forecasts do no diverge). We found that starting on November 13, all volumes for this intersection began being recorded as zero. This was due to a change in the configuration made by the customer, which was unexpected.

To highlight the strength of using these aggregated error statistics from our forecasts in automating the process of identifying problems, Figure C.21 shows the measured and forecasted volumes versus time for intersection 39, which has the highest errors from both algorithms but does not experience divergence. This clearly reveals a dramatic change in volumes that would not be expected from the previously measured volumes. There is a period at which the measured volumes all become zero while the forecasts predict the typical highs and lows. This example is associated with a change the customer made to the configuration file for this intersection, and is a case where Miovision should reach out to the customer. So by simply starting with the intersection with the worst error we immediately found a problem rather than having to look through each intersection hoping to find something worth the effort of searching.

C.6.4 Future work

As the forecast residuals in Figure C.17 show, there is still room for improvement in these models to consistently produce accurate predictions of volumes. The models presented here only have historical volumes as inputs so there is plenty of opportunity to add features with additional predictive power. Information as simple as if the prediction day is a weekday, a holiday, or lands on daylight saving time is potentially extremely useful. Weather conditions can have an impact on traffic behaviour and should be considered as inputs to these models.

A straightforward improvement to this process would be adding more intersections to the sample. One of the main goals of this work is to build infrastructure to be continuously and automatically learning about intersections and monitoring them for changes. With more intersections to investigate we will learn more and can drive improvements to this forecasting and intersection optimization more quickly.

Improvements to these forecasts should also include producing some form of forecast intervals around the point forecasts shown here. Accurately estimating how certain each forecast is will be an important step in building trust in these forecasts and in making the forecasts more complete.

It could also be useful to train separate models that will predict out to different horizons. So maybe a forecast of the next 24 hours, at 5 minute intervals could be made separately from these week long forecasts. Another set of models that produce forecasts of peak vehicle volumes out to several weeks or months could also be made.

Investigations into producing automatic alerts from these forecasts should also be undertaken. Previous alerts have primarily been built on thresholds for the measurements being too high, too low, etc. A strength of making predictions regularly, based on what was recently happening at an intersection means much more complex searches for changes can be accomplished. Rather than having to think of and implement thresholds around every change, the forecasts simply provide the answer to "is traffic behaving like it was previously?" If the answer is "no" then someone should probably look into what has changed, as simple as that. There is a large variety of improvements and extensions this work could undergo which would provide significant value to Miovision and its customers.

Bibliography

Bester C. J., Meyers W. L., 2007, in South African Transport Conf. Ser.. Available at: https://repository.up.ac.za/handle/2263/5672, p. 560

Kluyver T., et al., 2016, in Loizides F., Scmidt B., eds, 20th International Conference on Electronic Publishing. Positioning and Power in Academic Publishing: Players, Agents and Agendas. IOS Press, Netherlands, p. 87

McKinney W., 2010, in Stéfan van der Walt Jarrod Millman eds, Python in Science Conf. Ser.. Available at: http://conference.scipy.org/proceedings/scipy2010/, p. 56

Oliphant T. E., 2006, A guide to NumPy. Vol. 1, Trelgol Publishing USA

Pedregosa F., et al., 2011, Journal of Machine Learning Research, 12, 2825

Shao C., Liu X.-m., 2012, Discrete Dynamics in Nature and Society, 2012

Transportation Research Board 2016, Highway capacity manual : a guide for multimodal mobility analysis. The National Academies Press, Washington, D.C.